

REPORT DOCUMENTATION PAGE			Form Approved OMB No. 0704-0188	
Public reporting burden for this collection of information is estimated to average 1 hour per response, including the time for reviewing instructions, searching existing data sources, gathering and maintaining the data needed, and completing and reviewing the collection of information. Send comments regarding this burden estimate or any other aspect of this collection of information, including suggestions for reducing this burden, to Washington Headquarters Services, Directorate for Information Operations and Reports, 1215 Jefferson Davis Highway, Suite 1204, Arlington, VA 22202-4302, and to the Office of Management and Budget, Paperwork Reduction Project (0704-0188), Washington, DC 20503.				
1. AGENCY USE ONLY (Leave blank)		2. REPORT DATE 9 Jan 97		3. REPORT TYPE AND DATES COVERED
4. TITLE AND SUBTITLE A Climatology of Mesoscale Wave Disturbances Seen In Mesonet Data During Storm-Fest			5. FUNDING NUMBERS	
6. AUTHOR(S) Leanne Marie Siedlarz				
7. PERFORMING ORGANIZATION NAME(S) AND ADDRESS(ES) North Carolina State University			8. PERFORMING ORGANIZATION REPORT NUMBER  96-140	
9. SPONSORING/MONITORING AGENCY NAME(S) AND ADDRESS(ES) DEPARTMENT OF THE AIR FORCE AFIT/CIA 2950 P STREET WPAFB OH 45433-7765			10. SPONSORING/MONITORING AGENCY REPORT NUMBER	
11. SUPPLEMENTARY NOTES				
12a. DISTRIBUTION AVAILABILITY STATEMENT Unlimited			12b. DISTRIBUTION CODE	
13. ABSTRACT (Maximum 200 words)			<div style="border: 1px solid black; padding: 5px; text-align: center;"> <b>DISTRIBUTION STATEMENT A</b>  Approved for public release  Distribution Unlimited </div> <div style="font-size: 2em; text-align: center; margin-top: 20px;">19970117 188</div>	
14. SUBJECT TERMS			15. NUMBER OF PAGES 200	
			16. PRICE CODE	
17. SECURITY CLASSIFICATION OF REPORT	18. SECURITY CLASSIFICATION OF THIS PAGE	19. SECURITY CLASSIFICATION OF ABSTRACT	20. LIMITATION OF ABSTRACT	

## ABSTRACT

SIEDLARZ, LEANNE M. A Climatology of Mesoscale Wave Disturbances Seen in Mesonet Data During STORM-FEST. (Under the direction of Dr. Steven E. Koch.)

Many studies have found mesoscale gravity waves to be the likely trigger in severe weather outbreaks. In order to better recognize a gravity wave as such and move towards predicting an event and the weather changes associated with it, we must increase our basic knowledge of these waves by answering questions on their frequency of occurrence, typical magnitude and the conditions under which they occur. This study is an effort to do just that by examining the mesoscale surface data collected during the STORM-Fronts Experiment System Test, STORM-FEST experiment performed by the US Weather Research Program in the central US from 1 February through 15 March 1992.

Thirteen pressure pulse events (amplitude  $\geq 0.2$  mb, period 1 - 6 hrs) were identified in the surface pressure data gathered during STORM-FEST, involving 34% of the total hours investigated. These events were ranked according to their average amplitude. The three top-ranked events were analyzed in detail and all three of the events displayed evidence of a gravity wave in the high perturbation pressure-wind covariances and in the continuity of the wave signatures. A variety of wave types were evident in each of the cases, including wavelets, wave trains and waves of elevation and depression.

Four wave-detection techniques were compared. It was found that the wave was easiest to follow in the Barnes Time-to-Space Conversion (TSC) objective analysis, since it produced the impression of an animated wave. Sensitivity tests were performed on the variables used in the objective analysis including the TSC interval, grid spacing, use of single instead of multiple TSC advection vectors, and choice of bandpass filter width. The comparative results involving a single and multiple advection vectors suggested a single vector would likely do fairly well at representing a planar wave, while multiple advection vectors would be recommended for arc-shaped waves. It was determined that the TSC interval needs to be sufficiently large (~ 45 min) to allow for the advantages of this analysis

method to be realized. The results from using a grid-length larger than the customarily recommended value produced more desirable, smoother wave features.

The characteristics of the wave features in the February 14 - 15 event displayed phase velocities of  $21.6 \text{ ms}^{-1} \pm 5.9 \text{ ms}^{-1}$  (standard deviation), wavelengths of  $200 \text{ km} \pm 41 \text{ km}$  and periods of  $2.3 \text{ hr} \pm 1.2 \text{ hr}$ . The characteristics from the February 16 - 18 event were  $19.9 \text{ ms}^{-1} \pm 6.2 \text{ ms}^{-1}$  for phase velocity,  $225 \text{ km} \pm 31 \text{ km}$  for wavelength and  $3.5 \text{ hr} \pm 3 \text{ hr}$  for the period. The March 9 event displayed phase velocities of  $27.9 \text{ ms}^{-1} \pm 6.8 \text{ ms}^{-1}$ , wavelengths of  $260 \text{ km} \pm 32 \text{ km}$  and periods of  $2.6 \text{ hr} \pm 1.2 \text{ hr}$ .

The positive pressure perturbation areas in the objective analysis were very closely aligned with the cloudbands which at times caused the suggested wave shape to be less smooth. In addition, the cloudbands and waves appeared to move together at nearly the same speeds, suggesting that some type of co-dependency existed between the waves and bands. At times the waves were evident before the cloudbands suggesting that the bands perhaps developed in response to the waves whereas, in other cases, convection developed before the waves and the waves appeared to develop in response to the convection. The pressure-wind correlations in the February 14 - 15 case appeared closely related to the strength of the wave signatures. High correlations were found in the last two waves observed during the February 16 - 18 event which appeared to be forced by convection.

Four events occurred in an environment consistent with the Uccellini and Koch (1987) conceptual model of synoptic-scale features typically found during mesoscale gravity wave events. These wave events displayed the largest average pressure amplitudes. Three of these events were analyzed in detail, and each showed evidence of a gravity wave. Since these three were among the four events that fit the model, the results support the use of this synoptic model as a mesoscale gravity wave forecasting tool. In addition, results from investigating the single criterion of a jet streak near the inflection axis suggest that this feature is a sufficient but not necessary condition for a gravity wave to occur.

**A CLIMATOLOGY OF MESOSCALE WAVE DISTURBANCES  
SEEN IN MESONET DATA DURING STORM-FEST**

by

**LEANNE MARIE SIEDLARZ**

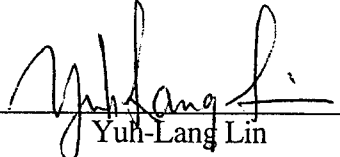
A Thesis submitted to the Graduate Faculty of  
North Carolina State University  
in partial fulfillment of the  
requirements for the Degree of  
Master of Science

**MARINE, EARTH AND ATMOSPHERIC SCIENCES**

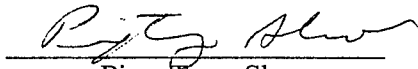
Raleigh

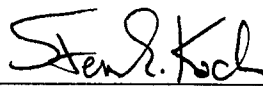
1996

**APPROVED BY:**

  
Yuh-Lang Lin

  
John Monahan

  
Ping-Tung Shaw

  
Steven E. Koch  
Chairman of Advisory Committee



## DEDICATION

To my loving husband for his unrelenting support and encouragement, and to our Lord  
through whom all things are possible.

## BIOGRAPHY

Leanne Marie Siedlarz is currently an Air Force Weather Officer assigned to the Air Force Institute of Technology (AFIT).

She [REDACTED] and lived in Pennsylvania throughout her childhood. She attended Kent State University in Kent, Ohio on a 4-year United States Air Force scholarship and graduated Magna Cum Laude in May, 1988 with a Bachelors Degree in Applied Mathematics at which time she was commissioned as a Second Lieutenant. The following December she entered the Air Force's Basic Meteorology Program as a student at Texas Agricultural and Mechanical University. Upon completion in December, 1989 Leanne was assigned to Pope Air Force Base, North Carolina as a Wing Weather Officer. Her subsequent assignment in 1992 was as the Assistant Staff Weather Officer to the Army's XVIII Airborne Corps at Fort Bragg, North Carolina. Leanne was promoted to the rank of Captain in May 1992. At the end of her tour at Fort Bragg, she was selected by AFIT to attend North Carolina State University to obtain an advanced degree in meteorology.

Upon completion of her Masters Degree, Leanne will be assigned to the Air Education and Training Center (AETC) in San Antonio, Texas where she will monitor the NEXRAD and Automated Weather Distribution System programs of those units under AETC command.

Leanne Marie Siedlarz is married to Captain Joseph Francis Siedlarz of Vincentown, New Jersey.

## ACKNOWLEDGMENTS

The United States Air Force and Air Force Institute of Technology provided the opportunity and funding required to obtain this advanced degree. Additional monetary support was provided by the COMET Outreach Project grant #S96-75675.

I wish to thank my committee members, Dr. Steven E. Koch (Chairman), Dr. Yuh-Lang Lin, Dr. John Monahan and Dr. Ping-Tung Shaw, for their time and guidance. Their support was instrumental in this study and the completion of this endeavor.

I would like to express my thanks to the developers of the Zeb data-display software and those responsible for the STORM-FEST data collection and subsequent distribution. Without the data, the ease with which access to it were possible and the varied display options, this study would not have been possible.

I am grateful to Devin Kramer for developing the Time-to Space Conversion (TSC) program, for his programming insight and scripts, and for his willingness to take the time to explain whatever was asked. Thanks also to Chris O'Handley for his guidance on the use of the programs used in the analysis and for his various suggestions. I would like to thank Yi Jin for producing the MM4 model data, Mike Trexler for his GEMPAK and Zeb tutoring sessions, and Kyle Turner and Gail Andrews for their work with digitizing barographs and data manipulation. One of the most rewarding benefits from this pursuit has been the friendships that have developed through working with these individuals. I would also like to acknowledge additional fellow students: Bob Rozumalski, Mike Adams, Chris Vandersip and Tony Krogh, who have had an impact on the successful completion of this degree.

# TABLE OF CONTENTS

	Page
LIST OF TABLES.....	vii
LIST OF FIGURES.....	viii
1. INTRODUCTION.....	1
2. LITERATURE REVIEW.....	5
2.1 Gravity Wave Theory.....	5
2.2 Gravity Wave Generation Mechanisms.....	14
2.2.1 Geostrophic Adjustment.....	14
2.2.2 Shearing Instability.....	17
2.2.3 Unbalanced Frontogenesis.....	18
2.2.4 Topography.....	19
2.2.5 Convection.....	22
2.3 Gravity Wave Maintenance Mechanisms.....	28
2.3.1 Constant Energy Supply.....	28
2.3.2 Energy-Loss Prevention.....	30
2.3.3 Solitary Waves.....	31
2.4 Detection Techniques.....	31
3. DATA.....	34
3.1 Surface Data.....	34
3.2 Upper-Air Data.....	35
3.3 Satellite and Radar Data.....	36
4. OBJECTIVES AND ANALYSIS METHODOLOGY.....	38
4.1 Objectives.....	38
4.1.1 Identifying potential gravity wave occurrences.....	39
4.1.2 Evaluation of the Uccellini and Koch (1987) Gravity Wave Synoptic Model.....	41
4.2 Gravity Wave Analysis Methods Using Surface Data.....	41
4.2.1 Data Handling.....	42
4.2.2 Spectral Analysis.....	42
4.2.3 Bandpass Filtering.....	45
4.2.4 Determining Wave Phase Velocities.....	49
4.2.5 Pressure-Wind Covariance.....	50
4.2.6 Time-to-Space Conversion Objective Analysis.....	51
5. SENSITIVITY TESTS.....	56

5.1	Choice of Filter Bandpass Interval .....	56
5.1.1	Filter Effects on Pressure Traces .....	56
5.1.2	Filter Effects on Objective Analysis .....	58
5.2	Wave Tracking Techniques .....	59
5.2.1	Subjective Analysis of Pressure-Perturbation Fields .....	60
5.2.2	Conventional Barnes Objective Analysis of Pressure Perturbation Values .....	62
5.2.3	Use of Single or Multiple Advection Vectors in Objective Analysis .....	62
5.3	Sensitivity of Analysis to Time-to-Space Conversion Interval .....	63
5.4	Sensitivity of Analysis to Choice of Grid-length .....	64
6.	CASE STUDIES .....	66
6.1	Case Selection and Results from Synoptic Model Verification .....	66
6.2	February 14 - 15 1992 .....	69
6.2.1	Synoptic Overview .....	69
6.2.2	Analysis Results .....	71
6.3	February 16 - 18 1992 .....	83
6.3.1	Synoptic Overview .....	83
6.3.2	Analysis Results .....	85
6.4	March 8 - 10 1992 .....	98
6.4.1	Synoptic Overview .....	99
6.4.2	Analysis Results .....	101
7.	CONCLUSIONS .....	111
8.	REFERENCES .....	116

## LIST OF TABLES

		Page
Table 5.1	Sensitivity tests.....	56
Table 6.1	Pressure pulse ranking from STORM-FEST data of the 13 identified events.....	66
Table 6.2	Contingency table-jet streak near inflection axis.....	68
Table 6.3	Phase speeds, wavelengths, periods and phase directions for the waves identified in the February 14-15 gravity wave event.....	73
Table 6.4	Phase speeds, wavelengths, periods and phase directions for the waves identified in the February 16-18 gravity wave event.....	88
Table 6.5	Phase speeds, wavelengths, periods and phase directions for the waves identified in the March 9 gravity wave event.....	102

## LIST OF FIGURES

	Page
Figure 2.1	Internal gravity wave intrinsic frequency of horizontal wavenumber ..... 122
Figure 2.2	Gravity-wave energy and phase propagation ..... 123
Figure 2.3	Gravity-wave trapping by atmospheric temperature structure..... 124
Figure 2.4	Idealized vertical cross section of a linear plane gravity wave ..... 125
Figure 2.5	Height variations in the phase relations between the horizontal wind component in the direction of wave propagation and the wave-induced vertical motions for an erect and tilted wave ..... 126
Figure 2.6	A wave disturbance larger than what can be supported by the atmosphere..... 127
Figure 2.7	Schematic of transverse ageostrophic wind components and patterns of divergence and convergence associated with the entrance and exit region of the jet streak ..... 128
Figure 2.8	Schematic relating the along-stream ageostrophic wind at upper levels to patterns of divergence and convergence associated with an upper-level baroclinic wave and surface high- and low-pressure couplet..... 129
Figure 2.9	Surface and 300 mb synoptic features which characterize mesoscale gravity-wave events..... 130
Figure 2.10	Schematic of surface pressure and wind field during the mature stage of a squall-line thunderstorm..... 131
Figure 2.11	Surface pressure, wind fields and precipitation distribution during squall line mature stage ..... 132
Figure 2.12	Pressure trace from a typical undular bore ..... 133
Figure 3.1	Locations of the ASOS, AWOS and barograph surface observation stations during STORM-FEST ..... 134
Figure 3.2	Locations of the ICN surface stations..... 135
Figure 3.3	Locations of the PAM II surface stations during STORM-FEST..... 136
Figure 4.1	Raw pressure trace from station P12 from February 14-15, 1992 ..... 137
Figure 4.2	Raw Pressure trace from station P43 from February 14-15, 1992..... 138
Figure 4.3	Sample autospectrum for station P43 of pressure from the February 14 gravity-wave event ..... 139

Figure 4.4	Histogram of significant peaks identified from the autospectral analysis from the February 14 gravity-wave event.....	140
Figure 4.5	Depiction of axis-tracking method used to determine the wave-phase velocity at each individual station.....	141
Figure 4.6	Average $\overline{p'u^*}$ correlation values (*100) determined over the 6-hr period of wave activity at each station for the February 14 gravity-wave event.....	142
Figure 5.1	Raw, narrow-filtered and wide-filtered pressure traces from the February 14 gravity-wave event.....	143
Figure 5.2	Time-to-Space Conversion $p'$ plots from the 14 February gravity-wave event for Test 1 .....	144
Figure 5.3	Subjectively analyzed wave isochrones from the 14 February gravity-wave event for A-, B- and C-.....	145
Figure 5.4	Objectively determined wave isochrones from the 14 February gravity-wave event for A-, B- and C-.....	146
Figure 5.5	Conventional Barnes analysis of the 14 February gravity-wave event....	147
Figure 5.6	Time-to-Space Conversion $p'$ plots from the 14 February gravity-wave event for Test 4 .....	148
Figure 5.7	Time-to-Space Conversion $p'$ plots from the 14 February gravity-wave event for Test 2 .....	149
Figure 5.8	Time-to-Space Conversion $p'$ plots from the 14 February gravity-wave event for Test 3 .....	150
Figure 6.1	Infrared satellite imagery valid 1201 UTC 14 February with surface features.....	151
Figure 6.2	Infrared satellite imagery valid (a) 1332 UTC and (b) 2032 UTC 14 February.....	152
Figure 6.3	Radar imagery valid 2102 UTC, 2132 UTC, 2202 UTC and 2232 UTC 14 February .....	153
Figure 6.4	Infrared satellite imagery valid (a) 2202 UTC 14 February and 0032 UTC 15 February .....	154
Figure 6.5	Time-to-Space Conversion output for wide-filter bandpass pressure data with a grid-length value of 25 km and a tau value of 50 min .....	155
Figure 6.6	Radar imagery valid 0202 UTC 14 February .....	159
Figure 6.7	Infrared satellite imagery valid 0232 UTC 15 February .....	159



Figure 6.8	Raw pressure traces from the 14 February gravity-wave event for stations DDC, MHK, P16, P17 and P18.....	160
Figure 6.9	Wave types as seen in the raw pressure traces from selected locations for 14 and 15 February .....	161
Figure 6.10	Raw pressure trace from station P19 showing a strong wave of elevation within a train.....	162
Figure 6.11	MM4 model 24-hr forecast of 300 mb heights, actual winds and geostrophic winds valid 14 February 1200 UTC.....	163
Figure 6.12	Infrared satellite imagery valid 17 February 0002 UTC.....	164
Figure 6.13	Radar and infrared satellite imagery valid (a) 0202 UTC and (b) 0502 UTC 17 February.....	165
Figure 6.14	Radar and infrared satellite imagery valid 1002 UTC 17 February.....	166
Figure 6.15	Radar imagery valid 1202 UTC 17 February .....	166
Figure 6.16	Radar and infrared satellite imagery valid (a) 1502 UTC and (b) 1702 UTC 17 February.....	167
Figure 6.17	Radar and infrared satellite imagery valid (a) 2002 UTC and (b) 2202 UTC 17 February.....	168
Figure 6.18	Histogram of significant peaks identified in the autospectral analysis for 45 stations during the 17 February gravity-wave event .....	169
Figure 6.19	Average $\overline{p'u^*}$ correlation values (*100) determined over a 3-hr period of wave activity at each station for the 17 February gravity-wave event.....	170
Figure 6.20	Time-to-Space Conversion output for the bandpassed ( $f_{c1} = 0.002 \text{ min}^{-1}$ and $f_{c2} = 0.01 \text{ min}^{-1}$ ) pressure data with a grid-length of 32 km, and a tau value of 50 min for 17 February gravity-wave event.....	171
Figure 6.21	Objectively determined wave isochrones from the 17 February gravity-wave event .....	176
Figure 6.22	Raw pressure trace from station P29 from February 17/1500 - 18/0000 UTC.....	178
Figure 6.23	Raw pressure trace from station P02 from February 17/0200 - 2100 UTC.....	179
Figure 6.24	MM4 model 11-hr forecast of 300 mb heights, actual winds and geostrophic winds valid 2300 UTC 16 February.....	180
Figure 6.25	Satellite imagery valid 0102 UTC 9 March.....	181
Figure 6.26	Analysis valid 0000 UTC 9 March for (a) surface and (b) 500 mb .....	182

Figure 6.27	Analysis valid 0300 UTC 9 March for (a) surface and (b) 500 mb .....	183
Figure 6.28	Depiction of the relationship between the dryline, CFA and developing convection .....	184
Figure 6.29	Radar imagery valid (a) 0202 UTC, (b) 0302 UTC, (c) 0402 UTC (d) 0602 UTC, (e) 0702 UTC, (f) 0802 UTC, (g) 0902 UTC and (h) 1002 UTC 9 March .....	185
Figure 6.30	Analysis valid 0600 UTC 9 March for (a) surface and (b) 500 mb .....	189
Figure 6.31	Response for filter used in the 9 March gravity-wave event .....	190
Figure 6.32	Isochrones from the objective analysis for the 9 March gravity-wave event.....	191
Figure 6.33	Time-to-Space Conversion output for the bandpassed ( $f_{c1} = 0.0028 \text{ min}^{-1}$ and $f_{c2} = 0.0330 \text{ min}^{-1}$ ) pressure data from 9 March with a grid-length of 32 km, and a tau value of 50 min from 9 March.....	194
Figure 6.34	Digitized pressure trace from Salina, Kansas valid 0300 - 0700 UTC 9 March.....	198
Figure 6.35	Raw pressure trace from Princeton, Missouri valid 0000 - 1200 UTC 9 March.....	199
Figure 6.36	Average $\overline{p'u^*}$ correlation values (*100) determined over a 3-hr period of wave activity at each station for the 9 March gravity-wave event.....	200

## 1. Introduction

As observation methods improve, there is an increasing awareness of the existence and importance of atmospheric wave disturbances, including mesoscale (approximately 50 - 500 km) gravity waves, by both observational and research meteorologists. New observing systems such as Automated Surface Observing Systems (ASOS), wind profilers, WSR-88D Doppler radar, the new series of Geostationary Operational Environmental Satellites I-M and the Advanced Microwave Sounding Units are providing an increase in atmospheric information available on a more frequent basis and at resolutions not previously available or economically feasible (Friday 1993). Wind profiler data have been used to study the vertical structure of gravity waves (Ralph et al. 1993; Trexler et al. 1996). The methods used in the present study involve the analysis primarily of surface data, of which ASOS data are an integral contributor. ASOS was developed to provide a continuous weather watch with over 850 surface observing stations. One benefit of the system is a significant increase in the number of observing sites (Friday 1993). This increase has led to a decrease in average station spacing across the United States which has made it easier to follow mesoscale gravity waves, especially those of shorter wavelengths. A much more important advantage is the ability to obtain high temporal resolution (1 - 5 min), digital data. With the addition of ASOS data and objective wave tracking methods that exploit the temporal details, there has been an increase in interest in the detection and possible forecasting of gravity wave events (Koch and O'Handley 1996). Whether it be in clouds, precipitation bands or severe weather, observations and numerical experiments indicate that gravity waves are an integral factor in the weather we experience.

Gravity waves were first discovered by glider pilots and were described as "thermal waves". A sailplane pilot would climb in a spiral motion under a cumulus cloud, then shoot to the upshear side of the cloud, climb and then ride the wave. In journal articles from the 1940s, 1950s and early 1960s, reference was made to pressure pulsations,

oscillations and short period variations in pressure and winds. The term gravity wave started to appear more frequently beginning in the 1960s. Some of the early investigators who used this term include Wagner (1962), Bosart and Cussen (1973), Uccellini (1975) and Eom (1975).

The majority of mesoscale gravity wave case studies are of large-amplitude ( $>2.0$  mb half-amplitude) wave events despite the fact that these events are not that common. Bosart and Sanders (1986) state that their New England experience with a large-amplitude gravity wave confirms the claim by Pecnick and Young (1984) that the type of large-amplitude event they analyzed occurs at a given midwestern point perhaps only once per year.

In the large-amplitude case investigated by Schneider (1990), the wave passage was accompanied by pressure falls, winds in excess of  $25 \text{ ms}^{-1}$ , cloud-to-ground lightning and heavy snowfall. The largest amplitude wave was characterized by a surface minimum lower than that of the cyclone. During interaction with the wave disturbance, the cyclone's pressure fell 7 mb in 1 hr. No large-amplitude waves were identified in the STORM-FEST dataset in the present research; however, evidence suggests that smaller-amplitude waves can still play a significant role in determining the weather.

As stated by Einaudi (1989), the frequency of occurrence, and the amplitude, period, horizontal wavelength and vertical structure of gravity waves will determine the statistical significance of their role in tropospheric dynamics as well as their importance as a forecasting consideration. Objectives of the present study include determining such mesoscale gravity wave characteristics, using the surface data obtained during the intensive data-gathering effort of STORM-FEST (Cunnings and Williams 1993). The primary objectives of STORM-FEST included investigating the structure and evolution of fronts, embedded precipitation and associated mesoscale phenomena in winter storms over the

central United States. The field phase of STORM-FEST during which data was gathered was 1 February through 15 March 1992.

Additional main objectives of the present study include performing an analysis of the synoptic situation in the STORM-FEST region for 2 February through 13 March to determine whether features were present that have been identified by Uccellini and Koch (1987) as typically being found during mesoscale gravity wave events. The typical characteristics of these waves were: wavelength of 50-500 km, period between 1-4 hr, surface pressure perturbations of 0.2-7 mb and phase velocities of 10-25  $\text{ms}^{-1}$ . Their 13-case climatology showed that the waves appeared to be excited in the exit region of a jet streak that was propagating out of the base of a negatively tilted short wave trough. The waves then propagated over an area bounded to the southwest by the axis of inflection, to the northeast by the ridge in the 300 mb height field, to the northwest by the jet streak and to the southeast by a stationary or warm front. No explanation was provided for the northern boundary, though it may be related to the moisture field (Powers and Reed 1993). The synoptic patterns for the STORM-FEST cases are analyzed in Section 6. Identifying potential gravity wave events during STORM-FEST and determining how often they occurred are also of interest. The effects of applying a bandpass filter to the raw data are investigated as are various wave tracking techniques. Sensitivity tests are also performed on the objective wave detection method used. Possible mesoscale gravity generation mechanisms, although not examined in detail, are qualitatively considered.

The ultimate goal is to be able to identify a gravity wave as such and forecast when it will occur or reach a given location as well as what changes in the weather are likely to accompany the wave. Although not all aspects of this goal are addressed in the present study, the synoptic conceptual model apparently conducive to gravity wave development, is tested using the STORM-FEST data. This model, depending on applicability, will allow a forecaster to identify ideal conditions for development in advance. Further documentation

on weather modifications apparently brought on by the wave, including wave-convection interactions, is provided in the case studies herein. Finally, a reliable method for detecting and tracking mesoscale gravity waves with 5-min surface data is presented as a chief means of obtaining the goal of forecasting the weather associated with propagating gravity waves.

The details of gravity wave theory, wave source mechanisms, identified maintenance mechanisms and typical gravity wave analysis methods are presented in Section 2. Data used in the study are summarized in Section 3. The objectives of the present study are presented and the methods used are explained in detail in Section 4. Sensitivity tests performed on the February 14 1992 case, including filter bandpass interval effects and a comparison of wave tracking techniques, are presented in Section 5. Results from the three detailed case studies that showed the greatest potential for being an actual gravity wave are presented in Section 6. Such features as wavelength, period, phase velocity and inferred vertical structure are presented for those events analyzed. Also discussed is a summary of which days displayed mesoscale wave signals.

## 2. Literature Review

### 2.1 Gravity Wave Theory

In addition to modulating every atmospheric variable, gravity waves are responsible for the transport of momentum and energy vertically and horizontally (Hooke 1986). Gravity waves can release potential instability that can lead to convection and severe weather. Another potentially dangerous product of gravity waves, particularly for small aircraft, is Clear Air Turbulence (CAT). Since gravity waves are capable of playing a role in a variety of meteorological phenomena, it is obvious why there is an interest in studying these waves. The gravity wave theory presented here applies to internal gravity waves, although it is extended to include gravity-inertia waves.

Internal gravity waves are those disturbances in which the restoring force of buoyancy acts on parcels displaced from hydrostatic equilibrium. Consider the oscillation of a parcel of air which has been displaced vertically along a dry adiabat from its equilibrium position. Of interest is the range of parcel displacements where pressure equilibrium is maintained, but thermal equilibrium is not (i.e., the pressure deviations between parcels and their environment are ignored.) If the total variables in the equation of state,  $p = \rho RT$  (where  $p$  represents pressure,  $\rho$  density,  $R$  the universal gas constant and  $T$  temperature in °K), are written as a mean value plus a perturbation value and are logarithmically differentiated, the result is

$$\frac{p'}{p} = \frac{\rho'}{\rho} + \frac{T'}{T}. \quad (2.1)$$

In an unstable atmosphere, when the parcel is lifted, it finds itself at a higher temperature than its surroundings. From (2.1), since pressure equilibrium is maintained, the parcel is less dense and therefore continues to rise and convection is initiated. However, in a statically stable atmosphere, when the parcel is displaced upward, it has a lower temperature than its environment, and therefore is less dense than its surroundings. The

parcel slows, sinks and overshoots its equilibrium level, begins to rise again, overshoots and the oscillatory process continues. The atmosphere communicates this density disequilibrium through the generation of gravity waves (Hooke 1986). In an ideal atmosphere, the parcel oscillations occur at the Brunt-Väisälä frequency,  $N$ , where

$$N^2 = \frac{g}{\bar{\theta}} \frac{d\bar{\theta}}{dz} \quad (2.2)$$

and  $\bar{\theta}$  is the basic-state potential temperature,  $g$  is the acceleration due to gravity and  $z$  is the vertical coordinate.

In deriving a wave equation that is representative of a mesoscale gravity wave, a two-dimensional, nonrotating, inviscid, Boussinesq atmosphere is assumed. The applicable governing equations written in Cartesian coordinates are as follows:

$$\text{Horizontal Momentum} \quad \frac{Du}{Dt} + \frac{1}{\rho} \frac{\partial p}{\partial x} = 0 \quad (2.3)$$

$$\text{Vertical Momentum} \quad \frac{Dw}{Dt} + g + \frac{1}{\rho} \frac{\partial p}{\partial z} = 0 \quad (2.4)$$

$$\text{Boussinesq Eq. of Continuity} \quad \frac{\partial u}{\partial x} + \frac{\partial w}{\partial z} = 0 \quad (2.5)$$

$$\text{Thermodynamic} \quad \frac{D\theta}{Dt} = 0 \quad (2.6)$$

where

$$\frac{D}{Dt} = \frac{\partial}{\partial t} + u \frac{\partial}{\partial x} \quad (2.7)$$

The variables represent conventional values: ( $u$ ) horizontal motion, ( $w$ ) vertical motion, ( $t$ ) time and ( $x$ ) horizontal coordinate. The wave motions are then introduced as small amplitude perturbations allowing the equations to be linearized. Assuming a unidirectional wind shear  $\bar{u}(z)$ , and a hydrostatic atmosphere, the equation variables are represented as follows:



$$\begin{aligned}
u &= \bar{u}(z) + u'(x, z, t) \\
w &= w'(x, z, t) \\
\rho &= \rho_o + \rho'(x, z, t) \\
p &= \bar{p}(z) + p'(x, z, t) \\
\theta &= \bar{\theta}(z) + \theta'(x, z, t) \\
\frac{\partial \bar{p}}{\partial z} &= \frac{-\rho_o}{g}.
\end{aligned} \tag{2.8}$$

The left side of the variables listed in (2.8) represent total values, while the right side of the equality is expressing the total state in terms of a mean value, indicated by an overbar, and a perturbation, indicated by a “ ’ ”. A mean value refers to the value a variable would have if averaged over many wavelengths at a given altitude. After equations (2.8) are inserted into (2.3 - 2.6) and linearization is accomplished, assuming  $\bar{u} = 0$ , the equations become

$$\frac{\partial u'}{\partial t} + \frac{1}{\rho_o} \frac{\partial p'}{\partial x} = 0, \tag{2.9}$$

$$\frac{\partial w'}{\partial t} - g \frac{\theta'}{\bar{\theta}} + \frac{1}{\rho_o} \frac{\partial p'}{\partial z} = 0, \tag{2.10}$$

$$\frac{\partial u'}{\partial x} + \frac{\partial w'}{\partial z} = 0, \tag{2.11}$$

$$\frac{\partial \theta'}{\partial t} + w' \frac{\partial \bar{\theta}}{\partial z} = 0. \tag{2.12}$$

When (2.2) is substituted into (2.12), the result is

$$\frac{\partial \theta'}{\partial t} + \frac{N^2}{g} \bar{\theta} w' = 0. \tag{2.13}$$

Subtracting  $\frac{\partial}{\partial z}$ (2.9) from  $\frac{\partial}{\partial x}$ (2.10) allows  $p'$  to be eliminated and leads to

$$\frac{\partial}{\partial t} \left( \frac{\partial w'}{\partial x} - \frac{\partial u'}{\partial z} \right) - \frac{g}{\bar{\theta}} \frac{\partial \theta'}{\partial x} = 0. \tag{2.14}$$

Taking  $\frac{\partial}{\partial t}$ (2.14) leads to

$$\frac{\partial^2}{\partial t^2} \left( \frac{\partial w'}{\partial x} - \frac{\partial u'}{\partial z} \right) - \frac{g}{\theta} \frac{\partial}{\partial t} \left( \frac{\partial \theta'}{\partial x} \right) = 0, \quad (2.15)$$

and when  $\frac{\partial}{\partial x}$ (2.12) is solved for  $\frac{\partial \theta'}{\partial x}$  and substituted into (2.15), the result is

$$\frac{\partial^2}{\partial t^2} \left( \frac{\partial w'}{\partial x} - \frac{\partial u'}{\partial z} \right) - N^2 \frac{\partial w'}{\partial x} = 0. \quad (2.16)$$

Finally, substituting from (2.11) for  $\frac{\partial u'}{\partial x}$  in (2.16) and take  $\frac{\partial}{\partial x}$  of the resultant equation gives

$$\frac{\partial^2}{\partial t^2} \left( \frac{\partial^2 w'}{\partial x^2} + \frac{\partial^2 w'}{\partial z^2} \right) + N^2 \frac{\partial^2 w'}{\partial x^2} = 0. \quad (2.17)$$

Assume (2.17) has harmonic solutions of the form

$$w' = \hat{w}(z) e^{i(kx - \omega t)} \quad (2.18)$$

where  $\hat{w}(z) = w_R(z) + i w_I(z)$  is a complex amplitude,  $k = 2\pi/\lambda_x$  is the horizontal wavenumber,  $\lambda_x$  is the horizontal wavelength and  $\omega$  is frequency. The intrinsic frequency, which is the frequency relative to the mean motion, is

$$v = k(c - \bar{u}) \quad (2.19)$$

where  $c = dx/dt = v/k$  is the horizontal wave phase speed. Equation (2.19) can be substituted for  $\omega$  in (2.18) to allow for a mean motion  $\bar{u}(z)$  with no loss of generality.

Substituting (2.18) into (2.17) results in

$$\frac{\partial^2 \hat{w}}{\partial z^2} + k^2 \left( \frac{N^2 - v^2}{v^2} \right) \hat{w} = 0, \quad (2.20)$$

and making the substitution

$$m^2 = k^2 \frac{(N^2 - v^2)}{v^2}, \quad (2.21)$$

leads to

$$\frac{\partial^2 \hat{w}}{\partial z^2} + m^2 \hat{w} = 0, \quad (2.22)$$

which is known as the Taylor-Goldstein wave equation.

If the vertical and horizontal components of the wave are separated and it is assumed that  $\hat{w}(z) = w_0 e^{imz}$ , then the wave dispersion equation (2.21) can be generalized to allow for vertical wave propagation as well as a mean motion. Thus,

$$w' = w_0 e^{i(kx + mz - \nu t)} \quad (2.23)$$

where  $m = 2\pi / \lambda_z$  is the vertical wavenumber with the vertical wavelength as  $\lambda_z$ . Equation (2.23) is the plane-wave solution for a two-dimensional traveling wave. Equation (2.21) can be alternatively expressed in terms of frequency

$$\nu^2 = \frac{N^2 k^2}{k^2 + m^2}, \quad (2.24)$$

which is the internal gravity wave dispersion equation. A dispersion equation is one that relates the intrinsic frequency,  $\nu$ , to the horizontal wavenumber,  $k$ . Substituting (2.19) into (2.24), allowing  $c$  to represent the ground-relative horizontal phase speed,  $c_x = \omega / k = \nu / k + \bar{u}$ , and reorganizing leads to the expression for the trace speed

$$c_x = \bar{u} \pm \frac{N}{\sqrt{k^2 + m^2}}. \quad (2.25)$$

If  $c_x$  depends on  $k$ , then the wave will be dispersive (generally, when the longer waves propagate faster than the shorter waves).

The dispersion equation for a three-dimensional hydrostatic gravity-inertia wave where the Coriolis effect cannot necessarily be neglected, is

$$\nu^2 = f^2 + \frac{N^2}{m^2} (k^2 + l^2) \quad (2.26)$$

where  $l = 2\pi/\lambda_y$ . Thus, from (2.26), for vertical propagation ( $m$  real) the intrinsic frequency must satisfy  $|f| < |v| < N$ . For eastward propagating waves and  $l = 0$ , to determine if the Coriolis effects can in fact be neglected,

$$v = 2\pi \left( \frac{1}{T} - \frac{\bar{u}}{\lambda_x} \right) \quad (2.27)$$

can be used to see if the wave characteristics are such that Coriolis effects can be ignored ( $v \gg f$ ). Here  $T$  represents the period of the wave.

The range of possible wave numbers is given by the dispersion equation, (2.24). Figure 2.1 shows that at  $k = 0$ , the intrinsic frequency is equal to zero, and as  $k \Rightarrow \infty$ ,  $m^2 + k^2 \approx k^2$ , so the intrinsic frequency approaches  $N$ . The result is a dispersion curve because phase velocity and group velocity are not the same, thus longer waves move faster than short waves (Fig. 2.1). Thus, the structure of a dispersive gravity wave changes with time resulting in different pressure traces at the surface as it passes each station. Near constant characteristic traces result from non-dispersive or only slightly dispersive waves (Schneider 1990).

Horizontal group velocity is represented by

$$c_g = \frac{\partial v}{\partial k}. \quad (2.28)$$

The group velocity measures the movement of the entire wave envelope and represents the wave energy propagation, while the wave phase velocity represents the movement of the wave fronts. Individual wave components may move through the group as the group propagates along. The group generally broadens in the course of time; that is, the energy is dispersed. The individual air parcels move up and down at an angle given by  $\cos \alpha$ , where  $\alpha$  is the angle the wave vector makes with the horizontal. These various motions and the wave envelope are displayed in Figure 2.2.

According to (2.21), when  $N > v$  ( $v/N < 1$ ), then  $m$  is real, the wave is internal and it does not lose amplitude with height. The solution in this case is of the form  $w' = \hat{w} \cos mz$ . Unlike external waves, internal waves can propagate vertically. If  $m$  is imaginary,  $N < v$  so that  $v/N > 1$  and the wave is evanescent in the vertical. The solution in this case is of the form  $w' = \hat{w} e^{-imz}$ . Any wave component having intrinsic frequencies less than the maximum value of  $N$  in that region but greater than the values of  $N$  that prevail both above and below will be internal within the duct and will be trapped (Fig. 2.3). These waves will be evanescent outside the layer and decay exponentially. Trapped modes dominate gravity wave observations because freely propagating modes decay in energy as  $1/r_D^2$  where  $r_D$  is the radial distance from the source (Hooke 1986).

If the wave front is not vertically propagating, then parcel acceleration is different from the Brunt-Väisälä frequency. A parcel of air moving vertically experiences a restoring force  $\propto g$  (thus  $v = N$ ), but a parcel of air moving off-vertically only experiences a restoring force  $\propto g(\cos \alpha)$ , which is determined only by the wave frequency for a given stability,  $N$ . In this case, the parcel's intrinsic frequency will be reduced. The parcel's acceleration can be expressed in terms of buoyancy accelerations:

Parcel acceleration = Buoyancy acceleration

$$\frac{d^2(\delta s)}{dt^2} = -(N \cos \alpha)^2 \delta s \quad (2.29)$$

A measure of the frequency is given by  $N \cos \alpha$  and  $\delta s$  represents the displacement distance. Thus, the solution for the parcel is given as,  $\delta s = e^{\pm i(N \cos \alpha)t}$ .

The shortest intrinsic period for non-hydrostatic internal gravity waves propagating through an undisturbed atmosphere theoretically is given by the Brunt-Väisälä period, typically about 10 min ( $2\pi/N = \tau_B$ ). The much longer period of the mesoscale waves encountered in most studies suggest that they are close to hydrostatic balance, i.e.  $\alpha \gg 0$ .

Gravity waves may occur as a single wave of depression, a single wave of elevation or as a wave packet. A gravity wave packet is a disturbed region of the atmosphere of limited dimensions. The packet changes in appearance as it propagates away from the source region (Hooke 1986), since longer waves tend to propagate more rapidly while shorter waves are slower.

A simple model for an idealized linear plane gravity wave with no basic current was developed by Eom (1975) that is widely accepted and used in the analysis of gravity waves (Fig. 2.4). In general, decreased cloudiness and stronger winds at the surface, from the direction in which the wave is propagating, are observed in the pressure trough (L). Conversely, the pressure ridge (H) is typically accompanied by winds from the direction from which the wave is moving, (i.e. winds that have backed with the passage of the trough). Convergence occurs at the wave nodal point (R = rising pressure) between the trough and the following ridge while divergence is observed at the nodal point (F = falling pressure) between the ridge and the following trough. The upward vertical motion dictated by mass continuity (2.11) creates the anomalously cold mid-level air (K) associated with the pressure ridge through upward adiabatic displacement of a low-level stable layer (2.12). The deep cloudiness and largest precipitation rate associated with this idealized wave are expected between the upward vertical motion maximum (R) and the trailing wave ridge axis (H), because of the time lag between ascent and precipitation formation. Many observational gravity wave studies support this model (Eom 1975, Uccellini 1975, Stobie et al. 1983, Pecnick and Young 1984, Bosart and Sanders 1986, Koch et al. 1988, Ramamurthy 1993).

Observed gravity waves do not always fit the Eom model. Koch and Golus (1988) note that if the wave tilts upstream with height, the maximum precipitation rate can occur during or even slightly after ridge axis passage (Fig. 2.5). In the Schneider (1990) case, passage of the ridge trailing a wave trough was followed by heavy snow and ice pellets,

thunder and lightning. Pecnick and Young (1984) observed a vertical tilt with height in the wave they analyzed, opposite to the propagation direction and thus consistent with an upper-tropospheric energy source. However, the convergence/divergence pattern was consistent with the Eom model for a propagating internal gravity wave. The conclusion here would be that the surface signatures of a gravity wave may not be aligned with the upper-level features, in accordance with the simple Eom model, if the wave tilts in the vertical.

Other complications of the simple Eom model have been observed. In studies of gravity waves characterized by a single negative pressure perturbation that is not accompanied by a trailing positive pressure perturbation, it has been suggested that subsidence ahead of the pressure minimum was associated with the dissipation of mid-level clouds and the end of an extended period of precipitation (Bosart and Cussen 1973, Bosart and Seimon 1988). Results from Ramamurthy et al (1993) differed from the Eom model, but were similar to those from Bosart and Cussen (1973). Both studies observed that once the gravity wave had passed, the precipitation had completely ended. It is obvious that the precipitation pattern associated with a gravity wave can differ significantly depending on the environmental stability, water vapor content, and the actual vertical structure of the wave (Koch and Golus 1988).

Gravity waves are affected by various atmospheric variables. Wind effects are addressed in the next two sub-sections. The temperature structure affects the wave since it determines the Brunt-Väisälä frequency, and therefore the wave refraction and wave energy trapping. Another atmospheric variable that affects gravity waves is moisture, which changes the Brunt-Väisälä frequency because water vapor and dry air have different molecular weights. Moisture also plays a role in triggering convective instability during updraft phases of the wave motion when stability is marginal. This can lead to solitary waves which can propagate for long distances without changing shape (Hooke 1986).

Solitary waves (Lin and Goff 1988, Ramamurthy 1993, Rottman and Einaudi 1993) are a stable, large-amplitude gravity wave whose surface pressure signature is singular in nature. A balance exists between the steepening effect of nonlinearity and the flattening effects of frequency dispersion that keep the wave from changing significantly. Typically a wave disturbance larger than what can be supported by the atmosphere is initiated, but usually the dispersion effects are a greater influence than are nonlinear effects, so the disturbance breaks up into smaller waves. As previously mentioned, shorter waves tend to move slower, so if phase velocity depends on the horizontal wave number,  $k$ , then dispersion effects will cause the initial disturbance to change shape (Fig. 2.6). The mode that can best be supported by the atmosphere then becomes the solution to the wave. Nonlinear effects, on the other hand, make the shorter waves move faster while dispersion continues to make the shorter waves move more slowly, and when these two effects are in balance, a solitary wave results. To get a solitary wave, the initial conditions must be just right so that a singular signature results that is maintained by the balance between dispersive and nonlinear effects.

## *2.2 Gravity Wave Generation Mechanisms*

Gravity waves are generated in one of two ways, by shear instability or external forcing (Hooke 1986). With shear instability, the energy of the shear flow is converted into wave energy contained in fluctuations in the wave field. Forcing can be dynamical or thermal or a combination of the two. Shearing instability is mentioned often in gravity wave studies, however, geostrophic adjustment and convection appear to be significant generation mechanisms as well.

### *2.2.1 GEOSTROPHIC ADJUSTMENT*



Mass-momentum imbalances can lead to excitation of inertia-gravity waves, which act to adjust the mass and momentum distributions so that the flow tends to return toward balance. The process by which balance is achieved is called the adjustment process. To better understand this process, an explanation of balanced ageostrophic motions is necessary. The general definition provided is valid for the dynamical approach of quasi- or semi-geostrophic theory, as well as for the nonlinear balance equation.

Cross-stream ageostrophic motion is related to parcel accelerations in the jet entrance region and decelerations in the exit region. Quasi- and semi-geostrophic theory require these motions in order to sustain thermal wind balance. The semi-geostrophic momentum equation predicts ageostrophic flow as

$$\vec{V}_{ag} = \frac{1}{f} \vec{k} \times \frac{d\vec{V}_g}{dt} = \frac{1}{f} \vec{k} \times \left( \frac{\partial \vec{V}_g}{\partial t} + \vec{V} \cdot \nabla \vec{V}_g \right). \quad (2.30)$$

In the solitary, straight jet model (Fig. 2.7) where the streak is in quasi-geostrophic balance, as an air parcel enters a jet streak, it accelerates downstream under the influence of the pressure gradient force ( $d\vec{V}_g/dt > 0$ ). From (2.30),  $V_{ag}$  blows perpendicular and to the left, which in this case is toward lower heights. The energy principle approach indicates that an air parcel in this region accelerates and gains kinetic energy, which is consistent with flow from higher heights to lower heights. In the exit region of the jet maximum, the parcel decelerates,  $d\vec{V}_g/dt$  is negative and  $V_{ag}$  blows perpendicular and to the right toward higher heights. Again, from the energy perspective, the parcel is losing kinetic energy and gaining potential energy. This gain in potential energy is consistent with flow from lower to greater heights.

Curvature in the upper level heights produces an along-stream pattern of convergence and divergence due to the effects of centripetal accelerations (Fig. 2.8). When curvature effects are applied to the straight jet model with a jet streak located in the pressure

trough, the result is enhancement of vertical motions on the cyclonic side of the jet with strongest divergence in the left exit region and strongest convergence in the left entrance region. These effects are consistent with quasi-geostrophic theory and a gradient wind balance then exists. Although curvature affects the pattern of ageostrophic motion, these effects are felt only in the along-stream component of the ageostrophic wind and the result again is in gradient wind balance. The effect of thermal advection on the straight jet model is a shift the four-cell convergence/divergence pattern (Fig. 2.7) either to the left or the right, but the result is still a balanced flow field.

Geostrophic adjustment between the mass and momentum fields occurs in unbalanced jet streaks, which are ones that do not display the flow behavior just discussed. Uccellini and Koch (1987) identified a conceptual model that appeared to favor geostrophic adjustment (Fig. 2.9). Notice that the exit region of the geostrophic jet maximum, which is the region where ageostrophic flow toward higher heights is anticipated, is where the ageostrophic flow associated with the actual jet maximum is directed toward lower heights. There is cross stream ageostrophic flow toward the cyclonic side of the geostrophic jet streak in the exit region and the flow, therefore, is unbalanced. This happens as a result of a displacement between the actual jet maximum and the geostrophic maximum, in which case,  $\bar{V} \cdot \nabla \bar{V} \neq \bar{V} \cdot \nabla \bar{V}_g$  which is in contradistinction to the assumption expressed by (2.30). In the case of quasi- or semi-geostrophic theory, this situation results in an erroneous prediction of the ageostrophic flow. The geometric configuration in the upper level mass and wind fields that often leads to this separation of the actual jet from the geostrophic maximum is one in which the jet streak propagates from the base of a negatively tilted trough, to a diffluent region. At the same time, quasi-geostrophic theory places the geostrophic jet at the base of the trough, therefore, what is depicted as the exit region of a geostrophic jet maximum is the entrance region of the actual jet maximum.

Geostrophic adjustment must occur to correct this imbalance. Downstream of this unbalanced flow is where gravity waves are typically found (Uccellini and Koch 1987).

More recent case studies that qualitatively support geostrophic adjustment as a genesis mechanism and fit the Uccellini and Koch (1987) conceptual model include Ramamurthy et al. (1993), Sanders and Bosart (1985) and Schneider (1990). In the cases analyzed in Section 6, a qualitative assessment is made as to the role geostrophic adjustment may have played in the genesis of the gravity waves observed.

### 2.2.2 SHEARING INSTABILITY

According to the Miles (1961)-Howard (1961) theorem, shear instability can occur only in regions where the Richardson number ( $Ri$ ) is  $< 1/4$  at a critical level, where

$$Ri = \frac{g \partial \ln \theta / \partial z}{(\partial |V| / \partial z)^2}. \quad (2.31)$$

The  $Ri$  is a measure of the importance of the buoyancy force to inertial accelerations, or of static stability to wind shear. A critical level is a level at which the component of the background wind speed,  $u(z)$ , in the direction of wave propagation, is equal to the horizontal wave phase speed. Einaudi and Lalas (1975) claimed that these conditions were sufficient to supply energy to the wave by the mean flow and to allow for wave growth. A number of gravity-wave studies have used this criteria to determine if the vertical shear associated with the upper-level jet was the energy source for the wave. Gossard and Hooke (1975) found that wind shear was typically the likely wave source for nondispersive waves, i.e. those waves for which the wave group and phase velocities are identical or nearly so. Since there is vertical shear associated with a jet streak, it can be expected that determining whether wave generation in the region of a jet was due to shearing instability or geostrophic adjustment can be rather difficult, as noted by Koch and Dorian (1988). Since the focus of this study is on surface analysis of gravity waves,  $Ri$  values were not

calculated; therefore, shearing instability as a possible generation mechanism was not evaluated.

### 2.2.3 UNBALANCED FRONTOGENESIS

Reeder and Keyser (1988) found that with semi- and quasi-geostrophic models, the assumption of cross-front thermal wind balance was an excellent approximation when the cross-front geostrophic wind shear  $(\partial \bar{u}_g / \partial z)$  was weak. When  $(\partial \bar{u}_g / \partial z)$  was strong however, the unbalanced along-front ageostrophic wind was proportional to the vertical advection of the cross-front velocity, and thermal wind balance was not satisfied. Strong vertical shear, usually associated with a strong jet, means  $(\partial \bar{u}_g / \partial z)$  is positive and is increasing. This implies an along-front temperature gradient through the thermal wind relation,

$$\frac{\partial u_g}{\partial z} = \Lambda \frac{\partial \theta}{\partial y}, \quad (2.32)$$

where  $\Lambda = -\frac{g}{f\theta_o}$  and  $\theta_o$  is the potential temperature of an undisturbed atmosphere.

Reeder and Keyser (1988) showed that the shearing deformation forcing term of the Sawyer-Eliassen frontogenesis equation,

$$\frac{\partial v_g}{\partial x} \frac{\partial \theta}{\partial y}, \quad (2.33)$$

was related to the ageostrophic streamfunction ( $\psi$ ). As the geostrophic deformation got stronger, so did the ageostrophic circulation, which is of the same sign as the along-front geostrophic velocity ( $v_g$ ). The intensification of the ageostrophic circulation must therefore be supported by increasing values of  $v$ . In the process,  $v$  becomes supergeostrophic and is therefore unbalanced according to the thermal wind equation. Reeder and Keyser (1988)

found inertia-gravity waves to be the natural response of the atmosphere to unbalanced conditions associated with upper-level jet/front systems. This process is similar to geostrophic adjustment where gravity waves are generated in an effort by the atmosphere to establish balance once the imbalance in mass and momentum are realized.

In a study investigating gravity waves generated during low-level frontogenesis, Gall et al. (1988) found waves above the surface front to be stationary, hydrostatic waves forced by nongeostrophic and nonhydrostatic accelerations in the frontal zone. Gall et al. (1988) stated that gravity waves should always be produced during frontogenesis and that these waves will be produced regardless of whether or not precipitation is occurring. They concluded that these waves could account for banding in those portions of the front where there is little precipitation and that these waves should also be produced in those portions of the front where precipitation is occurring. Results from a study by Ley and Peltier (1978) also support the role of the gradient of ageostrophic cross-front accelerations  $\left(\partial/\partial x(\partial u_{ag}/\partial t)\right)$  as the important factor in unbalanced frontogenesis as a generation mechanism. Bosart and Sanders (1985) found the gravity wave in their case to be a northward extension of the front which was distinguished from the front by the lack of a significant temperature change accompanying its passage.

Frontogenesis as a genesis mechanism for the observed gravity waves in Section 6 is qualitatively analyzed. The existence of a frontal system and whether that system was developing is examined, but no attempt is made to quantitatively diagnose the dynamical state of the atmosphere.

#### 2.2.4 TOPOGRAPHY

A disturbance is created when stably stratified air is forced over a topographic barrier. The energy associated with that disturbance is usually carried away from the source region by gravity waves, commonly referred to as mountain waves. In order for

mountain waves of any type to exist, a sufficiently strong wind must be directed across the mountain at the ridge-top level. The minimum wind speed required for waves varies with the size and shape of the mountain. Large-amplitude mountain waves can lead to CAT and strong surface winds that blow down the mountain along its lee slope. The behavior of linear mountain waves depends entirely on the shape of the terrain profile and the mean atmospheric structure. The mountain wave theory presented here was taken from Durran (1990).

Most of the fundamental properties of small-amplitude mountain waves can be examined by making some simplifications to airflow over an infinite series of periodic ridges of the form

$$h(x) = h_m \cos kx \quad (2.34)$$

where  $h_m$  is the maximum mountain height. Assuming the airflow is steady-state and two-dimensional, the Rossby number is large, the atmosphere is inviscid and Boussinesq and the mean horizontal wind speed is constant, the governing equations are similar to (2.3) - (2.6) except that each time derivative  $\partial/\partial t$  is replaced by an advection term,  $\bar{u}\partial/\partial x$ . The perturbation velocity field in waves forced by the sinusoidal terrain is then

$$w(x, z) = \begin{cases} -\bar{u}h_m k e^{-\mu z} \sin kx, & \bar{u}k > N \\ -\bar{u}h_m k \sin(kx + mz), & \bar{u}k < N \end{cases} \quad (2.35)$$

where  $\mu = (k^2 - N^2/\bar{u}^2)^{1/2}$ . In the case where  $\bar{u}k > N$ , the waves decay exponentially with height and the wave crests are aligned vertically. When  $\bar{u}k < N$ ,  $m$  is real and the appropriate upper boundary condition is the "radiation condition" which requires that all waves at an arbitrary height above the mountain must be transporting energy away from the mountain. An upstream-tilting wave is associated with upward energy flux while a wave tilting downstream is associated with downward energy flux. In this case ( $\bar{u}k < N$ ) the

waves propagate vertically without loss of amplitude. The waves decay away from the forcing when the intrinsic frequency exceeds the Brunt-Väisälä frequency ( $\bar{u}k > N$ ) because the buoyancy restoring forces cannot support the oscillations.

If there is only a single ridge, the isolated mountain can generally be constructed from periodic functions by taking the Fourier transform of the governing Taylor-Goldstein equation, assuming  $N$  and  $\bar{u}$  are constant. The relative weight attached to each individual wavenumber in the composite solution is determined by Fourier transform of the terrain profile,

$$h(x) = \frac{h_m a^2}{a^2 + x^2} \quad (2.36)$$

where  $a$  determines the mountain width. For a very narrow mountain,  $\bar{u}a^{-1} \gg N$ , the profile is dominated by wavenumbers greater than  $N/\bar{u}$ , and the mountain forces primarily evanescent waves (note the similarity to (2.21)). In this case, the wave pattern is symmetric with respect to the ridge crest. For a wide mountain,  $\bar{u}a^{-1} \ll N$ , the dominant wavenumbers are less than  $N/\bar{u}$ , and the waves propagate vertically with lines of constant phase tilting upstream. If  $\bar{u}a^{-1} = N$ , the result is nonhydrostatic vertically propagating waves, where the phase lines still tilt upstream and energy is transported upward; however, in this case, energy can also be transported downstream. If an isolated mountain is wide enough to force only hydrostatic waves yet not so wide that Coriolis effects must be considered, there will only be one wave crest in the air flowing over the mountain. Additional crests do not appear downstream unless nonhydrostatic effects are significant. Trapped lee waves are the most obvious way in which nonhydrostatic effects manifest themselves (Durrán 1990). For lee waves, if the mountain width is increased, the amplitude of the vertically propagating waves would increase and the amplitude of the trapped waves would decrease. If the ridge is wide enough then the Coriolis force will affect the wave motion. Consider  $N$ ,  $\bar{u}$  and  $f$  to be constant and define  $\Omega = \nu - k\bar{u}$

which is the Doppler shifted frequency. In this case, if  $\Omega > N > f$  then the waves will be evanescent, whereas if  $N > \Omega > f$  the waves will be vertically propagating. If  $N > f > \Omega$  then the waves will also be evanescent.

Scorer (1949) showed that trapped waves arise as a result of vertical variations in  $N(z)$  and  $\bar{u}(z)$  and he introduced the Scorer parameter, defined as  $l^2 = N^2 / \bar{u}^2$  for non-shear flow. He considered the case where  $l$  was constant within each of two layers, and he showed that a necessary condition for trapped waves was

$$l_L^2 - l_U^2 > \frac{\pi^2}{4H^2} \quad (2.37)$$

where  $L$  and  $U$  represent the lower and upper layers respectively, and  $H$  represents the depth of the lower layer. Applying the Scorer parameter to the requirements stated earlier for vertically propagating waves to an environment with vertical wind shear, simply leads to the general required condition of  $k < l$ . Trapped waves have no tilt because the wave energy is repeatedly reflected from the upper layer and the ground downstream from the mountain. The downstream disturbance is then the superposition of equal-amplitude upward and downward propagating waves and the combination has no tilt. For the present study, the potential role of topography as a genesis mechanism was investigated simply through tracing the waves back as far as possible and examining the topography of the surrounding area, but once again, no study was made of the atmospheric structure.

#### 2.2.5 CONVECTION

The relationship between convection and gravity waves can be quite complicated. In this sub-section, other aspects of this relationship are addressed in addition to convection as a wave genesis mechanism. Convection can lead to gravity wave generation either through the release of latent heat in shear flow or Wave-Conditional Instability of the Second Kind (CISK). In this study, satellite pictures were used to help determine if



convection existed before the gravity wave events or if any developed after the wave was evident, thus determining the relationship, although simply examined, between convection and the gravity waves.

Convection can play a size-sorting role, similar to the way topography does in selecting one of the many unstable wavenumbers. For example, the size of the Mesoscale Convective Complex (MCC) may aid in the selection of an unstable wave mode. Another possibility is that of a thunderstorm updraft impinging upon the tropopause (penetrative convection) causing a rippling effect that can be seen traveling along the top of the cloud deck below the stable tropopause. A somewhat similar situation was described by Hung and Tsao (1991) where the gravity waves produced in laboratory experiments were excited when convective elements overshot the top of the mixed layer and penetrated a short distance upward into the stable layer.

Latent heat release associated with moist convection is capable of mesoscale wave generation or intensification. Ley and Peltier (1981) proposed that a freely propagating internal gravity wave packet may be forced by the release of latent heat into the atmosphere in pulses. Schneider (1990) found latent heat to have played a role, in addition to shearing instabilities, in the generation of the waves he observed. The available evidence in the Lin and Goff (1988) case points to an initial disturbance caused by latent heat that was produced near a mid-tropospheric inversion as the initiating factor in the development of an internal solitary wave of depression. Chimonas et al. (1980), showed that latent heat released at a critical level should enhance gravity wave growth.

In a baroclinic atmosphere, convection and the latent heat release can lead to geostrophic adjustment. Because the mass field is disturbed, there is no longer a balance between mass and momentum; therefore, there is no longer a thermal wind balance. The result is a perturbation in pressure (thickness), to which the wind field adjusts in an attempt to restore balance.

Uccellini (1975) concluded that mesoscale gravity waves are capable of releasing convective instability and initiating thunderstorm development in areas that have the necessary amount and proper vertical distribution of moisture. The waves weaken the inversion that precludes convection and, in an adequately moist, conditionally unstable atmosphere, the motion of the waves provides the mechanical lift necessary to raise a parcel to its Lifted Condensation Level (LCL) or Level of Free Convection (LFC). Stobie et. al. (1983) identified two waves in their study, one of which developed in a region of weak or no convection but then initiated deep and more intense convection clusters downstream from the point of origin. Rapid amplification of the waves and the growth of the convection occurred simultaneously, several hours after the waves were first detected. This was an indication that the convection may have played a role in sustaining and strengthening the wave over a long period of time.

According to Wave-CISK theory, precipitating convection and the gravity wave are coupled and therefore they move together as a system. Thus, the updraft core and latent heating must occur near a critical level, which is also called the steering level. The wave supplies the divergence and convergence patterns necessary for the convective heating and cooling (see Fig. 2.4). Low-level convergence maintains the energy for the system, since the convergence leads to an updraft, condensation results, and latent heat is liberated. Rain falls in the downdraft, cooling occurs as a result of the loss of latent heat due to evaporation, and under this downdraft an area of divergence occurs. Gravity waves are, in turn, supplied energy by the divergence of cumulus mass fluxes (Raymond 1983).

Wave-CISK was suggested as being responsible for the gravity waves in the Powers and Reed (1993) model simulation of the Schneider (1990) gravity wave event. The waves were generated by mesoscale convection above a stable duct. All of the waves grew in tandem with the propagating mesoscale convection, while decaying waves were characterized by weaker or no convective cores aloft, no strong downstream subsidence

aloft, and steering levels above the updraft core. For the growing wave, the positioning of the updraft core resulted in precipitation at the ridge, whereas the Eom model suggests precipitation prior to the ridge, that may have reinforced the cold anomaly through evaporative cooling. This was also found to be the case by Koch et. al. (1988).

Gravity waves can also be generated by cumulus clouds. A buoyancy-sorting process can lead to an environmental gravity wave response. In this process, Bretherton and Smolariwicz (1989) found that each mixed parcel settled to a level at which it was neutrally buoyant with respect to a moist adiabat, determined by the low-level inflow into the cloud. This adiabat was generally not neutrally buoyant with respect to the undisturbed environment. It is believed that this disparity led to the gravity wave response which compensated for the vertical mass flux inside the cloud.

An interesting finding supported by field data and numerical results is the obstacle hypothesis where wind speed and vertical motion react some distance upwind of the cloud entry indicating a possible upstream effect of an obstacle (Kuettner et al. 1987). Air flowing over these "obstacles" deflects the overlying layers vertically. The result is the launching of vertically propagating internal gravity waves and if they are trapped, the gravity wave system develops its own scale selection. An adjustment process occurs and gravity waves feed back by organizing the clouds into bands (Clark et al. 1986). However, the waves generated by penetrative convection are much smaller in scale than the 50 - 500 km scale mesoscale gravity waves of interest in the present study.

Convection can also change an incipient gravity wave. A local change in the typical pressure/wind relationship was found to occur near a severe thunderstorm in a gravity wave event (Koch et al. 1988). The wind perturbation, which had earlier been in phase with the pressure perturbation, advanced ahead of the pressure field. The wind maximum became associated with the pressure-nodal line, which is 90° out of phase from the typical relationship (see Fig. 2.5). In addition, wave propagation became slower and deviated to

the right of the former wave velocity, because new cell formation along a gust front occurred preferentially on the right flank. Koch et al. (1988) noted that the decrease in  $\overline{p'u^*}$  correlations, change in phase velocity, increase in wave amplitude and reduction in wavelength near the active storm cores, together suggest that the original wave signal was reduced or even lost locally in the presence of the storms. The wave they observed became nonlinear and nonplanar (arc-shaped wavefronts resulted). The original gravity wave signal, however, remained intact just outside the influence of the thunderstorm. In addition, they concluded that deep convection did not significantly mask evidence for the gravity wave in the surface pressure and wind fields unless a gust front was also present.

Rauber et al. (1995) however, found the positive correlation between the surface pressure and winds increased after the onset of convection for one of the cases analyzed in this study (14 February 1992). The role of gravity waves in the propagation and internal flow characteristics of a simulated squall line was examined by Schmidt and Cotton (1990). With vertical wind shear, the waves experienced a Doppler shift in phase speed and a change in magnitude. The magnitude change was most noticeable in the lower stable layer as a large-amplitude gravity wave. This wave in turn determined the propagation speed of the squall line and was instrumental in lifting the low level air to the LFC. During the latter three stages of Tripoli's (1986) conceptual model representing the six-stage life cycle of an evolving MCS, gravity waves were produced. Greater trapping of the waves developed as cloud top radiational cooling created small  $N$  values. With increased moisture available above the nocturnal inversion, the higher amplitude gravity waves could excite new convective elements away from the main core of convection. In another interesting case (Johnson and Hamilton 1988), the thunderstorm track was coincident with the track of the most intense mesohigh along the squall line, which is not unlike what gravity wave theory would dictate. Southeasterly winds were observed to gradually increase in speed reaching a peak shortly after the passage of the wake low, consistent with gravity wave theory.

They saw that the back end of the wake low was characterized by an abrupt 4.0 mb increase in pressure and a gradual wind shift in time to a westnorthwesterly direction, reaching a peak speed at the end of the pressure rise. The pressure and wind fields agree with the Eom model. Fujita's (1955) squall line life cycle schematic (Fig. 2.10) illustrates airflow into the center of the wake low; however Johnson and Hamilton (1988) found that the axis of surface confluence in the wake low area occurred 20-50 km behind the low center (Fig. 2.11), which places it in accord with the Eom model of a gravity wave. It is unknown whether this phase shift is large enough to categorically state that it is indicative of a gravity wave instead of a classical wake low, since the station spacing was approximately 50 km.

Koch et al. (1991) describe a situation where a dissipating gravity current, which was a mesohigh produced by the cold outflow from a dissipating squall line, led to the generation of an internal bore. A bore is a propagating gravity wave disturbance that causes a step-like increase in the thickness of the waveguide layer of stable air. When the bore is modulated by a sequence of waves that may evolve from it, it is called an undular bore (Mahapatra et al. 1991) (Fig. 2.12). A bore may develop when stable layers in contact with the earth's surface form, for example, when thunderstorm outflows spread over the ground or a nocturnal inversion develops. Subsequent thunderstorm outflows that impact this stable layer can lead to the generation of an undular bore.

Bores are similar to gravity currents in that they both are accompanied by a wind shift into the direction of disturbance movement, and a net cooling in the lower atmosphere that is consistent with the sustained surface pressure increase that follows the initial sudden pressure rise. The difference between them is that the cooling associated with a gravity current is due to horizontal advection of mass while adiabatic ascent is the cause of cooling in the case of a bore. Surface cooling is not characteristic of bores and actually the temperature often rises as a result of turbulent downward mixing of warmer air from above

the inversion (Koch et al. 1991). A phenomenon known as the 'morning glory', a low roll cloud or succession of roll clouds that occurs early in the morning, is associated with solitary wave disturbances at the leading edge of an undular bore that propagates on a low-level maritime stable layer (Clarke et al. 1981). The 'morning glory' phenomena is most frequently observed in the southern Gulf of Carpentaria region of northern Australia (Smith 1988). Bores are common means by which surface pressure fluctuations appear, and were considered when examining the data in this study.

### 2.3 Gravity Wave Maintenance Mechanisms

The vertical group velocity equation ( $\partial v / \partial m$  from (2.24))

$$C_{gz} = \frac{-mv^3}{k^2 N^2}, \quad (2.38)$$

reveals that real, non-zero vertical group velocities are possible only for real values of the vertical wavenumber  $m$ , which from (2.21) requires that  $N > v$ . Therefore only internal wave modes can propagate energy vertically (see Fig. 2.3). Mesoscale gravity waves fall into this range because they have an intrinsic frequency that is generally less than  $N$ . Uccellini and Koch (1987), using an estimate of the vertical group velocity from Pecnick and Young (1984), showed that untrapped waves would quickly lose most of their energy before traveling even one horizontal wavelength. These waves, however, are often observed and tracked for a significant period of time, in excess of 12 hr in some cases. The three processes that can maintain gravity waves are a constant supply of energy, prevention of energy loss as well as those processes responsible for solitary waves.

#### 2.3.1 CONSTANT ENERGY SUPPLY

The constant energy supply can come from Wave-CISK, described in the previous section, or through critical level interactions where  $Ri < 1/4$  at a critical level in the

atmosphere. These critical level interactions allow the wave to extract energy from the basic flow (Lindzen and Tung 1976, Stobie 1983, Pecnick and Young 1984, Ferretti et al. 1988, Koch and Dorian 1988).

The over-reflection mechanism, where the reflection coefficient is  $> 100\%$ , was also addressed by Lindzen and Tung (1976). Strong shear at the critical level (i.e. low  $Ri$  values) allows the wave to be overreflected at each contact with the critical level, with partial reflection and some frictional dissipation of the wave occurring at each contact with the ground. The reflected energy is therefore greater than the incident energy.

Over-reflection is suggested by a decrease in the kinetic energy of the mean flow above the critical level and an increase below the critical level with the passage of the wave. The expression for the vertical fluxes of energy  $F_E$  and horizontal momentum  $F_M$  are:

$$F_M = \bar{\rho} \int_{-\infty}^{\infty} (u'w') dx \quad (2.39)$$

$$F_E = \int_{-\infty}^{\infty} (p'w') dx. \quad (2.40)$$

The theorem by Eliassen and Palm (1960), based on the perturbation wave energy equation for a steady, adiabatic, frictionless atmosphere containing vertical wind shear, states the energy and momentum fluxes are related as

$$F_E = [c - \bar{u}(z)] F_M. \quad (2.41)$$

Eliassen and Palm (1960) also showed when  $[c - \bar{u}(z)] \neq 0$  that  $F_M$  is constant with height. Therefore,  $-F_E \propto [c - \bar{u}(z)]$ . Thus, the vertical profile of the energy flux  $F_E(z)$  is given by the profile  $[c - \bar{u}(z)]$ . A downward increase in  $-F_E$  implies boundary layer dissipation and a net energy flux divergence  $dF_E/dz > 0$  above the planetary boundary layer. This flux divergence demands a positive conversion  $-(d\bar{u}/dz)F_M$  of kinetic energy from the mean flow into the gravity wave (Eliassen and Palm 1960). In other words, if

there is an energy flux divergence, waves will extract kinetic energy from the mean flow, i.e. that level is the wave source.

Koch et al. (1993) found negative momentum flux in a region where the wave displayed no tilt within the evanescent layer below the lowest critical level. Strong divergence of the momentum flux was found near each of the lower critical levels. Within the layer of multiple critical levels, the momentum and energy fluxes were out of phase, as expected from the Eliassen and Palm (1960) theorem. Koch et al. (1993) concluded that there was a conversion of kinetic energy from the mean flow to the gravity wave and that the wave transported energy away from the critical level.

### 2.3.2 ENERGY-LOSS PREVENTION

Energy-loss prevention is a result of wave ducting by an inversion or an over-reflection mechanism in the presence of a critical level. Requirements for a highly reflective wave duct have been outlined in the linear theory by Lindzen and Tung (1976). The four requirements are: 1) the existence of a statically stable lower layer, such as a temperature inversion, 2) a critical level with low  $Ri$  values in the upper layer with conditional instability (the reflection efficiency at the critical level is determined by the  $Ri$ ), 3) no critical level in the duct since a critical level with a large  $Ri$  absorbs wave energy and 4) a duct which has a thickness of  $n \lambda_z / 4$ , where  $n$  is an integer, for a given wave phase speed within the duct.

Since the region where mesoscale gravity waves are typically found (Uccellini and Koch 1987) is quite dynamically active, it is often impossible to determine the specific process responsible for the generation and/or maintenance of the wave. For example, Koch et al. (1993) concluded that geostrophic adjustment, shearing instability and topography may all have played various roles in generating and/or helping to maintain the waves.



### 2.3.3 SOLITARY WAVES

Lin and Goff (1988) noted that the requirements for a stable duct are not often met by observed mesoscale waves of isolated form. No critical level was observed in the solitary gravity wave event they studied nor was Wave-CISK suggested; however, the effects of nonlinearity and dispersion were of the same order of magnitude. With solitary waves, the dispersion due to modest nonhydrostatic effects is neutralized by nonlinear self-advection for a sufficiently strong amplitude. Lin and Goff (1988) therefore suggest the wave they observed was maintained through its solitary nature. Rottman and Einaudi (1993) found that for internal solitary wave propagation, the upper layer must be very weakly stratified in order for solitary waves in the lower layer to persist for very long. This is because a smaller amount of energy is lost due to radiative damping under these conditions. Pecnick and Young (1984) suggest the reason the wave they observed had such a long lifetime was because it was a solitary wave of depression and that the dispersion effects were countered by the nonlinear effects.

If wave-CISK appears to be a potential maintenance mechanism judging from the satellite and radar imagery from the cases analyzed in this study, then that was noted. Otherwise, gravity wave maintenance mechanisms are not addressed primarily because of the upper-air analysis required for such an investigation, which is beyond the purposes herein.

### 2.4 *Detection Techniques*

A number of techniques have been used to detect gravity wave signatures at the surface and throughout the atmosphere. Typical surface analysis techniques involve first obtaining surface observations including barograph traces that require digitization from the region of interest. A bandpass filter is then applied to the time series to reveal the presence

of the waves as pressure perturbations ( $p'$ ). The filter is typically chosen based on the results from power spectrum analysis of the pressure data, or the frequency band to be passed can be for some pre-selected wave period. Objective analysis or cross spectral analysis is used to find the propagation velocity of the wave. Finally, an attempt is made to subjectively analyze the wave patterns from the  $p'$  fields, together with satellite and radar imagery. A more objective approach such as Time-to-Space Conversion (TSC), discussed in Section 4, can also be used to analyze the wave, which is less time consuming and typically presents a clear indication of the wave position through time. These methods have been used, at least subjectively, by a number of gravity wave investigators (Uccellini 1975, Stobie et al. 1983, Pecnick and Young 1984, Bosart and Sanders 1986, Koch et al. 1988), although Koch and O'Handley (1996) have extended the concept of TSC to be included into an objective analysis. The surface analysis method used in the present study is explained in detail in Section 4.

In the current study, if the wave placement with respect to any cloudbands suggests a particular vertical profile as in Fig. 2.5, then that was noted for the case studies. Although direct analysis of the vertical structure of the wave was not conducted, remote sensing methods that have been used are presented here just for informational purposes. For example, the vertical structure of gravity waves has been examined using Raman lidar (Koch et al. 1991) which displays the mixing ratio as the moisture variable. A product generated from the lidar is the aerosol backscattering ratio which is an indicator of cloud thickness. Koch et al. (1993) used multiple Doppler radar analyses to study the wave's vertical structure, where wave-induced pressure perturbation fields were derived from triple-Doppler wind fields. Another active ground-based remote sensing system used to study gravity waves is an acoustic sounder. Koch et al. (1993) notes that these systems are good for studying lower-tropospheric waves, but that the structure of deep-tropospheric waves are best examined through the use of active remote sensing systems like FM-CW

radar, and UHF-VHF pulsed Doppler wind profilers. Doppler profilers were used by Ralph et al. (1993) to examine the vertical structure of a gravity wave event, and Trexler et al. (1996) are using this type of data from the February 14 1992 case which is examined in Section 6 of this study from a surface perspective.

Changes in the clouds and thunderstorm activity have also been used to aid in the determination of wave location. Since a wave of depression requires adiabatic warming in the overlying layers, which might extend throughout the troposphere including the cirrus level (Pecnick and Young 1984), cloud depressions can be expected. In IR satellite pictures, these depressions are seen as darker areas as noted in the Pecnick and Young (1984) gravity wave study. Tepper (1951) also documented the desiccation of a cloud bank by a propagating pressure wave. Bosart and Sanders (1986) took a different approach when they observed thunderstorm activity to be approximately synchronous with the maximum hourly pressure rise. Koch et al. (1988) used satellite cloudbands to assist in the identification of gravity waves as they propagated between the sparsely-spaced barograph stations beyond the dense mesonet used to detect the waves. In the present study, the shape and location of cloud and precipitation bands is frequently used to verify the results of the complex pressure perturbation field analysis, and to determine both the effects of gravity waves on the weather as well as indirectly assess possible convective feedback effects on the waves.

### 3. Data

Data types used in this study include surface, upper air and satellite, which were stored as part of the intense data gathering that occurred during STORM-FEST. The majority of the data used in this study was retrieved through the STORM-FEST Data Management System called the Cooperative Distributed Interactive Atmospheric Catalog System (CODIAC) via the internet. The charts used in Section 4.1.4 were obtained directly from the STORM-FEST Operations Summary and Data Inventory book (Cunnings and Williams 1993).

#### 3.1 *Surface Data*

Surface data available in 5-min intervals from STORM-FEST include observations from ASOS, Illinois Climate Network (ICN), National Center for Atmospheric Research (NCAR) Portable Automated Mesonet (PAM) and Aviation Weather Observation System (AWOS) data. An initial quality control was performed by the STORM-FEST Data Management system flagging data according to a Mesoscale Analysis and Prediction System Model (MAPS) comparison and station "buddy" checks. National Weather Service (NWS) barograph data from the National Climate Data Center, digitized to 15-min intervals and then linearly interpolated to 5-min intervals, was used to fill in areas where the digital mesonet data was missing or in data-sparse regions including the periphery of the data-collection region (Fig 3.1). Although Fig. 3.1 depicts the locations of the stations considered or available, usable data was not received from all the stations all the time. Such is the case with all the station maps in this section.

The ASOS stations are being installed nationally by the NWS, Federal Aviation Administration (FAA) and US Navy as part of the NWS modernization plan, FAA airport upgrades and DOD installations. Forty-five stations were installed by the end of STORM-FEST, primarily in Kansas and Oklahoma (Fig. 3.1). Five-minute averages of air

temperature, dewpoint, wind speed and direction, barometric pressure, visibility, sky conditions, altimeter, density altitude and precipitation (5-min totals) were collected. During STORM-FEST, only a few of the PAM stations had actually been commissioned. At the other locations, the NWS took manual observations.

The AWOS data collected for STORM-FEST contained observations from a network of 48 airports in the STORM-FEST domain (Fig. 3.1). Most of the AWOS data consisted of 20-min averages of air temperature, dewpoint, altimeter, visibility, wind speed and direction, barometric pressure, sky conditions, density altitude and precipitation averages. AWOS observations were used in the analysis of the February 14 gravity wave case only. Linear interpolation was used to get the data into 5-min intervals.

The ICN 19-station network, with sites throughout Illinois, was operated by the Midwest Climate Center (Fig. 3.2). These stations collected 5-min averages of air temperature, relative humidity, pressure, wind speed and direction and precipitation. High resolution pressure sensors provided by NASA were installed in the network for STORM-FEST.

Forty-five NCAR second generation PAM II stations were utilized during STORM-FEST (Fig. 3.3). Nine stations were located in the STORM-FEST boundary layer network near Seneca Kansas, while most of the remaining stations were located in Missouri. A PAM station was also collocated with an ASOS station at Topeka, Kansas. The PAM stations measured 5-min averages of temperature, relative humidity, barometric pressure, 10-m wind speed and direction and rainfall totals.

### 3.2 *Upper Air Data*

Upper air data was used in Section 6 during the case study analysis. In addition to the conventional systems (NWS and Military), upper air soundings for STORM-FEST were provided by research systems as well, including the Cross-chain Loran Atmospheric

Sounding System (CLASS) and the Naval Postgraduate School (NPGS) "picket fence" networks. The upper air data were retrieved from North Carolina State University archives and displayed using the GEneral Meteorological data assimilation, analysis and display software PAcKage (GEMPAK). GEMPAK allows for a discrete data file to be created and different meteorological fields to be analyzed. Unfortunately, not all available soundings were included in the upper-air database.

National Weather Service took standard and special soundings from 33 stations in the western and central US. Data available consisted of pressure, temperature, relative humidity, wind speed and direction. Standard and special US Military soundings were taken from certain military installations in support of STORM-FEST. Data consisted of mandatory and significant levels of pressure, temperature, relative humidity, wind speed and direction. Eight fixed site CLASS rawinsonde stations were operated by NCAR, and the National Severe Storms Laboratory (NSSL) operated four systems in the STORM-FEST inner domain. Pressure, temperature and relative humidity measurements were provided by these systems. The NPGS at Monterey, California was responsible for a network of seven special rawinsonde stations. The purpose of this 15-station "picket fence" network was to provide observations from the environment upstream of the STORM-FEST operational area.

### *3.3 Satellite and Radar Data*

The satellite data archived during STORM-FEST was obtained from the Geostationary Operational Environmental Satellite (GOES-7). The instrumentation on GOES-7 was primarily the Visible and Infrared Spin-Scan Radiometer (VISSR), which produced day and night Infrared (IR), and day visible (VIS) radiometric images at 30-min intervals. Radar reflectivity data from individual NWS radar were used to produce regional NWS radar composites (NOWRAD) every 15-min during STORM-FEST. Satellite and

radar imagery used in the case studies were retrieved using Zeb software (Corbet et al. 1994). Zeb is a comprehensive graphical integration and display program that provides a variety of displays.

## 4. Objectives and Analysis Methodology

### 4.1 Objectives

The five general objectives to be met in this study are to:

1. Determine bandpass filtering effects on the data. The effects of two different sized filters on the raw data and on TSC are presented in Section 5. These tests were performed to determine the timing errors produced in the filtered data as compared to the raw pressure traces. In addition, the impact on the objective analysis of the waves were also investigated. The details of the filtering process are presented in Section 4.2, while the particulars for the filters used in the sensitivity tests are given in Section 5.1.

2. Evaluate various wave detection/tracking techniques. Four wave-detection methods were examined: subjective-analysis of the filtered pressure perturbation values, GEMPAK Barnes objective analysis, Barnes TSC with multiple advection vectors and Barnes TSC with a single advection vector. The dual goal was to determine if a Barnes objective analysis resulted in an adequate analysis, and if use of a single advection vector instead of multiple advection vectors degraded the TSC results and to what degree. The subjectively-analyzed waves were used in evaluating the Barnes objective analyses. In addition, the wave advection vectors suggested by the subjective-analysis were used in the Barnes TSC program. These evaluations are presented in Section 5.2.

3. Determine gravity wave characteristics and wave-convection interactions. Such characteristics as wave period and amplitude, wavelength, phase velocity, wave shape, perturbation pressure-wind covariance and a qualitative evaluation of the vertical structure of the wave were determined for the cases analyzed in detail and are presented in Section 6. Wave-convection relationships and possible interactions were also evaluated for these cases. Such an evaluation could provide an indication as to the responsible wave genesis and maintenance mechanisms as well as to the vertical structure of the wave.



4. Identify potential gravity wave occurrences. This was accomplished by looking at the raw pressure traces from the 41 days of the STORM-FEST dataset for evidence of mesoscale wave signatures. If the pressure trace for a given day suggested a period of less than 6 hr and an amplitude greater than 0.2 mb, then it was considered to be a pressure-pulse event. These events were ranked according to their average amplitude value to help determine which events were most likely a gravity wave. The duration of the event was recorded and the type of wave signature such as a solitary wave, wave train or wavelet was also noted.

5. Evaluate the applicability of the Uccellini and Koch (1987) conceptual model. The synoptic situations in the STORM-FEST region for 2 February through 13 March 1992 were analyzed to determine which features were present that have been suggested as typical during gravity wave events. These results are correlated with the frequency of occurrence of pressure pulses determined as described above.

The last two objectives are described in detail in the following sub-sections.

#### 4.1.1 IDENTIFYING POTENTIAL GRAVITY WAVE OCCURRENCES

The initial step was to determine the number of potential mesoscale gravity wave cases. Pressure traces from a majority of the stations in eastern Kansas, Missouri and Illinois were gathered and perused. The reason for concentrating on this area was because this was where the station density was greatest, allowing for optimum wave detection.

Pressure traces from 40 or more stations for each day were examined beginning on February 2, and peaks and troughs were identified in the traces. Then, the time between either peaks or troughs was determined and the magnitude of the peak-to-peak pressure change was calculated. The trough-to-crest pressure change had to be greater than 0.4 mb (0.2 mb amplitude) before considering an event for further analysis. If the time between peaks or troughs was less than 1 hr, the event was ignored because the wave would not be

able to be followed between stations. If the time between the pressure fluctuations was longer than 6 hours, the event was ignored because such periods exceed the 1 - 4 hr period characterizing mesoscale gravity waves (Uccellini and Koch 1997), in addition to the fact that there is a semi-diurnal pressure change that begins to affect the data after a 6-hr interval between pressure perturbations.

An example of the technique is presented in Fig. 4.1, where there were three peaks in pressure at approximately 0200 UTC, 0335 UTC and 0530 UTC. The peak-to-trough amplitudes were subjectively determined to be in the range 0.8 - 1.6 mb. This process of analysis was utilized for wave trains. If the wave was singular, there would be a significant peak or trough but no subsequent peaks or troughs. An example of such a case is presented in Fig. 4.2 in which the subjectively determined amplitude was 1.5 mb.

Next, the amplitudes were plotted along with the time of wave-like activity on a map of the stations. Temporal and spatial coherency of the pressure pulse signatures were noted. Those days in which the pressure traces displayed wavelike tendencies with periods of 1 - 6 hr and amplitudes  $\geq 0.2$  mb were classified as a pressure pulse event. The pressure pulse events were further investigated to determine their duration which involved checking to see if activity on one day extended into the next. For each of the pressure pulse events, 50 pressure traces from each day involved in the event were used in determining the average amplitude. Traces chosen for this analysis were subjectively determined by first looking at those traces from stations nearest the wave activity and then extending out from there. If a station showed no evidence of wave activity then it was not included in the average amplitude calculations. The amplitudes were recorded and after looking at all the values for the events, categories of ranges were chosen and the number of amplitudes in each category were counted for each individual event. The first category began as 0.1 mb and a new category started every 0.3 mb through to the highest amplitude calculated. The average amplitude for each event was then calculated using

$$\hat{A} = \frac{1}{S} \sum_{i=1}^m S_i \bar{A}_i \quad (4.1)$$

where  $S$  is the total number of stations with activity present for each pressure pulse event,  $m$  is the number of amplitude categories used,  $S_i$  is the number of observations within a  $\Delta p$  category and  $\bar{A}_i$  is a central value from the amplitude category,  $i$ . The results from this identification process are presented in Section 6.1.

#### 4.1.2 EVALUATION OF THE UCCELLINI AND KOCH (1987) GRAVITY WAVE SYNOPTIC MODEL

In an attempt to determine whether gravity waves occur under a general synoptic pattern, 500 mb wind and height charts along with surface charts from NOAA's "Daily Weather Map" series, both valid at 1200 UTC, were studied for each of the 41 days. This was done with the conceptual wave environment model identified by Uccellini and Koch (1987) (Fig. 2.8) in mind. Although they used the 300 mb height fields and winds, the 500 mb charts for STORM-FEST were readily available and were considered to be a viable substitute for the 300 mb charts.

The upper-level synoptic pattern governing the area of interest centered over Kansas, Missouri and Illinois was identified. The three criteria examined over the STORM-FEST region were: a jet streak near an inflection axis, a diffluent trough, and a front to the south or southeast of the "wave" region. These results are also presented in Section 6.1.

#### 4.2. Gravity Wave Analysis Methods Using Surface Data

The analysis methods presented here were those used in the examination of the individual cases presented in Section 6. As mentioned earlier, these surface analysis methods have been used by a number of gravity-wave investigators.

#### 4.2.1 DATA HANDLING

The raw digital 5-minute STORM-FEST observational data were obtained from the University Corporation for Atmospheric Research (UCAR) Office of Field Project Support (OFPS) CODIAC system. The data were converted into a format that was easier to use and readable by GEMPAK. The NWS barograph traces were digitized in 15-min intervals and then expanded to 5-min intervals through linear interpolation for purposes of combining these data with the digital 5-min surface STORM-FEST data.

Next the data were checked for quality. This was the most time intensive step. Data from each station to be used in the analysis had to be checked for errors. The data from each individual station to be used in the analysis was examined and each 5-min observation of pressure and wind was checked to see if it was reasonable from a meteorological perspective. Outliers and gaps, perhaps due to a power outage for example, were interrogated. If there were data gaps less than 30 minutes, linear interpolation was used to fill these gaps. The filter program assigned a central value to the missing data. Pressure and wind time series plots were examined to ensure that the changes made were accurate and adequate.

#### 4.2.2 SPECTRAL ANALYSIS

Auto-spectral analysis was used to determine the significant frequencies present in the pressure traces. Significant autocorrelations from 40 or more stations primarily from the central and eastern sections of the STORM-FEST region were identified. This region was chosen because the waves needed to be tracked for a period of time; therefore, it was required that the wave activity be obvious in the center of the area.

The surface pressure traces are time series that can be analyzed in the time or the frequency domain. The frequency domain analysis, which describes the fluctuations of

time series in terms of sinusoidal behavior at various frequencies, is used here. Fourier analysis concepts assume that any periodic function can be represented as a series of harmonically related sinusoids. Because Fourier analysis is based on the assumption of fixed amplitudes, frequencies and phases, it breaks down when applied to time series (Jenkins and Watts 1968). Time series, on the other hand, are characterized by random changes of frequencies, amplitudes and phases. Therefore, spectral analysis is an ideal tool since it was developed in response to these inherent problems and incorporates the adaptations required for time series analysis (Jenkins and Watts 1968).

Spectral analysis is a method that describes the tendency for oscillations of a given frequency to appear in the data. The Fourier transform of the autocovariance function in the time domain is represented in the frequency domain by what is referred to as the spectrum, at least for a stationary process. The spectrum and the autocovariance sequence therefore form a Fourier-transform pair, with one being uniquely determined from the other. Hence, the time domain approach and the frequency domain approach are theoretically equivalent (Wei 1994). A peak in the spectrum indicates an important contribution to the variance from the component at frequencies in the corresponding interval and is an indication of the energy associated with that frequency. The energy of the time series is typically considered per unit time, and is called the power of the sequence (Wei 1994) or spectral density. Thus, the spectrum shows how the variance or average power of the time series is distributed over frequency.

The most basic property of the sinusoids that makes them generally suitable for the analysis of time series is their simple behavior in time (Bloomfield 1976). Even though there are changes over time to the pressure traces used in this study and the behavior of the traces is not simple, this approach is still valid. This is because a discrete window is chosen around the time of wave activity for each station, and a truncated Fourier series may

be regarded as the infinite series with the coefficients multiplied by a boxcar function (Bloomfield, 1976).

The spectral analysis methods used in this study are identical to those used by Koch and Golus (1988), and the details are taken from their paper. To begin the process of power spectrum analysis, the mean and any trend were removed using second-order polynomial fits to the data in order to reduce the undesirable leakage of "red noise" variance from spectral peaks in the low-frequency domain to higher frequencies. If the autocorrelation values from the detrended time series still did not decay exponentially as lag increased, then the series was differenced using a filter that created a new time series  $y(t)$  from the original series  $x(t)$  according to

$$y(t) = x(t) - x(t - \Delta t). \quad (4.2)$$

This filter produces no phase alterations in the data (Jenkins and Watts 1968). The sample autospectrum estimator used was the Fourier transform of the autocovariance function,  $c_{11}(\epsilon)$ , after the Tukey window has been applied in the time domain,

$$c_{11}(f) = \int_{-M}^M w(\epsilon) c_{11}(\epsilon) e^{-2\pi i f \epsilon} d\epsilon \quad (4.3)$$

where  $w(\epsilon)$  is the Tukey window weight at lag  $\epsilon$ ,  $M$  is the maximum lag and  $f$  is frequency. The Tukey window was used to smooth the autospectrum, and the amount of smoothing that occurred was inversely proportional to the spectral bandwidth,  $M/N$ , where  $N$  is the number of data points used in the analysis. The reason behind smoothing the sample spectrum is that an improved estimator of the spectrum can be obtained by doing so (Jenkins and Watts 1968). As the amount of smoothing increases, unfortunately so does the bias (distortion of the frequencies of spectral peaks), hence a compromise has to be achieved between bias and variance. In the autospectrum graphs, three bandwidths were shown so as to aid in determining where the spectral peak was, while keeping this compromise in mind. Because of the range of values of the spectral density, it was plotted

on a logarithmic scale, and since the bandwidth is constant with frequency, the frequency scale was linear. The spectral density plot of the time-series window for station P43 shown in Fig. 4.3 encompasses the period occupied by the pressure perturbation evident in Fig. 4.2.

Chi-squared confidence intervals were calculated for the Tukey window and added to the autospectrum plots. Peaks in the autospectrum were considered significant only when: 1) the peak exceeded the estimated white noise variance level by at least the 95% confidence level; 2) this peak was separated from any adjacent significant peak by a frequency interval exceeding the Tukey spectral bandwidth and 3) the peak was not the obvious result of aliasing or leakage. Thus, for example, the spectral peak at  $f = 0.006 \text{ min}^{-1}$  in Fig. 4.3 was considered significant. The peak in Fig 4.3 is typical of those that occurred in the cases analyzed. Although a single peak may not be considered significant in itself since the time series used in the spectral analysis were relatively short, the fact that many of them occurred and that they all looked about the same is significant. It is important to note that the desired cutoff frequency extremes were determined to be those corresponding to periods of 30 min and 6 hr. The purpose of performing the spectral analysis was simply to determine how the bandwidth could be "tweaked" so as to reduce the attenuation of those frequencies at which the majority of the significant peaks occurred.

#### 4.2.3 BANDPASS FILTERING

The spectral peaks in the pressure-trace time series from individual observing stations were identified and recorded according to the requirements listed above for a significant peak. Next, peak frequencies obtained from the spectral analysis were displayed in a histogram of frequency versus the number of occurrences so as to aid in the determination of the appropriate cutoff frequencies for the band-pass filter (Fig 4.4).

The purpose of filtering the time series is to alter the Fourier amplitudes that describe the series in a predictable manner. The Lanczos filtering process used in this study was the same as that described by Duchon (1979). The modification of the time series was accomplished with a set of weights called the filter weight function. The filter weight function forms a Fourier series transform pair with what is known as the frequency response function.

To describe this relationship, it is important to begin by stating that Fourier analysis methods simplify the analysis of time invariant linear systems. Non-linear systems, such as the ones in this analysis, can be linearized so that, for small perturbations in the input, the equations presented here can be used as an approximate representation of the system (Jenkins and Watts 1968). It may be shown that in general, the solution to equations for such systems may be written as a convolution integral

$$y(t) = \int_{-\infty}^{\infty} q(b)x(t-b)db \quad (4.4)$$

where  $y(t)$  is the solution and  $x(t)$  is the forcing function. Thus, the output,  $y(t)$ , may be written as a weighted sum of past values of the input,  $x(t)$ . In other words, the output is a convolution of the input with the weighting function,  $q(b)$  (Jenkins and Watts 1968). The solution may be simplified by Fourier transforms which lead to

$$Y(f) = Q(f) X(f) \quad (4.5)$$

where  $Y(f)$ ,  $Q(f)$  and  $X(f)$  are the Fourier transforms of  $y(t)$ ,  $q(t)$  and  $x(t)$ . Thus, convolution in the time domain transforms to multiplication in the frequency domain (Jenkins and Watts 1968). Equation (4.5) states that the component at frequency  $f$  in the output is obtained by multiplying the component of the same frequency in the input by  $H(f)$ , the frequency response function of that frequency. Thus, knowledge of the frequency response function for a filter operating on a time series permits one to determine which frequencies are filtered out and which ones remain unaffected.



The Lanczos filtering procedure used here required only two input items, the cut-off frequencies and the number of weights to be used, and there were only three fundamental steps involved in this procedure. The desired form of the response function was determined and cut-off frequencies established, and the number of weights and the weight function were determined. Finally, the actual response was calculated and applied to the series. Although these steps are straightforward, they were not performed independently of one another, but rather in consideration of one another as explained later.

The ideal band-pass filter would show a boxcar response function, i.e. zero response from  $f = 0$  to the initial frequency in the desired band ( $f_{c1}$ ) a response of 1.0 between this frequency and the frequency at the opposite end of the desired band ( $f_{c2}$ ) and a response of zero again from this frequency to the Nyquist frequency ( $1/2\Delta t$ ) which in this case is  $0.1 \text{ min}^{-1}$  since  $\Delta t = 5 \text{ min}$ . However, since the time series used in this analysis were truncated and a finite number of weights were used, the computed response function exhibited weak oscillations known as the Gibbs phenomenon (Fig. 4.4). The fewer the number of weights, the larger the oscillations. Lanczos (1956) showed that the error in a truncated Fourier series has the form of a "modulated carrier wave" which contributes significantly to the amplitude of the Gibbs oscillation. Therefore, he proposed that this carrier frequency be filtered out. This can be done by convolving a rectangular function, whose width is the period of the carrier wave, with the desired response function. The result is a smoothed response function. The Fourier coefficients for the smoothed response function are determined by multiplying the original weight function by a function known as the "sigma factor" (Duchon 1979).

When a bandpass filter is applied to a series, basically two low-pass filters are applied, LP1 and LP2, one for each of the cut-off values. The smoothed response function used in this study can be written as

$$\bar{R}_{LP}(f) = (v_o)_{LP} + 2 \sum_{k=1}^{n+1} (\bar{v}_k)_{LP} \cos(2\pi f k) \quad (4.6)$$

where  $v_o$  is the central weight,  $k$  is the counter for the weights, and the “sigma”-smoothed weights are given by

$$(\bar{v}_k)_{LP} = \left( \frac{\sin 2\pi f_c k}{2k} \right) \left( \frac{\sin \pi k / n}{\pi k / n} \right) = v_k \sigma_k. \quad (4.7)$$

The number of weights is  $N$ ,  $n = (N - 1)/2$  is the number of one-sided weights and  $f_c$  is the cut-off frequency which is also where the response function has a value of 0.5. In order to have the maximum response value at the band-pass center, the following criterion must be met:

$$n \geq 1.3 / (f_{c2} - f_{c1}). \quad (4.8)$$

If the criterion is not met, the response at the center of the band-pass filter will be attenuated; however, the number of observations lost from the series due to the number of weights must also be considered. A value of  $n = 65$  was used in the case studies. Values chosen for  $f_{c1}$  and  $f_{c2}$  in the first two case studies depended on the results from the spectral analysis and the fact that  $n = 65$ . A predetermined band was used in the third case study based on the results from sensitivity tests presented in Section 5 and on the typical period of a mesoscale gravity wave (1 - 4 hr). The smoothed weights for the band-pass filter can be written as the difference in weight functions for two low-pass filters as

$$(\bar{v}_k)_{BP} = (\bar{v}_k)_{LP2} - (\bar{v}_k)_{LP1}. \quad (4.9)$$

When the band-pass weights are normalized, so that the sum of the weights equals one, they can be written as

$$(\bar{\bar{v}}_k)_{BP} = \frac{\bar{v}_{LP2}}{\sum \bar{v}_{LP2}} - \frac{\bar{v}_{LP1}}{\sum \bar{v}_{LP1}} \quad (4.10)$$

and the band-pass response function can be represented as

$$\overline{\overline{R}}_{BP}(f) = \overline{\overline{R}}_{LP2}(f) - \overline{\overline{R}}_{LP1}(f). \quad (4.11)$$

The transform in this case is obtained as the solution of a difference equation (Jenkins and Watts 1968).

The advantage of the Lanczos filter over another popular filter, the Hanning filter, is that the cutoff frequency can be controlled independently of the number of weights. The response function of the Lanczos filter is very similar to that of the Craddock filter; however, the advantage of the Lanczos filter in this case is that it has a wider bandpass and smaller side lobes (Duchon 1979).

Once the pressure series had been filtered, additional smoothing was accomplished using a simple 3-point (1-2-1) smoother. An expression for the final smoothed series is

$$fds(i) = .25 [fd(i - 1)] + .50 [fd(i)] + .25 [fd(i + 1)] \quad (4.12)$$

where  $fd$  represents the filtered data and  $i$  is simply a counter variable. The final output from the filtering process were pressure perturbations,  $p'$ . The initial time series were 39 - 42 hr, depending on the case. The filtering process led to the loss of a total of  $N$  observations (2.7 hr from both ends of the series).

#### 4.2.4 DETERMINING WAVE PHASE VELOCITIES

Once the  $p'$  values were obtained for each station, they were plotted on a map every 30-min and subjectively analyzed for troughs of low-pressure perturbations. The "wave axis" tracking method (Koch and Golus 1988), was used to help determine the movement of the wave (Fig. 4.6). To determine the direction of the wave movement at each station using this method, a perpendicular line was drawn between consecutive subjectively analyzed negative pressure perturbation isochrones and through the station or close to it. The speed of the wave as it passed a given station was determined by the distance between the isochrones closest to that station. Both a direction and speed were

determined for each station as the wave trough passed by. The direction of wave movement was used in the filtering of the winds (see below) and the wave velocity was required input in the TSC program. An average wave velocity was also determined by placing a single line through the centers of the wave trough axes to determine the direction of movement. The wave speed at the center of the wave between each hourly isochrone was determined and these values were averaged over the span of wave activity. The single advection vector used in sensitivity test 4 presented in Section 5 was determined in this manner.

#### 4.2.5 PRESSURE-WIND COVARIANCE

The filtering process described above for the pressure was also used on the winds. Before the filter was applied however, the wind component axes were rotated into the direction of wave movement such that

$$u^* = -u \sin\beta - v \cos\beta, \quad (4.13)$$

where  $u$  and  $v$  are the Cartesian wind components (positive toward the east and north, respectively) and  $\beta$  is the direction from which the wavefronts were propagating (measured clockwise from north), as determined from the above procedure applied to the  $p'$  data. The  $u^*$  values were calculated assuming a two-dimensional, propagating plane wave, which is a common approach among gravity wave investigators (Pecnick and Young 1984, Einaudi et al. 1987, Koch and Golus 1988). Only the  $u^*$  component was filtered and the resulting values were wind perturbations in the direction of wave propagation ( $u^{*'}).$

Next,  $\overline{p'u^{*'}}$  correlation values were calculated over a three- or six-hour period and plotted, centered around the time of wave activity for each station (Fig. 4.6). Correlations above 0.32 are statistically significant at the 95 % level. Gravity wave theory implies these

correlation values will be positive (see Fig. 2.4), and many investigators have used this technique to identify events as gravity waves (Bosart and Cussen 1973, Koch 1979, Bosart and Sanders 1986, Koch and Golus 1988). Since the pressure-wind correlation is a direct measure of the wave signal-to-noise ratio (Gossard and Sweezy 1974) a high value would be indicative of a strong wave signal, as opposed to some other phenomena (e.g. a thunderstorm) that could cause pressure fluctuations.

#### 4.2.6 TIME-TO-SPACE CONVERSION OBJECTIVE ANALYSIS

The principle of time-to-space methodology was originally described by Fujita (1963). The conversion of time sections to space sections is accomplished by plotting the time sections along the applicable vectors through each observing station. Consider a given meteorological parameter  $A$ . If an arbitrary point within the area of analysis is considered,  $P(x,y)$ , the change in the meteorological parameter ( $\delta A$ ), referred to a point  $P$ , is represented by

$$\frac{\delta A}{\delta t} = \frac{\partial A}{\partial t} + \mathbf{C} \cdot \nabla A \quad (4.14)$$

where  $\mathbf{C}$  is the velocity of the point  $P$ .

If the mesoscale disturbance is considered to be characterized by a simple translational motion with velocity  $\mathbf{C}$ , there is no individual change as long as the point  $P$  moves at the same translational velocity as the disturbance. In this case, the above equation becomes

$$\frac{\partial A}{\partial t} = -\mathbf{C} \cdot \nabla A \quad (4.15)$$

or in one dimension,

$$\frac{\partial A}{\partial X'} = -\frac{1}{c} \frac{\partial A}{\partial t} \quad (4.16)$$

or in finite difference form,

$$\frac{\Delta A}{\Delta X'} = -\frac{\Delta A}{c\Delta t'} \quad (4.17)$$

where  $X'$  is the new coordinate parallel to the velocity of point  $P$ . Equation (4.17) indicates that the time section of the pressure in this case, can be converted into space sections by reversing the sign of the time-progress after division by the speed  $c$ .

The TSC computer program used in this study was based on the Barnes (1973) objective analysis technique. The Barnes TSC technique is similar to the subjective TSC technique of Fujita (1963) described above; however, the Barnes method is an objective map analysis scheme that does not require the system (gravity wave) properties to be in exact steady state. Instead, it allows for a decrease in wave conservation with increasing time away from the on-time value (McCarthy and Koch 1982). For this study, each station generated a series of  $N = 21$  observations (one on-time value and twenty off-values, i.e.  $\pm 50$  min from the map time) as suggested by Koch and O'Handley (1996) as being optimum. These observations were distributed along the wave translational velocity vector  $C$  at distances of  $C\Delta t$  (where  $\Delta t = 5$  min is the time between successive observations). The Barnes TSC technique assumes an exponentially decreasing degree of steady state of the system over the conversion period  $\tau = (N - 1)\Delta t$ .

The details on the Barnes TSC method were taken from Koch and O'Handley (1996). The original Barnes objective analysis scheme (without TSC) is a simple, Gaussian weighted-averaging technique which weights observations to obtain interpolated values at individual grid points of a rectangular mesh. The weighting function is analogous to a Gaussian low-pass filter in which the response function can be determined beforehand. The weight assigned to an observation is a function of the spatial distance ( $r_i$ ) between the observation at the station and the grid point being computed. For a given grid point, the

weight assigned to station-observation  $i$  depends on the distance to the observation  $r_i$  according to:

$$w_i = \exp(-r_i^2 / \kappa^*). \quad (4.18)$$

A modification of the spatial weight parameter from that used in the GEMPAK version of the Barnes scheme (Koch et al. 1983), is recommended in Koch and O'Handley (1996) for use in the Barnes TSC scheme. Thus,

$$\kappa^* = .693(2\Delta n / \pi)^2 \quad (4.19)$$

is a spatial weight parameter whose value is based on the mean station spacing ( $\Delta n$ ). The value for  $\kappa^*$  determines the filter response function. (The Barnes scheme is effectively a low-pass filter.) Koch et al. (1983) showed that the use of smaller values of  $\kappa^*$  results in greater filter response during the first pass, particularly for the short waves.

The GEMPAK Barnes method applies one correction pass through the initial interpolated field. The weighting function for the Barnes TSC becomes

$$w_i = \exp\left(\frac{-r_i^2}{\kappa} - \frac{\Delta t^2}{\tau^2}\right). \quad (4.20)$$

In this correction pass,  $\kappa = \kappa^* \gamma$ ,  $\Delta t$  is the difference between the analysis time and the data time and  $\tau$  is a parameter that controls the time response. An acceptable degree of analysis convergence is forced by the parameter  $\gamma$ . When  $0 < \gamma < 1$ , a high degree of convergence between the observation field and the correction pass interpolated field is forced. When  $\gamma < 0.5$ , the effect is even greater, allowing more of the actual data to come through the low-pass filter inherently contained in the TSC technique. A value of  $\gamma = 0.2$  is used in this study since the maximum response and best fidelity characteristics of the scheme's inherent low-pass filter are associated with this value. Koch and O'Handley (1996) showed that the second pass response for the  $2\Delta n$  wave (using (4.19) and  $\gamma = 0.2$ ) is 0.94. Koch et al. (1983) showed that when  $\gamma$  is chosen small enough, there is no

real benefit in making more than one correction pass because of how quickly convergence is approached. They also state that maximum detail is obtained with this value for  $\gamma$ , but that small values for  $\gamma$  are justifiable only when errors in the data are a small fraction of the signal present over the field and when the observations are not substantially contaminated by subgrid-scale atmospheric processes. The latter requirement is assumed herein, and since great care was taken in quality controlling the data, the use of a small value for  $\gamma$  is fine. No general analytical expression for the filter response function of the TSC scheme has been derived; however, Koch and O'Handley (1996) suggest an objective method for determining  $\tau$ ,

$$\tau \geq \lambda/(4c), \quad (4.21)$$

which for typical mesoscale gravity waves ( $\lambda \cong 200$  km) and phase speeds ( $c \cong 20$  ms<sup>-1</sup>) results in a recommended value of  $\tau \cong 45$  min. They also suggest that larger values for  $\tau$  (i.e., a larger time interval over which TSC is applied to each observation) be used for relatively steady disturbances, and smaller values be used for rapidly changing ones. Values for  $c$  were estimated using the average wave speed determined from the subjectively analyzed waves as described in Section 4.2.4. Values used for  $\tau$  are discussed in the individual case studies and in Section 5 where sensitivity tests on  $\tau$  are presented.

The correction pass grid field is the result of adding to the first pass field the smoothed residual difference between the observed data values and the first pass estimate values at the actual data locations. The response function of the second pass indicates how closely the interpolated values agree with the observed values after the second pass.

Another factor to consider is the radius of influence. Beyond this radius, measured from a grid point out to neighboring data points, the weight assigned to an observation is essentially zero. The weighting function (4.20) is such that as this distance increases, the weight approaches zero asymptotically. An additional feature of the weighting function is



that during the correction pass, the radius of influence is essentially shortened and the weights decrease more rapidly with distance than they did during the initial pass given the same distance (because  $\kappa < \kappa^*$ ).

The mesoscale analyses are constructed from the filtered data at the stations spaced an average distance of  $\Delta n$  apart and interpolated to a square mesh of grid spacing  $\Delta x$ . The values of  $\Delta n$  and  $\Delta x$  varied in each of the case studies. Since five grid points are required to represent the wave on a grid, the  $\Delta x$  value of the grid must be no larger than  $1/2 \Delta n$  in order to properly represent the resolvable wavelengths. (The sizes of  $\Delta x$  and  $\Delta n$  are addressed in each of the individual case studies and Section 5 where appropriate.) This analysis tool does not apply if the actual atmosphere is much unlike the assumptions of quasi-conservation and no dispersion. However, proper use can help to clarify analysis features when there is sparse spatial or temporal resolution (McCarthy and Koch 1982).

## 5. Sensitivity Tests

Table 5.1 shows the TSC sensitivity tests performed and the identification and particulars of each run of the program. The different wave-tracking techniques are also evaluated in this section.

*Table 5.1 Sensitivity Tests. Sensitivity tests performed (Test 1, Test 2, Test 3 and Test 4) and the values for the various variables being tested. An identification has been assigned to each of the TSC objective analysis.*

	Identification	Filter	Tau (min)	Grid-length (km)	Advection Vector
Test 1	NF	Narrow	50	25	Multiple
	WF	Wide	50	25	Multiple
Test 2	T50	Wide	50	40	Multiple
	T15	Wide	15	40	Multiple
Test 3	GL40	Wide	50	40	Multiple
	GL25	Wide	50	25	Multiple
Test 4	MULT	Wide	50	25	Multiple
	SGL	Wide	50	25	Single

### 5.1 Choice of Filter Bandpass Interval

#### 5.1.1 FILTER EFFECTS ON PRESSURE TRACES

Two different filters were applied to the February 14 data set, one wide and one relatively narrow. The narrow filter was determined as described in Section 4.2.3. A wider filter, identical to that used by Koch and O'Handley (1996) in their analysis of the same gravity wave event, was chosen to test the sensitivity of the pressure perturbations to the width of the filter. In order to determine this sensitivity, the filtered pressure traces were compared to the raw data traces. Fifty-seven significant trough and ridge features were compared from a total of 40 stations. Three waves of depression were identified in the February 14 case and they are referred to as A-, B- and C-. The ridges between the troughs are referred to as A+ and B+. This nomenclature is used throughout this study with the lettered "+" representing the ridge following the trough (-) of the same letter.

The cutoff frequencies for the narrow filter were  $f_{c1} = 0.004 \text{ min}^{-1}$  and  $f_{c2} = 0.010 \text{ min}^{-1}$ . According to (4.8), the required number of one-sided weights to reach a response of 1.0 is 44; however, this would lead to approximately 3.7 hrs of data lost on either end of the time series. Since the size of the time series had already been decided upon and "building" these time series was the most time consuming process in the entire analysis, the decision was to use 32 one-sided weights and to accept a center response of 0.88 (see Figs. 4.4.a and 4.4.b), which equates to a 12 % decrease in perturbation amplitudes. With the narrow filter, 27 features showed up on the filtered traces before the actual event appeared on the raw time series. Twenty-five features were evident after the actual occurrences. There was one difference of 55 min (Fig. 5.1), where the actual trough occurred at 0110 UTC while the filter placed it at 0015 UTC, one of 50 min, one of 40 min, six of 35 min and five of 30 min so that less than 25 % of the time errors were of 30 min or greater.

A total of 32 one-sided weights were also used with the wide filter; however, the cutoff frequencies were  $f_1 = 0.004 \text{ min}^{-1}$  and  $f_2 = 0.034 \text{ min}^{-1}$ . Equation (4.8) suggests that 9 one-sided weights were needed and therefore the response function (see Fig. 4.4.a and 4.4.c) had a value of approximately 1.0 for the frequencies at the center of the frequency range. With the wide filter, twenty features occurred at the same time while the filter put 22 (15) features before (after) their actual occurrences; however, of greater importance is the fact that the time differences were much less than were noted with the narrow filter. There were only six differences of 15 min and the rest were 10 min or less, which is considered insignificant for the current applications.

When the narrow filtered trace was compared to the wide filtered trace, the majority of the time differences were either both before the actual event or both after the event. Figure 5.1 shows the narrow-filtered and wide-filtered traces on the same graph as the actual trace for station P18. An actual trough occurred at 0210 UTC 15 Feb. The narrow filter depicted the corresponding trough at around 0225 UTC while the wide filtered trough

was at approximately 0205 UTC. Overall, this indicates that, whereas the filter width had little effect on whether the feature was misplaced before or after the actual event, it significantly affected the size of the phase error. This could be expected due to the smoothing involved with the filtering process, in that the narrower filter eliminated the higher frequency components (periods shorter than approximately 100 min).

Some other interesting findings came from looking at two or three features, such as a trough-ridge-trough, in a row from ten stations. With the narrow filter, whether the first feature was a ridge or a trough, the pressure perturbation trace showed the first feature before the actual feature in the raw pressure trace at each of the ten stations. The subsequent  $p'$  feature was placed after the actual feature. (Note in Fig. 5.1 that the actual ridge and trough occurred at 0120 UTC and 0210 UTC respectively, whereas the narrow-filtered ridge and trough occurred at 0105 UTC and 0225 UTC.) This was also the case with the wide filter at the majority of the stations, but a larger number of features occurred in the filtered trace at the same time as the actual ones. Only two stations showed filtered features on opposite sides of the actual features. The conclusion here is that both filters tended to incorrectly broaden the temporal separation between trough and ridge features, though this was much less of a problem for the wider filter. Again, this can be attributed to the smoothing effects of the filtering process. This effect should be considered when choosing a bandpass filter width for such applications as those herein. Even though a histogram may suggest a certain bandwidth, in order to lessen the broadening effect and hence potential phase errors, it may be beneficial to extend the width.

#### 5.1.2 FILTER EFFECTS ON OBJECTIVE ANALYSIS

The TSC Barnes analysis was run with both the narrow and the wide filter to see what effects the different filter width had on the pressure perturbation map analysis. Multiple advection vectors were used with  $\tau = 50$  min and a grid-length of 25 km for both

filter selections. Given the filter response functions, it was not unexpected to find that the narrow filter (NF) did not produce as high of a pressure perturbation amplitude as the wide filter (WF). In general, the WF waves (Fig. 5.2.a) were also more detailed and the intensities were stronger; however, the lack of detail present in the NF waves (Fig. 5.2.b) made them slightly easier to follow. An example of the difference in perturbation values was evident at 2030 UTC when the maximum perturbation value for B- was - 1.6 and -0.9 for WF and NF, respectively. The basic wave shapes in the fields produced by the two filters were quite similar. At various times, the wave placement and/or shape varied slightly between the filters, although some of the difference could have been due to the subjectivity involved since the wave troughs were hand-analyzed from the output.

Another of the differences between the two sets of analyses was that the shape of the B- and B+ features appeared more wave-like in the WF analysis than the NF analysis at 2030 UTC. Another difference was that at 0300 UTC, WF had a positive bulls-eye in east-central Missouri of 0.8 mb while NF displayed no apparent feature. Overall, despite the large timing errors noted above in the narrow-filtered pressure traces, the TSC results from the different filters did not lead to much of a disparity in wave placement. The greatest differences were in the intensity, as was expected, and ease of tracking the waves. Since WF produced  $p'$  values closer to the actual values, it was used in Section 6 as well as the remaining comparisons involving multiple advection vectors with  $\tau = 50$  and grid-length  $\Delta x = \Delta y = 25$  km.

## 5.2 Wave Tracking Techniques

Four wave-detection methods were examined in this study: subjective-analysis of the filtered pressure perturbation values, GEMPAK Barnes objective analysis, Barnes TSC with multiple advection vectors and Barnes TSC with one advection vector. The goal was two-part: (1) determine if a Barnes objective analysis resulted in an adequate analysis, and

(2) determine if use of a single advection vector instead of multiple advection vectors degraded the TSC results and to what degree.

#### 5.2.1 SUBJECTIVE ANALYSIS OF PRESSURE-PERTURBATION FIELDS

The pressure perturbations plotted at station locations from the narrow-filtered time series were subjectively analyzed every 15 minutes in order to compare the analysis results using this method to the objective Barnes TSC. In addition, the wave advection vectors obtained for each station from the subjective analysis were used to advect the wave in the Barnes TSC. Three depression waves were identified and the hourly pressure trough isochrones for A-, B- and C-, are given in Figs. 5.3.a, 5.3.b and 5.3.c, respectively. Since A- and B- were the strongest waves (Fig. 5.2), they received the most emphasis. In this hand analysis, extreme care was taken to follow the wave as precisely as possible between stations and through data sparse areas in an attempt to reduce the undesirable consequences of performing a subjective analysis. The waves were easy to follow for the most part. Wave B- became weak and difficult to distinguish in Missouri and into Illinois. When the B- wave was in this area, there were times when its position was fairly evident but then the next hour it was hardly discernible because of uncertainties arising from the development of new, smaller scale waves as B- entered Missouri.

The relationship between the subjective analysis and the filtered data was examined by comparing 24 pressure minima from 21 stations using the times the perturbations were evident in the actual traces, the position of the perturbations in the narrow-filtered traces, and the position of the hand analyzed waves on the  $p'$  maps. As expected, the subjectively analyzed waves, which were based on the narrow-filter product, agreed with the filtered traces as far as placing the minimum perturbation, and therefore the wave trough, either before or after the actual occurrence. In determining the time difference between when the subjectively analyzed wave moved through a station versus when the filtered time series

displayed the pressure perturbation, it was found that the largest discrepancy was 1 hr. At least 54 % of the differences were 10 min or less. Of the 13 locations where the differences were more obvious, the subjectively analyzed wave passed a given station before the filter as nearly as often as after.

Each of the subjectively-analyzed waves was compared to the waves analyzed from the WF output. Figures 5.4.a, 5.4.b and 5.4.c show the wide-filtered TSC wave-trough isochrones. Initially, the hand-analyzed A- was not arc-shaped like it appeared in the TSC analysis. This difference highlights the subjectivity of the subjective-analysis, and the fact that the location of A- early in the run was located in a fairly data-sparse area. The subjectively-analyzed A- wave began to curve slightly after 2100 UTC. The wave was located in approximately the same location in Figs. 5.3.a and 5.4.a until 0100 UTC when the TSC wave pulled out ahead of the subjectively analyzed position by almost one hour.

The B- wave in both the subjective-analysis and the TSC was arc-shaped from the beginning. The TSC analysis split the wave at 2200 UTC, whereas the subjectively-analyzed wave was drawn with the southern and northern parts connected through Missouri. As previously noted, the wave is weakly represented in this area and portrayal is left to the individual conducting the analysis. (It is also pertinent that the  $\overline{p'u^{*}}$  correlation (Fig. 4.6) weakened here.) In this case, the portrayal of a unified wave front was considered desirable by the analyst. The TSC B- wave moved ahead of the subjectively-analyzed wave after 0200 UTC, oddly enough in the same area as did the A- wave.

The two representations of the C- wave were in close agreement until 0300 UTC, when the TSC output showed two distinct areas of maximum negative perturbations (see Figs. 5.3.c and 5.4.c) separated by a weak ridge. The subjectively-analyzed wave agreed with the slower perturbation that tracks more towards the northeast versus southeast.

It was much easier to follow the wave in the TSC analysis than in the subjective analysis. The objective analysis brings the wave to life in the sense that it is almost

animated when a plot from a given time is compared to consecutive plots. In addition, an objective analysis method is almost always preferred over a subjective method. An example of where plots of the  $p'$  values used in the subjective analysis provided necessary information not available in the TSC is given in the interpretation of the  $\overline{p'u^*}$  analysis for the February 16-18 case study in Section 6.

#### 5.2.2 CONVENTIONAL BARNES OBJECTIVE ANALYSIS OF PRESSURE PERTURBATION VALUES

Conventional Barnes analysis (Fig. 5.5) somewhat captures both the A- and the B-waves; however, at times these features disappeared and then reappeared a short time (one to two hours) later. The perturbation values were less than the actual pressure perturbation values in many cases. The pressure perturbation maxima tended to be circular instead of displaying wave-like characteristics, causing the shape of the isochrones drawn using these values to change and appear less continuous than a typical wave feature. Therefore, using a Barnes analysis to track the wave would not be recommended.

#### 5.2.3 USE OF SINGLE OR MULTIPLE ADVECTION VECTOR IN OBJECTIVE ANALYSIS

The single advection vector (SGL) used in this section was determined as described in Section 4.2.4. A value of  $\tau = 50$  min was used and the grid-length was 25 km. As could be expected, the overall contour shape of the SGL ( $220^\circ/15.7 \text{ ms}^{-1}$ ) output (Fig 5.6.b), was unrealistically planar, yet the intensities of the perturbation maxima and wave locations were pleasingly similar in the two different TSC experiments.

One of the variations between the two analyses occurred at the southern end of A-, where the use of the single vector did not consistently curve the wave back toward the southwest as displayed in the multiple advection analysis (Fig. 5.6.a, 2200 UTC). At



0200 UTC, it was rather difficult to determine the placement of A- in the SGL output due to the corrugated appearance. The representation of C- was quite different between the two experiments after 0100 UTC. The fact that this wave was considerably weaker than the other two waves (except for the time B- was "lost" in central Missouri) may suggest that a single vector does not greatly hinder the tracking of the wave as long as the signatures are fairly strong. Even though SGL exhibited some difficulty in accurately representing the arc-shaped features of the waves, it still did surprisingly well; however, it would probably be wise to use multiple advection vectors when the wave is known to be arc-shaped. If clouds are present with the wave features, they should give some indication as to the shape of the wave. Koch and O'Handley (1996) have proposed a method to predict the spatial distribution of the phase velocity from wave ducting theory.

### 5.3 *Sensitivity of Analysis to Time-to-Space Conversion Interval*

The TSC results using two different tau values,  $\tau = 15$  min (T15) and  $\tau = 50$  min (T50), were compared. Of all the tests on the TSC program, this one displayed the greatest variations. For the February 14 case, the overall average wave speed and wavelength were determined to be  $21.6 \text{ ms}^{-1}$  and 200 km (see Table 6.3). Equation (4.21) therefore suggests a  $\tau$  value greater than or equal to 39 min, which means T15 involves a value below the suggested one. With  $\tau = 15$  min, not much TSC was occurring since only three observations on either side of the observation being converted were involved, whereas with  $\tau = 50$  min, 10 observations were considered on either side of the central observation which effectively created off-time data to  $\pm 47$  km from each station (0.8 times the average station separation).

The T15 results (Fig. 5.7.a) had more bulls-eyes and most of the time they were less wavelike than the T50 results (Fig. 5.7.b) and more like the conventional Barnes without TSC (Fig. 5.5). An example of these variations can be seen at 2100 UTC. It was

definitely easier to identify the waves in T50 than it was in T15. The B- feature seemed to fade in and out in T15 -- at times it was significantly stronger than in T50 (2000 UTC), whereas at other times (0100 UTC) the features in T50 were much stronger. From 0300 UTC to the end of the run at 0600 UTC, the patterns in Illinois were quite different. This was the area where B- and B+ were located at this time. Two mesolows appeared in the T15 analysis through 0600 UTC, and the ridge between them faded in and out through time.

Judging from this comparison, a larger  $\tau$  (50 min) appears to produce more desirable results in that they are more wavelike and exhibited better space-time continuity. Koch and O'Handley (1996) have provided guidance on the optimal value for  $\tau$  based on the average wave characteristics ( $\tau \sim 45$  min). These results offer additional support for their argument.

#### *5.4 Sensitivity of Analysis to Choice of Grid-length*

The two different grid-lengths used in this comparison were 25 km and 40 km. Since the average station spacing for the February 14 case was approximately 56 km, the requirement that the grid-length be no larger than one-half the average station spacing is met in GL25 but not in GL40. The smaller grid-length should allow for more detail since more grid points appear on the same sized plot than with the larger grid-length. This is exactly what was observed in the results from this comparison; however, the added detail was not necessarily a desired characteristic in that it made the wave features slightly more difficult to pinpoint. Actually, the wave signatures in the GL40 product (Fig. 5.8.b) were the easiest of all the TSC outputs to follow, and gave the best insight as to the actual locations of the waves.

The basic pattern and placement were very similar in the two tests. However, the pressure perturbation maxima tended to be slightly stronger in the GL25 results (Fig.

5.8.a), which also produced more closed contours, and the contours displayed more “wiggles”. This is most obvious if the A+ wave at 0400 UTC is compared.

In summary, the sensitivity tests performed here suggest that additional care should be taken when choosing a bandpass-filter width than simply choosing one that encompasses the evident wave frequencies. In addition, guidelines such as those suggested by Koch and O’Handley (1996) should be used when choosing a value for the time-to-space conversion interval ( $\tau$ ), with lower values being used for rapidly changing waves and larger values for steady waves. A value too small does not allow for much conversion to occur and therefore there is not much improvement over a conventional Barnes analysis, which is not recommended for tracking mesoscale gravity waves. A value is also suggested for the best grid-length; however, the results from using a larger value than  $\Delta n/3 < \Delta x < \Delta n/2$  that is recommended to ensure proper representation of the wave produced more desirable wave features. Results suggest that a single advection vector would likely do fairly well at representing a planer wave, while multiple advection vectors are recommended for waves that are arc-shaped.

## 6. Case Studies

### 6.1 Case Selection and Results Synoptic Model Verification.

Table 6.1 is a summary of the ranking of the pressure pulse events according to their average amplitudes. Thirteen events were identified out of the 41 days (32%) in STORM-FEST. Taking a different approach, the number of pressure perturbation hours, determined from counting the total number of hours under duration in Table 6.1, is 34 % of the total hours investigated. It is uncertain how many of these events actually involve gravity waves; however, this does provide some idea of the ubiquitousness of periodic mesoscale pressure disturbances. Pressure traces from mesonet stations for the 13 cases displayed various characteristics. All events excepting that of February 20 showed some

Table 6.1. *Pressure Pulse Ranking from STORM-FEST Data of the 13 Identified Events. The pressure pulse events are ranked according to their average amplitude values. The first hour the event was observed through the last hour of activity is included in the duration (day/hour). The results from the Uccellini and Koch (1987) synoptic conceptual model verification are included for all three criteria--a jet streak near the inflection axis, a diffluent trough and a front to the south or southeast of the wave region, as well as for when a jet streak near the inflection axis was considered alone.*

Date	Average - Amplitude (mb)	Duration	Jet Streak Near Inflection Axis	Three Criteria Examined
February 14	0.67	14/18-15/08	X	X
February 17	0.51	16/23-18/05	X	X
March 9	0.49	09/00-10/12	X	X
March 4	0.46	04/01-04/16	X	X
March 8	0.45	08/01-08/24	X	
March 6	0.35	06/00-07/09		
February 11	0.31	11/02-12/16		
March 5	0.31	05/01-05/21	X	
February 4	0.27	04/00-05/02		
February 25	0.27	25/00-25/22		
February 20	0.27	20/00-20/17		
February 2	0.26	02/00-02/17	X	
February 13	0.25	13/00-13/24		

combination of solitary waves of depression and elevation, wavelets and wave trains. For the purpose of this study, the following definitions were employed. A wave of depression/elevation (WOD/WOE) had to display a wave half-period shorter than 90 min

and the pressure perturbation amplitude had to be  $p' \geq 0.5$  mb. The same amplitude requirements also applied to a wavelet, but a wavelet had to display a full wave of elevation and wave of depression couplet with a complete cycle occurring within 90 min. Those wave troughs and ridges that did not meet the period or amplitude requirements for a wavelet, or occurred over a period of time greater than 90 min were considered to be a wave train.

All 41 days were analyzed to see whether they exhibited the three synoptic features typically found by Uccellini and Koch (1987) to be present during mesoscale gravity wave events. Only four days showed evidence that the three criteria existed, but they happened to be during those days with the strongest pressure pulse events as shown in Table 6.1. The results for using just one of the criteria -- a jet streak near an inflection axis -- are also presented. The reason this criteria was chosen and the others were not is because it produced no false alarms whereas the other two criteria did. The contingency table for the single criteria (Table 6.2) suggests that a jet streak approaching the inflection axis is a sufficient but not necessary condition for a gravity wave to occur. In addition, a two-sample t-test performed on the pressure pulse events of Table 6.1 suggested that a larger amplitude occurs when a jet streak is near the inflection axis at above the 95 % level. Logistical regression on the events suggested that for an average pressure amplitude  $\geq 0.35$  there is a 93 % likelihood the jet streak criteria will also be met. This further suggests geostrophic adjustment as having some role in the genesis of the strongest gravity waves since the geostrophic wind maximum would likely be located upstream from the jet streak at the base of the trough (see Fig. 2.9).

The first three events listed in Table 6.1 are those analyzed in detail later in this section. The following comments pertain to the March 4 and March 8 cases that were not analyzed, yet had relatively comparable average amplitudes to those events that were analyzed in detail. In the March 4 event, there were significant drops in the pressure traces

TABLE 6.2 *Contingency Table-Jet Streak Near Inflection Axis*

Observed Gravity Wave	Predicted Gravity Wave	
	YES	NO
YES	7	6
NO	0	28

at many locations, but the pressure didn't climb back up to the same values as before the trough in most cases. Traces from Oklahoma, which mark the beginning of the detectable wave event, were the only ones that showed values after the trough passed to be nearly equally to those before the trough. Even though the Oklahoma City trace had a wave-amplitude of 2.2 mb (a large-amplitude event), the next highest value found was 1.5 mb and other traces exhibited considerably weaker features. Therefore, the event was not considered to be a large-amplitude event. In addition, there was no evidence of a pressure drop moving into Missouri, so it was assumed that either the wave could not be continuously supported by the atmosphere, or the wave was moving more directly east versus northeast; however, the STORM-FEST region did not extend to the east into Arkansas.

On March 8, the pressure perturbations occurred within a narrow corridor that extended from eastern Oklahoma, through most of Missouri and into Illinois. The western portion of the region was in the surface warm sector, which could have played some role in the apparent corridor.

No large-amplitude ( $> 2.0$  mb) waves occurred in any of the STORM-FEST days, which is not surprising. Young and Richards (1973) found in their climatology of surface pressure events during 33 winter seasons at Madison, Wisconsin that an average of one wave amplitude greater than 3.5 mb occurred only once per winter season. Even though many of the perturbation amplitudes were rather small, that certainly does not necessarily mean they were irrelevant to the weather as is demonstrated below. Uccellini and Koch (1987) found no apparent correlation between wave amplitude and convection, suggesting

that given ideal conditions, even small-amplitude waves can lead to noticeable changes in observable weather conditions, and the case studies that follow support this claim.

## 6.2 *February 14-15 1992*

### 6.2.1 SYNOPTIC OVERVIEW

During the first 12 hrs of February 14 (0000 - 1200 UTC), a surface cyclone developed and the center tracked southeastward from Wyoming into southeastern Colorado. The synoptic situation at 1200 UTC (Fig. 6.1) consisted of a surface front that extended to the east of the low pressure and a cold front that dipped southwestward before turning back toward the northwest. A dryline was present between the warm and cold front over west Texas. The dryline moved eastward with the surface cyclone into Oklahoma. Warm frontal overrunning led to a large area of precipitation north of the warm front that moved eastward from Kansas and Oklahoma into Missouri by 1200 UTC and continued to move eastward. Subsequently, the surface low continued to move southeastward across the Oklahoma panhandle, then it turned northeastward and moved across Kansas.

During this time, rapid occlusion occurred as evidenced in the surface temperature field and satellite pictures. On the 14th at 1200 UTC (Fig. 6.1), the head of the occlusion was bent back into eastern Colorado, and a clearing in the western Plains suggested a dry air intrusion existed. A closer look at the satellite pictures showed the area of clearing due to the dry air intrusion continued to expand until 1400 UTC. According to Bluestein (1993), the region to the west and northwest of a classical midlatitude cyclone is characterized by cold air advection and vorticity advection becoming more anticyclonic with height and hence there is sinking motion there. Air that has had a history of descent is likely to be dry. Air enters the equatorward side of the cyclone at all levels from the west. This air has had a history of subsidence and is therefore dry and clear. Some of this air

flows southward of the cyclone's center and is then diverted poleward around the east side of the cyclone. This tongue of air is what is known as the dry intrusion. It is lifted as it curves to the east and northeast of the surface cyclone. However, middle and upper-level clouds are usually not present because the air is so dry. When the dry slot rides over a mass of moist air near the surface, potential instability is increased and a nearly dry adiabatic layer is superimposed upon the moist air; the threat of severe cumulus convection is thus also increased.

At 1230 UTC, what appeared to be the initial trace of a cloudband was observed in the Oklahoma panhandle in the dry slot caused by the dry air intrusion. This cloudband is shown in Fig 6.2.a (1330 UTC) in the southwestern corner of Kansas, just east of the occluding surface low pressure center. The cloudband expanded and began to fill the area cleared by the dry air intrusion after this time. The cloudband began to precipitate around 1600 UTC in southwestern/south-central Kansas. The precipitation continued to intensify, took on rainband characteristics, and hugged the fairly sharp back edge of the cloudband.

The clouds in the area of the occluded low became colder (brighter in IR satellite pictures, indicating higher tops and therefore, cloud growth), after the precipitation had begun. Precipitation also began in an area north of the rainband at this time. This precipitation area expanded, and as it wrapped around the developing low pressure system, a comma cloud pattern became apparent (Fig. 6.4.a). Notice that another precipitation feature began in the lower region of the bowed rainband. This bowing effect became more pronounced and precipitation intensified in this southern extension as it moved across the Kansas/Missouri border. After 0000 UTC, large hail and numerous cloud-to-ground lightning strikes were observed in Missouri and Illinois as this rainband continued to intensify.

It is apparent that the distinction between the cloud/rainband and head of the comma cloud became less defined at 2200 UTC (Fig. 6.4.a) and, in fact, they appeared to move as



a single entity through 15 February, 0600 UTC; however, a thin region devoid of mid- and upper-altitude clouds existed between these two features (Fig. 6.4.a) which propagated toward the northwest edge of this cloudband through time as seen in Fig 6.4.b, valid 0032 UTC 15 February. As it did so, the higher cloud tops continued to extend back toward the northwest limit of the cloud region. A second cloudband (CB2) with associated precipitation appeared at 0030 UTC (Fig. 6.4.b) to the southwest of the original cloudband (CB1), still within the original clear slot. This second cloud mass moved along right behind the first until 0600 UTC when it became difficult to distinguish the two features, primarily due to the fact that the initial cloud mass continued to grow larger and its back edge became less defined. From 0200 UTC on, the cloud bands appear to get caught in the "wrapping" effect associated with the occluding low, giving the appearance that they were tied to the occluding low in some manner. It could simply be that the effect of the local circulation in the basic flow pattern in the region caused the cloudbands to move in this manner.

#### 6.2.2 ANALYSIS RESULTS

A total of 147 stations were used including NWS digitized barograph stations and AWOS stations, both of which were linearly interpolated to 5 min intervals. The average station spacing ( $\Delta n$ ) was 56 km. Although data had been quality controlled before it was received, all pressure and wind traces were plotted and checked for any obviously bad data. ASOS stations were missing data early in the time period used in this analysis; therefore, the time series were shifted so that they were aligned with the others.

Spectral analysis was accomplished on 80 stations from the STORM-FEST region where wave activity was evident. No differencing was required and 6-hr windows around the time of wave activity were used. The histogram of peak frequencies from the autospectral analysis is presented in Fig. 4.4. A single mode is suggested as is a frequency

range of  $0.004 - 0.010 \text{ min}^{-1}$  which corresponds to a period of 100 - 250 min. Even though the histogram supports the chosen range, when the response function was plotted over the histogram (Fig. 4.4), it became obvious that the most frequently observed frequencies would be attenuated by  $\sim 20 \%$ . This was because these frequencies did not lie in the center of the chosen frequency range and therefore were not being passed to the fullest extent possible by the filter. Filtered perturbation values were therefore smaller than the actual values as a result.

Another contributing factor to cause weaker filtered perturbations had to do with the cutoff frequencies and the number of weights as described in Section 5. Nevertheless, the filter was applied to the pressure time series and the pressure perturbations were plotted and hand analyzed. The wave velocity at each station was determined from these isochrones using the wave axis tracking method described in Section 5.

Pressure trough B- was the middle wave analyzed and it was also located on the back edge of the most active rainband; therefore, the direction of movement for B- (see Fig. 5.4) was chosen to be used in the filtering of the winds, except for the stations east of where the B- isochrones ended, in which case the movement of wave A- was used (Fig. 5.3). The average phase speed from these values was  $15.7 \text{ ms}^{-1}$  and the general direction of movement, when a line was drawn through the central region of the B- isochrones, was from the southwest ( $220^\circ$ ). The average wavelength early in the life of the wave when it was strongest was 150 km, which suggests an average period of 2.65 hr. The phase speed averages and standard deviations ( $\pm \text{SD}$ ) determined for the central region of each wave are given in Table 6.3.

The response function for the wider filter described in Section 5, with the larger  $f_{c2}$  which allowed shorter wavelengths to pass through, had the desired value of 1.0 at its center. Even though the most frequently observed frequencies are still attenuated, the attenuation is less than what occurred with the narrow filter because the response function

had a larger value. The wide-filtered data are used throughout the rest of the analysis for this case.

The wave direction of movement, which ranged from  $180^\circ$  (i.e., toward the north) to  $295^\circ$  (i.e., toward the southeast), from each station was used in filtering the winds and the  $\overline{p'u^*}$  correlation values were calculated and plotted. The highest positive values occurred primarily in northeastern Kansas and across the northern half of Missouri and Illinois (see Fig. 4.6). Values  $\geq 0.7$  were also found further south, particularly in southern Missouri, but a distinct minimum occurred in western Missouri. The possible relationship between the wave characteristics and convection as implied by these results is examined at

Table 6.3. *Phase speeds, horizontal wavelengths, periods and phase directions for the waves identified in the February 14-15 gravity wave event. The phase speeds were determined from the subjectively analyzed waves, while the other wave characteristics were determined from the objectively analyzed waves. An average value as well as the standard deviation are presented. For the period, a range was derived from the SDs of phase speed and wavelength.*

Wave	Phase Speed ( $\text{ms}^{-1}$ )	Phase Direction (deg)	Wavelength (km)	Period Average & (Range) (hr)
A-	$23.5 \pm 5.3$	$251 \pm 19$	$215 \pm 59$	2.3 (1.4 - 3.7)
B-	$20.1 \pm 6.0$	$249 \pm 9$	$170 \pm 28$	2.0 (1.2 - 3.5)
C-	$21.3 \pm 6.5$	$255 \pm 24$	$210 \pm 30$	2.5 (1.7 - 4.2)

the end of the section.

The TSC results using the wide filter are plotted in Fig. 6.5 every half hour. Table 6.3 contains horizontal wavelength, period and phase direction average values and standard deviations for each wave as determined from the objective analysis. Calculations were determined from the central region of the wave. The characteristics presented are all within the ranges suggested by the Uccellini and Koch's (1987) gravity-wave climatology except for the period of time when the phase speeds, which were determined from the subjective analysis, for both A- and B- were  $\geq 25 \text{ ms}^{-1}$ ; however, other mesoscale gravity wave studies have found phase speeds in excess of this value. For example, the wave analyzed

by Pecnick and Young (1984) traveled at  $32 \text{ ms}^{-1}$ , while one of the waves in the Bosart and Sanders (1986) study reached a speed of  $42 \text{ ms}^{-1}$ .

The average vertical wavelength ( $\lambda_z$ ) was calculated using equations (2.19) and (2.21) as well as the definitions for horizontal wavenumber and vertical wavelength, to be approximately 1610 m ( $\lambda_z/2 = 805 \text{ m}$ ). The duct was approximately 1000 m thick; therefore, support exists for the given wavelength. The error was within 20 % of the dispersion equation.

The A- and B- waves followed basically the same corridor extending from the Oklahoma panhandle toward the northeast (see Fig. 5.4). Wave C-, which was the weakest of the three, followed a more eastward path. Wave A- weakened as it moved into eastern Kansas and began to strengthen as it reached central Missouri. The B- wave also weakened as it propagated into Missouri, but then strengthened as it moved into Illinois. Since waves A- and B- were the strongest of the three, most of the emphasis is placed on them during this study.

A summary of wave activity and the relationship of this activity to the cloudbands is presented below. Wave activity was first detectable in the TSC analysis across the Texas and Oklahoma panhandles at 1530 UTC. At this time, there was weak evidence in the TSC for A- as well as for B-. Wave B- appears to be more closely related to CB1 in that it was geographically closer to the band than was A-. While evidence for B- continued, the next time A- showed up and remained at magnitudes greater than 0.2 mb for any length of time was 1800 UTC. At this time, B- was also stronger and a pressure ridge began to develop between these two troughs. A third wave (C-) was located across the Texas Panhandle. Figure 6.5 should be used as a reference for this summary along with the satellite pictures as indicated.

14/1900 UTC

A- began to weaken as it approached the northeastern corner of Kansas.

2030 UTC

Pressure ridge A+ matched area of CB1 with A- slightly out ahead and B- hugging the back edge of the band (Fig. 6.2.b). The strongest B- signature occurred at this time with a value of -1.6 mb.

2130 UTC

CB1 was centered between A- and B- (Fig. 6.3.b). (Since the back edge of the cloudband was sharper than the front, in the radar depiction the convective area appears nearer B- rather than centered between A- and B-.) A second cloud region was evident between B- and C-, yet it was not well organized.

2200 UTC

A- was getting stronger. Even though the A+ signature was fairly strong, it was less wavelike and smaller. The southern part of A- appeared to become better established farther east.

2230 UTC

The satellite picture suggested that A- had moved further ahead of CB1 while B- was still hugging the back edge of CB1 (Fig. 6.3.d).

2330 UTC

A- was slightly ahead of CB1. B- was into the back edge in the northern part of the cloudband. The relationship between the  $p'$  field and the cloudband was less clear in the southern region of the cloudband.

15/0030 UTC

The satellite picture indicated a cloudband (CB2) had developed between CB1 and the cloud mass first mentioned at 2130 UTC (Fig. 6.4.b). A- was hugging the front edge of CB1 and the northern extension of B- extended

into CB1. The southern split of B- extended along the back edge of CB1, slightly ahead of CB2. A+ was beginning to split in the southern part, in approximately the same location as where cloud coverage was less in the central region of CB1.

0130 UTC

The southern section of B- was evident while the northern section was hardly even negative. The strongest signature for A+ occurred with a value of 1.7 mb.

0200 UTC

There was a maximum negative  $p'$  area in north central Missouri to the west of where the main part of B- was located.

0230 UTC

A+ matched the cloud pattern closely. A- showed its strongest signature with -1.5 mb. A- was hugging the front edge of CB1 while the discernible southern part of B- was hugging the southern back edge of CB1 (Fig. 6.7). The maximum negative  $p'$  mentioned at 0200 UTC was hugging the back edge of CB2, and is referred to as B-\*.

0330 UTC

A- was still hugging the front edge of CB1. A southern extension of A- was along the back edge of another little cloud mass in south-central Illinois. The southern section of B- was somewhat along the back edge of CB1, and was actually closer to the back edge of the higher cloud tops within the cloudband. B-\* was stronger than the main part of B- and it was into the back edge of CB2.

0400 UTC

The southern section of the main B- wave was hardly even negative. B-\* had expanded and there was a wavelike feature involving this B-\* signature.

0430 UTC

A+ and B+ appeared as though they may have come together.

0500 UTC

A- was moving off the map. A+ was strong and wavelike even though it most likely had parts of the original B+ in it. There was some evidence of B- and B+ in central and northwestern Illinois while B-\* appeared in western Illinois with a B+\* behind it.

In summary, the southern parts of A- and B- were generally less defined than the northern sections. There was a lot of activity in the TSC in this area, making it difficult at times to follow exactly what changes were occurring. The most notable features in the analysis were A+ and the associated cloudband. From this initial investigation, it appears as though the wave/convection interactions led to changes in the wave signature, making it less wavelike at times. The maximum positive  $p'$  areas in the TSC output closely matched the shape and location of the cloudbands. In addition, C- was not associated with any cloudbands. This could have been because C- was too weak to raise parcels to their LCL.

In many cases, a wave trough was located near the back edge as well as the front edge of the cloud bands, and the pressure ridge (A+) was co-located with the cloudband; therefore suggesting that the A- to B- wave complex was tilted in the vertical (see Fig. 2.5). Results from Trexler et al. (1996), where the February 14 case was analyzed using profiler data, also suggests that the wave was tilted in the vertical as do the modeling results for the same case by Jin et al. (1996).

On February 14, the strongest amplitudes were at stations in northeast Kansas with weaker signatures in the south and in Missouri. As the wave activity continued through Missouri the following day and entered into Illinois, the stronger amplitudes were at

stations in the northeast quarter of Missouri into Illinois, and it appears that wave amplitudes increased with time. The largest amplitude on February 14 (1.5 mb) occurred at St. Joseph, Missouri (STJ), while the largest on February 15 (1.9 mb) occurred at Montgomery City, Missouri (P19) where the pressure fell nearly 4.0 mb in 25 min. (Refer to Fig. 6.9 for station locations).

The waves propagated along and north of a warm front. The initial wave signatures are somewhat confusing. The wave of depression noted at Dodge City, Kansas (DDC) was associated with B- while downstream, A- appeared first at a given location with B- following in the form of a wave train. By the time A- reached Powhattan, Kansas (P40), it had weakened considerably; therefore, the raw pressure trace showed only a single wave of depression associated with B-. These changes are portrayed in Fig. 6.8 through pressure traces from stations along the path of wave activity. Again, the most notable feature was A+. (Note that the pressure trace for DDC represents a WOD, MHK represents a wavelet (A- to A+ to B-) and P17 represents a wave train.) There were more waves of depression noted early in the wave activity, where more of a variety of wave signatures were noted on the 15th, including wavelets and trains marked by a strong wave of elevation (Fig. 6.9). Since a wave of depression was noted at P40 and Pittsburg, Kansas (P26) after convection had started, it is not believed that convection was the single factor that led to the change in the wave characteristics; however, it could very well have played a role. Upon inspection of the TSC analysis, it was apparent that the wave features closely mirrored those changes evident in Fig. 6.9.

Since convection began early in the life of the wave, the relationship between the two is somewhat more difficult to determine. The precipitation band grew in area of coverage and intensity from 1600 to 2100 UTC, at which time the northern section began to slim while the southern section began to grow and intensify (Fig. 6.3). Eventually the two sections merged and the band continued to move off towards the northeast, which



pulled the band out of southern Missouri (compare Figs. 6.4.a and 6.4.b). Figure 6.3 shows the southern section of CB1 grew northward as the southern end of the northern section slowly eroded. During this time, the TSC output tended to account for these two separate sections as can be seen in Fig. 6.5, at 2230 UTC for example, where the amplitude was weaker in the central region of wave B-. Actually, the TSC positive perturbation areas appeared to be very closely related to the location of the convection which at times caused the suggested wave shape to be less smooth than is desired for a wave. (Note A- at 0200 UTC in Fig. 6.5.) Whether the convection or the wave was the dependent factor, or if some type of co-dependency existed was not determined.

Strong thunderstorms developed after 2100 UTC associated with CB1. According to Koch et al. (1988), a pronounced change in phase velocity, sharply reduced  $p'u^*$  correlations and higher wave amplitude should develop following strong convection (defined by the presence of a gust front). Figure 5.4.b suggests a change in velocity for B- at this time, and the amplitude of the southern part of B- increased slightly (Fig. 6.5). In an attempt to determine if the size of the wave amplitude was related to convective activity, attention was first focused on the southeastern corner of Kansas at Chanute (CNU), Parsons (PPF) and P26. At 2100 UTC (Fig. 6.3), the southern section of rainband 1 (RB1), associated with CB1, was just beginning in this region, and was producing large hail shortly thereafter. No significant wave activity was noted in the pressure traces from CNU and PPF; however, slightly east at P26, an amplitude of 0.8 - 1.0 was observed. This increase could have been related to the fact that the southern section of the rainband had intensified by the time it reached P26. However, contrary to that suggestion is the fact that as the rainband passed over the Kansas/Missouri border, relatively small amplitudes of 0.4 - 0.5 were observed at Garnett, Kansas (P14), Butler, Missouri (P15) and Olathe, Kansas (OJC); therefore, these results are inconclusive on the relationship of wave amplitude and convection. However, there is no dispute that the amplitudes increased as

strong convection erupted along the wave, which continued northeastward into northeastern Missouri and Illinois to the highest values recorded for the event (amplitude of 1.9 mb at P19). RB1 was expanding horizontally and the second rainband was evident (see Fig. 6.6), during the period when the TSC results showed a large pressure perturbation ridge in the area (Fig. 6.5) and raw pressure traces from seven stations, including P19, portrayed a strong wave of elevation as part of a wavelet or train (Fig. 6.10).

As for the surface pressure and wind field correlations, the  $\overline{p'u^*}$  plot (Fig. 4.6) indicates values greater than 0.7 began to show up in the northeast quadrant of Kansas as the intensifying wave moved into that region. The correlation values were fairly large in the northern section of the STORM-FEST region which was also where the wave signature remained strong and coherent. Weaker values occurred along the Kansas/Missouri border which is the same location noted above where the wave signature was relatively weak; however, stronger values occurred east of this area where the wave and associated convection intensified. The southeast corner of Kansas (addressed above) where convection was just beginning and intensifying, showed low correlation values; however, values  $\geq 0.8$  occurred to the east at Stockton, Missouri (P27) and Ava, Missouri (P33). This was the region where TSC showed a mesohigh associated with B- yet separate from the primary wave signature to the north. It is possible that the mesohigh was convectively forced, judging from the 0.8 - 1.5 °C drop in temperatures as the mesohigh passed.

It appears as though the  $\overline{p'u^*}$  correlation values were closely related to the strength of the wave signature. Since Koch et al. (1988) found that convection didn't significantly mask the wave in the surface pressure and wind fields unless a gust front was also present, evidence for one was sought in the raw pressure traces from stations located along the Kansas/Missouri because the  $\overline{p'u^*}$  were relatively weak as the wave passed

through this area. A typical pressure trace in response to a gust front would first indicate a trough followed by a strong high associated with the downdraft and evaporatively cooled air. No evidence of a gust front was found along the Kansas/Missouri border; however, pressure traces from the stations identified in Fig. 6.9 did display gust front signatures. None of these stations reported gusty winds that would be expected with a gust front, near the time the WOE passed by. Temperature traces from the stations indicated as many increases as decreases with the passage of the WOE. Although there was a precipitation spike at all stations affected by the WOE, only one displayed a rainfall rate above that considered to be associated with strong convection. (P17 had a rainfall rate of 25.8 mm/hr.) Therefore, there is not convincing evidence for a gust front; however, it is believed that convection could still be responsible for the strong amplitudes of A+. The  $\overline{p'u^*}$  correlations remained strong in the region where the pressure traces suggested a gust front as the wave moved through these stations which would be contrary to the findings by Koch et al. (1988). There is the possibility that convection was indirectly related to the correlation values through its potential impact on the strength of the wave amplitude, which would support the claim by Rauber et al. (1995) that the positive correlations between the surface pressure and winds increased after the onset of convection in the February 14 case. Again, whether the convection or the wave was the dependent factor has not determined in the present study; however, the fact that there was some type of interaction has been established. The results here are similar to those of Stobie et al. (1983) where they found rapid amplification of the waves and growth of the convection occurred simultaneously.

As for potential genesis mechanisms, convection was eliminated as a likely genesis mechanism for the main waves (waves A-, B- and C-) since there was no convection in the local vicinity of the gravity wave genesis region. However, convection certainly appeared to help sustain the wave (Wave-CISK), and convection also appears to have been involved in the development of the B-\* feature that developed behind CB2.

With the Rocky Mountain ridge just to the west of the genesis region, the possible role of topography cannot be neglected. However, upper-level analysis and model results will have to determine if the mountains played a direct role or more of an indirect role.

The surface frontal system located just south of the genesis region was not rapidly developing as suggested by Reeder and Keyser (1988) for situations in which unbalanced frontogenesis plays a role in gravity wave genesis. However, evidence strongly indicates that upper-level dynamics were highly unbalanced in the wave source region in western Kansas.

At 1200 UTC, a negatively tilted 500 mb short wave trough extended from Wyoming through Colorado into New Mexico and the height contours suggested diffluent flow coming out of the trough. The ridge axis was most pronounced from Iowa into the Missouri/Tennessee border area. By 15 February 0000 UTC, the 500 mb trough had moved into Iowa and Missouri, while the ridge had moved over the eastern US. This configuration suggests a pattern conducive to geostrophic adjustment at the 500 mb level. Plots were made using GEMPAK with the observed and geostrophic winds analyses superimposed over the 300 mb and 500 mb height contours. The plots depicted a geostrophic jet either collocated with or ahead of the observed jet, which does not suggest geostrophic adjustment as a likely genesis mechanism. However, the average station spacing was approximately 562 km and therefore, the resolution may have been too poor to accurately depict the situation. By contrast, the 24 hr 300 mb forecast from the NCAR Mesoscale Model (MM4), with 60 km resolution, showed the geostrophic maximum in east-central New Mexico with the actual wind maximum just south of the Texas panhandle at 14 February 1200 UTC (Fig. 6.11). This places the geostrophic wind maximum behind the jet streak location which does support geostrophic adjustment. Whether one of these potential genesis mechanisms was solely responsible or if there was a combination of contributing factors is not clear; however, a cyclone passing over the Rocky Mountains in

conjunction with support for geostrophic adjustment suggests a combination of these factors was involved, and a list in order of importance cannot be surmised. The fact that a few mechanisms were present further supports the likelihood that a gravity wave event did occur on 14 and 15 February.

### *6.3 February 16 -18 1992*

#### 6.3.1 SYNOPTIC OVERVIEW

On February 16, a surface low pressure developed over the Utah/Colorado border in the lee of the Rockies, similar to the 14 February case, and moved eastward throughout the day. A diffluent short wave trough extended through Nevada and into Arizona at 500 mb. By 1800 UTC, two features of interest were a Pacific cold front through Colorado into Utah and a dryline in the western Texas Panhandle. Precipitation began at 1800 UTC ahead of the low in the southeastern corner of Colorado. By 0000 UTC on 17 February, the dryline extended southward along the eastern Texas Panhandle while the cold front extended through southern Colorado then turned northwestward through Utah (Fig. 6.12). By 1200 UTC, the occluding surface cyclone was located over western Kansas and precipitation was confined to the north and east quadrants of the storm. The surface low continued to track to the northeast and had made it to the Nebraska/Iowa border by 1200 UTC on 18 February.

Turning to the satellite and radar imagery, an initial arc-shaped cloudband appeared to spin off of the developing upper-level low, evident in the circulation of the clouds on 16 February at 1600 UTC. This cloudband moved off to the northeast with no associated precipitation and was north of the STORM-FEST region by 0000 UTC 17 February as pointed out by the black arrow in Fig. 6.12. An area of precipitation began to develop near the surface low as the upper level cyclonic circulation tightened and became clearly evident. Two cloudbands (CB1) and (CB2) with associated precipitation began to take shape within

this region of precipitation by 0200 UTC on February 17 (Fig. 6.13.a). As these bands moved off to the northeast, a clearing between the low and the bands suggested a dry air intrusion, similar to the February 14 case. The northern part of the cloudbands and associated precipitation started to merge after 0700 UTC along the northern Kansas/Missouri border as they neared the upper-level ridge. CB1 wrapped cyclonically to the northwest as though it were "connected" to the circulation around the low. By 1000 UTC, as the upper-level ridge moved off to the east, two areas of brighter clouds distinguished themselves with an area of clearing or lower tops between them (Fig. 6.14) in Missouri near where CB1 and CB2 had merged earlier. Since CB1 and CB2 had slowed as they approached the ridge, it is likely that these two areas of brighter clouds were the same features as these previous cloudbands, and therefore they are referred to as CB1 and CB2. (Because the intense cloud coverage between 0700 - 1000 UTC covered CB1 and CB2 and therefore made it impossible to track CB1 and CB2, it was also impossible to say that these newly distinguished brighter bands were definitely the same as the initial CB1 and CB2.) One area was located in central Missouri while the other was on the Kansas/Missouri border. A detached band of precipitation now appeared in southern Oklahoma, indicated by a black arrow in Fig. 6.14. This cloudband intensified and appeared to move with CB2 even though there was a large cloud-free area between them. These two sections traveled along together from 0800 - 1400 UTC, after which the southern cloudband finally dissipated.

Along the eastern edge of the dry air intrusion, another cloudband (CB3) with associated precipitation began to develop by 1500 UTC just east of the Kansas/Missouri border and west of CB2 (Fig. 6.16.a). Unlike the previous bands, CB3 was traceable back to a small, disorganized cloudy area in the eastern Texas Panhandle (see Fig. 6.13.b). After lingering there for several hours, the cloudy area started to move off to the northeast, and began to expand at 1100 UTC to later become the northern part of CB3. Between the

southern extensions of CB2 and CB3, a small yet intense band developed (CB2-3) by 1500 UTC (Fig. 6.16.a) that moved along ahead of CB3. As CB3 intensified, the highest cloud tops were located in its southern extension. By 1800 UTC, the northern section of CB3 seemed to have merged with CB2 just as the northern part of CB2 had earlier merged with CB1. This resulted in a pinwheel type of structure to the cloud and precipitation patterns. By 2100 UTC, CB2-3 had. It appeared that CB3 propagated in a more easterly direction than did CB1 and CB2 as it moved through the STORM-FEST region, and that it encompassed a much larger region than had its predecessors.

At just about the same time the initial signature of the cloudy area that became CB3 was detectable, the last cloudband of the day (CB4) began to propagate away from the low pressure center (see Fig. 6.13.b). The band had deteriorated to an unorganized cloudmass by 0700 UTC. As this cloudband first tracked to the east, through the dry air intrusion, then to the northeast through central Kansas, it slowly produced precipitation in association with a veering of the surface winds at stations to the south from the southeast to the southwest. The precipitation had taken on banded characteristics by 2000 UTC (Fig. 6.17.a). The band was oriented more east-to-west than the previous bands and it was of much smaller scale. Of interest is the fact that this band was quite similar in shape, size and location as CB2 of the February 14 case, noting in particular that both bands were closely related to the center of the circulation in the synoptic-low pressure system.

#### 6.3.2 ANALYSIS RESULTS

The dataset (from 16 February 1900 UTC through 18 February 1000 UTC) contained a total of 105 stations including 13 barograph stations which were digitized in 15-min intervals and linearly interpolated to 5-min observations. The average station spacing was 76 km. A quality control check was performed on the data by plotting the raw

traces as well as manually checking each pressure and wind entry for missing or meteorologically unsound data points.

Forty-five stations were considered in the spectral analysis performed on 8-hr time series windows centered around the period of maximum wave activity at each station. Even though the autocorrelation function for some of the stations was greater than 0.95 at lag one, which suggested differencing was required, no significant peaks occurred in the spectrum when differencing was used. A smaller, non-significant peak was typically present quite close to where the non-differenced time-series spectral peak occurred. Since these peak frequencies were plotted in a histogram simply to determine how the bandpass filter width may be tweaked so as to achieve the maximum response, the significant peak values of the non-differenced series were used in making the histogram (Fig. 6.18). Although there were a couple of higher frequencies, the great majority were located in the range of  $0.0035 - 0.0070 \text{ min}^{-1}$  which corresponds to a period of 143 - 286 min. A number of cutoff frequency ranges were examined and plotted over the histogram. It was determined that the best response function resulted from cutoff frequencies of  $f_{c1} = 0.002 \text{ min}^{-1}$  and  $f_{c2} = 0.010 \text{ min}^{-1}$ , even though, as with the February 14 case, the most frequently occurring frequencies were being slightly attenuated (see Fig. 6.18). Given these cutoff frequencies, (4.8) suggests the number of one-sided weights be equal or greater than 32.5 in order to achieve a response of 1.0 at the center of the band-pass filter. A total of 65 weights were used and therefore, as seen in Fig. 6.18, the response function was very close to unity at its center.

The filter was applied to the pressure time series and the pressure perturbations were plotted and subjectively analyzed. Four troughs were identified in the subjective analysis. Three of these waves followed basically the same path through the STORM-FEST region and at nearly the same speeds ( $\sim 10 - 20 \text{ ms}^{-1}$ ). The other wave, A-, had an average phase speed of  $32.2 \text{ ms}^{-1}$  which is in excess of that typically associated with a



mesoscale gravity wave; therefore, a single set of isochrones representing the movement of the three similar waves was used to determine the wave velocity at each station. The average wave velocity was determined to be  $17 \text{ ms}^{-1}$  from  $260^\circ$ . The average speeds calculated over the life of the waves are presented in Table 6.4. Even though some of the upper and lower limits of these ranges were outside that typically associated with mesoscale gravity waves ( $10 - 25 \text{ ms}^{-1}$ ), the averages for waves B-, C- and D- were well within that range.

The direction of wave movement at each station was used in filtering the winds and the  $\overline{p'u^*}$  correlation values were calculated and plotted for each of the four waves (Fig. 6.19). All four waves had significant areas of positive correlation values greater than 0.7 with numerous values in excess of 0.9. For the first wave (Fig. 6.19.a), the highest values occurred in eastern Kansas and across northern Missouri and Illinois. The highest values for the second wave (Fig. 6.19.b) occurred in northeast Oklahoma, through eastern Kansas and most of Missouri. This wave also had an area of values in excess of 0.7 in south-central Illinois. High positive correlations associated with wave three (Fig. 6.19.c) were evident in eastern Missouri through most of Illinois. The final wave had a patch of correlation values greater than 0.7 in southern Missouri (Fig. 6.19.d); however, high values occurred across nearly the entire state of Illinois with the majority greater than 0.9. These large surface pressure and wind field correlation values over fairly large areas in each case, indicate strong gravity waves was present.

The TSC results for this case are presented in Fig. 6.20. Given the average station spacing was 76 km, a grid-length of  $\Delta x = \Delta y = 32 \text{ km}$  was chosen in order to keep the grid-length between  $1/2$  and  $1/3$  the average station spacing. A value of 50 min was used for tau. Four major waves (A-, B-, C- and D-) were also evident in this objective analysis and the isochrones for each of the waves are presented in Fig. 6.21. Another weaker wave (B-\*) was also noted and isochrones for this short lived wave are included in Fig. 6.21.b.

The average wavelength and period for waves B-, C- and D- were 216 km and 3.5 hr . Given the average velocity of  $17 \text{ ms}^{-1}$ , equation (4.21) therefore suggests a value of 53 min or greater for tau in order to obtain a 50% overlap of the data which acts as an internal data quality check. The value of 50 min that was used resulted in an overlap only slightly less than a 50% and therefore was considered sufficient. The horizontal wavelength, period and phase direction averages and range of values for the major objectively analyzed waves are presented in Table 6.4.

Table 6.4. *Phase speeds, horizontal wavelengths, periods and phase directions for the major waves identified in the February 16-18 gravity wave event. The phase speeds were determined from the subjectively analyzed waves, while the other wave characteristics were determined from the objectively analyzed waves. An average value as well as the standard deviation are presented. For the period, a range was derived from the SDs of the phase speed and wavelength.*

Wave	Phase Speed ( $\text{ms}^{-1}$ )	Phase Direction (deg)	Wavelength (km)	Period Average & (Range) (hr)
A-	$32.2 \pm 5.3$	$253 \pm 13$	$255 \pm 21$	2.2 (1.7 - 2.9)
B-	$14.3 \pm 4.0$	$268 \pm 20$	$220 \pm 13$	4.3 (3.1 - 6.3)
C-	$13.4 \pm 6.7$	$258 \pm 23$	$230 \pm 48$	4.8 (2.5 - 11.5)
D-	$19.8 \pm 8.0$	$274 \pm 18$	$200 \pm 31$	2.8 (1.7 - 5.4)

The wavelength values are all well within the range of 50 - 500 km that is typical for mesoscale gravity waves; however, a number of the periods calculated for the waves are greater than the 1 - 4 hr typically found.

The average vertical wavelength ( $\lambda_z$ ) was found to be 5780 m ( $\lambda_z/2 = 2890$  m), whereas the duct was measured to be approximately 4000 m. In using equation (2.21) to calculate the vertical wavenumber, the curvature term was ignored which could explain the shorter vertical wavelength. In addition, the somewhat crude nature of the calculations could also account for some of the error. Nonetheless, the error was within 30 % of the dispersion equation

The isochrones (Fig. 6.21) suggest that the waves all followed basically an eastnortheast track through the center of the STORM-FEST region. Since both A- and B-

developed in central Kansas while C- and D- developed in central Missouri, this could suggest a translating genesis mechanism. However, it appears more likely that C- and D- were spawned by convection, as is discussed later. While the waves developed in different locations, they all grew longitudinally as they strengthened and then began to weaken within a few hours. A slight arc was evident in all the waves, particularly once they were relatively strong and established. A summary of wave activity and the relationship of this activity to the cloudbands is presented below. Since the subjective analysis first suggested wave activity at 2300 UTC on 16 February, the objective analysis was commenced at this time. Figure 6.20 should be used as a reference for this summary along with the satellite and radar imagery as indicated.

#### 16/2300 UTC

A- was evident behind what appeared to be an area of non-convective mid-level or low upper-level clouds, and to the west of a convectively active region located east of the low.

#### 17/0000 UTC

A- was slightly weaker yet more wave-like in shape. The cloudiness behind A- was shaping into a band (CB1). There were high cloud tops in the northern section of CB1 (as evidenced by the fact that the color scale had wrapped around.) The A+ ridge was just developing as was another wave (B-) which extended through a convective region located west of the convective region associated with A-.

#### 0200 UTC

A- had moved into a position where it was hugging the front edge of CB1 (see Fig. 6.13.a) A+ was located west of CB1 and in the clearing between CB1 and another cloudband (CB2) to the west.

#### 0400 UTC

A- (-1.2 mb) and A+ (1.3 mb) both reached their maximum strengths at this time and the wave shapes were clearly evident. A- continued along the front edge of CB1. A+ was now located just inside the back edge of CB1 which suggests a non-tilted wave, while B- had moved into the clearing between CB1 and CB2.

#### 0500 UTC

Cloudband 1 had expanded and the southern part was running into the upper-level ridge located to the southeast. A- had weakened in this southern section. B- had developed into a nice wave shape and B+ appeared just to the west of B- with a similar shape, both of which corresponded to the shape of CB2 (Fig. 6.13.b). A+ was again along the back edge of CB1 suggesting no tilt, while B+ was located closer to the center of CB2 which does suggest a tilt (see Fig. 2.5).

#### 0600 UTC

There was little evidence for A- at this time. The central region of A+ had expanded as had CB1. B- was strengthening and remained directly in front of CB2 as CB2 continued to develop. B- and B+ maintained their similar shape. A+ was located at the back edge of CB1 while B+ was west of the center of CB2. Both locations support a non-tilted wave.

#### 0700 UTC

A+ had become more arc-shaped in its northern part as if the southern part were held in place while the rest of the ridge continued eastward. By this time, A+ had also moved into the center of CB1 suggesting a tilted wave, whereas B+ was located in the center of northern CB2 and at the back edge of southern CB2, yet along the back edge of the highest cloud tops.

#### 0900 UTC

Cloudband 2 had expanded in width as had B+, while B- was weakening. B+ was located in the center of CB2 suggesting a tilted wave.

1000 UTC

The northern part of B- also became more arc-shaped as had A+ in this area along the Iowa/Missouri border. B- appeared to have traveled through the northern remains of CB1 and was at the front of the large area of clouds that was the northern combination of CB1 and CB2 (see Fig. 6.14). B+ was still located at the center of CB2.

1100 UTC

B- was fairly weak and while there was no evidence for this wave in the north, it had moved out ahead of CB2 in the south and B+ remained at the center of CB2.

1200 UTC

B- had re-established itself. B+ remained at the center of CB2. Both the southern part of the wave and CB2 were retreating northward. Another weak negative perturbation area (B-\*) was starting to develop at the back edge of B+ and hence CB2 (Fig. 6.15). Its relationship to CB2 suggests that it may be a wake trough forced by compensating subsidence from the convection (as in the conceptual model of Figs. 2.10 and 2.11).

1300 UTC

B- was becoming more arc-shaped as the southern part was lagging behind the rest of the wave. B-\* was expanding at the rear of CB2 but it was not strengthening as the previous waves had done. (No attempt is made to explain why this was the case.) By this time, B+ had almost moved east of the center of CB2.

1400 UTC

B- was moving into CB2 yet remained behind the highest tops in the center of the band while B+ had moved to the front of CB2.

1500 UTC

The wave features were weak. B- and B-\* signatures had joined to the north and gave the appearance of an arc around CB2.

1700 UTC

Evidence for a fourth wave (C-) was apparent in central Missouri and across the border into Arkansas, located just behind B+ and ahead of a band (CB3) that was developing along the eastern edge of the dry air intrusion in western Missouri (Fig. 6.16.b). It is possible that C- was convectively forced (an "inflow mesolow"), since it appeared only after the rapid intensification of CB3.

1800 UTC

Distinction between CB2 and CB3 was not clear in the northern part of the STORM-FEST region. B+ had split in the center as had CB2. C- had developed into a slightly arc-shaped wave from southern Iowa, extending southward through Missouri and into Arkansas. It was located just ahead of CB3. The shape of the back and front edges of CB3 were nearly identical to the shape of C-. A small area representing C+ was present at the back edge of the southern part of C-.

1900 UTC

B+ had weakened except for the southern section which was located slightly ahead of the southern section of CB2. C- had strengthened and developed to the north. C+ was into the middle of CB3 yet to the west of the highest tops.

2000 UTC

C- had continued to strengthen and its position matched the front edge of CB3 almost perfectly (see Fig. 6.17.a). CB3 expanded as it moved across Missouri. C+ was located slightly west of the center of CB3, which had built to the north as it eroded in the south. C+ was into the back edge of CB3 but not at the center which suggests a lack of tilt in the vertical.

2100 UTC

Except for the southern portion, C- had weakened as it moved into Illinois, approaching the upper-level ridge. C+ had strengthened and was located nearer the center of CB3 than previously, suggesting a tilt. Another wave (D-) appeared at the back edge of CB3. Its appearance is suggestive of a "wake low" (Figs. 2.10 and 2.11), similar in nature to that of B-\*.

2200 UTC

CB3 had expanded and was approaching the southern remnants of CB2. C- became weaker in that same region. C+ remained compressed as it moved across the Illinois border whereas the preceding ridges had expanded with the cloudband. D- was into the back edge of CB3, and C-, C+ and D- all appeared to have shifted east in relation to CB3 (Fig. 6.17.b). This moved C+ east of the highest observed cloud tops.

18/0000 UTC

C- was moving off the map. C+ remained strong and started to expand only slightly. It was still located near the center of CB3 suggesting a tilt. D- continued to be arc-shaped and was still well into the back edge of CB3.

0300 UTC

D+ had developed and was co-located with the eastern portion of CB4.

0355 UTC

D- had begun to weaken yet remained in a tight configuration as it approached the eastern extent of the map. D+ had moved to the front edge of CB4, similar to the manner in which the other wave features had moved through the earlier cloudbands.

Some generalizations can be drawn from the above summary. First of all, the waves all appeared to be related to the cloudbands in that they tended to travel together, except in the eastern section of the STORM-FEST region. The waves and bands were shaped similarly and appeared to strengthen in tandem. However, the cloudbands tended to remain pronounced after the waves had weakened. In addition, throughout the wave activity period, the location of the highest cloud tops in relation to the pressure perturbation maxima and minima was determined. It was found that the maximum cloud tops tended to be observed along a line connecting a pressure perturbation minimum to the following maximum to the west. The cloudbands appeared to decelerate once they reached the eastern STORM-FEST region, perhaps due to the upper level ridge, while the waves continued at a speed comparable to their earlier speed. Thus the waves started to move through the cloudband configuration. As this happened, the maximum pressure perturbations tended to be co-located with the highest cloud tops. The higher cloud tops began to diminish as this occurred. The overall location of the waves with respect to the cloudbands suggests that wave A- was not tilted in the vertical, whereas most of the observations support the B-wave being tilted upstream with height. Wave C- initially appeared not to be tilted, while later observations suggested the wave was tilted. It may be that the waves were not tilted, yet the effects of the upper-level ridge resulted in the waves appearing as though they were tilted when their surface position was compared to the cloudbands.

The raw pressure traces from those stations that showed evidence of wave activity portrayed a wave train configuration. A few traces had a WOE or a WOD within the train. Figure 6.22 shows an example of a WOE within a train. Figure 6.23 is a raw pressure



trace from Maryville, Missouri (P02) located in the northwest corner of Missouri. The positions of waves A-, B-, B-\* and possibly D- are identified. Wave C- developed to the east of this station. Figure 6.22 is a raw pressure trace from Salem, Missouri (P29) which is southeast of P02. This station was chosen to point out that the wave configuration remained fairly consistent throughout its life span.

As far as the wave characteristics being affected by convection, as stated above, the highest cloud tops generally appeared at the same time as the largest perturbation values and along the nodal line following the perturbation which suggests a co-dependent relationship. Cloudband 2 was evident before wave B- developed, as was CB3 before C- developed which would suggest that the wave may have been in response to the convection. The southern part of CB3 was intensifying as the first signatures of C- were evident at 1700 UTC (Fig. 6.16.b). Wave D- developed at the back edge of CB3 and there were no evident wave features associated with CB4, which was the weakest of the cloudbands; therefore, D- appeared to have developed in response to CB3, while CB4 was perhaps too weak to force a similar response. The waves tended to weaken while the cloudbands were still very strong (bright) which does not support a dependency of the wave strength solely on the intensity of the convection.

The  $\overline{p'u^*}$  correlation values for wave A- (Fig. 6.19.a) appeared to be associated with the strength of the wave as was suggested in the February 14 case. The strongest values were observed in northern Missouri which is where wave A- was strongest.

Fairly large correlation values were calculated along the path of wave B- as well (Fig. 6.19.b). The irregular southern edge of the  $\geq 0.7$  values contouring tended to mirror the strength of the southern part of the wave. There appeared to be a connection between the correlation values and the wave strength. As the wave disappeared along the Missouri/Illinois border, (see Fig. 6.20 at 1600 UTC), correlation values became negative. (Convection was weak in this area at this time.) When the wave reappeared at 1800 UTC

and propagated through Illinois, correlation values became positive again with values as high as 0.98.

Low correlation values (Fig. 6.19.c) , including negative values, were observed in central Missouri before wave C- became evident. Cloudband 3 had formed in this region and the area of precipitation associated with it was intensifying when wave C- developed. The correlation values just east of where wave C- developed were quite high (0.97 at station P33 in southern Missouri). Note that the shape of the 0.70 contour line through Missouri matches the shape of wave C- (see Fig. 6.21.c). This was also the case with wave D- which formed at the back of CB3. Initial evidence of the wave showed up at 2100 UTC (see Fig. 6.21.d) and the separate area of correlations  $> 0.70$  in southern Missouri in Fig. 6.19.d corresponds to the location of the southern tip of wave D- at 2100 UTC. Note that lower values as well as numerous negative values occurred north of this area before wave D- developed in eastern Missouri. Higher correlations were observed throughout Illinois including along the western border shortly after the wave developed in eastern Missouri and as it moved into Illinois. In this gravity wave event, the  $\overline{p'u^{*}}$  values tended to correspond with the strength of the wave signal of waves A- and B-. In the case of waves C- and D-, it appeared as though high pressure-wind correlations were found in waves forced by convection.

One way of explaining the negative correlation values that were observed prior to the development of wave C- and D- starts with the one-dimensional, inviscid, nonrotating, linearized momentum equation, applicable in the wave propagation plane,

$$\frac{\partial u^{*'}}{\partial t} + U \frac{\partial u^{*'}}{\partial x} + \frac{1}{\rho_0} \frac{\partial p'}{\partial x} = 0. \quad (6.1)$$

The advection term ( $U \frac{\partial u^{*'}}{\partial x}$ ) is typically ignored in linear gravity wave theory. The remaining two terms readily explain the in-phase relationships between  $u^{*}$  and  $p'$  that are

observed with gravity waves (if one substitutes a time-to-space conversion  $\frac{\partial u^{*'}}{\partial t} = c^{-1} \frac{\partial u^{*'}}{\partial x}$ ). However, when convection is present as was the case in the development of waves C- and D-, the wave becomes non-linear and the advection term becomes an important contributor in (6.1). Since its value is negative, the advection term therefore reduces the  $\overline{p'u^{*'}}$  correlations when non-linear effects are involved, and can even result in negative  $\overline{p'u^{*'}}$  correlation values.

The potential genesis mechanisms are basically the same for each of the waves identified in this case. The degree to which each of the mechanisms was responsible appears to have varied. Wave A- was first evident near a region of intensifying convection as was wave B-; therefore, convection may have played a role in the development of these waves. In the case of both waves C- and D-, the cloudband existed prior to wave development. The Rockies were located upstream which could suggest topography also played a role in the genesis of waves A- and B-; however, D- developed in central Missouri so the impact of the Rockies would be improbable at this distance. The fact that the waves developed near the frontal system (and just east of the occluding low) is highly suggestive of unbalanced frontogenesis. The cloudbands with which the waves were associated displayed an obvious dependency on the low pressure center in their movement (evident when the satellite imagery was looped) as well as their genesis. A cutoff low, with an associated negatively tilted diffluent trough, was evident at 500 mb over western Kansas. The MM4 forecast of 300 mb height contours with observed and geostrophic winds, valid 2300 UTC 16 February, showed an observed jet maximum co-located with the geostrophic maximum which does not suggest geostrophic adjustment. The observed wind maximum was however approaching a ridge, upstream of a negatively tilted, diffluent trough (Fig. 6.24). Further upper-level analysis and modeling will need to be accomplished in order to ascertain the balanced state of the area upstream of the gravity wave generation region.

The most important potential wave generation mechanisms for waves A- and B- would be the combination of unbalanced frontogenesis in the lee of the Rockies in the presence of geostrophic adjustment, with convection playing a less important role. In the case of waves C- and D-, on the other hand, convection appeared to be the most significant contributor to their generation. Geostrophic adjustment, then unbalanced frontogenesis would round out the list in order of likely importance of generation mechanisms for these waves.

There was significant evidence supporting the suggestion that a gravity wave event occurred during February 16 - 18. The most convincing evidence was presented in the surface pressure and wind field correlation plots and their relation to the location of the waves. Additional support was found in the fact that the shape of the waves so closely matched the shape of the cloudband, particularly wave C- and CB3. The synoptic setting in this case was surprisingly similar to the February 14 case with a cyclone developing on the lee side of the Rockies. Cloudbands and associated waves formed in the dry air intrusion east of this system in both cases and the cloudbands tended to show a dependency on the movement of the low pressure center.

#### *6.4 March 8 - 10 1992*

##### 6.4.1 SYNOPTIC OVERVIEW

A surface low was located in southeastern Colorado on 8 March 1992, with an associated front/dryline which pushed eastward into Texas and Oklahoma. A strong jet was moving around the upper-level cutoff low located in western Arizona which put the Oklahoma/Texas Panhandle in the exit region of the jet. An arctic front was pushing into Nebraska from the north. During the next 12 hrs, a deep surface low developed over southeast Colorado with a dryline that extended from the low through Oklahoma and Texas. A fairly weak cold front extended from the low, first dipping to the southwest

before turning toward the northwest through Colorado (see Fig. 6.25). During this time, the cyclone had a warm occluded-like structure as seen in the geopotential height and temperature analysis performed by Martin et al. (1994). Heavy snow fell as the arctic front moved into Colorado. The low continued to move off to the northeast while the arctic front pushed southward as the upper-level trough deepened, capturing the cutoff low.

Evident in the satellite and radar imagery at 1800 UTC on 8 March, was a cyclone with an associated comma cloud system along the Arizona/Utah border. During the following 6 hrs this system appeared to degenerated while another cyclone developed in eastern Colorado. (It could be that the initial cyclone only appeared to degenerate as it passed over the mountain range and had actually regenerated in the lee of the Rockies to become the primary cyclone of this case.) During this time, a cloudband (CB1) developed along a line from southwest Nebraska to central Oklahoma. This band moved northeastward through time, and was located in Missouri by 0100 UTC (Fig. 6.25). At 2300 UTC, it appeared as though cells started developing along the dryline that extended from southwestern Kansas through Oklahoma and into central Texas. The detailed analysis performed by Adams (1996) depicts a Cold Front Aloft (CFA) at 500 mb practically co-located with the dryline at the surface at 0000 UTC 9 March (Fig. 6.26). The precipitation (that later developed into cloudband 2) was slightly ahead of the dryline in the same location as the CFA. Throughout its existence, CB2 tended to move with the CFA. By 0100 UTC, a small cloudband (CB3) with minimal precipitation was located along the dryline in a clear zone between CB2 in central Oklahoma (see Fig. 6.25) and the clouds wrapping around the low in eastern Colorado.

Over the subsequent 3 hrs, thunderstorm formation along the CFA intensified. The southern section of CB1 dissipated while the northern section appeared to move into an area of precipitation associated with the arctic front and lost its banded features around 0800 UTC. By 0300 UTC (Fig. 6.27), RB2 was aligned with the CFA and had pulled

away from the dryline, however, RB3 was behind the CFA along the dryline. (Note that the terms rainband and cloudband are used interchangeably.) Figure 6.28 shows a close-up of the relationship between the dryline, CFA and developing convection at 0000 UTC and again at 0300 UTC. By 0400 UTC, the northern part of RB3 had nearly merged with RB2. The southern section of RB3 was located in central Kansas (Fig. 6.29.c), behind RB2. Radar and satellite imagery were missing from 0400 - 0600 UTC. At 0600 UTC, judging from the distance between the two features and their orientation at this time compared to 0400 UTC, there was still a slight separation between RB3 and a small area of convective precipitation ahead of it in eastern Oklahoma that was associated with RB2 (see Fig. 6.29.d). Figure 6.30 shows that RB2 had moved slightly out ahead of the CFA while RB3 had pulled ahead of the dryline and was aligned along the CFA. Rainband 3 continued to intensify until 0700 UTC at which time there was still a slight hint of separation between RB2 and RB3 (Fig. 6.29.e). The two rainbands temporarily joined by 0800 UTC and the precipitation-free zone that had existed between them along the southern edge of RB3 had filled (Fig. 6.29.f). However, by 1100 UTC the east to west separation between RB2 and RB3 had widened which could suggest separate features.

In general, the first two bands tracked more towards the east while RB3 appeared "connected" to the circulation about the low pressure center and therefore moved toward the northeast. Martin et al. (1994) suggest CB1 and CB2 were pre-drytrough and CFA rainbands respectively. They did not address band 3 separately but rather included it in the CFA rainband. The essential ingredient for the development of these rainbands according to Martin et al. (1995) was the passage of a synoptic-scale shortwave over the Rockies and the interaction of the cyclonic structure with the high terrain of the Rockies and Mexican Plateau, resulting in the presence of a dryline and lee trough (or drytrough). According to Martin et al. (1994), the pre-drytrough rainband developed at the warm edge of an isolated region of warm-air advection at middle levels that was located within a broad region of

convective instability created by the warm-frontal circulation associated with the drytrough. Wang et al. (1994) noted that a severe squall line developed and quickly became aligned along the leading edge of the cold-air advection in the middle troposphere and that therefore, the squall line was a CFA rainband. The band developed in a region of the atmosphere where there was a local maximum in lower tropospheric convective instability produced by the low-level, northward advection of high equivalent potential temperature air ahead of the drytrough. Shearing deformation frontogenesis, associated with the middle-level baroclinic zone, was argued to have provided the concentrated lifting necessary to trigger and sustain the convection. Nevertheless, the surface bandpass analysis presented next suggest the presence of clearly-defined gravity wave signatures closely linked to the cloud/rainbands (and thus, by implication, the CFA and differential advection features).

#### 6.4.2 ANALYSIS RESULTS

Data from 8 March 2100 UTC through 10 March 1200 UTC were processed in the analysis of this case. Pressure recordings from 90 stations were used including barograph data from 15 NWS stations, resulting in an average station spacing of 71 km. The ASOS data contained large temporal gaps, therefore barographs from 14 of the NWS stations, co-located with the ASOS stations, were digitized to fill these gaps. Digitization was accomplished in 15-min intervals and linear interpolation was used to achieve 5-min observations. The data were quality controlled in the usual manner.

In lieu of spectral analysis, a bandpass filter using cutoff periods (frequencies) from 30 min ( $f_{c2} = 0.0330 \text{ min}^{-1}$ ) to approximately 6 hrs ( $f_{c1} = 0.0028 \text{ min}^{-1}$ ) was applied to the pressure data, chosen based on the typical gravity wave periods and from experience gained during the previous two case studies. Given these frequencies, equation (4.8) suggests nine one-sided weights. As in the other case studies, the total number of weights

used was 65; therefore, a full response of 1.0 was obtained as apparent in the plot of the response function in Fig. 6.31.

A quick subjective analysis was performed on the pressure perturbations to see if there was in fact any evidence for waves. Four wave-like features were noted as were a few short-lived features that were of smaller scale than the waves. The isochrones depicted waves that were slightly arced that moved from approximately  $260^\circ$  at an average speed of  $28.6 \text{ ms}^{-1}$ . Given that the waves were only slightly arc-shaped, it was determined that a single advection vector ( $\bar{c} = 260^\circ, 28.6 \text{ ms}^{-1}$ ) could be used in the objective analysis. A grid-length of  $\Delta x = \Delta y = 32 \text{ km}$  was used in order to keep the grid-length between 1/2 and 1/3 the average station spacing, and  $\tau$  was kept at 50 min. Five waves were identified along with a smaller and less coherent feature that was of shorter duration. One of the waves (D-) was initially a small feature but then it appeared to develop more wavelike characteristics. The isochrones (Fig. 6.32) suggested that all five waves moved toward the east or northeast as they passed through the STORM-FEST region. Table 6.5 contains the characteristics of waves A-, B-, C- and E- as determined from the objective analysis. Given the overall average phase speed of  $28.6 \text{ ms}^{-1}$  and average wavelength of approximately 260 km, equation (4.21) suggests a tau of at least 38 min; therefore the 50-min value used in the objective analysis was adequate.

The average vertical wavelength ( $\lambda_z$ ) was found to be 1155 m ( $\lambda_z/2 = 580 \text{ m}$ ), and

Table 6.5. *Phase speeds, horizontal wavelengths, periods and phase directions for the major waves identified in the March 9 gravity wave event determined from the objectively analyzed waves. An average value as well as the standard deviation are presented. For the period, a range was derived from the SDs of the phase speed and wavelength.*

Wave	Phase Speed ( $\text{ms}^{-1}$ )	Phase Direction (deg)	Wavelength (km)	Period Average & (Range) (hr)
A-	$22.2 \pm 8.4$	$265 \pm 7$	$305 \pm 8$	3.8 (2.7 - 6.3)
B-	$30.0 \pm 5.1$	$257 \pm 12$	$275 \pm 28$	2.5 (2.0 - 3.4)
C-	$31.3 \pm 8.7$	$252 \pm 15$	$280 \pm 55$	2.5 (1.6 - 4.1)
E-	$28.2 \pm 3.5$	$266 \pm 19$	$170 \pm 12$	1.7 (1.4 - 2.0)



the duct was measured at approximately 780 m. The error is within 26 % of the dispersion equation, which can be considered adequate based on the reasoning presented earlier in this study.

Output from the objective analysis was available beginning at 0200 UTC on the 9th (Fig. 6.33); however, the raw pressure traces showed possible evidence of a wave train which would encompass wave A- late on 8 March. These supporting traces were from southeastern Kansas and eastern Oklahoma as well as western Missouri. A summary of wave activity and the relationship between the waves and the bands of precipitation is presented below. Note that the wave signatures were not nearly as strong or coherent in this case as in the previous cases.

#### 09/0200 UTC

A fairly weak wave (A-) was located along the front edge of rainband 1 (RB1) in the south and east of the band in the north. The wave ridge (A+) following A- was nearly twice as strong and its maximum values were aligned with the areas of precipitation. This situation was suggestive of a wave tilted in the vertical. A second wave (B-) was evident behind the convective cells of (RB2) along the front edge of another band (RB3) found between the dryline and the low pressure center to the northwest (Fig. 6.29.a). A small pressure perturbation feature ( $p' = 0.6$  mb) was located at the front edge of a circular area of intense cells on the central Kansas/Oklahoma border that had formed along the dryline. This pressure feature remained just ahead of these cells through 0400 UTC, after which time radar and satellite imagery were not available again until 0600 UTC. Another small feature ( $p' = 0.8$  mb) was positioned to the northwest of an intense circular convective area located in eastern Oklahoma, slightly ahead

of the precipitation forming RB2. This feature continued to be associated with this convection through 0400 UTC and by 0600 UTC had expanded and taken on more wave-like features (wave D-).

#### 0300 UTC

Wave A- had moved out ahead of RB1 and the largest values of A+ occurred where the precipitation was located. Wave B- was located along the front edge of RB3 (suggestive of no tilt in the vertical) which had almost joined with a group of cells associated with the convection of RB2 (Fig. 6.29.b).

#### 0400 UTC

Wave A- had split (as had the precipitation) into a northern and southern section. The wave was fairly far ahead of the precipitation in the south. The exact positioning in the north was difficult to determine because the radar and satellite imagery did not extend into this area. While A- had increased, A+ had decreased. Wave B- had lengthened and intensified ( $p' = -1.2$  mb) and extended along the front edge of RB3, behind RB2 (Fig. 6.29.c). Rainband 3 and its associated gravity wave train B-/B+ displayed an arc shape with a sharp retreating side very much reminiscent of wave B-/B+ in the February 14 case.

#### 0600 UTC

With the lapse in imagery, the wave/convection positioning was determined with less certainty than previously; however, it appeared as though B- had pulled out ahead of RB3 yet remained west of the cells associated with RB2. Wave B+ ( $p' = 1.4$  mb) had developed and was co-located with the precipitation band. This new configuration suggested wave B- tilted with height. A new wave (C-) was detected in the objective analysis at 0430

UTC and by 0600 UTC was located along the back edge of RB3 in the north and behind the band to the south (Fig. 6.29.d). Another wave (E-) was first evident in the objective analysis at 0500 UTC and at 0600 UTC it was located along the front of RB2 across the Missouri/Arkansas border. Wave D- was establishing itself ahead of E- through an area of convection extending eastward from RB2.

#### 0700 UTC

Wave B- had moved ahead of what appeared to be the northern extension of RB2 while C- had moved closer to the back edge of RB3 (Fig. 6.29.e). Wave B+ appeared to have been influenced by an impulse in central Nebraska (see Fig. 6.33) that is believed to be erroneous. There was no data north or west of this area (the nearest stations were to the east in the southeast corner of Nebraska), and furthermore, this intense region weakened significantly over just the next hour. At this time, RB3 was wrapping into RB2. Wave D- had strengthened to a maximum value between -1.2 and -1.4 mb.

#### 0800 UTC

Wave C- appeared to have strengthened tremendously in its northern extent; however, this was believed to be in response to an impulse such as the one mentioned above. Waves B- and C- were located on either side of the northern combination of RB2 and RB3 (labeled RB3 in Fig. 6.29.f) with B+ aligned with the convection. Evidence for wave C- was weak at its center and the southern section was well behind RB3. (Note that wave B- appears to propagate through RB2 from 0700 UTC to 0900 UTC. Compare Fig. 6.29.e to Fig. 6.29.g.)

#### 0900 UTC

Waves B- and C- were still located on either side of RB3, which had merged with the northern part of RB2 (Fig. 6.29.g). The southern extension of C-, even though west of CB3, was shaped like the back edge of the band. The maximum positive pressure perturbations remained collocated with regions of maximum precipitation. Wave E- was at the front edge of the southern part of CB2-3. (The radar imagery ended west of the wave.)

1000 UTC

No significant changes. See Fig. 6.29.h.

As noted in the summary above, the waves and the convective bands tended to travel together and the areas of positive perturbations were shaped similarly to the cloudbands, particularly in the north and central portions of the STORM-FEST region. Along the southern border of the objective analysis output, the positive perturbation values were often ahead of the convection. For the most part, the variations in the intensity of the waves occurred independently from the variations in convection as could be expected since the strongest convection associated with this event occurred south of the STORM-FEST region. Wave B- did initially grow and become more wave-shaped as the precipitation behind it increased. Indications were that wave A- was tilted in the vertical whereas wave B- initially appeared to have no tilt but then a tilt was suggested as the wave developed. Wave E- appeared not to tilt with height.

The raw pressure traces from stations located within the region of wave activity were quite noisy; however, a wave train configuration was suggested. Figure 6.34 is a digitized pressure trace from SLN located in central Kansas. The features in the center of the trace are wave B- and the peak that followed (B+). (The B+ feature can be classified as a wave of elevation.) The trace from Princeton, Missouri (P03) was less noisy than most and the positions of waves A-, B- and C- were easily identified (Fig. 6.35). (Note that the

signature in the trace from B- to the crest following C- constitutes a wavelet.) These two traces suggest that the configuration of B- changed very little as it propagated to the northeast.

The objective analysis output began at a time when both CB1 and CB3 were already developing as were waves A- and B-. Therefore it could not be determined if the waves or the convection had developed first. Wave C- developed at the back edge of CB3, as if in response to the convection (perhaps wave-CISK). Convective activity was plentiful in the southern section of the STORM-FEST region and both waves D- and E- established themselves at the front of established areas of precipitation, again suggesting that convection was likely involved in the generation and sustainment of these two wave.

The largest  $\overline{p'u^*}$  values and the strongest perturbations associated with wave A- were located in northern Missouri and eastern Illinois. There were scattered values  $> 0.7$  along southern Missouri and Illinois (Fig. 6.36.a). This could suggest a relationship between wave strength and correlations since the wave split into northern and southern sections; however, the wave was relatively weak in eastern Illinois and values were still strong in that area.

Correlation values associated with wave B- also showed some indications of being related to wave intensity. As the wave moved across the Missouri/Illinois border, the southern extension of the wave became less evident, and weaker (even negative) correlations were recorded in this area. Strong positive correlation values were associated with the southern section of wave B- while weak values were calculated in the area of weaker perturbation values between this feature and the northern section of wave B-.

Wave C- was weak at the time it moved through the mesonet in the northeastern corner of Kansas and across northern Missouri where the highest correlation values were recorded (Fig. 6.36.c). Even though the wave was weak, the high correlations did occur where the evidence for the wave did exist.

Pressure/wind correlations in excess of 0.7 were found all along the path of wave E- beginning in south-central Missouri. A couple of negative values were calculated as the wave passed through the southeastern corner of Missouri but then as the wave entered Illinois, the correlation values were in excess of 0.7 once again. The largest area of relatively high values occurred in southern Illinois which was the area through which the wave traveled.

Convection was present with all the waves; therefore, the negative correlations noted with waves B- and E- could be attributed to non-linear effects. Although the development of waves C- and E- appeared to have occurred in response to convection, high correlations were not observed directly following wave development as was the case with waves C- and D- from the February 16 - 18 gravity-wave event.

None of the possible gravity wave genesis mechanisms could be ruled out during this event. Convection was present with all the waves and wave C- was first detected at the back of a cloudband and waves D- and E- also formed in a convectively active area; therefore, convection could have been a source mechanism for these waves either through the release of latent heat or wave-CISK. Support for geostrophic adjustment and the Uccellini and Koch (1987) conceptual model exists partly based on the 500 mb chart with observed wind and deduction of geostrophic winds based on the height lines and theory. When this case was first identified as a pressure perturbation event it was determined that the STORM-FEST region was actually in the warm sector early in the event. Later in the day on 9 March, when the frontal system began pushing through from the north, the region was no longer in the warm sector, thus matching the Uccellini and Koch (1987) model. Since the gravity waves actually occurred early on 9 March, the event does not meet the frontal criteria for the model. Upon further investigation of the objective analysis of this event it became apparent that the pressure perturbations that continued into 10 March during this  $p'$  event were associated with the frontal movement through the region. Therefore, the

perturbation event matched the model; however, the gravity wave event did not. As for the potential of geostrophic adjustment, the MM4 24-hr forecast for 300 mb, valid 0000 UTC 9 March depicted the wind and the geostrophic maximums co-located as they came out of the base of the trough. However, Adams (1996) objectively analyzed the four terms that make up the non-linear balance equation and calculated the inertial Rossby number (values  $> 0.5$  indicate imbalance) for 500 mb and found evidence of an imbalance. At 0000 UTC the largest Rossby numbers (0.8) were located in eastern New Mexico while at 0600 UTC the largest values (0.8) were located in eastern New Mexico and another area existed along the Colorado/Kansas border. The Rockies were located upstream of the area in which the gravity waves were observed; hence, topography cannot be ruled out. However, the impact of the Rockies on the development of wave E- which occurred in central Missouri could be questionable. There was a developing low on the lee of the mountain range suggesting that unbalanced frontogenesis could have also been involved.

It is likely that the generation mechanism for waves A- and B- is the combination of a developing cyclone in the lee of the Rockies in the presence of geostrophic adjustment. As for waves C-, D- and E-, it appears as though convection was the primary generation mechanism while geostrophic adjustment followed by unbalanced frontogenesis likely played secondary roles in their development.

Support for the existence of gravity waves during this event was evident in the  $\overline{p'u^*}$  correlations. The highest positive correlation values appeared most related to the strength of the wave. Evidence has also been presented supporting the existence of three separate rainbands, whereas Martin et al. (1994) concentrated on the two larger scale bands (CB1 and CB2). The most impressive feature from this case was B+ located behind CB3 which (1) formed in a dry slot east of a developing low pressure center and (2) moved through the STORM-FEST region toward the northeast as though "connected" to the low pressure center to the west. Although there was evidence that A-, B-, C- and E- were

gravity waves, these two attributes make waves B- and C- located on either side of CB3 more like the gravity waves seen in the previous cases presented in this study. Waves B- and C- were the strongest negative perturbation waves while B+ and E+ were the strongest positive perturbation features. These were all features associated with what Martin et al (1994) referred to as the CFA rainband; however, it is suggested in the present study that B-, B+ and C- were actually associated with a separate rainband.



## 7. Conclusions

Thirteen pressure pulse events (amplitude  $\geq 0.2$ , period 1 - 6 hrs) were identified in the surface pressure data gathered during STORM-FEST, involving 34% of the total hours investigated. These pulse events were ranked according to their average amplitude value. The four events that were similar to the Uccellini and Koch (1987) synoptic model of features typically found during mesoscale gravity wave events--a jet streak near a 300 mb inflection axis, a diffluent trough upstream and a surface front to the south or southeast, were those with the largest average amplitudes. Results from investigating the single criterion of a jet streak near the inflection axis suggest that this feature is a sufficient but not necessary condition for a gravity wave to occur.

The three top-ranked pressure pulse events were analyzed in detail to determine if these events were in fact associated with mesoscale gravity waves. The analysis methods used include spectral analysis, bandpass filtering and pressure-wind covariance calculations. All three of the events analyzed displayed evidence of a gravity wave in the  $\overline{p'u^*}$  values and in the continuity of the wave signatures. There tended to be a variety of wave types evident in each of the cases, including wavelets, wave trains and waves of elevation and depression, which in some cases occurred within a wavelet or train.

Sensitivity tests were performed on the data from the first case (February 14 - 15) on the variables used in the objective analysis of the wave. The sensitivity tests suggested that care should be taken when choosing a bandpass-filter width since one that simply encompasses the evident wave frequencies may result in a response of less than unity which leads to attenuation of the pressure perturbations. In addition, a filter width slightly larger than that suggested by the histogram of significant spectral peaks frequencies involved less smoothing and as a result, the timing errors were less significant as evidenced when the filtered pressure traces were compared to the raw traces. It was determined that

the period of time-to-space conversion needs to be sufficiently large ( $\tau \cong 50$  min) to allow for the advantages of Time-to-Space Conversion (TSC) to be realized. Otherwise, there is not much improvement over conventional Barnes analysis. The results from using a grid-length larger than the customarily recommended value  $\Delta n/3 < \Delta x < \Delta n/2$  produced more desirable wave features in that they were smoother. However, a value within this range is recommended to ensure proper representation of the wave despite the fact that this may result in a slightly rougher representation of the wave.

Four wave-detection methods were examined in this study: subjective-analysis of the filtered pressure perturbation values, GEMPAK Barnes objective analysis, Barnes TSC with multiple advection vectors and Barnes TSC with one advection vector. The goal was two-part: (1) determine if a Barnes objective analysis resulted in an adequate analysis, and (2) determine if use of a single advection vector instead of multiple advection vectors degraded the TSC results and to what degree. It was much easier to follow the wave in the Barnes TSC analysis than on maps of simply the  $p'$  values used in the subjective analysis. The Barnes TSC objective analysis brought the wave to life in the sense that it was almost animated when a plot from a given time was compared to consecutive plots. By contrast, in a traditional Barnes analysis, the perturbation values were less than the actual pressure perturbation values in many cases, and the pressure perturbation maxima tended to be circular instead of displaying wave-like characteristics seen in the Barnes TSC products, causing the shape of the isochrones drawn using these values to change and appear less continuous than a typical wave feature. Therefore, using a Barnes analysis to track the wave would not be recommended. The comparison between the results involving a single advection vector and multiple advection vectors suggested a single vector would likely do fairly well at representing a planer wave, while multiple advection vectors would be recommended for waves that are arc-shaped.

The wave features in the February 14 - 15 event displayed phase velocities of  $21.6 \text{ ms}^{-1} \pm 5.9 \text{ ms}^{-1}$ , wavelengths of  $200 \text{ km} \pm 41 \text{ km}$  and periods of  $2.3 \text{ hr} \pm 1.2 \text{ hr}$ . The wave characteristics from the February 16 - 18 event were  $19.9 \text{ ms}^{-1} \pm 6.2 \text{ ms}^{-1}$  for phase velocity,  $225 \text{ km} \pm 31 \text{ km}$  for wavelength and  $3.5 \text{ hr} \pm 3 \text{ hr}$  for period. The waves in the March 9 gravity-wave event displayed phase velocities of  $27.9 \text{ ms}^{-1} \pm 6.8 \text{ ms}^{-1}$ , wavelengths of  $260 \text{ km} \pm 32 \text{ km}$  and periods of  $2.6 \text{ hr} \pm 1.2 \text{ hr}$ . Some of the observed periods were larger than those typically found in past studies as were some of the phase speeds, although the phase speeds observed in this study were well within the upper limit of those observed in past studies.

A relationship between the convection and the waves was observed as the cloudbands and the gravity waves tended to travel together. The positive pressure perturbation areas in the objective analysis appeared to be very closely related to the location of the convection which at times caused the suggested wave shape to be less smooth than is desired for a wave. In the February 16 - 18 case, the highest cloud tops generally appeared at the same time as the largest perturbation values and along a line that ran between the leading negative perturbation maximum and the trailing positive perturbation maximum which suggests a co-dependent relationship.

Other results varied between the events. For example, the waves were evident before the convection in the case of February 14 - 15, whereas two of the waves identified in the February 16 - 18 case developed after the associated cloudbands. The waves from the 9 March case were all associated with convection. As for surface pressure and wind field correlations, the large positive values appeared to be closely related to the strength of the wave signature in the February 14 event, and the wave amplification and growth of convection occurred simultaneously. In the case of the February 16 - 18 event, the  $\overline{p'u'}$  correlation values generally corresponded with the strength of the wave signal, although high correlations were found with waves C- and D- which were forced by moderate

convection, suggesting that these values were influenced by the convection. (Moderate referring to convection greater in intensity than simple showers yet not to the degree that would result in a gust front.) The  $\overline{p'u^*}$  correlations observed from the March 9 event were also stronger where the wave signature was strongest. Although the development of waves C- and E- appeared to have occurred in response to convection, high correlations were not observed directly following wave development as was the case with waves C- and D- from the February 16 - 18 gravity-wave event.

The gravity waves occurred in a meteorologically active region and therefore only one of the typical genesis mechanisms could possibly be eliminated in any of the cases. Some waves were evident prior to the cloudbands, therefore eliminating convection as a genesis mechanism while those waves that seemed to form in response to convection were generally farther east, thus reducing the likely impact of topography in the generation of these waves. Waves in each of the three events appeared to be associated with a low developing on the lee of the Rockies in a region downstream from where a jet streak was approaching an upper-level inflection axis. In addition, cloudbands and associated waves formed in the dry air intrusion east of this system and the pinwheel-like movement of the cloudbands that developed here suggested they were connected to the low to the west. However, determination of the responsible genesis mechanism(s) will need to wait for detailed analysis to be performed on the upper-level data and modeling results. Additional studies on waves that form under similar circumstances could perhaps lend support to the "trend" identified in this study. It appears as though the gravity waves (and cloudbands) form in the dry air intrusion associated with a developing cyclone as it passes over the Rocky Mountains. Many of the bands tend to move as though connected to the low pressure center and therefore their genesis and movement, as well as that of the mesoscale gravity waves, appear to depend on the low in some manner. Since some of these events did involve severe weather, it could prove beneficial to investigate the frequency of

occurrence of the trend observed in this study. Combining the criteria of a jet streak approaching the inflection axis and a low generating in the lee of the Rockies appears to lead to gravity waves that may in turn result in significant, even severe weather as observed in the events studied here.

## 8. References

- Adams, M., 1996: Terrain induced mid-tropospheric frontogenesis and jet streak development during STORM-FEST IOP 17, 8 and 9 March 1992. Ph.D. dissertation, North Carolina State University.
- Barnes, S. L., 1973: Mesoscale objective analysis using weighted time-series observations. NOAA Tech. Memo ERL NSSL-62, National Severe Storms Laboratory, 60 pp. [NTIS COM-73-10781].
- Bloomfield, Peter, 1976: Fourier Analysis of Time Series: An Introduction, John Wiley & Sons, Inc., New York, New York, 258 pp.
- Bluestein, Howard B., 1993: Synoptic-Dynamic Meteorology in Midlatitudes. Volume II: Observations and Theory of Weather Systems, Oxford University Press, Inc., New York, New York, 594 pp.
- Bosart, L. F., and J. P. Cussen, Jr., 1973: Gravity wave phenomena accompanying east coast cyclogenesis. *Mon. Wea. Rev.*, **101**, 446-454.
- , and F. Sanders, 1986: Mesoscale structure in the megalopolitan snowstorm of 11-12 February 1983. Part III: A large-amplitude gravity wave. *J. Atmos. Sci.*, **43**, 924-939.
- , and A. Seimon, 1988: A case study of an unusually intense atmospheric gravity wave. *Mon. Wea. Rev.*, **116**, 1857-1886.
- Bretherton, C. S., and P. K. Smolarkiewicz, 1989: Gravity waves, compensating subsidence and detrainment around cumulus clouds. *J. Atmos. Sci.*, **46**, 740-759.
- Chimonas, G., F. Einaudi and D. P. Lalas, 1980: A wave theory for the onset and initial growth of condensation in the atmosphere. *J. Atmos. Sci.*, **37**, 827-845.
- Clark, T. L., T. Hauf and J. P. Kuettner, 1986: Convectively forced internal gravity waves: Results from two-dimensional numerical experiments. *Quart. J. Meteor. Soc.*, **112**, 899-925.
- Clarke, R. H., R. K. Smith, and D. G. Reid, 1981: The morning glory of the Gulf of Carpentaria: An atmospheric undular bore. *Mon. Wea. Rev.*, **109**, 1726-1750.
- Corbet, J., C. Mueller, C. Burghart, K. Gould, and G. Granger, 1994: Zeb: Software for integration, display, and management of diverse environmental datasets. *Bull. Amer. Meteor. Soc.*, **75**, 783-792.
- Cunning, J. B., and S. F. Williams, 1993: STORM Fronts Experiment Systems Test Operations Summary and Data Inventory. USWRP STORM-FEST, 389 pp.
- Duchon, Claude E., 1979: Lanczos filtering in one and two dimensions. *Amer. Meteor. Soc.*, **18**, 1016-1022.

- Durran, D. R., 1990: Mountain waves and downslope winds, Atmospheric Processes over Complex Terrain, William Blumen, Ed., Amer. Meteor. Soc., 59-81.
- Einaudi, F., and D. P. Lalas, 1975: Wave-induced instabilities in an atmosphere near saturation. *J. Atmos. Sci.*, **32**, 536-547.
- \_\_\_\_\_, W. L. Clark, D. Fau, J. L. Green, and T. E. VanZandt, 1987: Gravity waves and convection in Colorado during July 1983. *J. Atmos. Sci.*, **44**, 1534-1553.
- \_\_\_\_\_, A. J. Bedard, Jr., and J. J. Finnigan, 1989: A climatology of gravity waves and other coherent disturbances at the Boulder Atmospheric Observatory during March-April 1984. *Amer. Meteor. Soc.*, **46**, 303-329.
- Eliassen, A., and E. Palm, 1960: On the transfer of energy in stationary mountain waves. *Geofys. Publ.*, **22**, 1-23.
- Eom, J. K., 1975: Analysis of the internal gravity wave occurrence of 19 April 1970 in the Midwest. *Mon. Wea. Rev.*, **103**, 217-226.
- Ferretti R., F. Einaudi, and L. W. Uccellini, 1988: Wave disturbances associated with the Red River Valley severe weather outbreak of 10-11 April 1979. *Meteor. Atmos. Phys.*, **39**, 132-168.
- Friday, E. W. Jr., 1993: Associated restructuring of the National Weather Service: An overview. *Bull. Amer. Meteor. Soc.*, **75**, 43-48.
- Fujita, T. T., 1955: Results of detailed synoptic studies of squall lines. *Tellus*, **7**, 405-436.
- Gall, R. L., R. T. Williams, and T. L. Clark, 1988: Gravity waves generated during frontogenesis. *Amer. Meteor. Soc.*, **45**, 2204-2219.
- Gossard, E. E., and W. H. Hooke, 1975: Waves in the atmosphere, Developments in the Atmospheric Sciences, Vol. 2, Elsevier, 456 pp.
- \_\_\_\_\_, and W. B. Sweezy, 1974: Dispersion and spectra of gravity waves in the atmosphere. *J. Atmos. Sci.*, **31**, 1540-1548.
- Hooke, W. H., 1986: Gravity waves, Mesoscale Meteorology and Forecasting, P. S. Ray, Ed., Boston, Amer. Meteor. Soc., 272-288.
- Howard, L. N., 1961: Note on a paper of John Miles. *J. Fluid Mech.*, **10**, 509-512.
- Hung, R. J., and Y. D. Tsau, 1991: Study of Ardmore, OK, storm clouds. I: Convective storm cloud initiation and development based on the remote sensing gravity-wave-induced convection. *Int. J. Remote Sensing*, **15**, 863-876.
- Jenkins, G. M., and D. G. Watts, 1968: Spectral Analysis and its Applications, Holden-Day, Inc., San Francisco, California, 525 pp.

- Jin, Yi, S. E. Koch, and L. Siedlarz, 1996: Detection and simulation of gravity wave events during STORM-FEST. Preprints, *7th Conference on Mesoscale Processes*, Reading, UK, Amer. Meteor. Soc., (in press).
- Johnson, R. H., and P. J. Hamilton, 1988: The relationship of surface pressure features to the precipitation and airflow structure of an intense midlatitude squall line. *Mon. Wea. Rev.*, **116**, 1444-1472.
- Koch, S. E., 1979: Mesoscale gravity waves as a possible trigger of severe convection along a dryline. Ph.D. thesis, University of Oklahoma, 195 pp.
- , M. desJardins, and P. Kocin, 1983: An interactive Barnes objective map analysis scheme for use with satellite and conventional data. *J. Climate and Applied Meteor.*, **22**, 1487-1503.
- , and P. B. Dorian, 1988: A mesoscale gravity wave event observed during CCOPE. Part III: Wave environment and probable source mechanisms. *Mon. Wea. Rev.*, **116**, 2570-2592.
- , and R. E. Golus, 1988: A mesoscale gravity wave event observed during CCOPE. Part I: Multi-scale statistical analysis of wave characteristics. *Mon. Wea. Rev.*, **116**, 2527-2544.
- , and C. O'Handley, 1996: Operational forecasting and detection of mesoscale gravity waves. *Wea. Forecasting* (submitted).
- , ———, and P. B. Dorian, 1988: A mesoscale gravity wave event observed during CCOPE. Part II: Interactions between mesoscale convective systems and the antecedent waves. *Mon. Wea. Rev.*, **116**, 2545-2569.
- , P. B. Dorian, R. Ferrare, S. H. Melfi, W. C. Skillman, and D. Whiteman, 1991: Structure of an internal bore and dissipating gravity wave current as revealed by Raman lidar. *Mon. Wea. Rev.*, **119**, 857-887.
- , F. Einaudi, P. B. Dorian, S. Lang, and G. M. Heymsfield, 1993: A mesoscale gravity wave event observed during CCOPE. Part IV: Stability analysis and Doppler-derived wave vertical structure. *Mon. Wea. Rev.*, **121**, 2483-2510.
- Kocin, P.J., and L. W. Uccellini, 1990: Snowstorms along the northeast coast of the United States: 1955 to 1985. Meteorological Monographs, Boston, MA, Amer. Meteor. Soc., 280 pp.
- Kuettner, J. P., P. A. Hildebrand, and T. L. Clark, 1987: Convection waves: Observations of gravity wave systems over convectively active boundary layers. *Quart. J. Roy. Meteor. Soc.*, **113**, 445-467.
- Lanczos, C., 1956: *Applied Analysis*, Prentice-Hall, 539 pp.
- Ley, B. E., and W. R. Peltier, 1978: Wave generation and frontal collapse. *J. Atmos. Sci.*, **35**, 3-17.



- \_\_\_\_\_, and, \_\_\_\_\_, 1981: Propagating mesoscale cloud bands. *J. Atmos. Sci.*, **38**, 1206-1219.
- Lin, Y.-L., and R. C. Goff, 1988: A study of a mesoscale solitary wave in the atmosphere originating near a region of deep convection. *J. Atmos. Sci.*, **45**, 194-205.
- Lindzen, R. S., and K. K. Tung, 1976: Banded convective activity and ducted gravity waves. *Mon. Wea. Rev.*, **104**, 1602-1617.
- Mahapatra, P. R., R. J. Doviak, and D. S. Zrnic, 1991: Multisensor observation of an atmospheric undular bore. *Bull. Amer. Meteor. Soc.*, **72**, 1468-1480.
- Martin, J. E., J. D. Locatelli, and P. V. Hobbs, 1994: A non-classical, synoptic-scale rainband in a winter cyclone in the central United States and its effects on the distribution of precipitation. Preprints, Proceedings of the *International symposium on the life cycle of extratropical cyclones*, Bergen, Norway, 156-161.
- Martin, J. E., J. D. Locatelli, P. V. Hobbs, P-Y Wang, and J. A. Castle, 1995: Structure and Evolution of winter cyclones in the central United States and their effects on the distribution of precipitation. Part I: A synoptic-scale rainband associated with a dryline and lee trough. *Amer. Meteor. Soc.*, **123**, 241-264.
- McCarthy, J., and S. E. Koch, 1982: The evolution of an Oklahoma dryline. Part I: A meso- and subsynoptic-scale analysis. *J. Atmos. Sci.*, **39**, 237-257.
- Miles, J. W., 1961: On the stability of heterogeneous shear flows. *J. Fluid Mech.*, **10**, 496-508.
- Pecnick, M. J., and J. A. Young, 1984: Mechanics of a strong subsynoptic gravity wave deduced from satellite and surface observations. *J. Atmos. Sci.*, **41**, 1850-1862.
- Powers, J. G., and R. J. Reed, 1993: Numerical simulation of the large-amplitude mesoscale gravity-wave event of 15 December 1987 in the central United States. *Mon. Wea. Rev.*, **121**, 2285-2306.
- Ralph, F. M., M. Crochet, and S. V. Venkateswaran, 1993: Observations of a mesoscale ducted gravity wave. *J. Atmos. Sci.*, **50**, 3277-3291.
- Ramamurthy, M. K., R. M. Rauber, B. P. Collins, and N. K. Malhotra, 1993: A comparative study of large-amplitude gravity wave events. *Mon. Wea. Rev.*, **121**, 2951-2974.
- Rauber, R. M., M. K. Ramamurthy, and D. L. Christensen, 1994: Structure of a mesoscale gravity wave observed during STORM-FEST. Preprints, *6th Conference on Mesoscale Processes*, Portland OR, Amer. Meteor. Soc., 228-230.

- Raymond, D. J., 1983: Wave-CISK in mass form. *J. Atmos. Sci.*, **40**, 2561-2571.
- Reeder, M. J., and D. Keyser, 1988: Balanced and unbalanced upper-level frontogenesis. *J. Atmos. Sci.*, **45**, 3366-3386.
- Rottman J. W., and F. Einaudi, 1993: Solitary waves in the atmosphere. *J. Atmos. Sci.*, **50**, 2116-2136.
- Sanders, F., and L. F. Bosart, 1985: Mesoscale structure in the megalopolitan snowstorm of 11-12 February 1983. Part I: Frontogenetical forcing and symmetric instability. *J. Atmos. Sci.*, **42**, 1050-1061.
- Schmidt, J. W., and W. R. Cotton, 1990: Interactions between upper and lower tropospheric gravity waves and squall line structure and maintenance. *J. Atmos. Sci.*, **47**, 1205-1222.
- Schneider, R. S., 1990: Large-amplitude mesoscale wave disturbances within the intense Midwest extratropical cyclone of 15 December 1987. *Wea. Forecasting*, **5**, 533-557.
- Scorer, R. S., 1949: Theory of waves in the lee of mountains. *Quart. J. Roy. Meteor. Soc.*, **75**, 41-56.
- Smith, R. K., 1988: Traveling waves and bores in the lower atmosphere: The 'Morning Glory' and related phenomena, *Earth-Science Reviews*, Vol. 25, Elsevier, 267-290.
- Stobie, J. G., F. Einaudi, and L. W. Uccellini, 1983: A case study of gravity waves-convective interactions: 9 May 1979. *J. Atmos. Sci.*, **40**, 2804-2830.
- Tepper, M., 1951: On the desiccation of a cloud bank by a propagated pressure wave. *Mon. Wea. Rev.*, **79**, 61-70.
- Trexler, C. M., S. E. Koch, and F. M. Ralph, 1996: Observational analysis of a mesoscale gravity wave detected during STORM-FEST. Preprints, *7th Conference on Mesoscale Processes*, Reading, UK, Amer. Meteor. Soc., (in press).
- Tripoli, G. J., 1986: A numerical investigation of an orogenic mesoscale convective system. Ph.D. Thesis, Colorado State University.
- Uccellini, L. W., 1975: A case study of apparent gravity wave initiation of severe convective storms. *Mon. Wea. Rev.*, **103**, 497-513.
- \_\_\_\_\_, and S. E. Koch, 1987: The synoptic setting and possible energy sources for mesoscale wave disturbances. *Mon. Wea. Rev.*, **115**, 721-729.
- Wagner, A. J., 1962: Gravity wave over New England. *Mon. Wea. Rev.*, **90**, 431-436.
- Wang, P-Y, J. E. Martin, J.D. Locatelli, and P.V. Hobbs, 1994: Recurrent precipitation bands within winter cyclones in the central United States. Preprints, *Proceedings of the 6th Conference on Mesoscale Processes*, Portland, Oregon, 215-217.

Wei, W. W. S., 1994: Time Series Analysis Univariate and Multivariate Methods,  
Addison-Wesley Publishing Company, Inc., 478 pp.

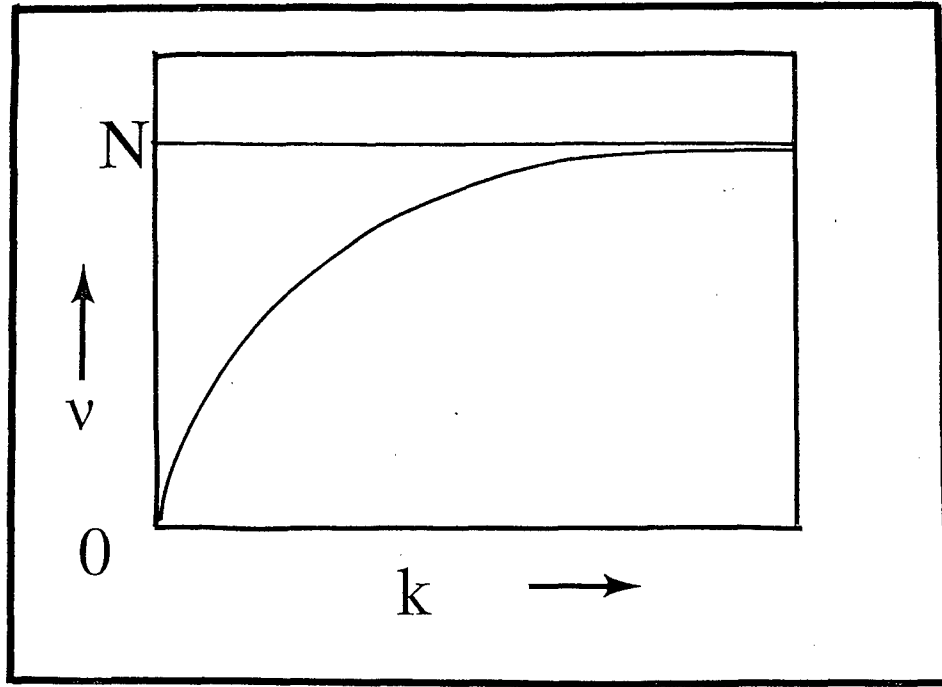


Figure 2.1. Internal gravity wave intrinsic frequency ( $\nu$ ) as a function of horizontal wavenumber ( $k$ ). As the horizontal wavenumber increases, the intrinsic frequency approaches the Brunt-Väisälä frequency ( $N$ ).

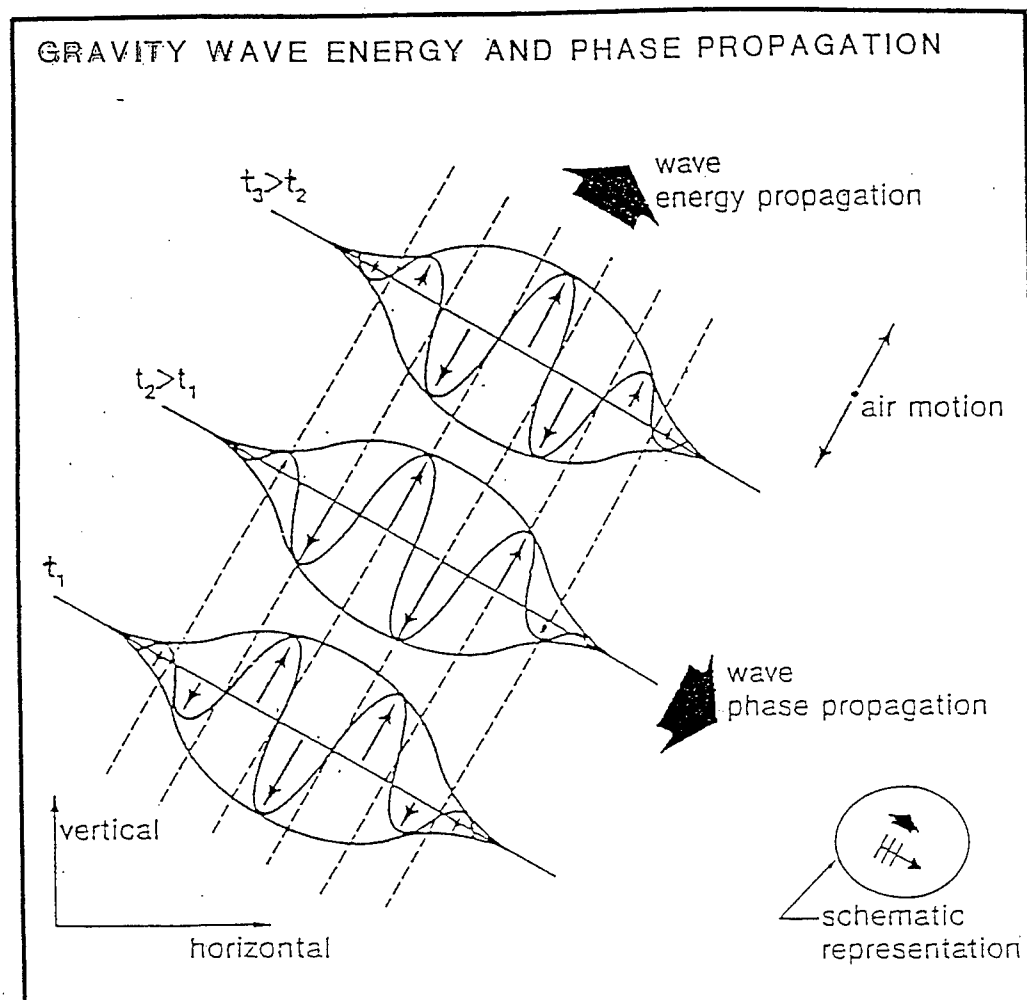


Figure 2.2. Gravity-wave energy and phase propagation. Waves are shown moving through the envelope at successive times,  $t$ . The dashed lines represent wave fronts (Hooke 1986).

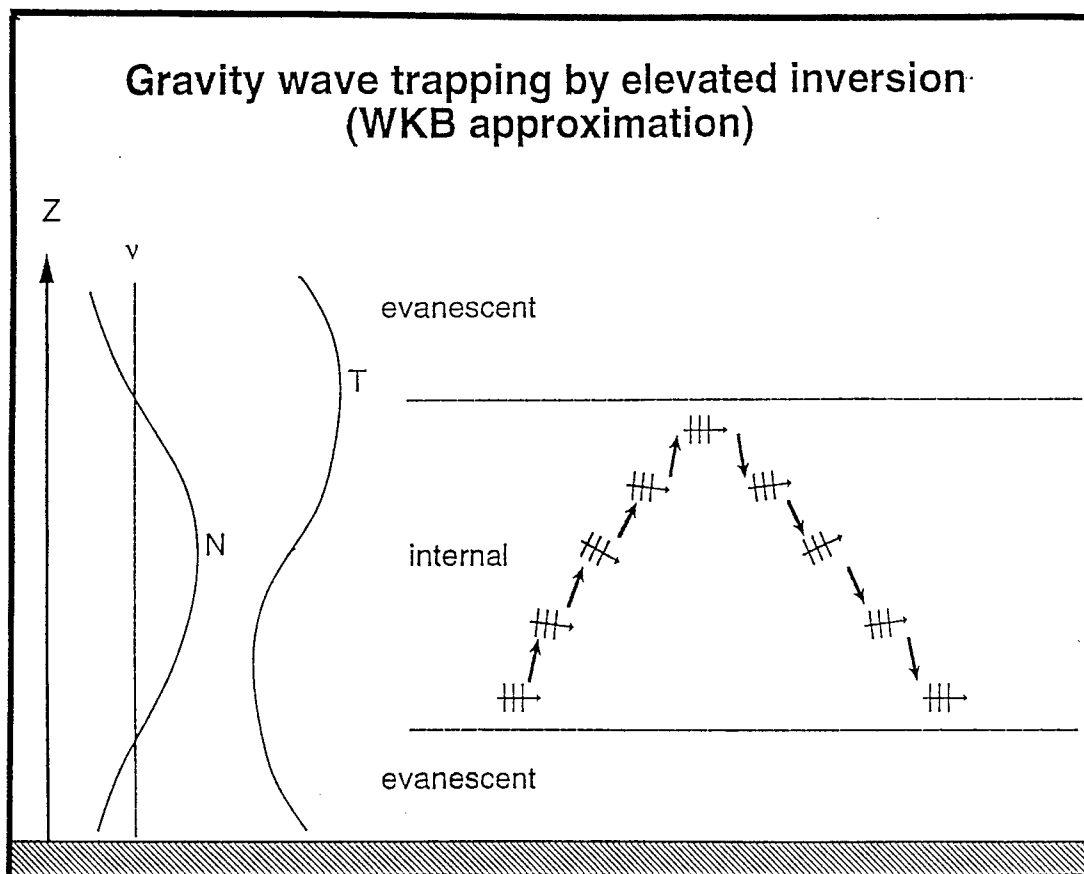


Figure 2.3. Gravity-wave trapping by atmospheric temperature structure where  $T$  represents temperature,  $N$  represents the Brunt-Väisälä frequency,  $Z$  represents the vertical coordinate and  $v$  represents the intrinsic frequency (Hooke 1986).

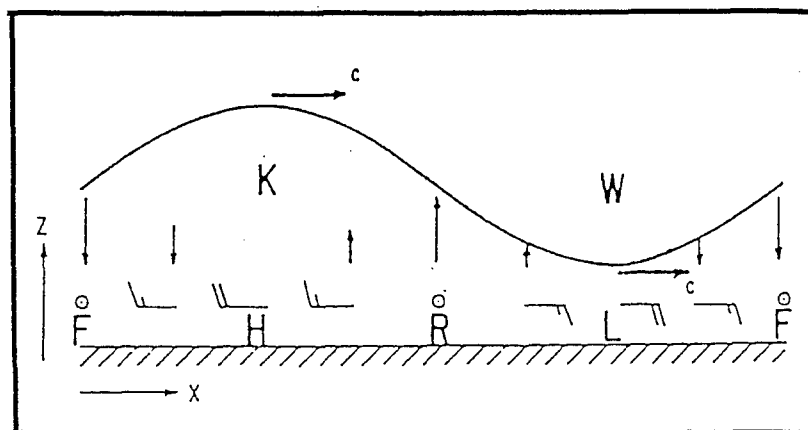


Figure 2.4. Idealized vertical cross section of a linear plane gravity wave with no basic current, propagating toward the right at speed,  $c$ . Surface pressure extrema are labeled  $H$  and  $L$ , while cold and warm temperature anomalies are denoted  $K$  and  $W$ , respectively. Rising motion is represented by an  $R$  and falling motion by an  $F$  (Eom 1975; reviewed in Bosart and Sanders 1986).

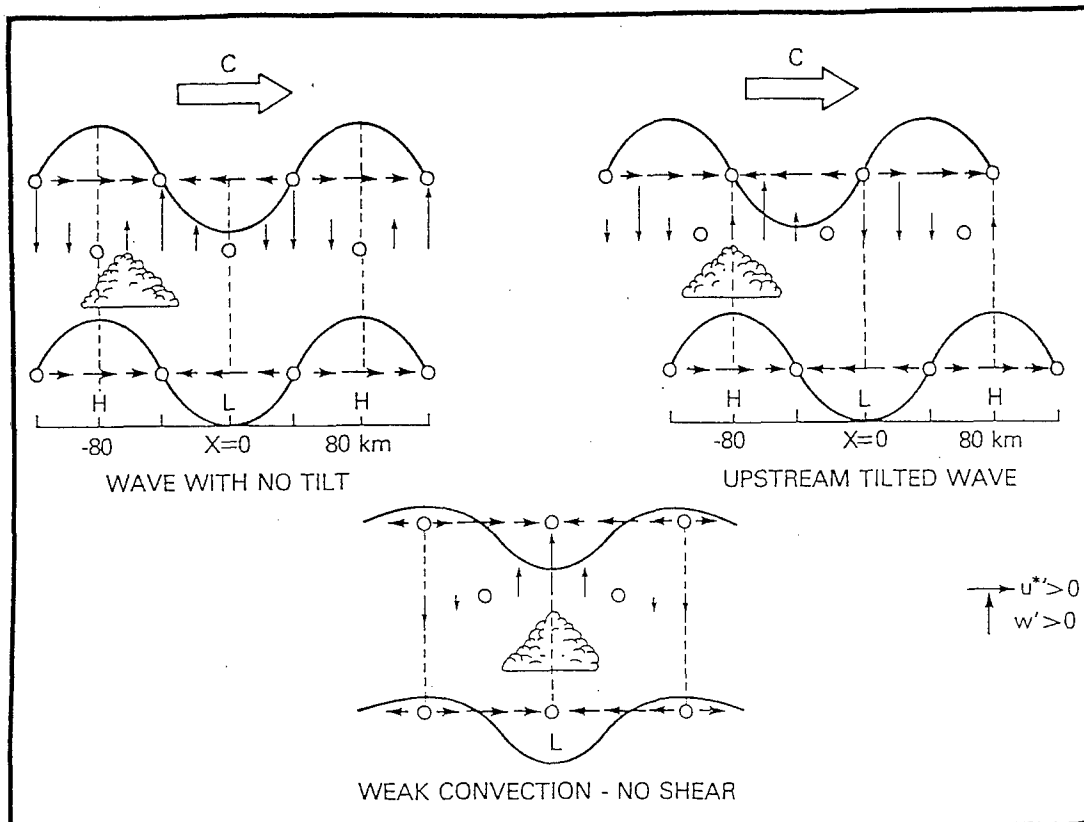


Figure 2.5. Height variation in the phase relations between the horizontal wind component in the direction of wave propagation and the wave-induced vertical motions for both an erect (left panel) and tilted (right panel) gravity wave, which is propagating toward the right at intrinsic speed,  $c$ . Also shown is location of strongest convection relative to gravity wave crest, assumed in both cases to be  $\pi/4$  behind the maximum updraft. Bottom panel depicts phase relations for weak convection in an unshered environment. H and L refer to pressure perturbations (Koch and Golus 1988).



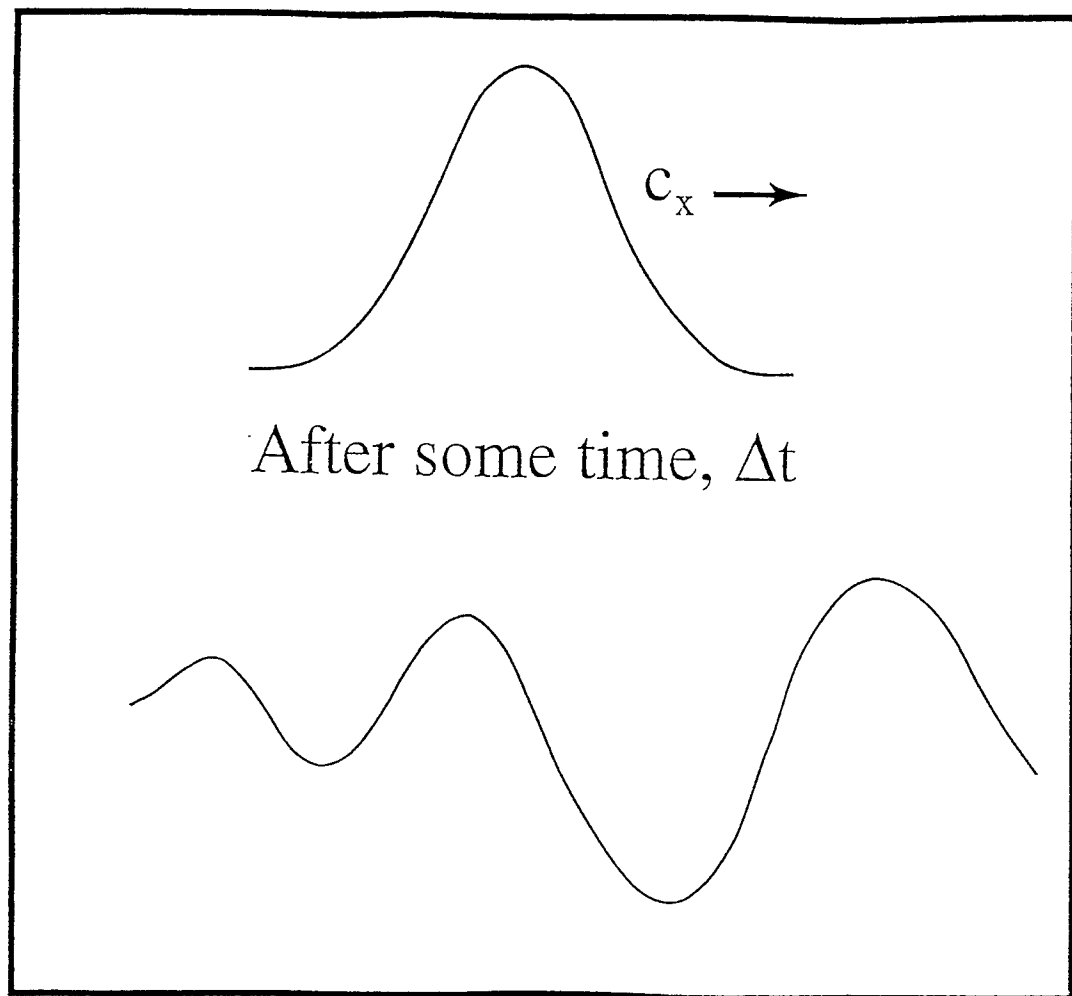


Figure 2.6. A wave disturbance larger than what can be supported by the atmosphere moving in the direction of  $c_x$ . The wave then changes shape due to the effects of dispersion where the shorter waves move more slowly.

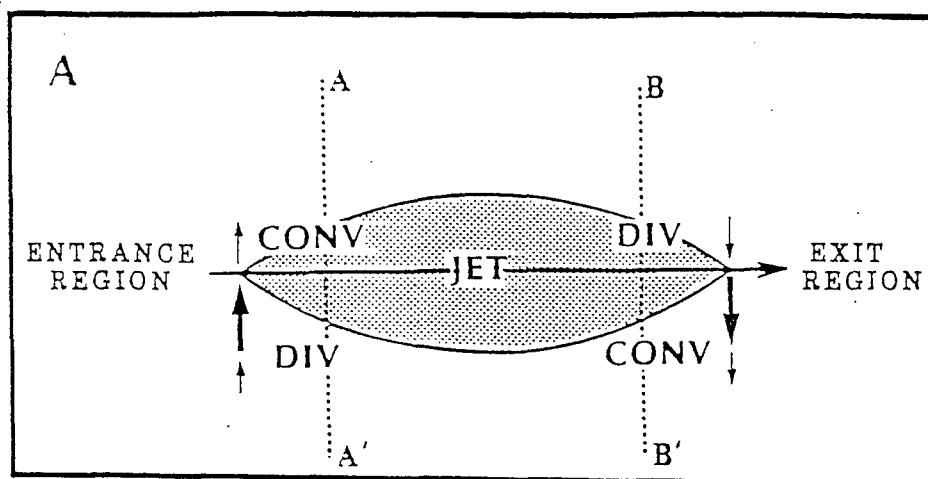


Figure 2.7. Schematic of transverse ageostrophic wind component and patterns of divergence (DIV) and convergence (CONV) associated with the entrance and exit regions of a straight jet streak (Kocin and Uccellini 1990).

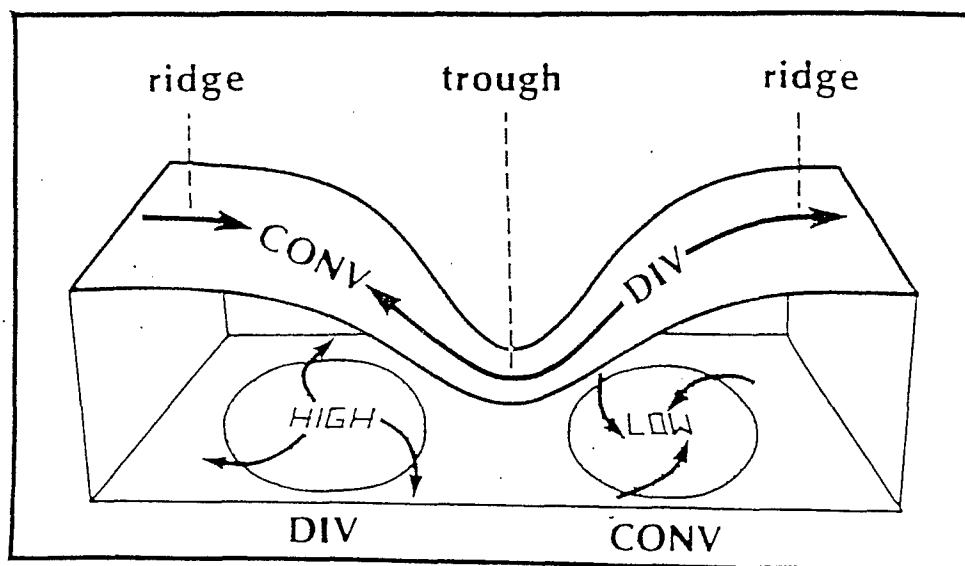


Figure 2.8. Schematic relating the along-stream ageostrophic wind at upper levels to patterns of divergence (DIV) and convergence (CONV) associated with an upper-level baroclinic wave and surface high- and low-pressure couplets (Kocin and Uccellini 1990).

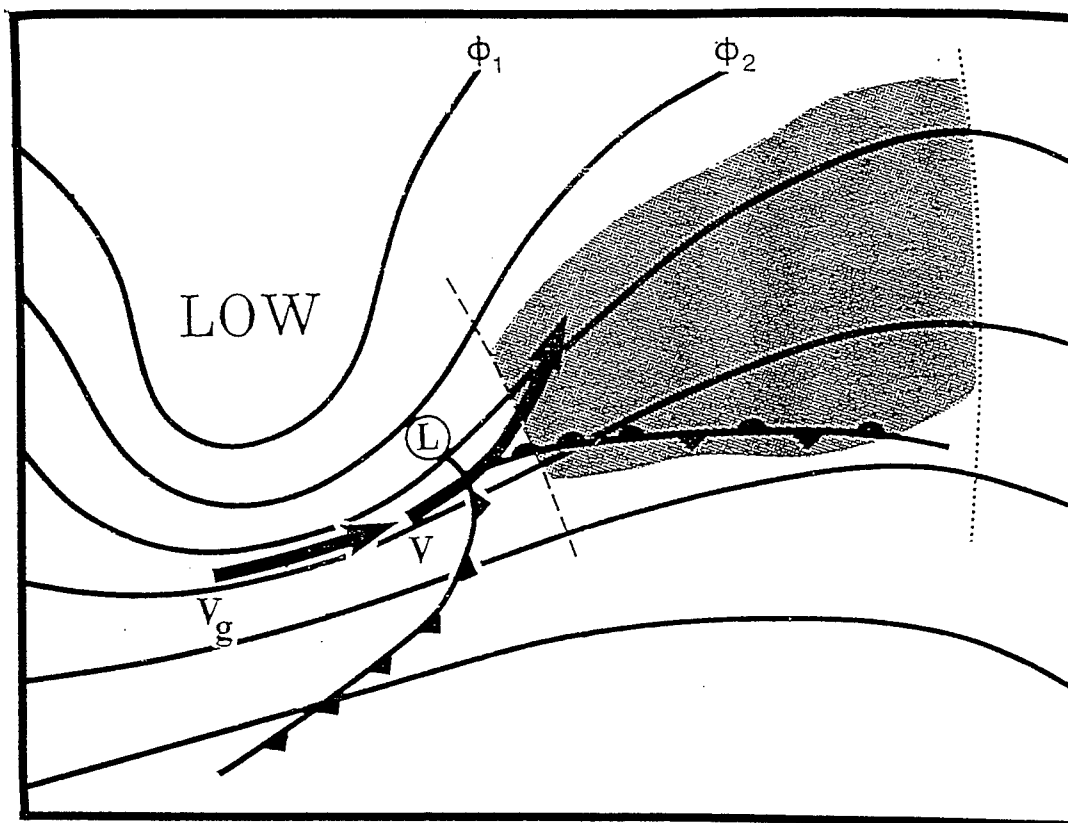


Figure 2.9. Surface and 300 mb synoptic features which characterize mesoscale gravity-wave events. The dotted line represents the 300 mb ridge axis, the dashed line represents the inflection axis and the shading represents the region mesoscale gravity waves typically occur. The observed and geostrophic jet maxima are represented by  $V$  and  $V_g$ , respectively (Uccellini and Koch 1987).

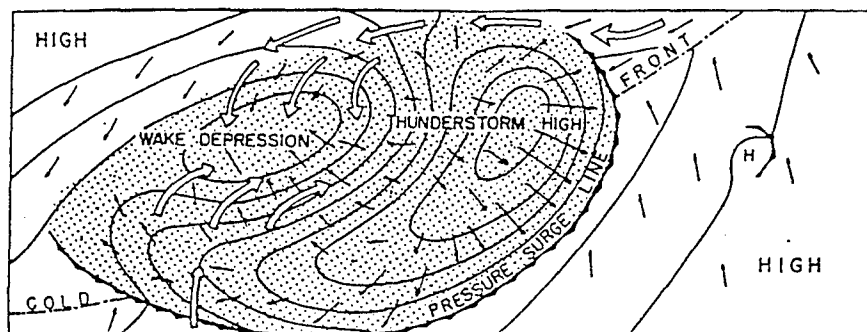


Figure 2.10. Schematic of surface pressure and wind field during the mature stage of a squall-line thunderstorm. Small arrows indicate surface wind; large arrows, relative flow into the wake (Fujita 1955).

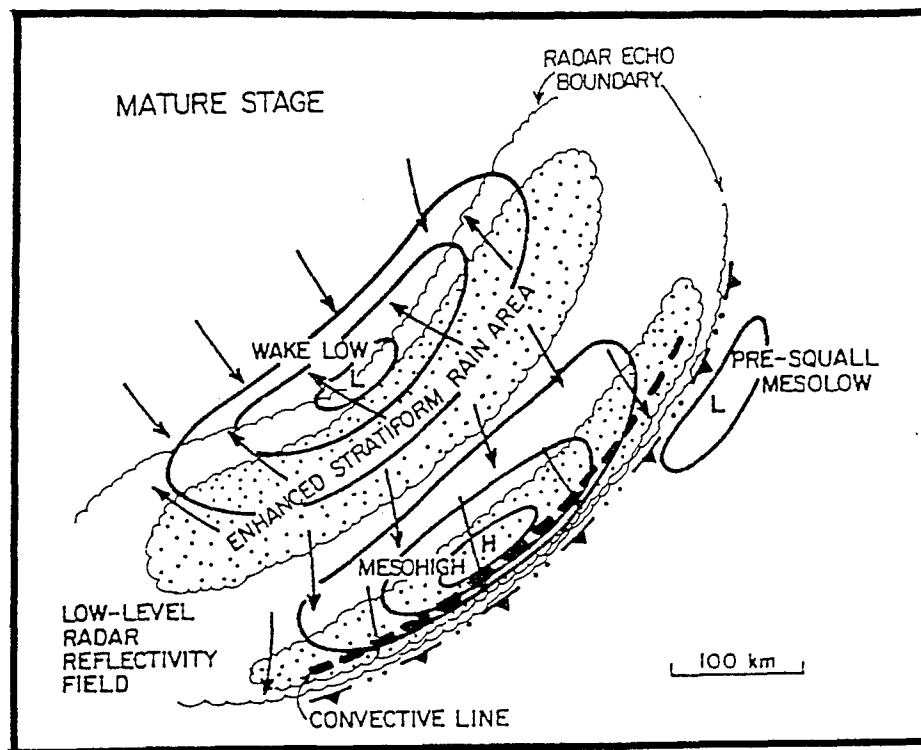


Figure 2.11. Surface pressure, wind fields and precipitation distribution during squall line mature stage. Arrows represent actual winds (Johnson and Hamilton 1988).

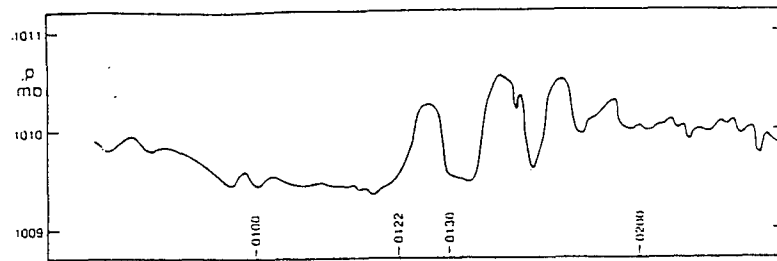
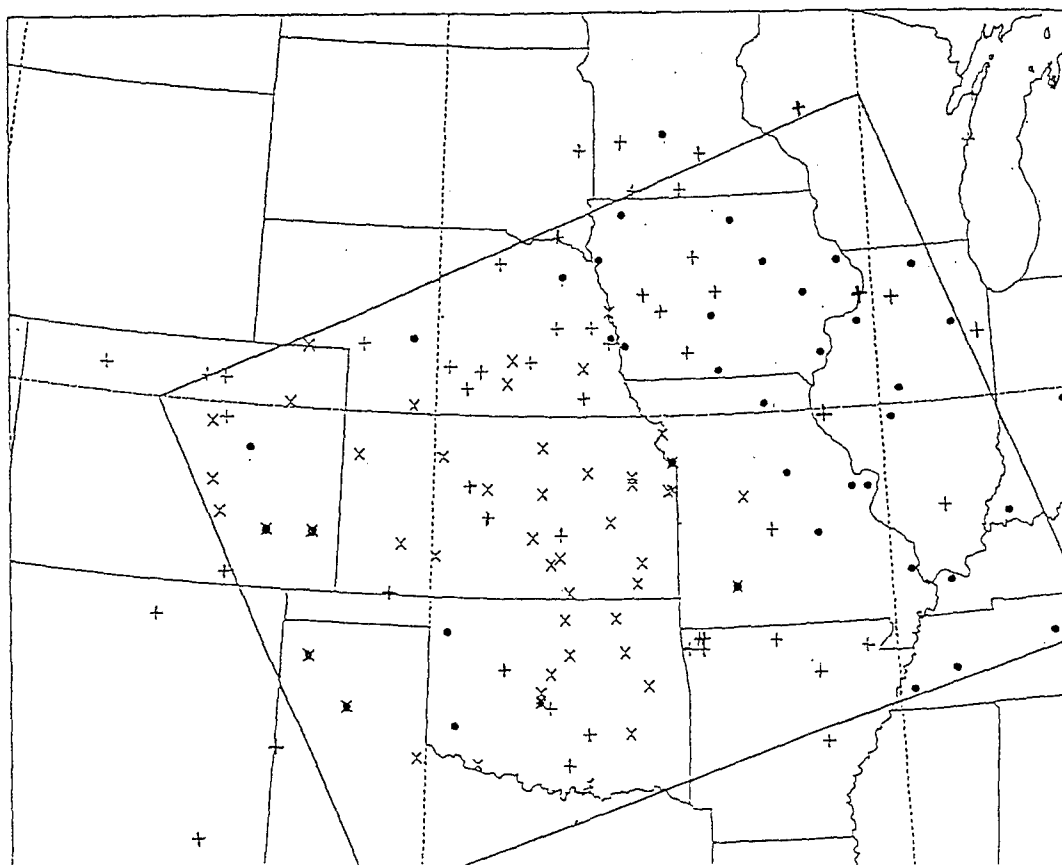


Figure 2.12. Typical undular bore pressure trace. The time scale is in regular hours and minutes. The solitary waves display periods (wavelengths) of 10 - 15 min (10 km) (Smith 1988).



ASOS   x   AWOS   +   BAROGRAPH •

Figure 3.1. Locations of the ASOS, AWOS and barograph surface observation stations during STORM-FEST.



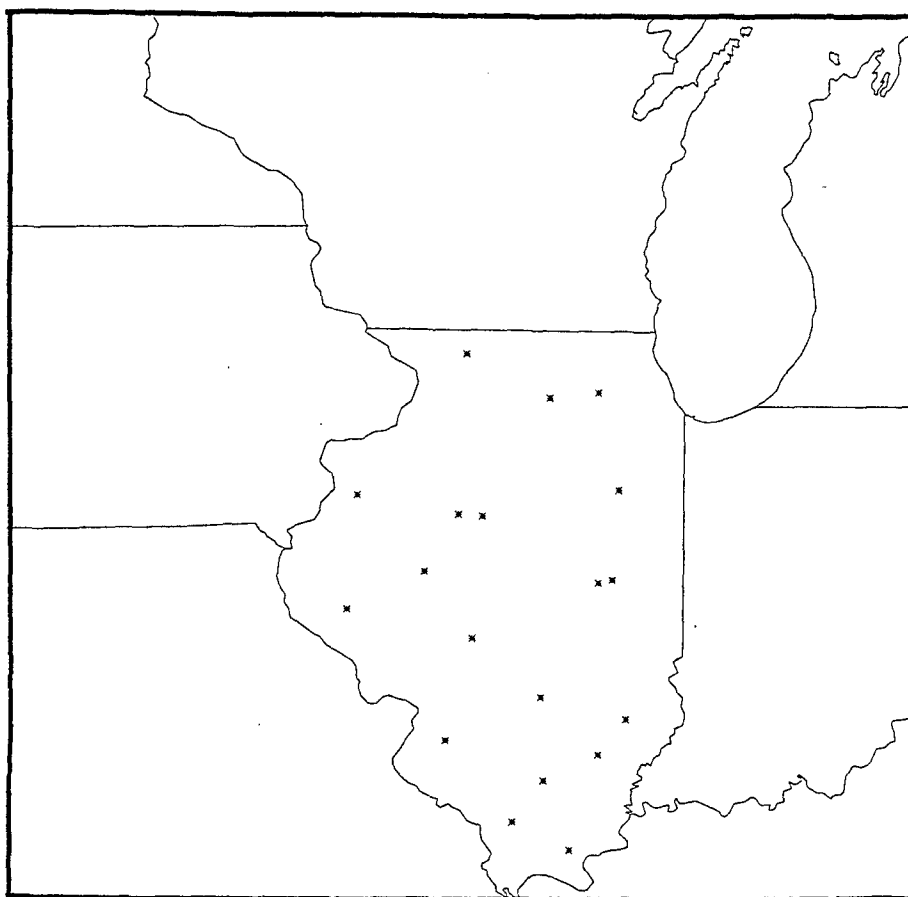


Figure 3.2. Locations of the ICN surface observation stations.

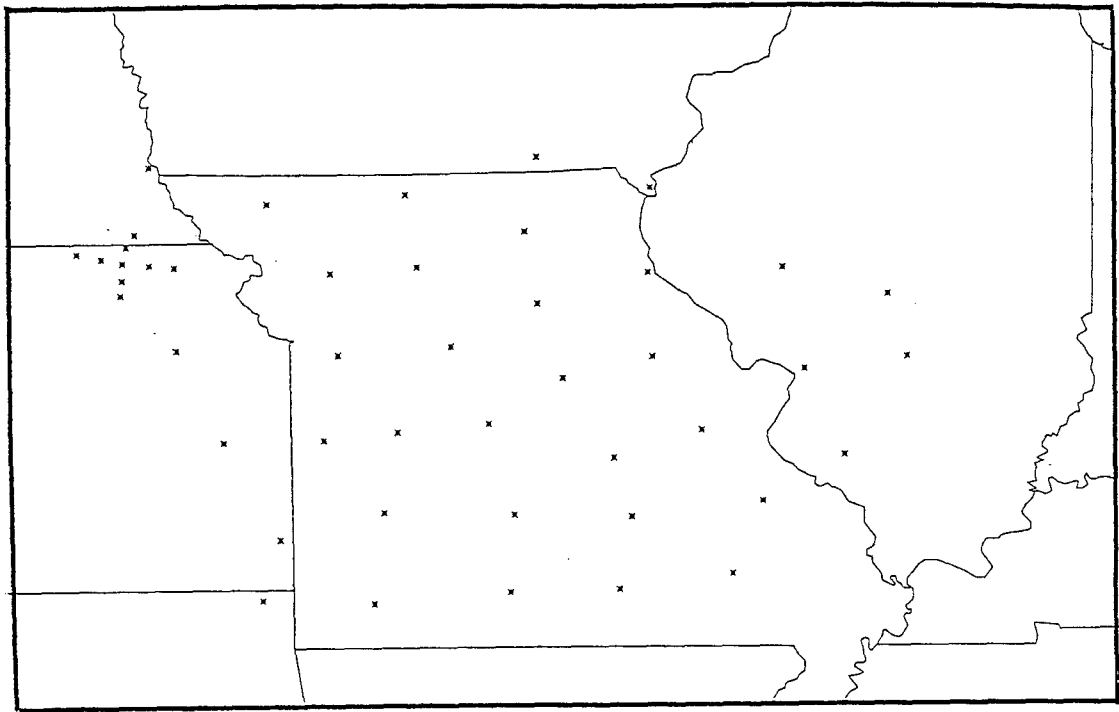


Figure 3.3. Locations of the PAM II surface observation stations during STORM-FEST.

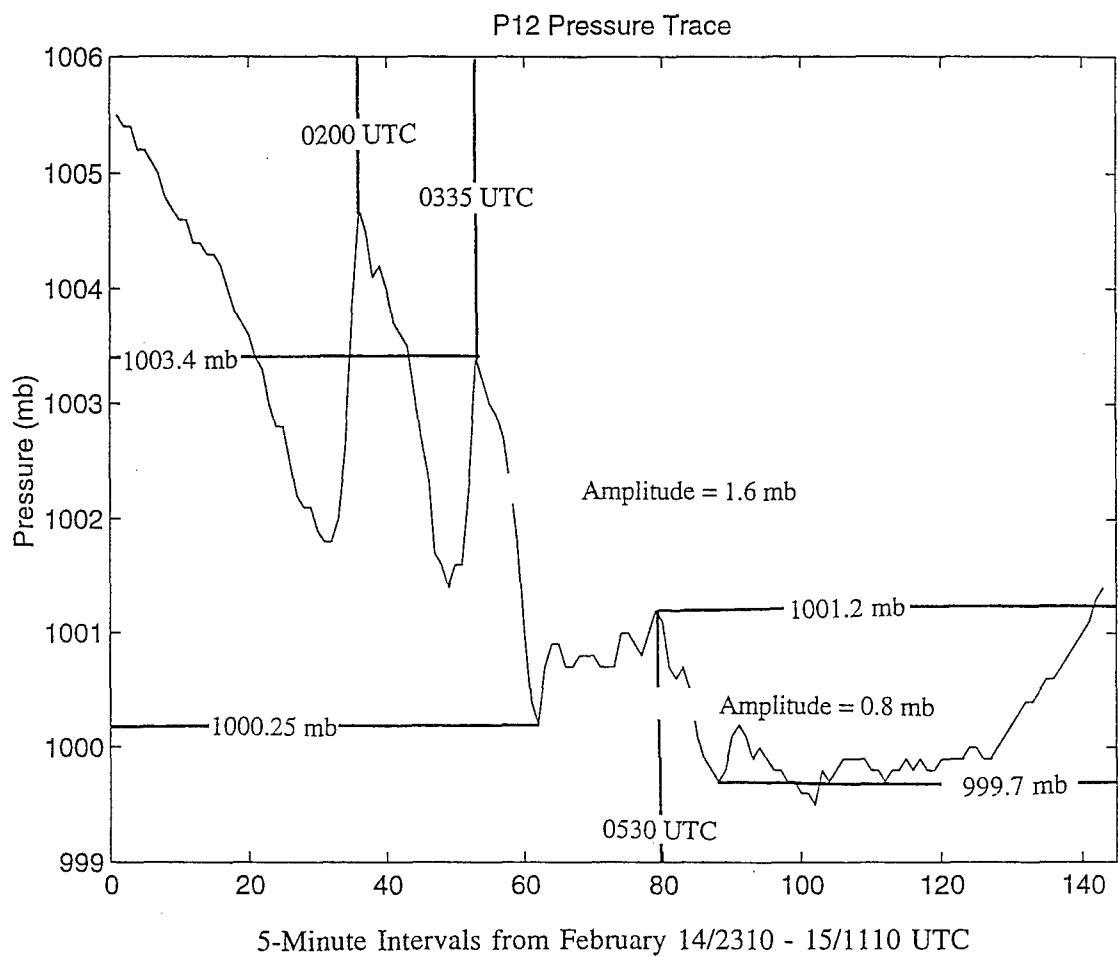


Figure 4.1. Raw pressure trace from station P12 from February 14-15, 1992, illustrating technique for subjective determination of wave peak-to-peak half-amplitudes and periods for a wave train.

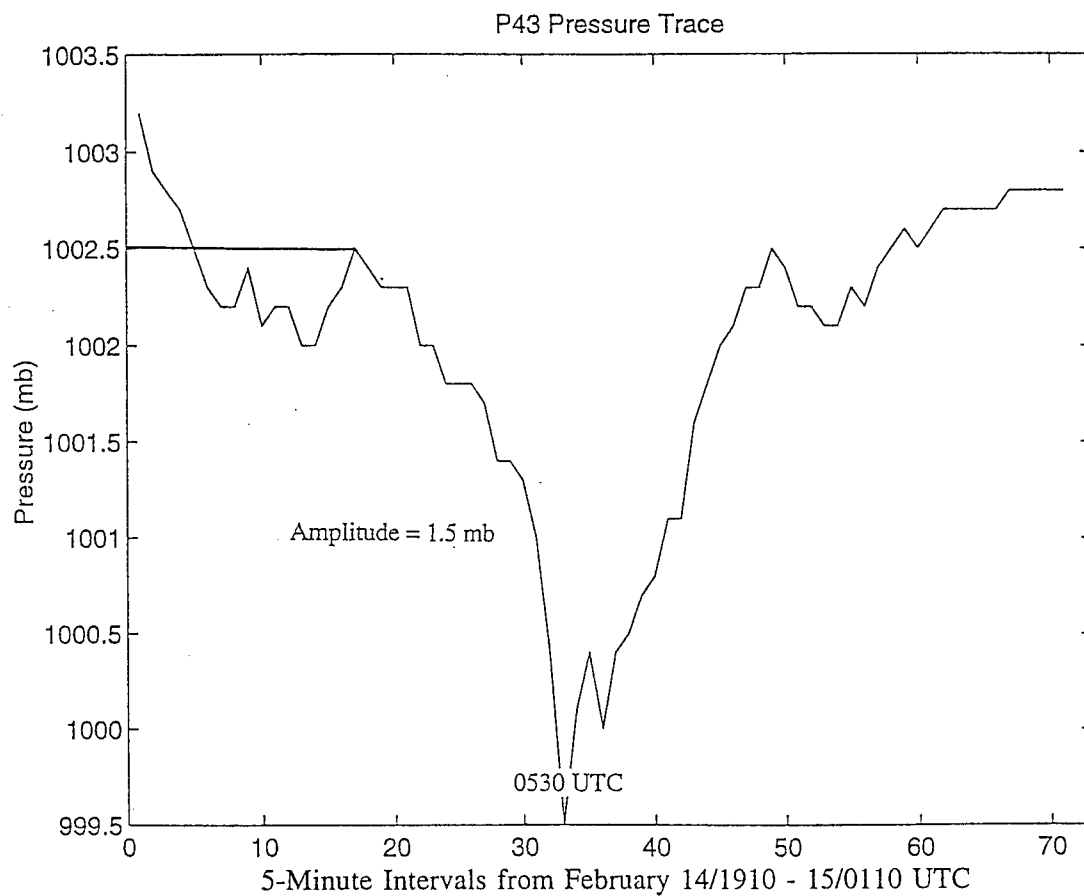


Figure 4.2. As in Fig. 4.1 except station P43 for a singular wave. The spectral analysis for the time beginning at point 19, which corresponds to 2030 UTC, through the end of the trace to 0225 UTC is presented in Fig. 4.3..

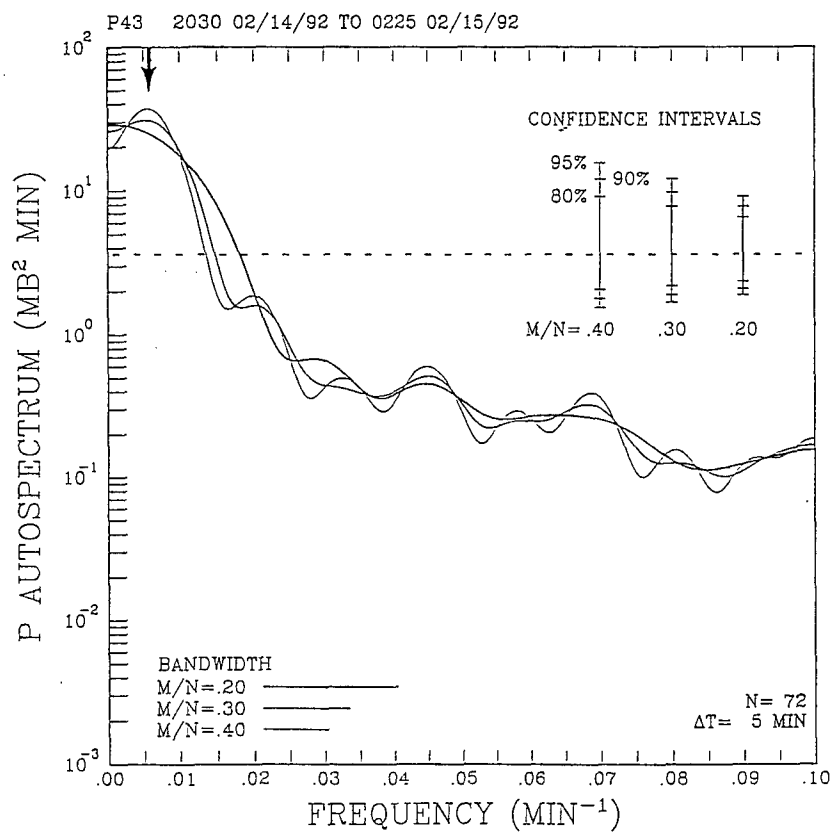


Figure 4.3. Sample autospectrum for station P43 of pressure from the February 14 gravity-wave event ( $M$  = maximum autocorrelation lag,  $N$  = data record length). The 6-hr time series encompasses the perturbation feature evident in Fig. 4.2, beginning at time point 19 which corresponds to 2030 UTC. Confidence intervals are displayed about a horizontal line denoting the expected value of the white noise variance. The arrow points to the significant peak at frequency  $0.006 \text{ min}^{-1}$ .

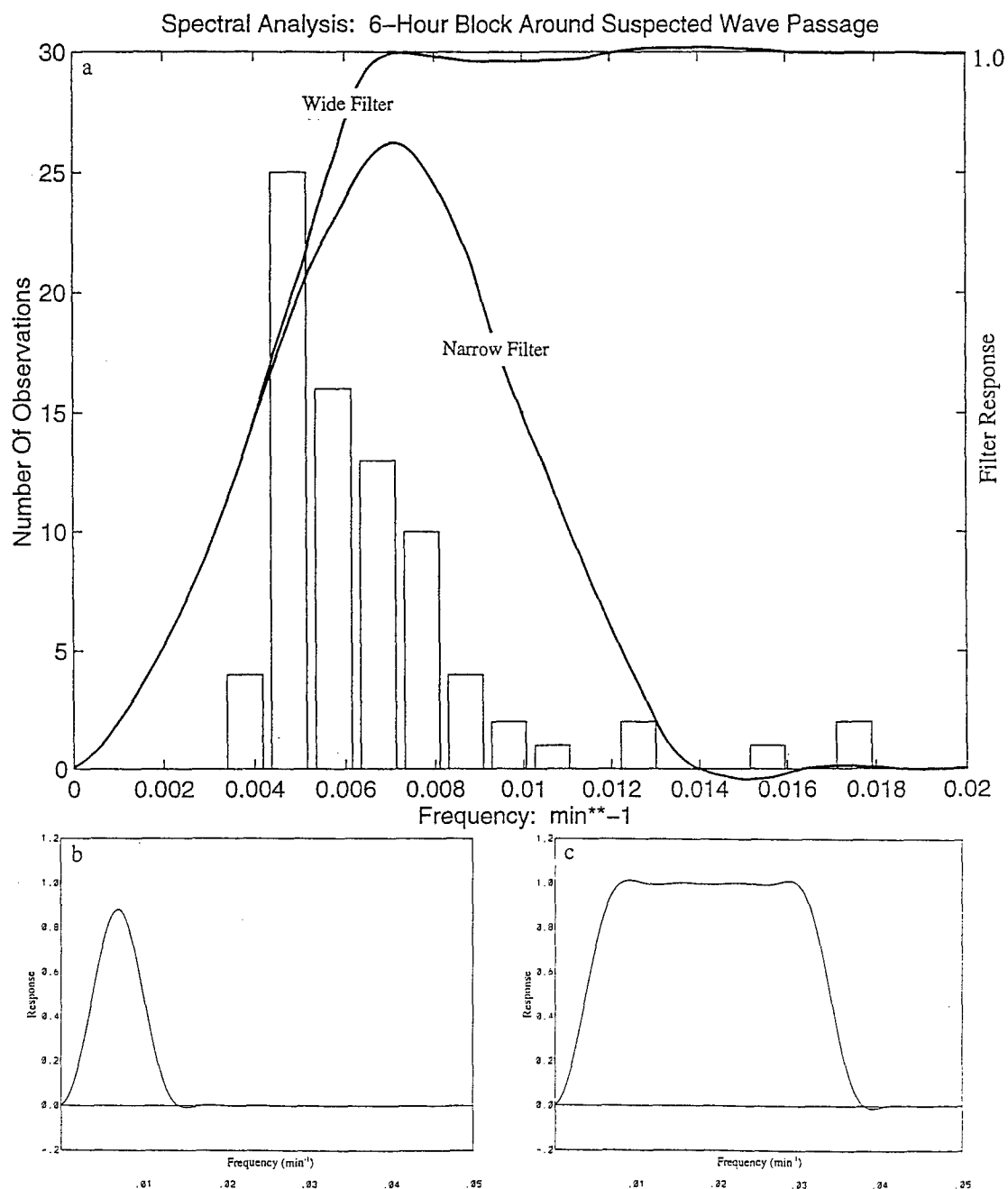


Figure 4.4. Histogram of significant peaks identified from the autospectral analysis for the February 14 gravity-wave event. The wide-filter ( $f_1 = 0.004 \text{ min}^{-1}$ ,  $f_2 = 0.034 \text{ min}^{-1}$ ) and the narrow-filter ( $f_1 = 0.004 \text{ min}^{-1}$ ,  $f_2 = 0.010 \text{ min}^{-1}$ ) responses have been added, (a). The narrow-filter response (b) and wide-filter response (c) are plotted over 1/2 the Nyquist frequency (0.10).

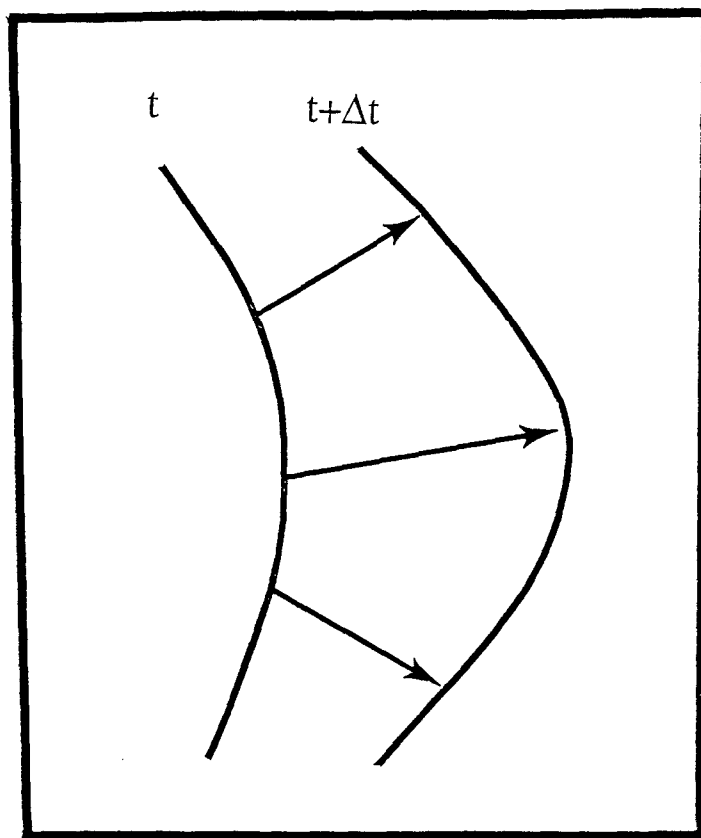


Figure 4.5 Depiction of axis-tracking method used to determine the wave-phase velocity at each individual station. The arrow represents a perpendicular line drawn between consecutive wave isochrones. Such a line is drawn through each station and the direction and length of the line represent the direction and distance traveled by the wave as it passed through the station in one hour. Phase velocity is then determined from the distance traveled.

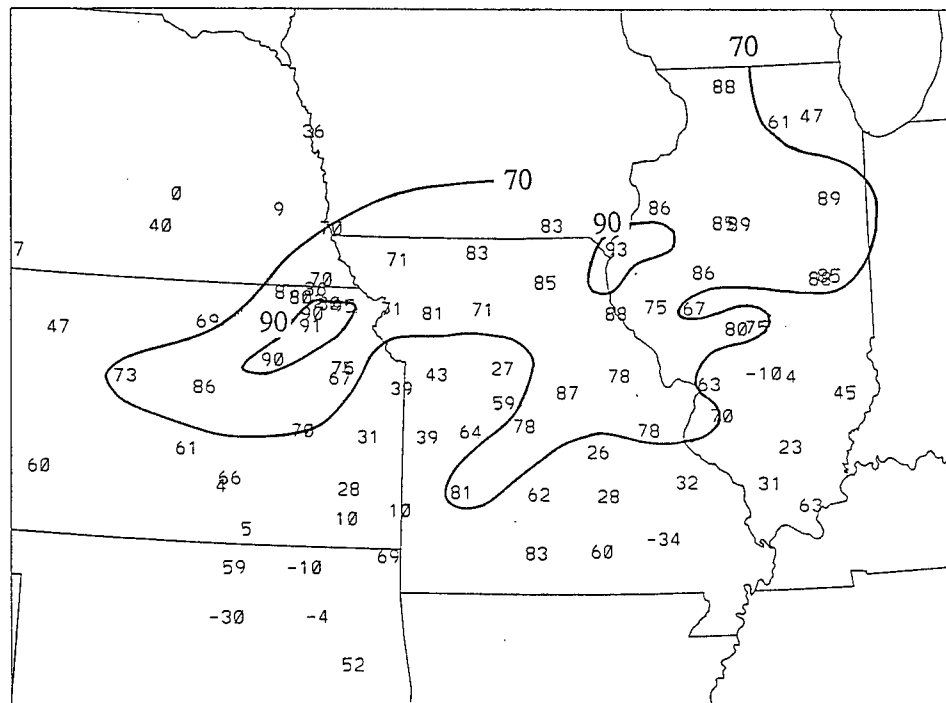


Figure 4.6. Average  $\overline{p'u'}$  correlation values (\*100) determined over the 6-hr period of wave activity at each station for the February 14 gravity-wave event.



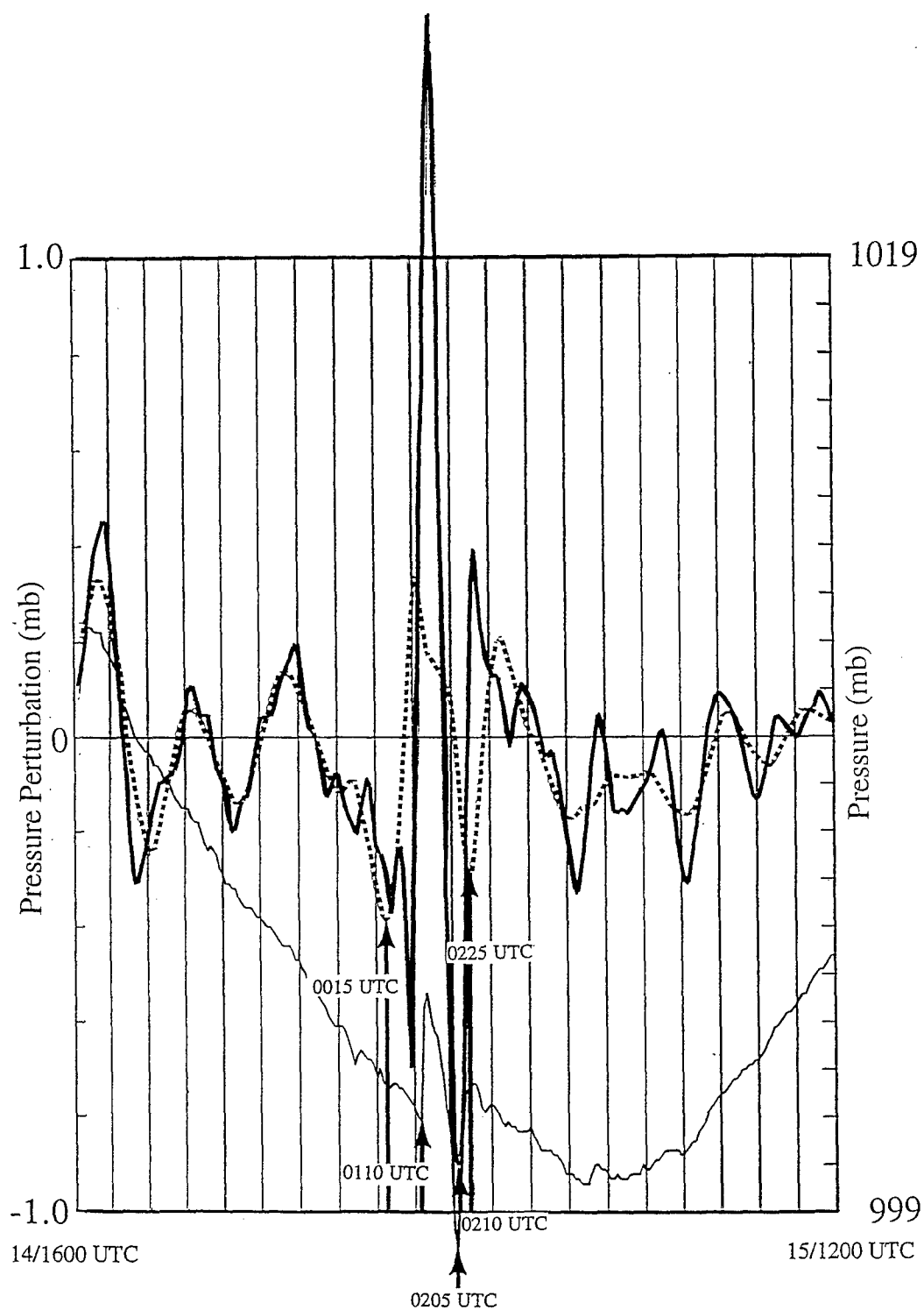


Figure 5.1. Raw (thin line), narrow-filtered (dotted line) and wide-filtered (heavy line) pressure traces from the February 14 gravity-wave event. Each vertical line represents 1 hr. Significant times are highlighted by arrows.

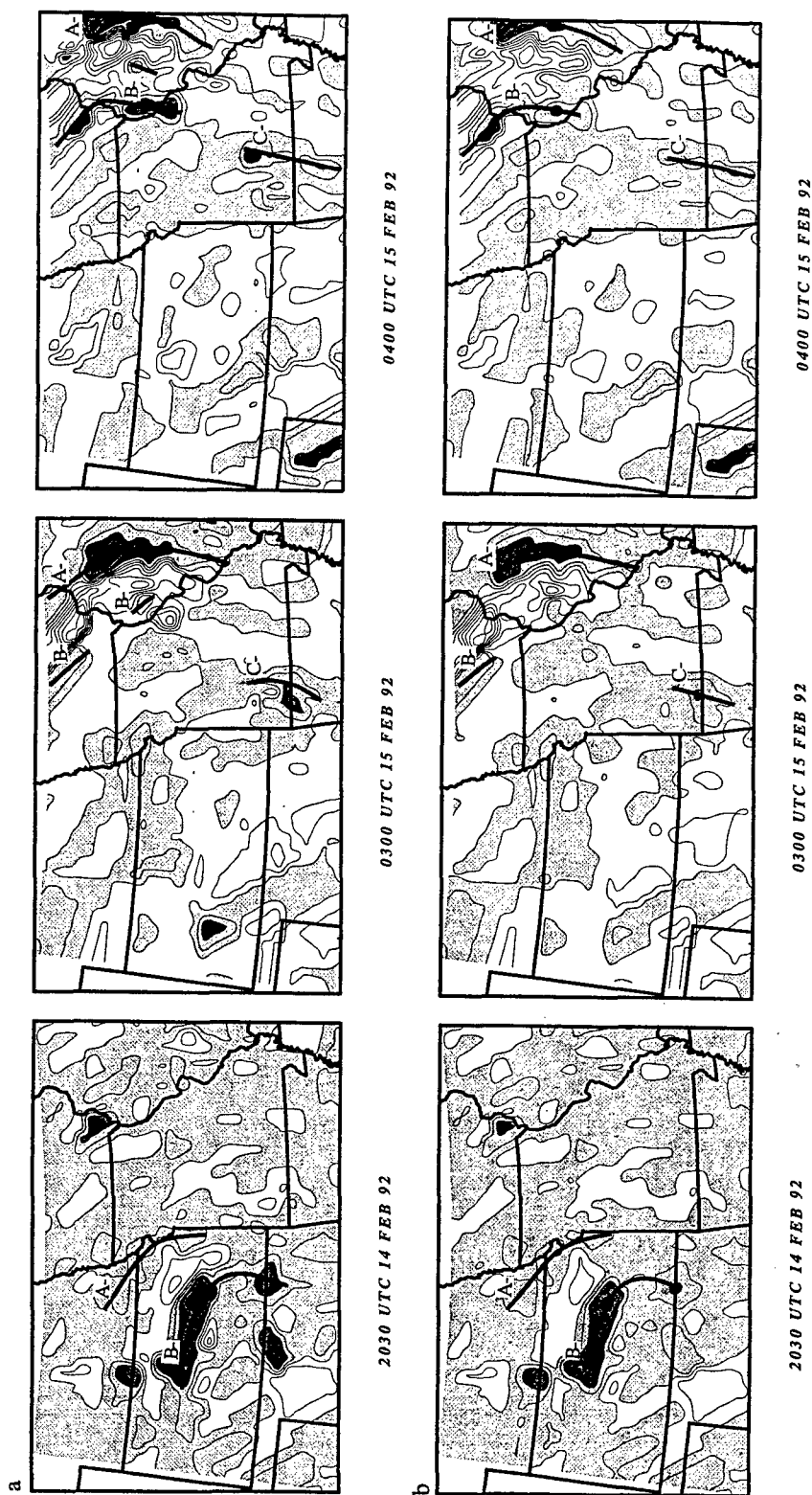


Figure 5.2. Time-to-Space Conversion  $p'$  plots from the February 14 gravity-wave event for Test 1 (effects of filter size). (a) wide filter ( $f_1 = 0.004 \text{ min}^{-1}$ ,  $f_2 = 0.034 \text{ min}^{-1}$ ) results and (b) narrow filter ( $f_1 = 0.004 \text{ min}^{-1}$ ,  $f_2 = 0.010 \text{ min}^{-1}$ ) results. Contouring is every 0.2 mb, with darker shading every 0.4 mb for negative values beginning at 0.0. Thick lines depict isochrones for A-, B- and C-.

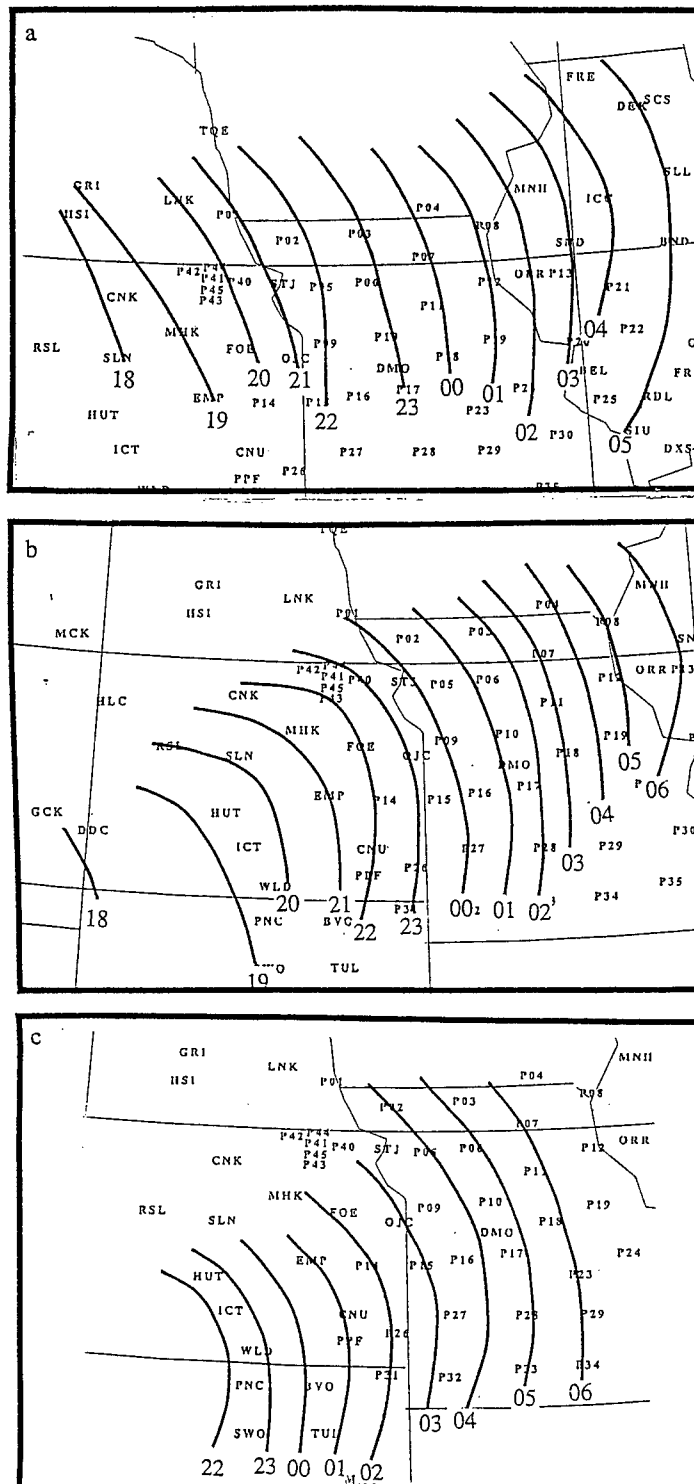


Figure 5.3. Subjectively analyzed wave isochrones from the February 14 gravity-wave event for (a) A-, (b) B- and (c) C-.

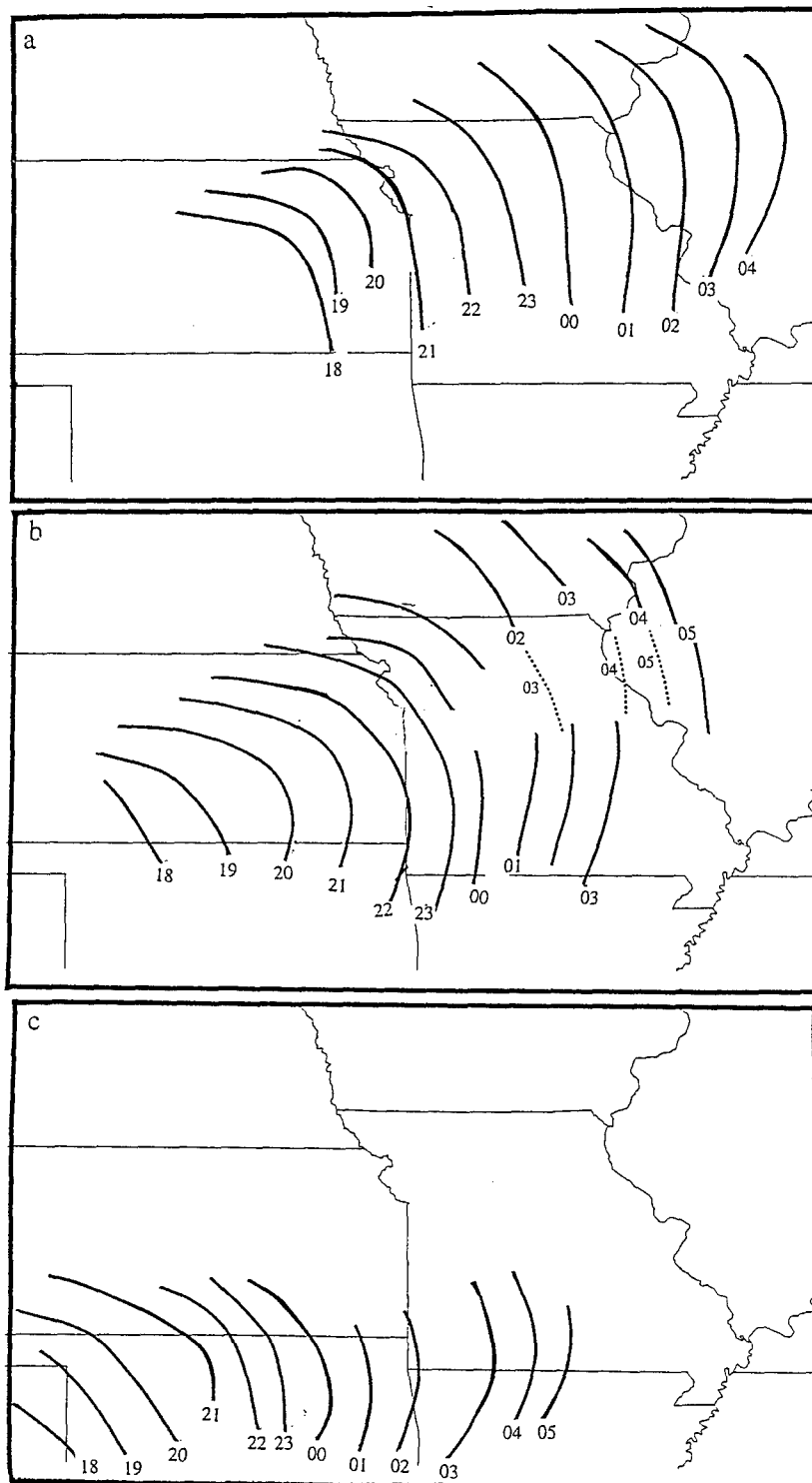


Figure 5.4. Objectively determined wave isochrones from the February 14 gravity-wave event for (a) A-, (b) B-, and (c) C-. Solid lines represent the primary isochrone locations, and the dashed lines in (b) represent coherent wave signatures (B-\*) that developed behind the primary isochrones.

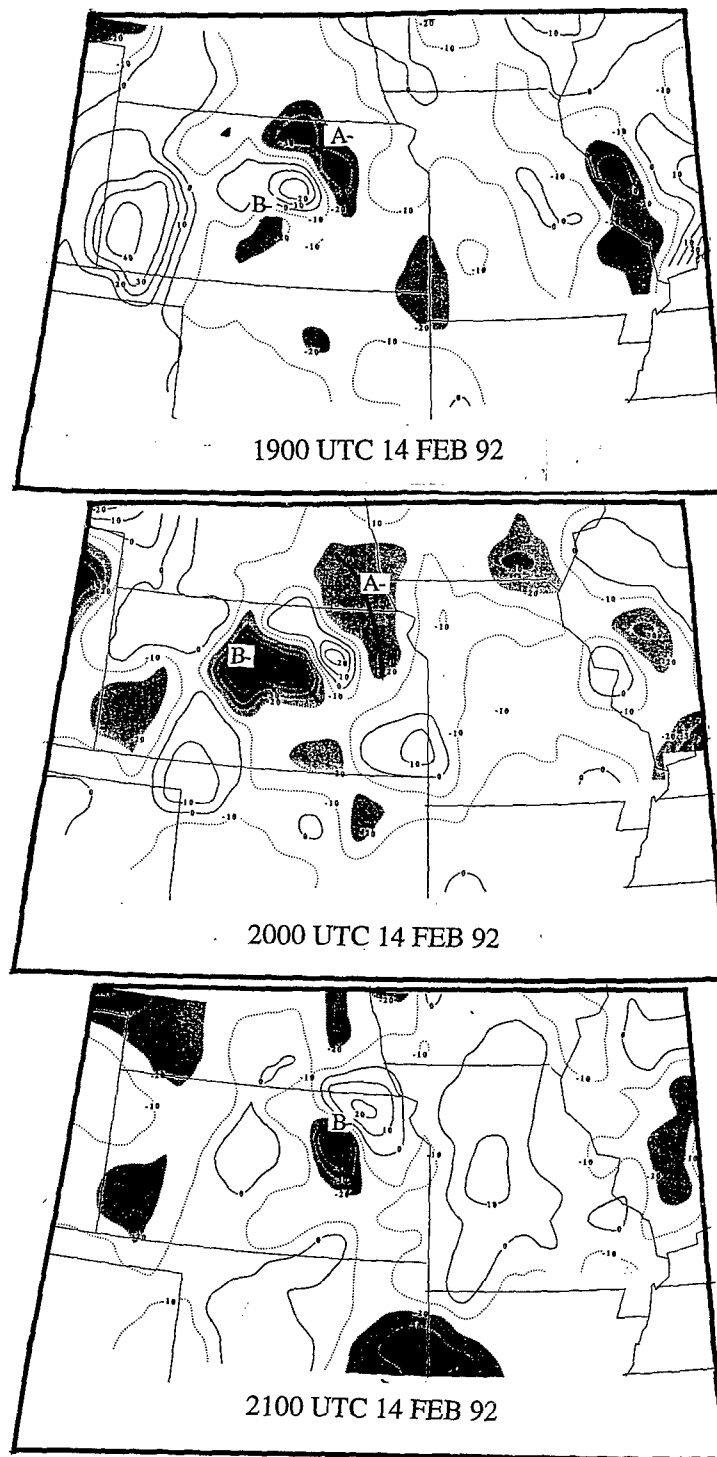


Figure 5.5. Conventional Barnes analysis of the February 14 gravity-wave event. Heavy lines are positive areas while the light lines represent negative areas. Contouring is every 0.1 mb with consecutively darker shading every 0.1 mb, for negative values only, beginning at -0.2 mb. Wave isochrones have been drawn through the negative maxima.

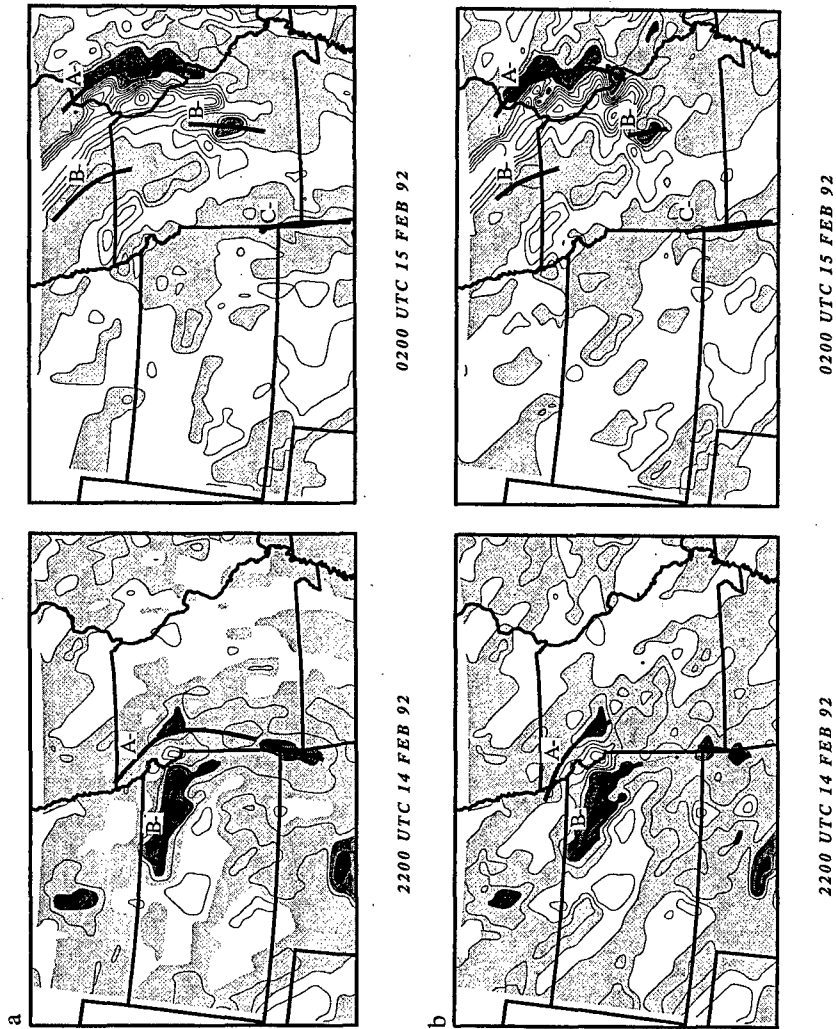


Figure 5.6. Time-to-Space Conversion  $p'$  plots from the February 14 gravity-wave event for Test 4 with (a) multiple advection vectors and (b) a single advection vector, ( $220^\circ$ ,  $15.7 \text{ ms}^{-1}$ ). Contouring is every 0.2 mb, with darker shading every 0.4 mb for negative values beginning at 0.0. Thick lines depict isochrones for A-, B- and C-.

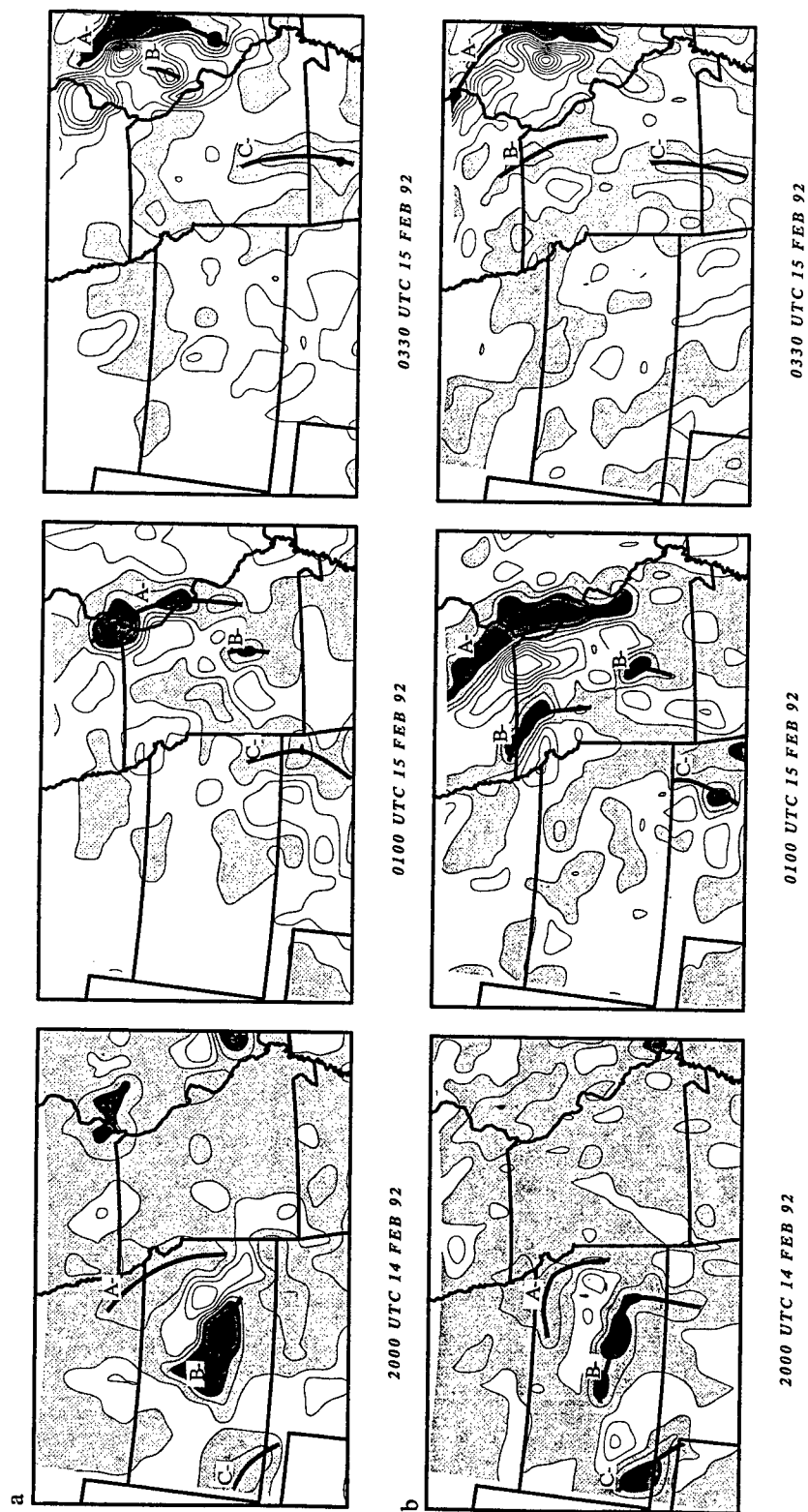


Figure 5.7. As in Fig. 5.6, except for Test 2 (effects of different sized tau). (a)  $\tau = 15$  min and, (b)  $\tau = 50$  min.

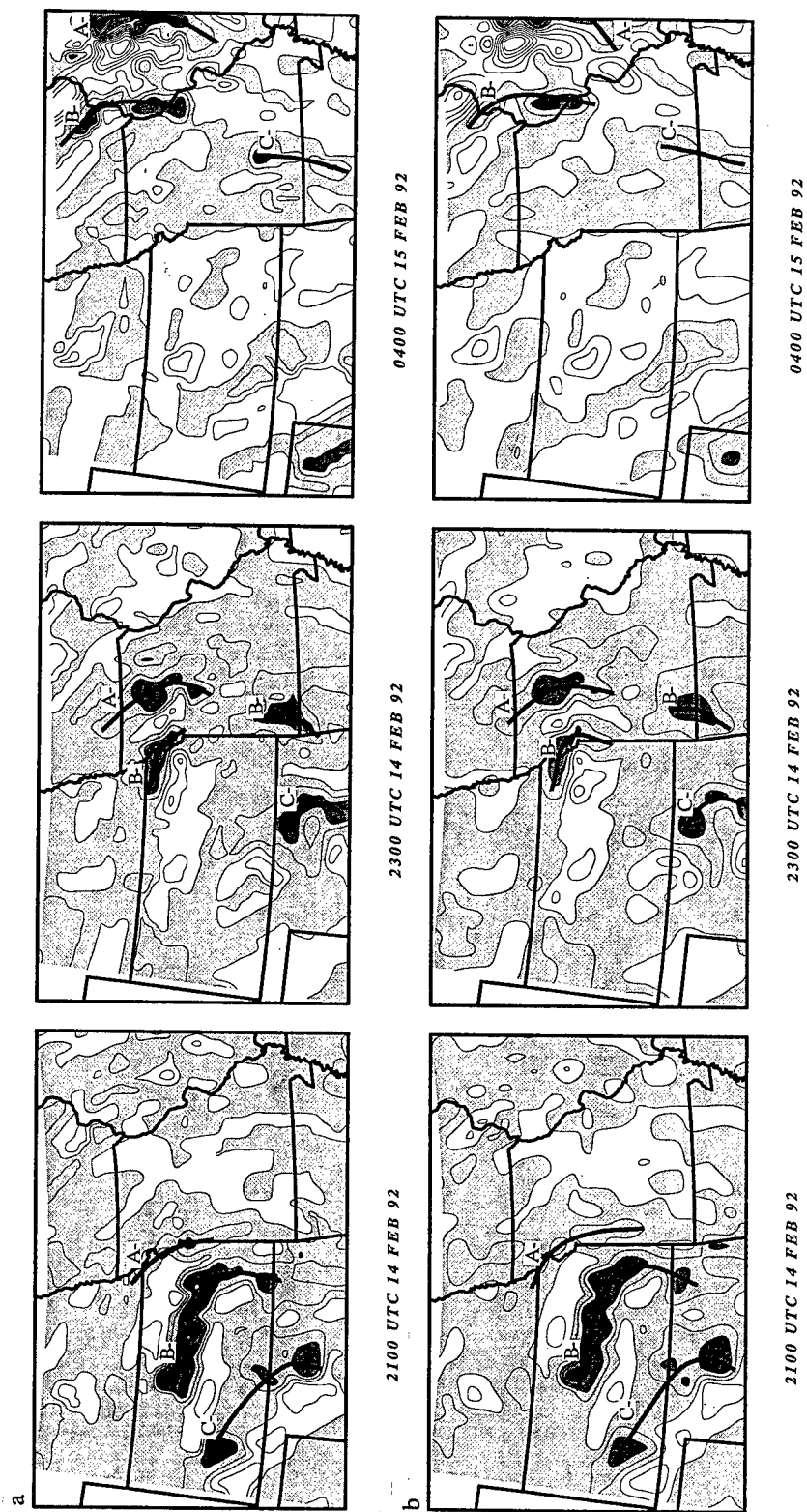


Figure 5.8. As in Fig. 5.6, except for Test 3 (effects of different sized grid-length). (a) grid-length of 25 km, and (b) grid-length of 40 km.



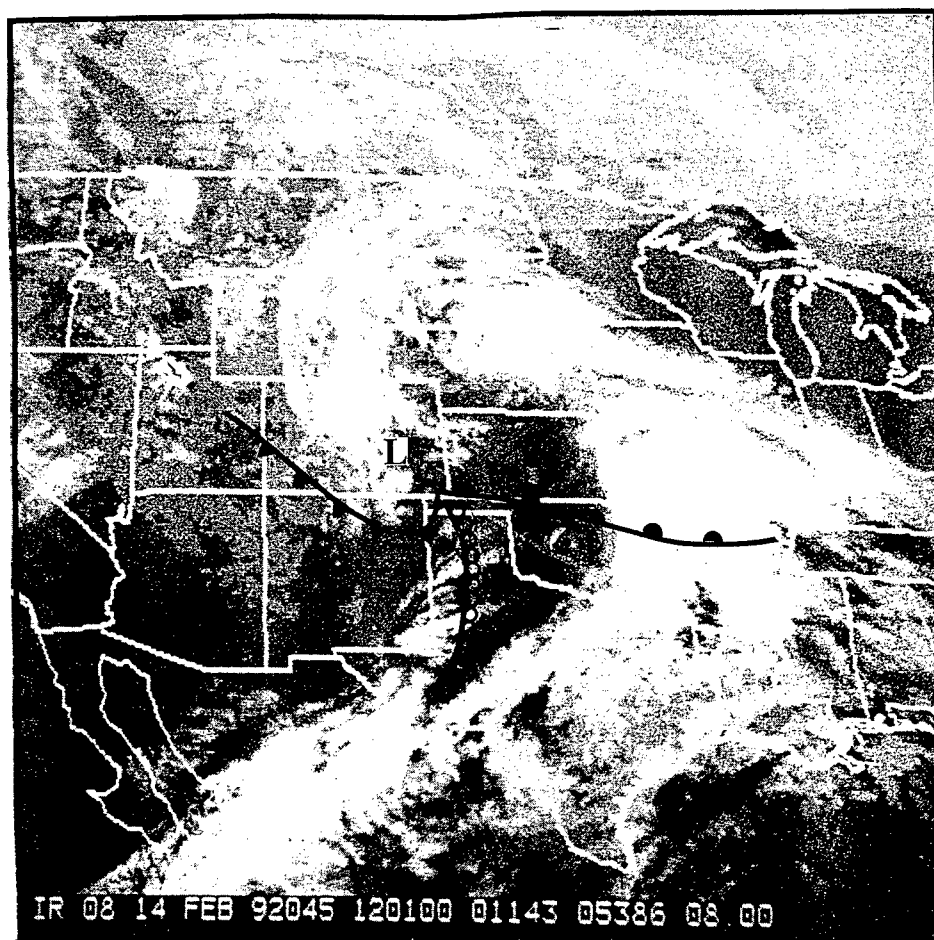


Figure 6.1. Infrared satellite imagery valid 1201 UTC 14 February with surface features, including the surface low pressure center (L), warm front, cold front and dryline.

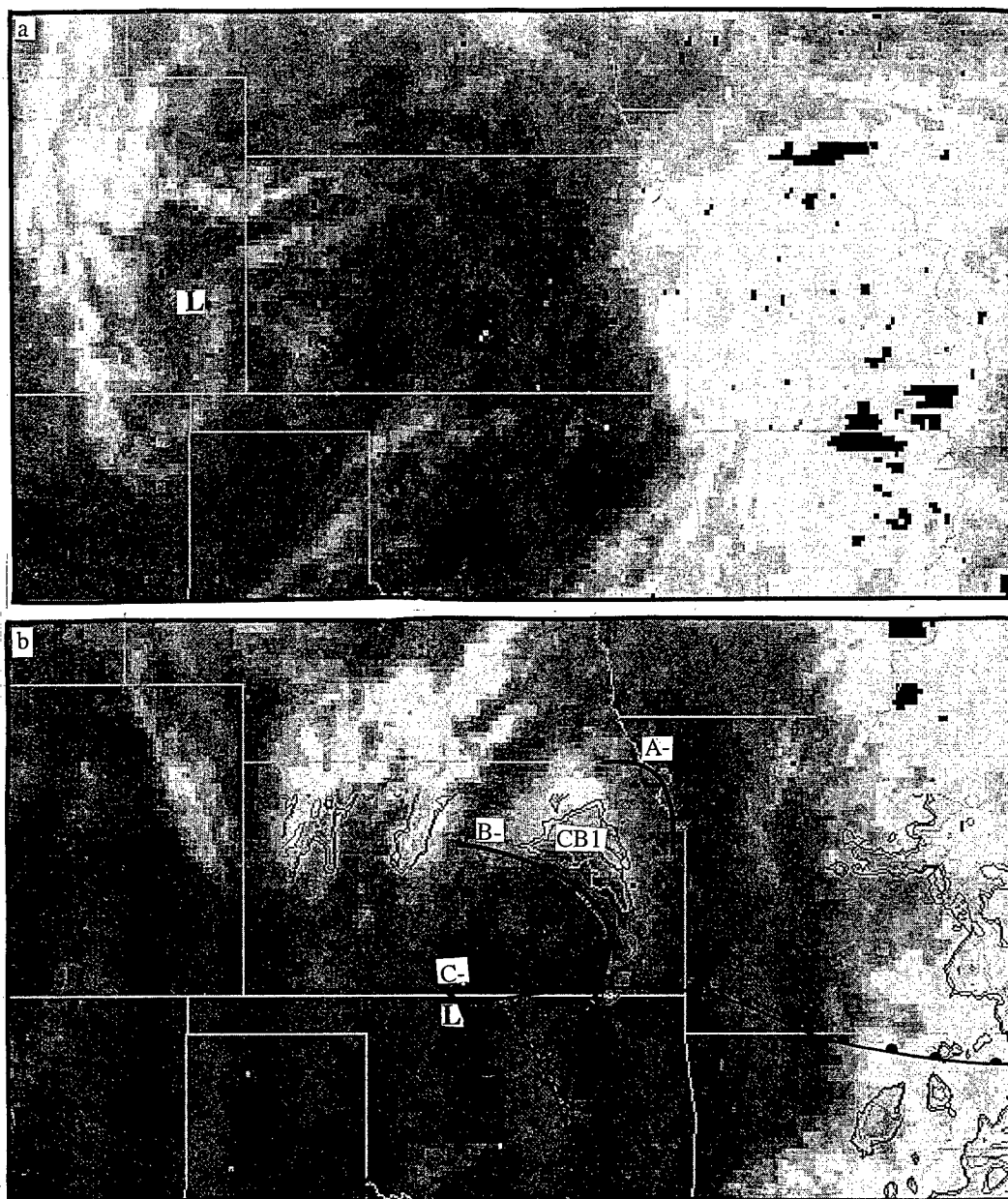


Figure 6.2. Infrared satellite imagery valid (a) 1332 UTC 14 February. The locations of the surface low pressure center (L) and cloudband 1, pointed out by the arrow, are indicated. Satellite and radar imagery valid (b) 2032 UTC with black lines indicating the locations of the A-, B- and C- isochrones and CB1 indicating the location of cloudband 1. Surface frontal features have also been added.



Figure 6.3. Radar imagery valid a) 2102 UTC with frontal features added, b) 2132 UTC, c) 2202 UTC and d) 2232 UTC 14 February. Black lines indicate the locations of the A-, B- and C- isochrones.

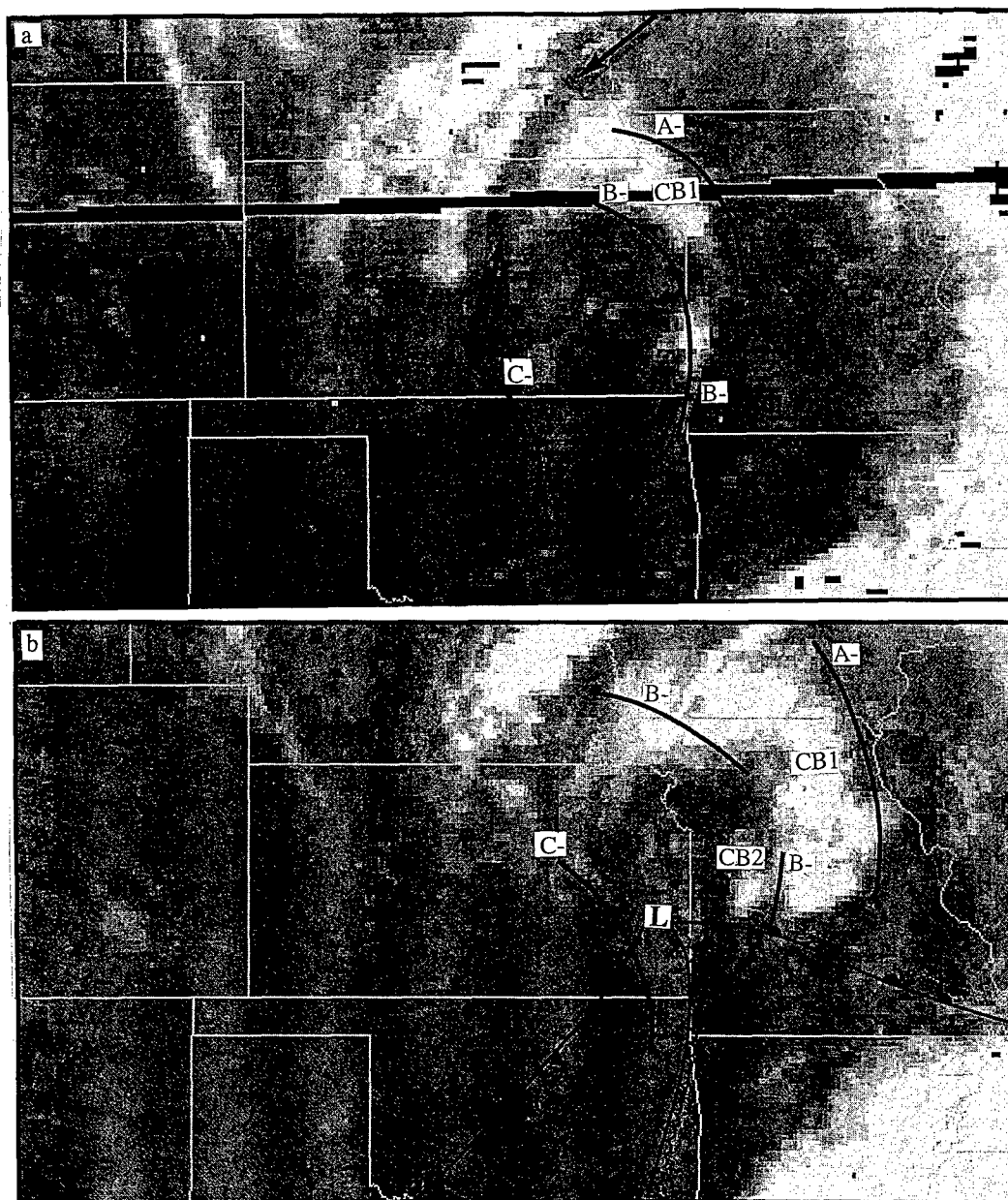


Figure 6.4. Infrared satellite imagery valid (a) 2202 UTC February 14, with the arrows pointing to an area free of mid- and upper-level clouds between the cloudband and the clouds wrapping around the low pressure center; (b) 0032 February 15. The black lines represent waves A-, B- and C- and cloudbands 1 and 2 have been labeled CB1 and CB2. Surface frontal features have also been added.

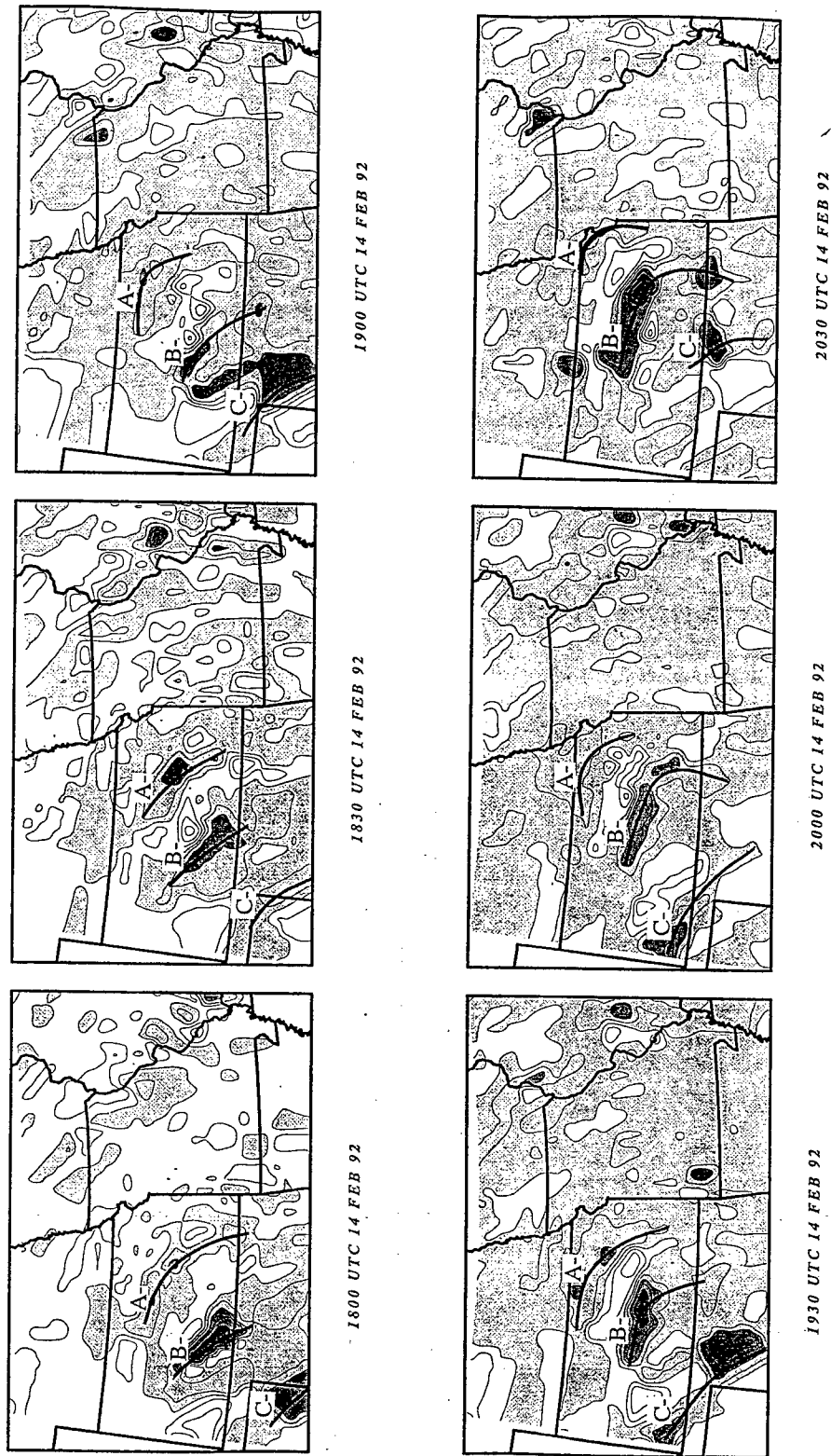
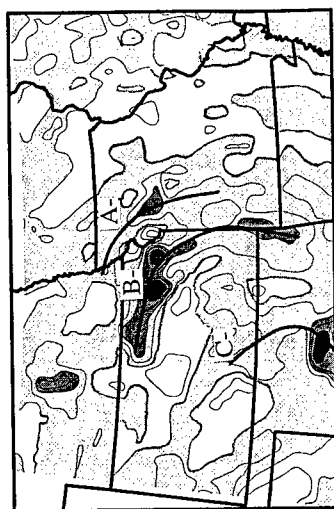
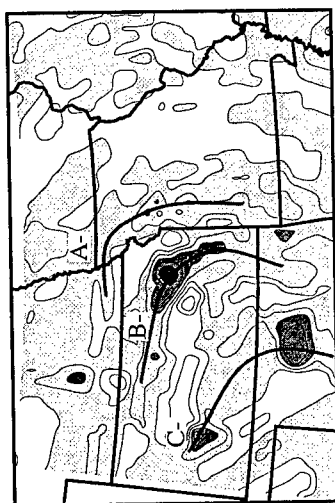


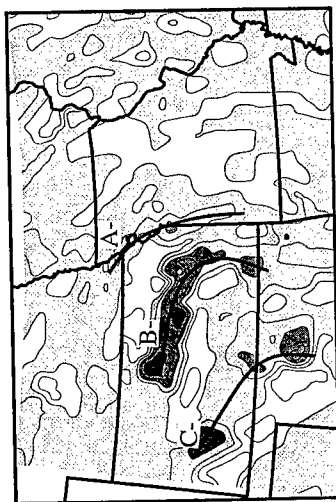
Figure 6.5. Time-to-Space Conversion output for wide-filter ( $f_1 = 0.004 \text{ min}^{-1}$ ,  $f_2 = 0.034 \text{ min}^{-1}$ ) banded pressure data with a grid-length value of 25 km and a tau value of 50 min. Plots begin at 1800 UTC 14 February and continue every half hour through 0530 UTC 15 February. Contouring is every 0.2 mb, with darker shading every 0.4 mb for negative values beginning at 0.0. The wave (A-, B-, B-\* and C-) isochrones are indicated by a black line.



2100 UTC 14 FEB 92



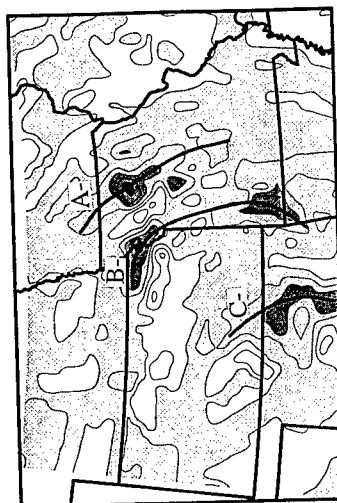
2130 UTC 14 FEB 92



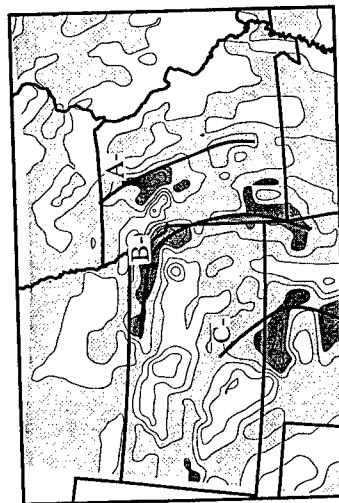
2200 UTC 14 FEB 92



2230 UTC 14 FEB 92



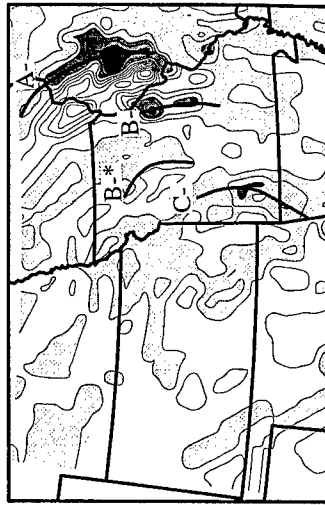
2300 UTC 14 FEB 92



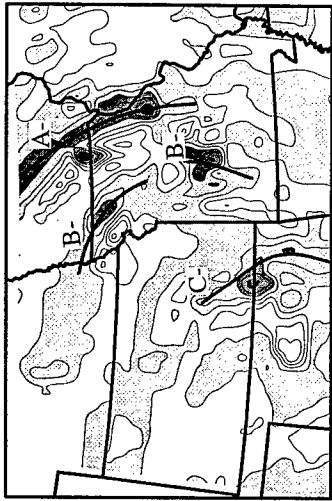
2330 UTC 14 FEB 92



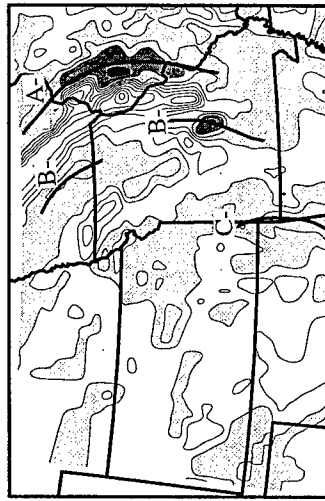
0100 UTC 15 FEB 92



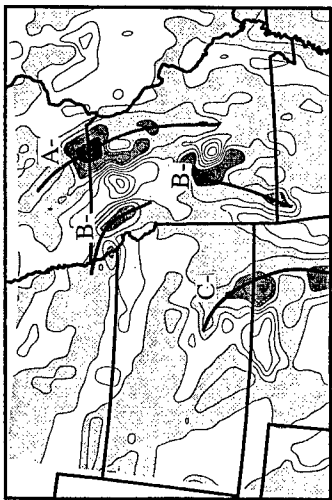
0230 UTC 15 FEB 92



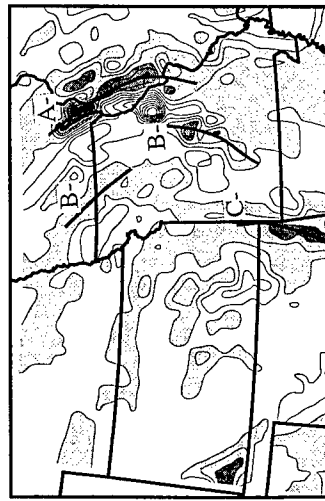
0030 UTC 15 FEB 92



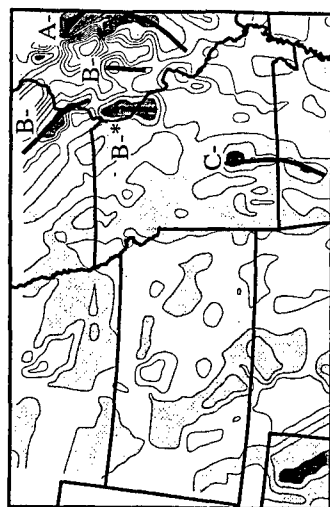
0200 UTC 15 FEB 92



0000 UTC 15 FEB 92



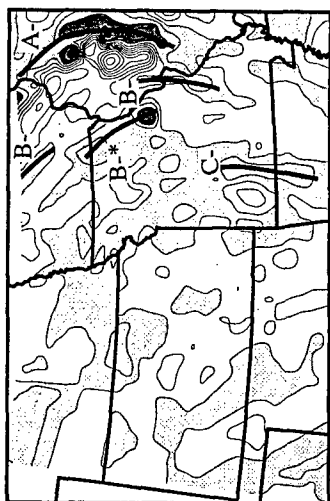
0130 UTC 15 FEB 92



0400 UTC 15 FEB 92



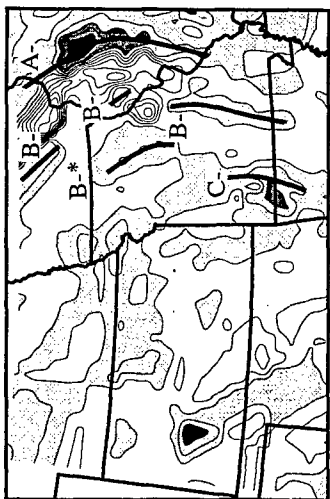
0530 UTC 15 FEB 92



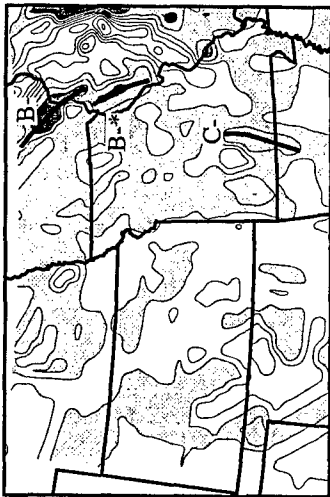
0330 UTC 15 FEB 92



0500 UTC 15 FEB 92



0300 UTC 15 FEB 92



0430 UTC 15 FEB 92



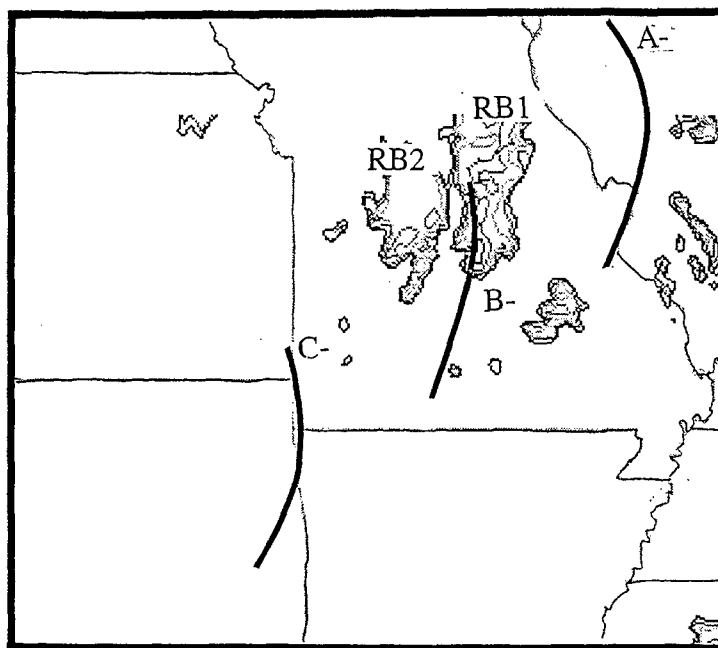


Figure 6.6. Radar imagery valid 0202 UTC 14 February. The black line denotes the location of the B- isochrone.

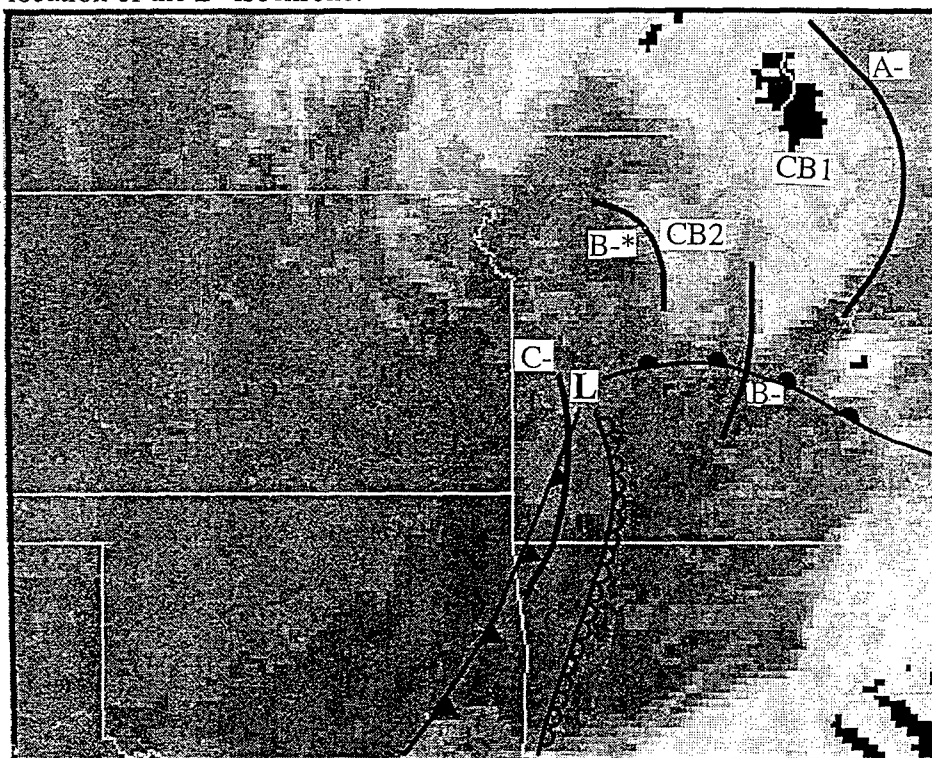


Figure 6.7. Infrared satellite imagery valid 0232 UTC 15 February. Black lines indicate the locations of the A-, B- and B-\* isochrones. The surface low pressure center and frontal features have been added.

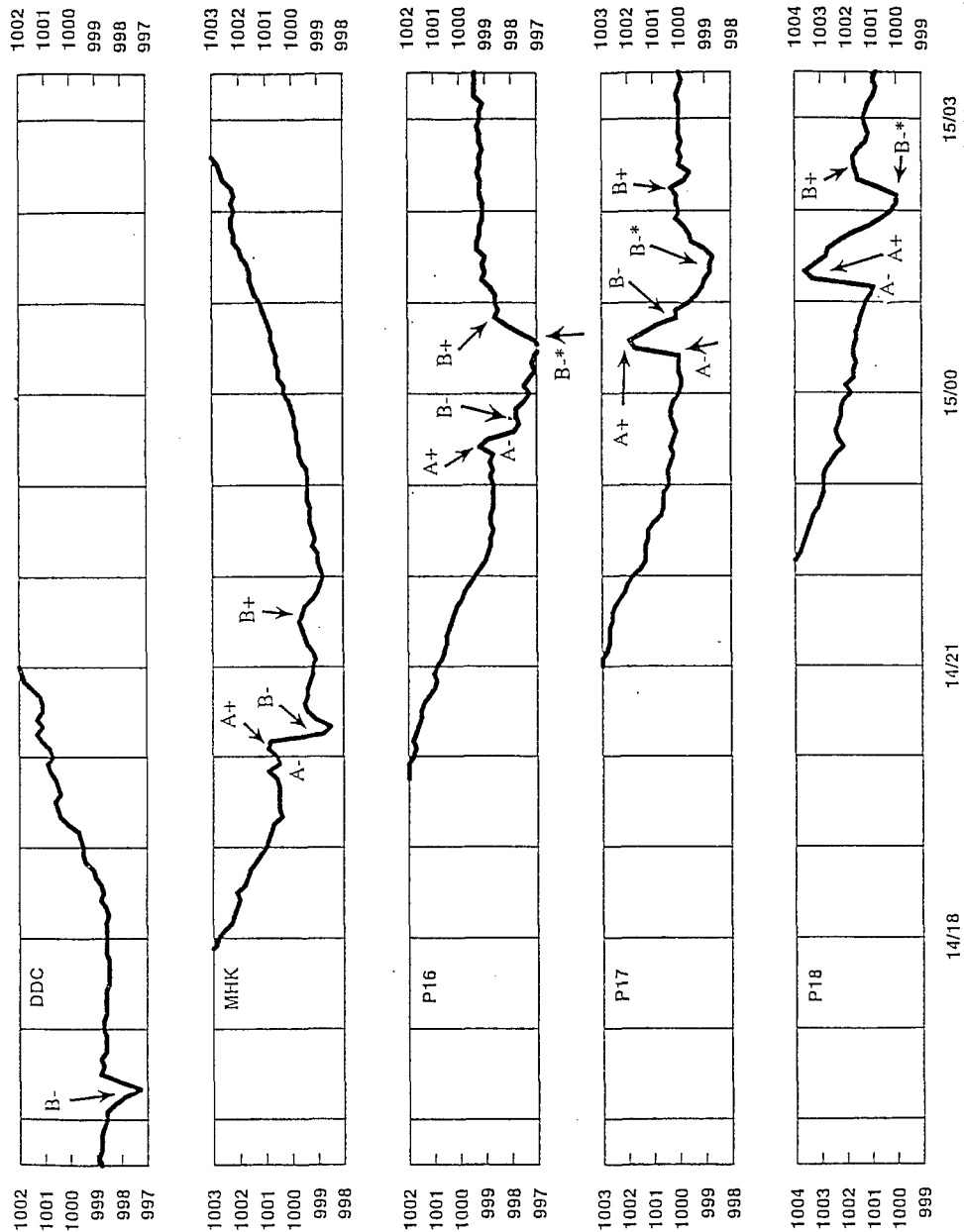


Figure 6.8. Raw pressure traces from the February 14 gravity-wave event for stations DDC, MHK, P16, P17 and P18. Pressure in mb is along the vertical axis while time (day/hour) is displayed along the horizontal axis. The pressure trace for DDC represents a wave of depression, MHK represents a wavelet (A- to A+) and P17 represents a wave train (Koch and O'Handley 1996).

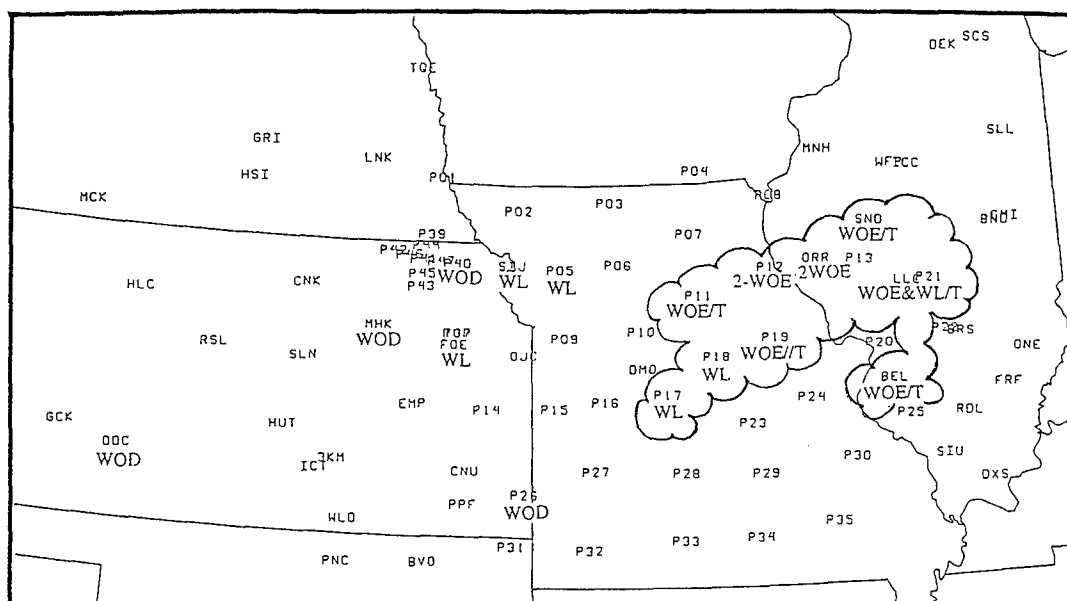


Figure 6.9. Wave types (wave of depression (WOD), wave of elevation (WOE), wavelet (WL) and train (T)) as seen in the raw pressure traces from selected locations for February 14 and 15. Those from the 15th have been scalloped. The “/” indicates that the wave type before the symbol was within the wave type after the symbol.

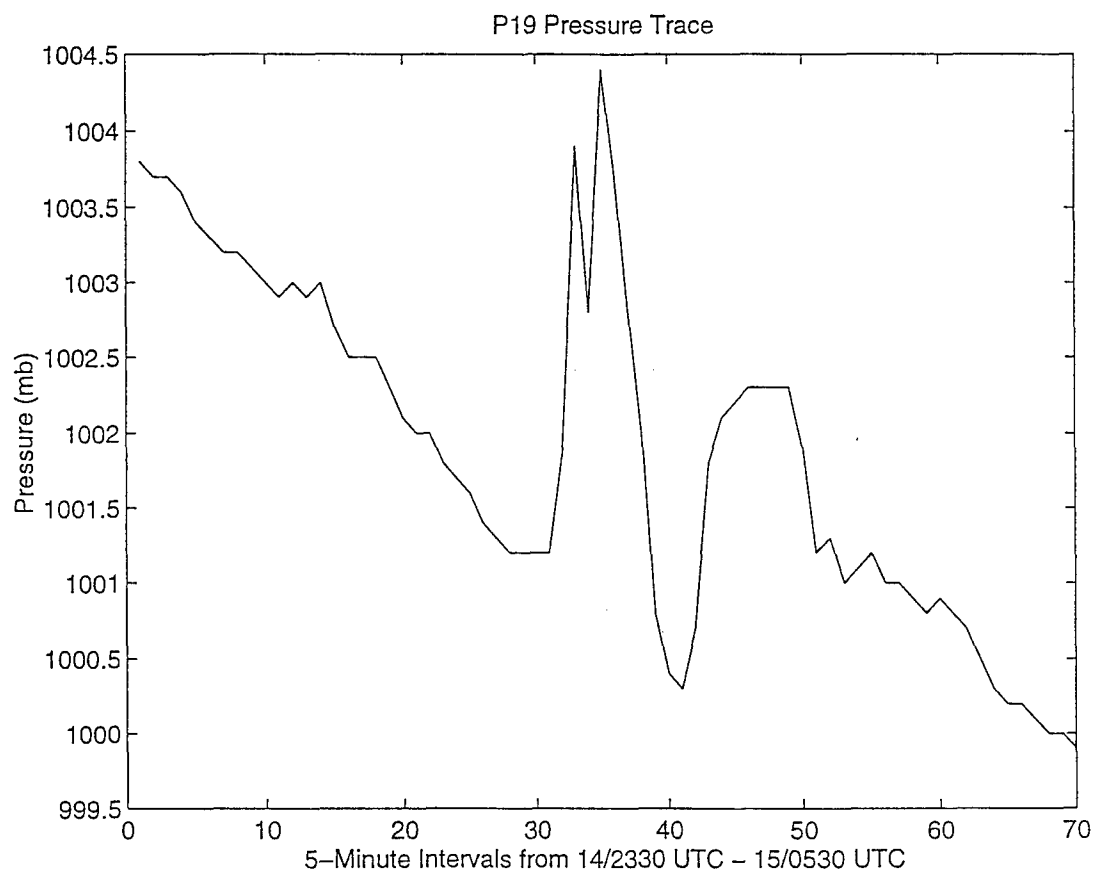


Figure 6.10. Raw pressure trace from station P19 showing a strong wave of elevation within a train.

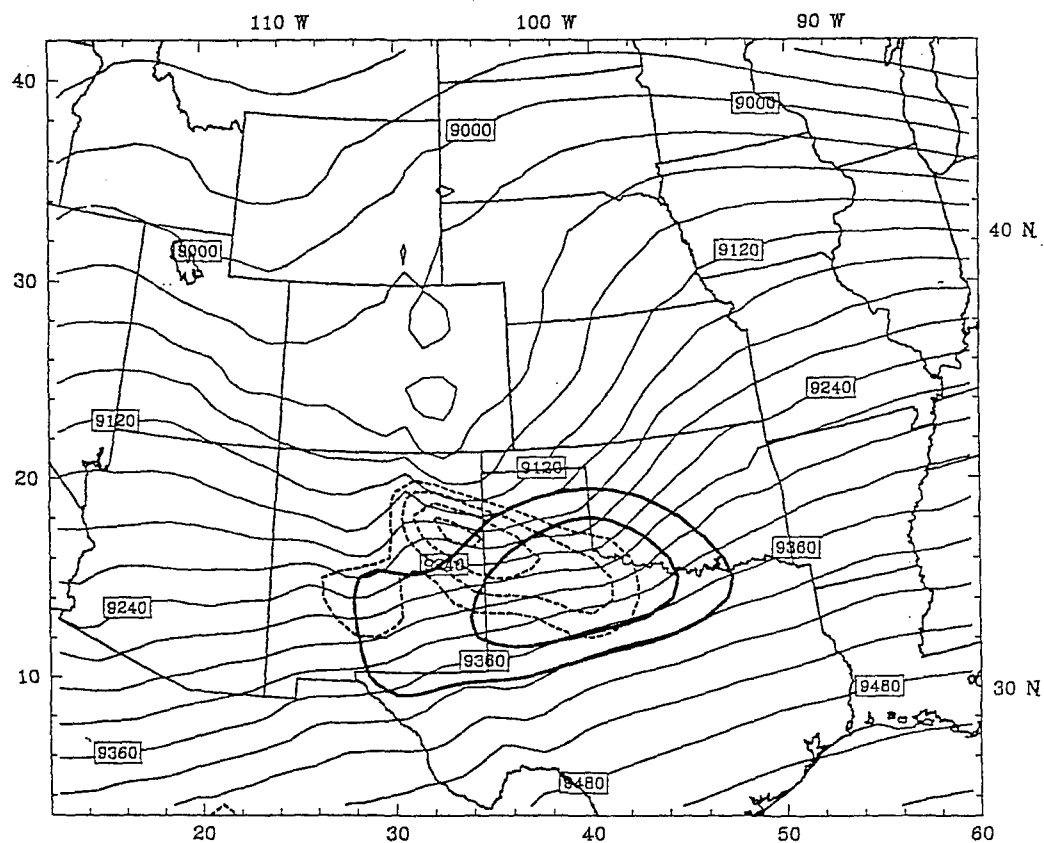


Figure 6.11. MM4 model 24-hr forecast of 300 mb heights (thin black lines), isotachs  $\geq 50 \text{ ms}^{-1}$ , contour interval = 5 (heavy black lines) and geostrophic winds  $\geq 58 \text{ ms}^{-1}$ , contour interval = 5 (dashed lines) valid 1200 UTC 14 February.

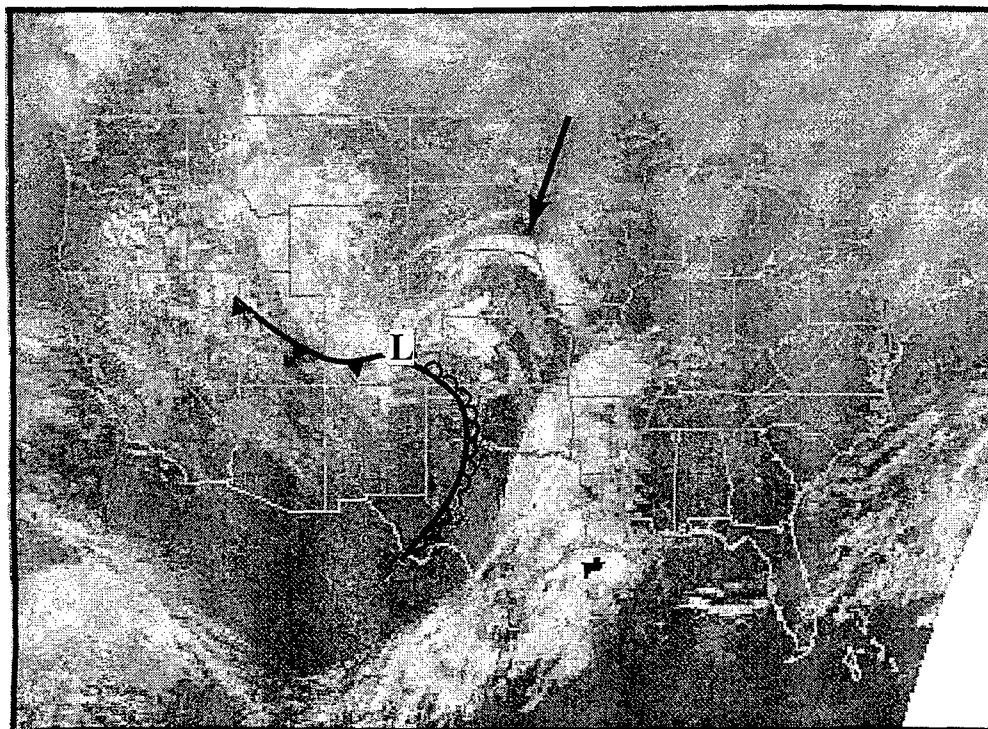


Figure 6.12. Infrared satellite imagery valid 0002 UTC 17 February with surface features, including the surface low pressure center (L), cold front and dryline. The black arrow is pointing to the initial cloudband (not analyzed).

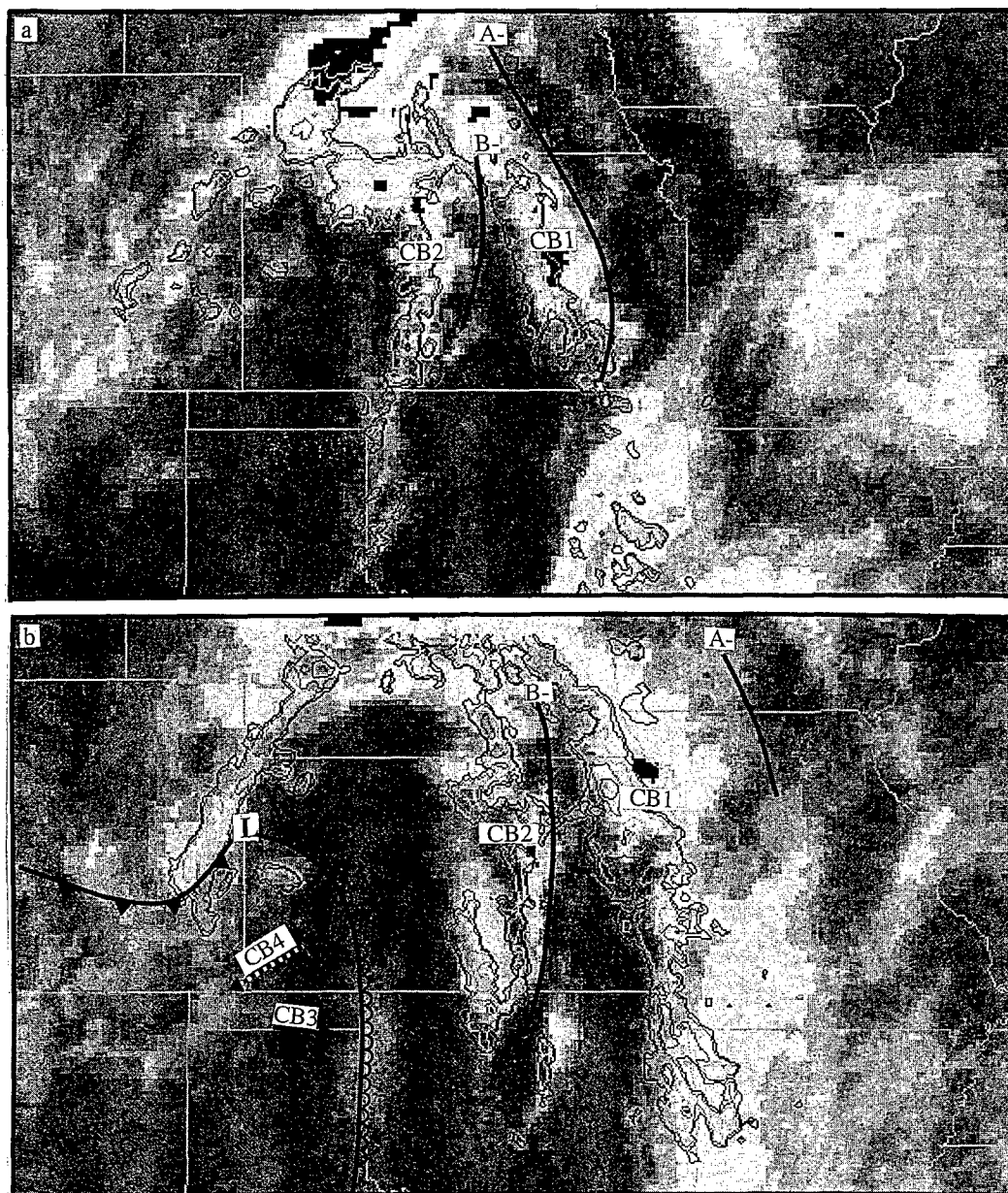


Figure 6.13. Radar and infrared satellite imagery valid (a) 0202 UTC with surface frontal feature and (b) 0502 UTC 17 February. The black line indicates the locations of waves A- and B-. Cloudband 1 (CB1) and 2 (CB2) are labeled. The dashed arrow identifies the band that spun off of the low that appeared to be associated with the development cloudband 4 (CB4). The black arrow identifies the cloudy region that later became the northern part of cloudband 3 (CB3).

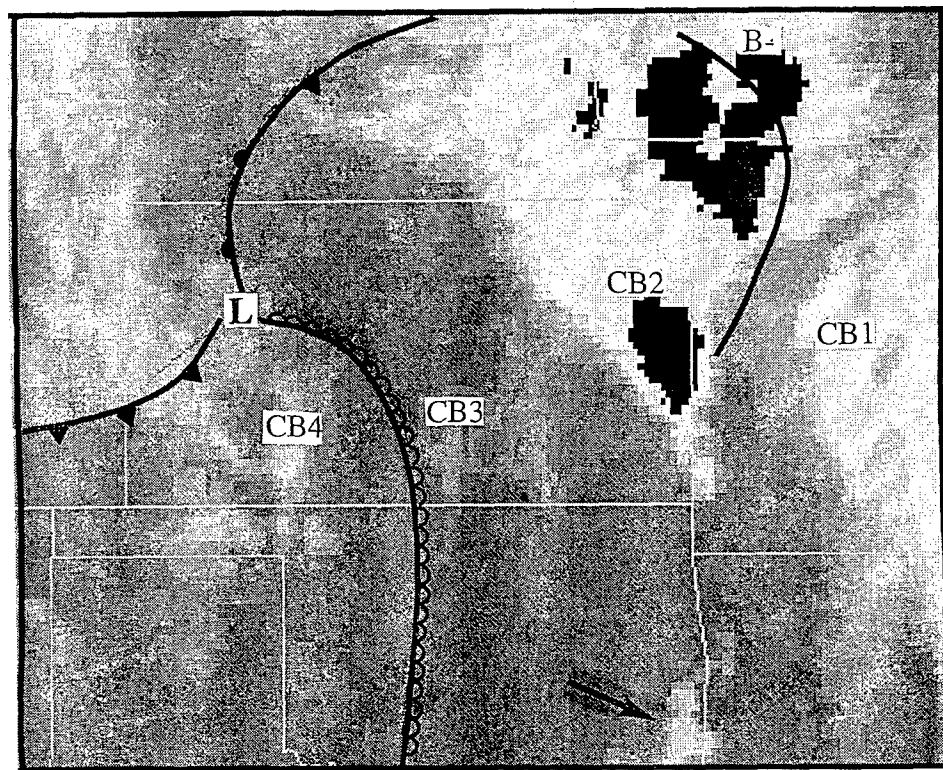


Figure 6.14. Radar and infrared satellite imagery valid 1002 UTC 17 February. The black line indicates the location of the B- isochrone. Rainband 1 (RB1) and rainband 2 (RB2) are labeled. The black arrow identifies the southern extension of CB2. The surface low pressure center and frontal features have been added.

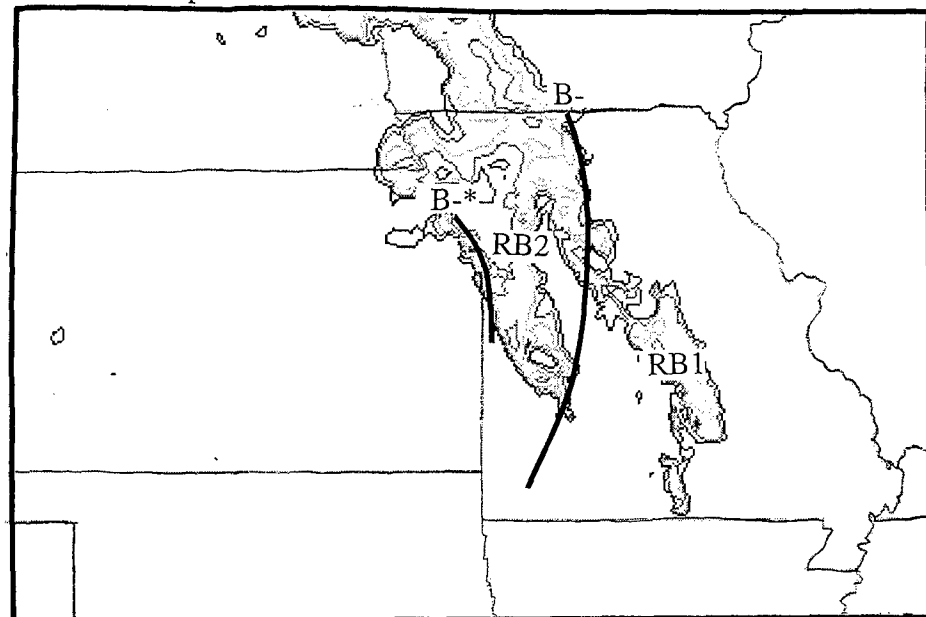


Figure 6.15. Radar imagery valid 1202 UTC 17 February. The black lines indicates the locations of the B- and B-\* isochrones.



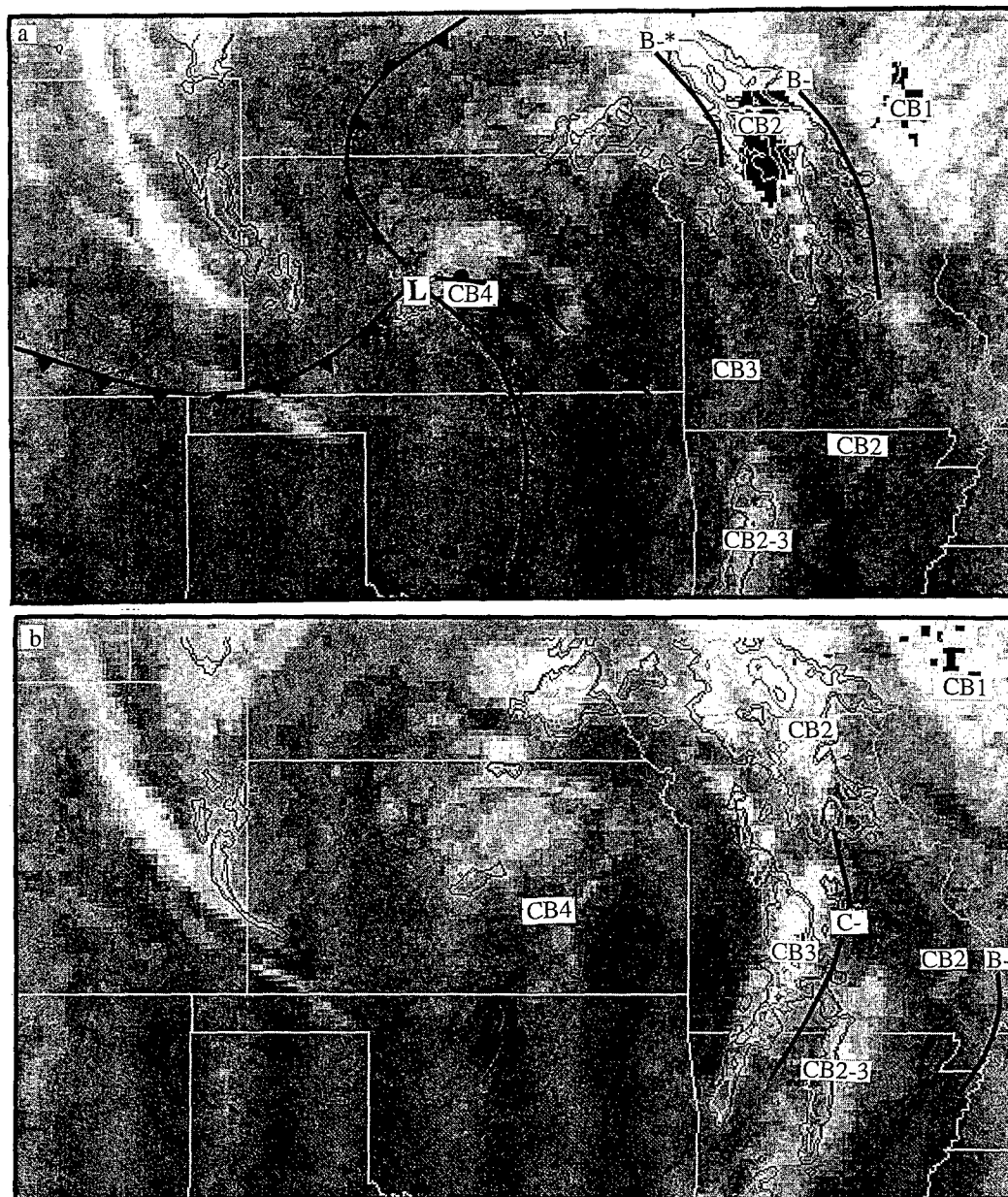


Figure 6.16 Radar and infrared satellite imagery valid (a) 1502 UTC with the surface low and associated frontal features, and (b) 1702 UTC 17 February 1997. The black lines indicate the locations of waves B-, B-\* and C-. The small yet intense band that developed between cloudbands 1 (CB1) and 2 (CB2) is labeled CB2-3. Cloudbands 3 and 4 have been labeled CB3 and CB4 respectively.

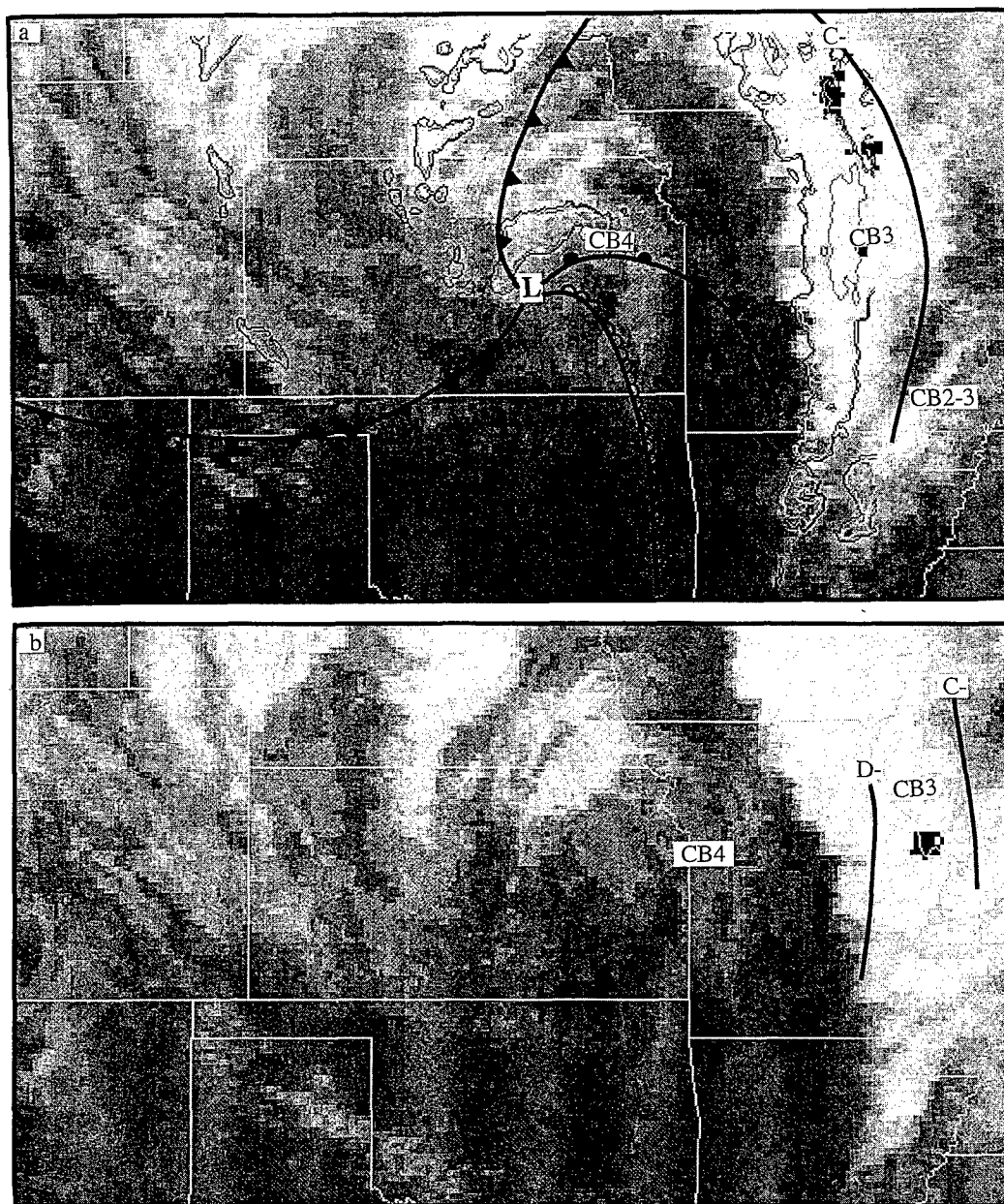


Figure 6.17. Radar and infrared satellite imagery valid (a) 2002 UTC with the surface low pressure center and associated frontal features, and (b) satellite imagery only valid 2202 UTC 17 February. The black line indicates the location of the C- and D- isochrones. The cloudband that developed between 2 and 3 is labeled CB2-3 while cloudbands 3 and 4 are labeled CB3 and CB4 respectively.

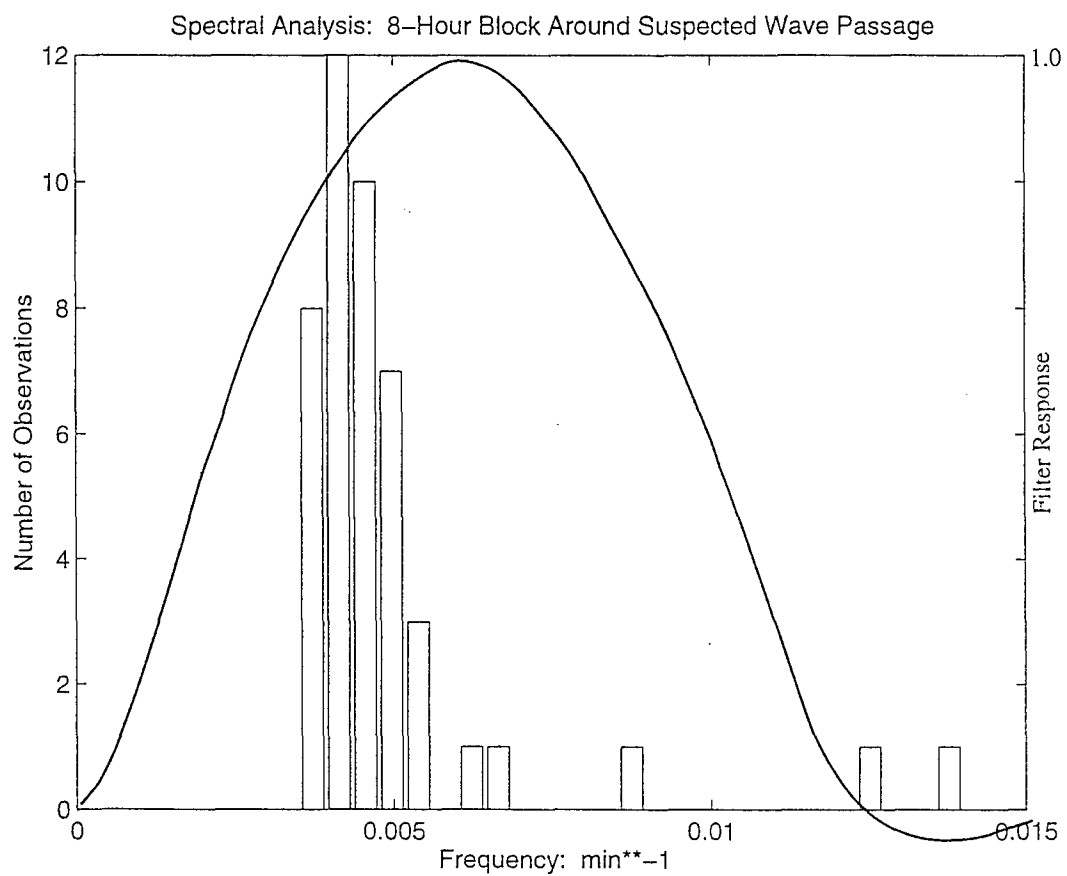


Figure 6.18. Histogram of significant peaks identified in the autospectral analysis from 45 stations during the February 17 gravity-wave event. The filter ( $f_{c1} = 0.002 \text{ min}^{-1}$  and  $f_{c2} = 0.01 \text{ min}^{-1}$ ) response is plotted over the histogram.

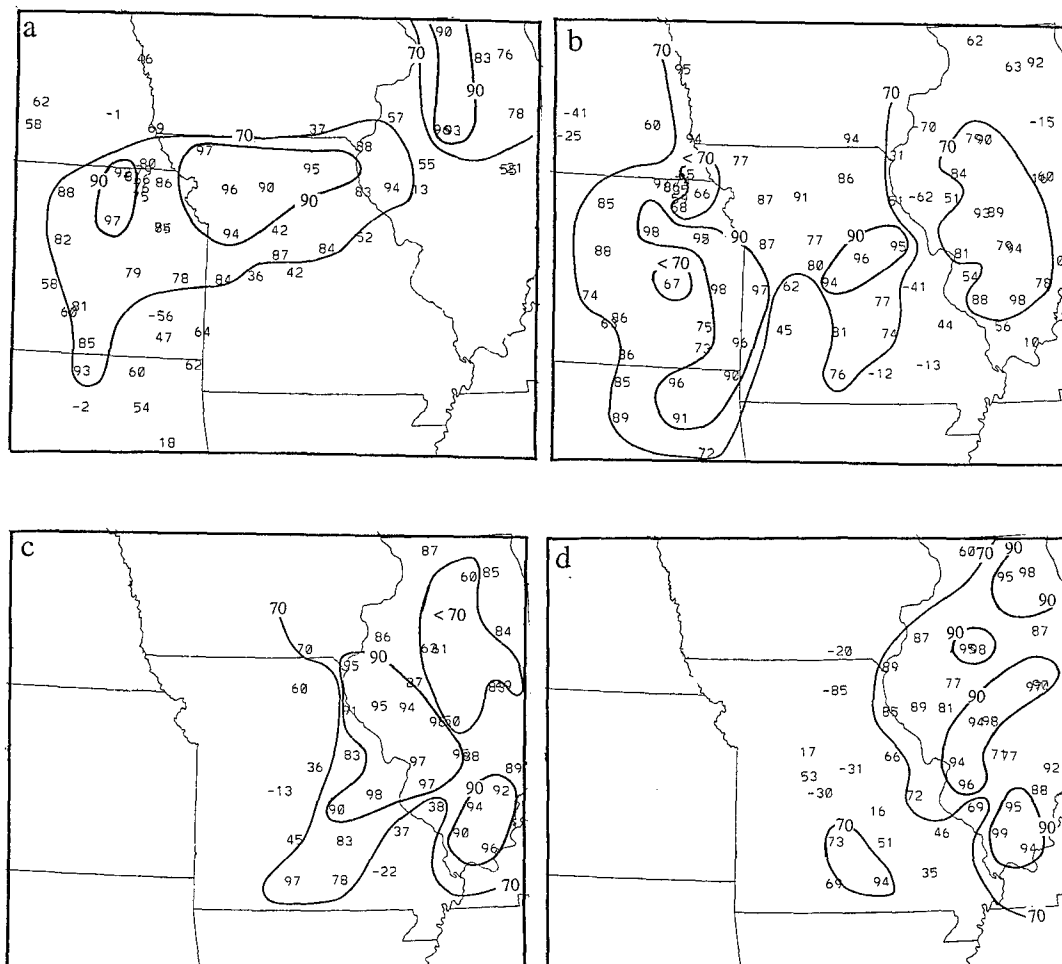


Figure 6.19. Average  $\overline{p'u^*}$  correlation values (\*100) determined over a 3-hr period of wave activity at each station for the February 17 gravity-wave event for waves (a) A-, (b) B-, (c) C- and (d) D-.

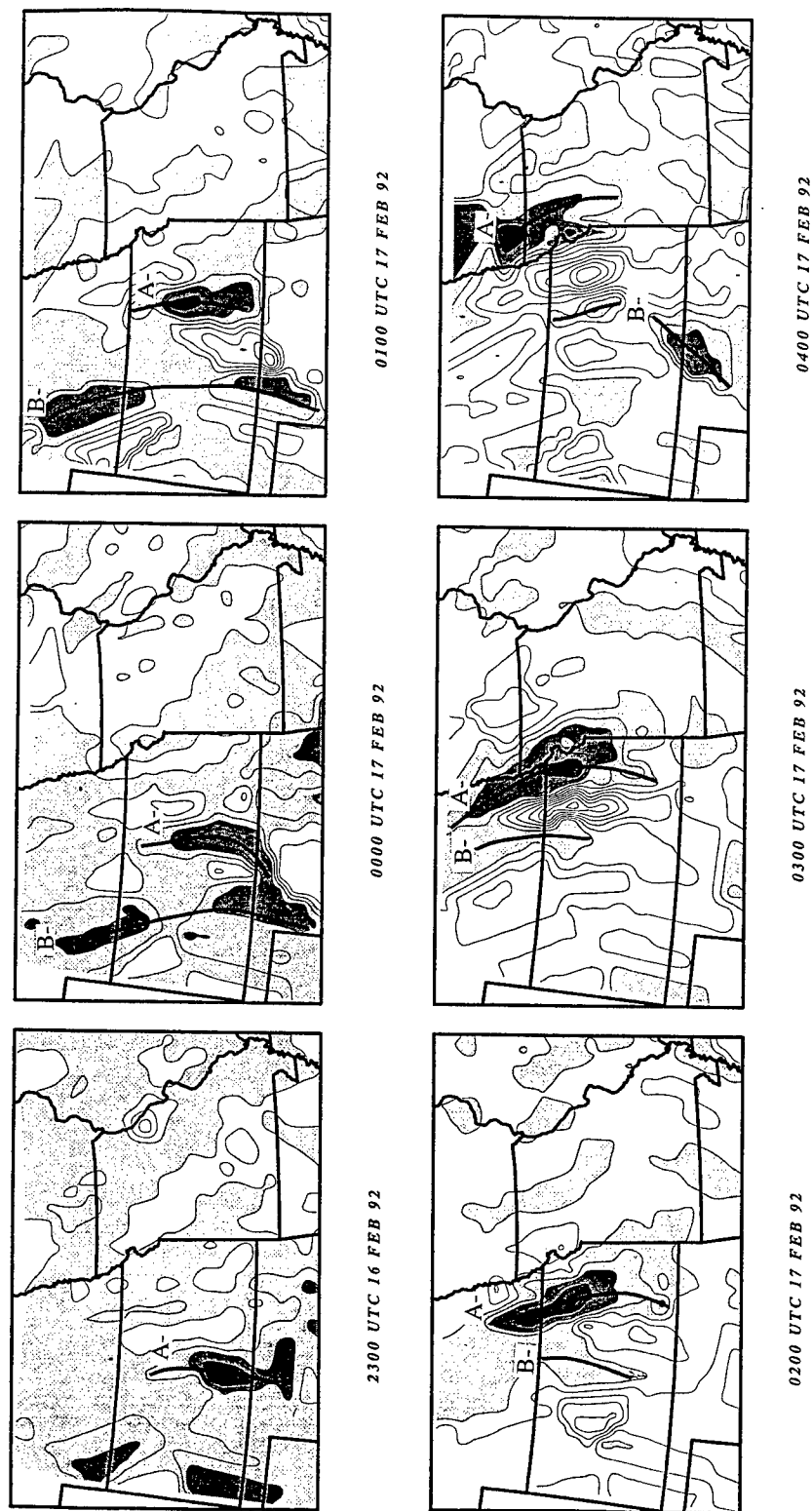
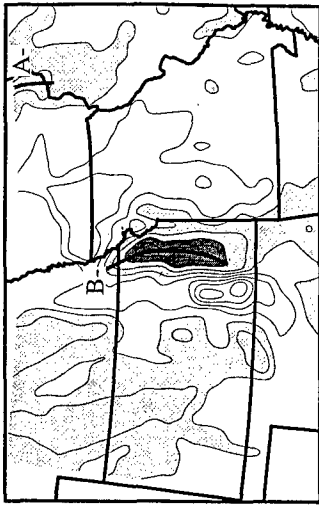
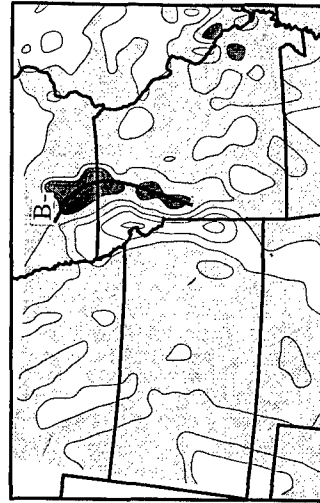


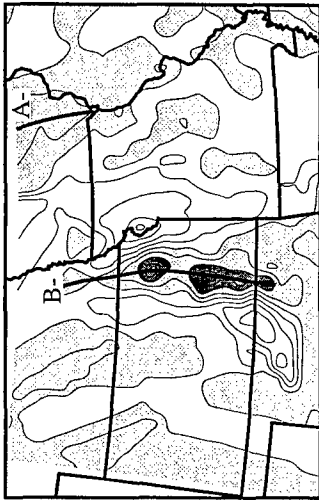
Figure 6.20. Time-to-Space Conversion output for the bandpassed ( $f_{c1} = 0.002 \text{ min}^{-1}$  and  $f_{c2} = 0.01 \text{ min}^{-1}$ ) pressure data with a grid-length of 32 km, and a tau value of 50 min. Plots begin at 16 February 2300 UTC and continue every hour through 18 February 0400 UTC (actually 0355 UTC). Contouring is every 0.2 mb, with darker shading every 0.4 mb for negative values beginning at 0.0. The wave (A-, B-, B-\*, C- and D-) isochrones are indicated by a black line.



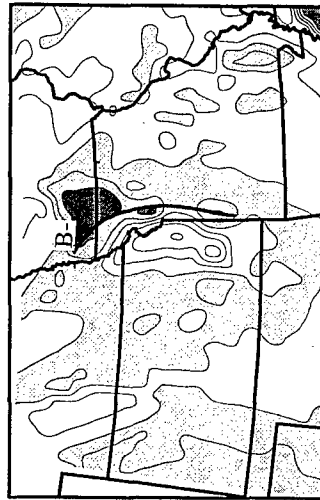
0700 UTC 17 FEB 92



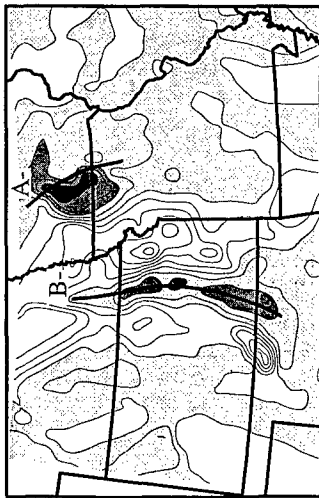
1000 UTC 17 FEB 92



0600 UTC 17 FEB 92



0900 UTC 17 FEB 92



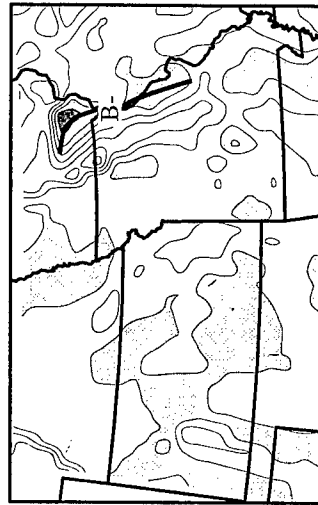
0500 UTC 17 FEB 92



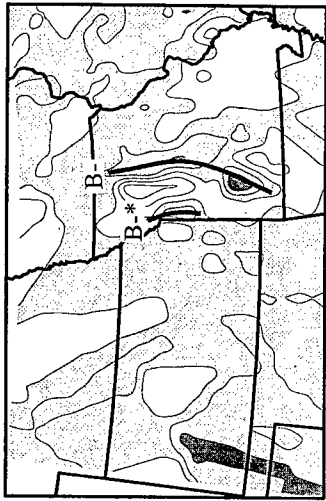
0800 UTC 17 FEB 92



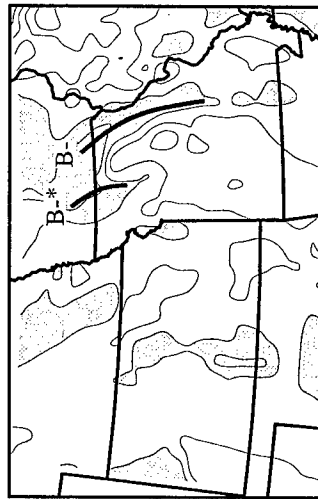
1300 UTC 17 FEB 92



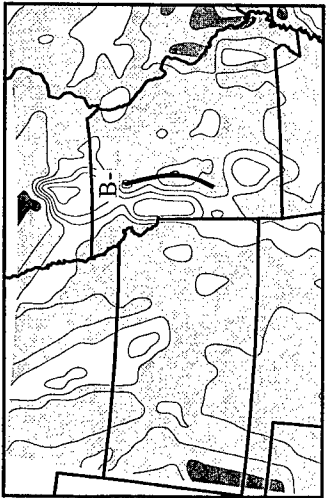
1600 UTC 17 FEB 92



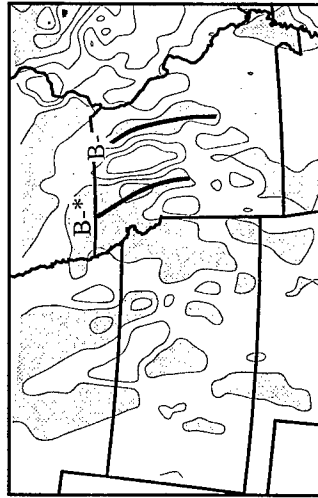
1200 UTC 17 FEB 92



1500 UTC 17 FEB 92



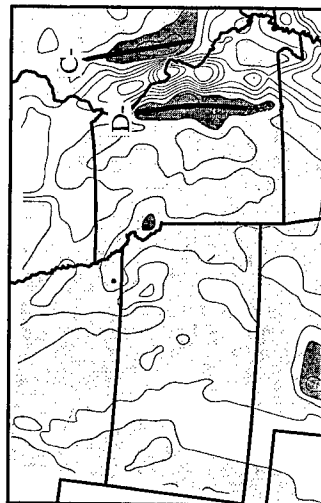
1100 UTC 17 FEB 92



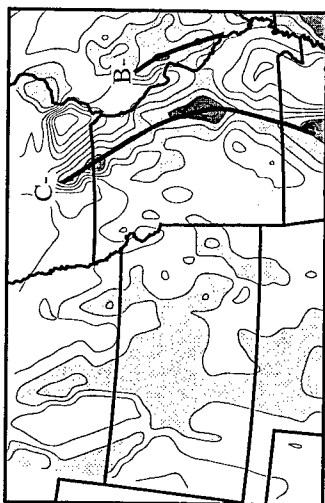
1400 UTC 17 FEB 92



1900 UTC 17 FEB 92



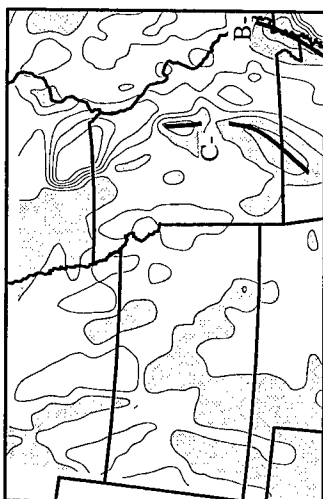
2200 UTC 17 FEB 92



1800 UTC 17 FEB 92



2100 UTC 17 FEB 92

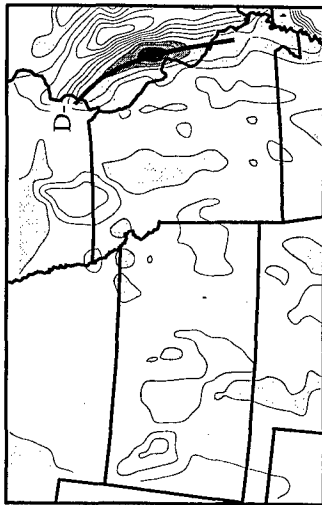


1700 UTC 17 FEB 92

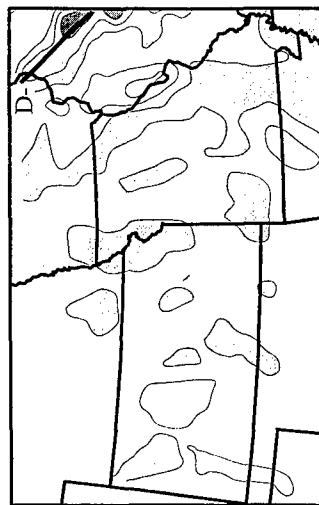


2000 UTC 17 FEB 92

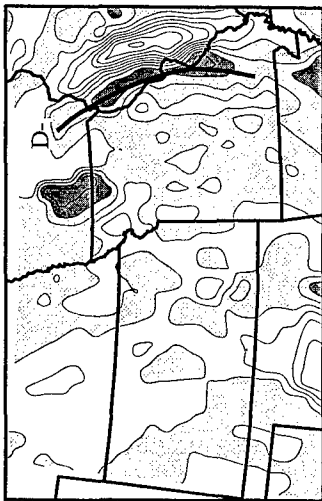




0100 UTC 1800 FEB 92



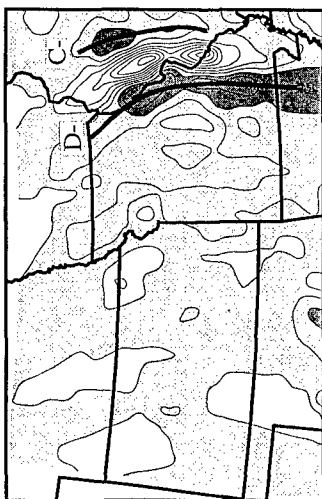
0355 UTC 1800 FEB 92



0000 UTC 18 FEB 92



0300 UTC 18 FEB 92

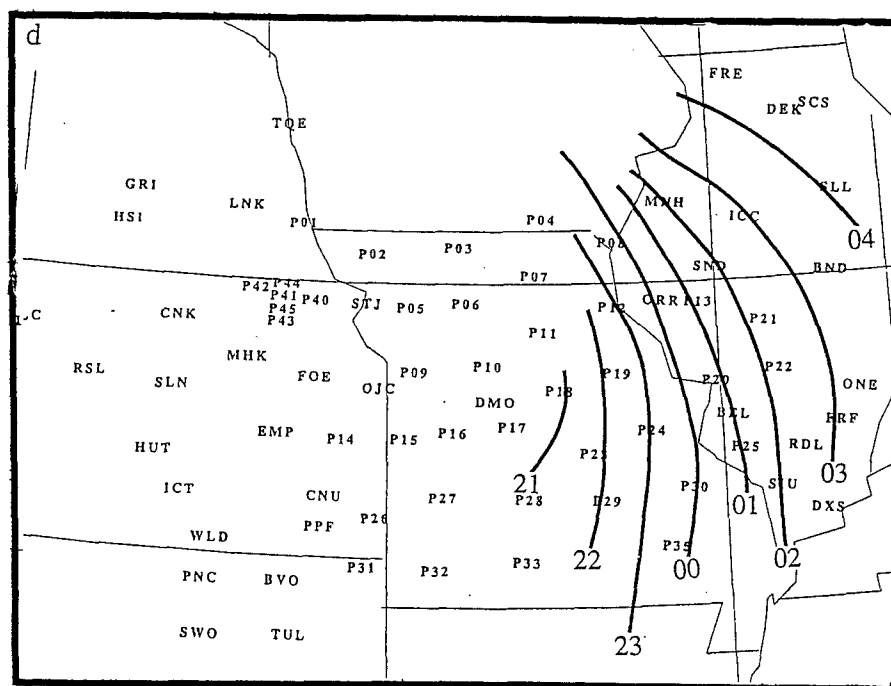
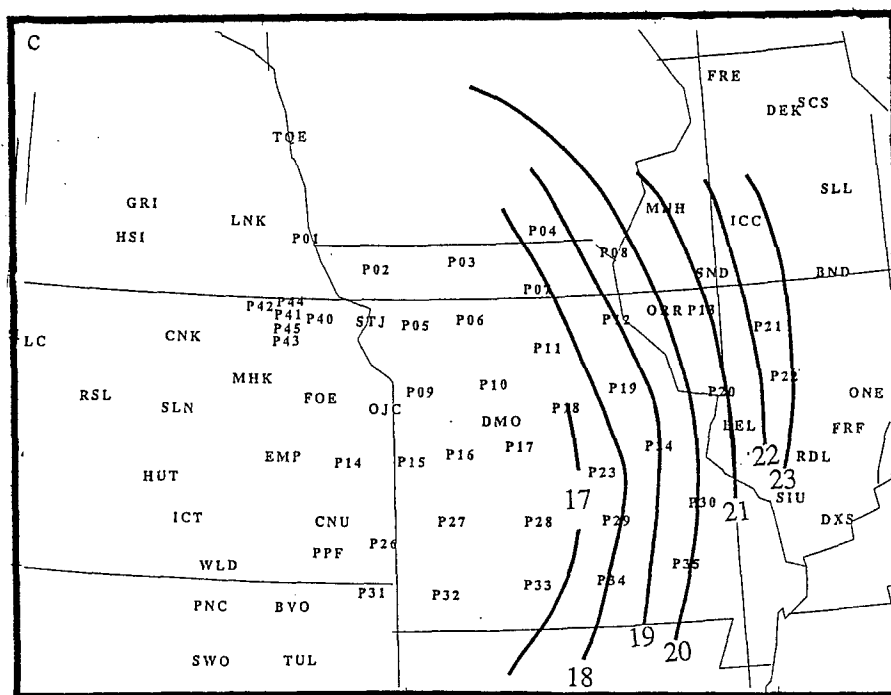


2300 UTC 17 FEB 92



0200 UTC 18 FEB 92





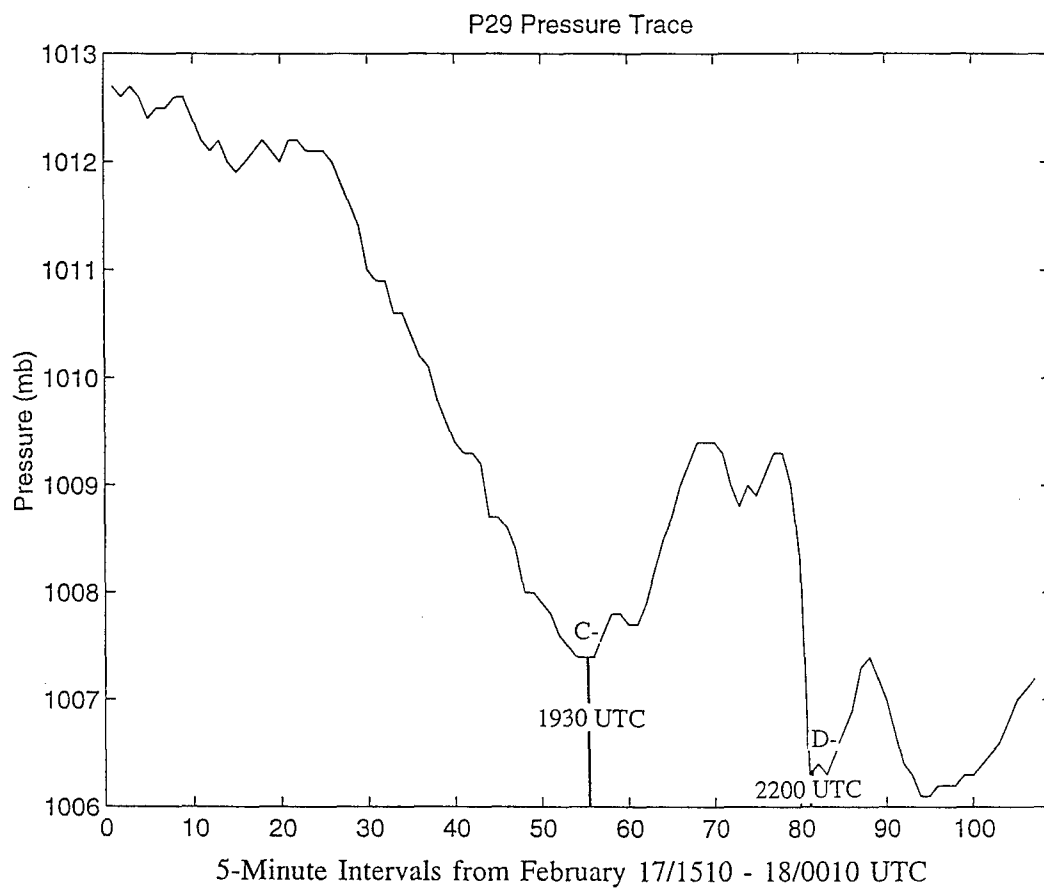


Figure 6.22. Raw pressure trace from station P29 from February 17/1500 - 18/0000 UTC. The wave signatures for C- and D- are indicated. A wave of elevation within the train occurred after 2200 UTC.

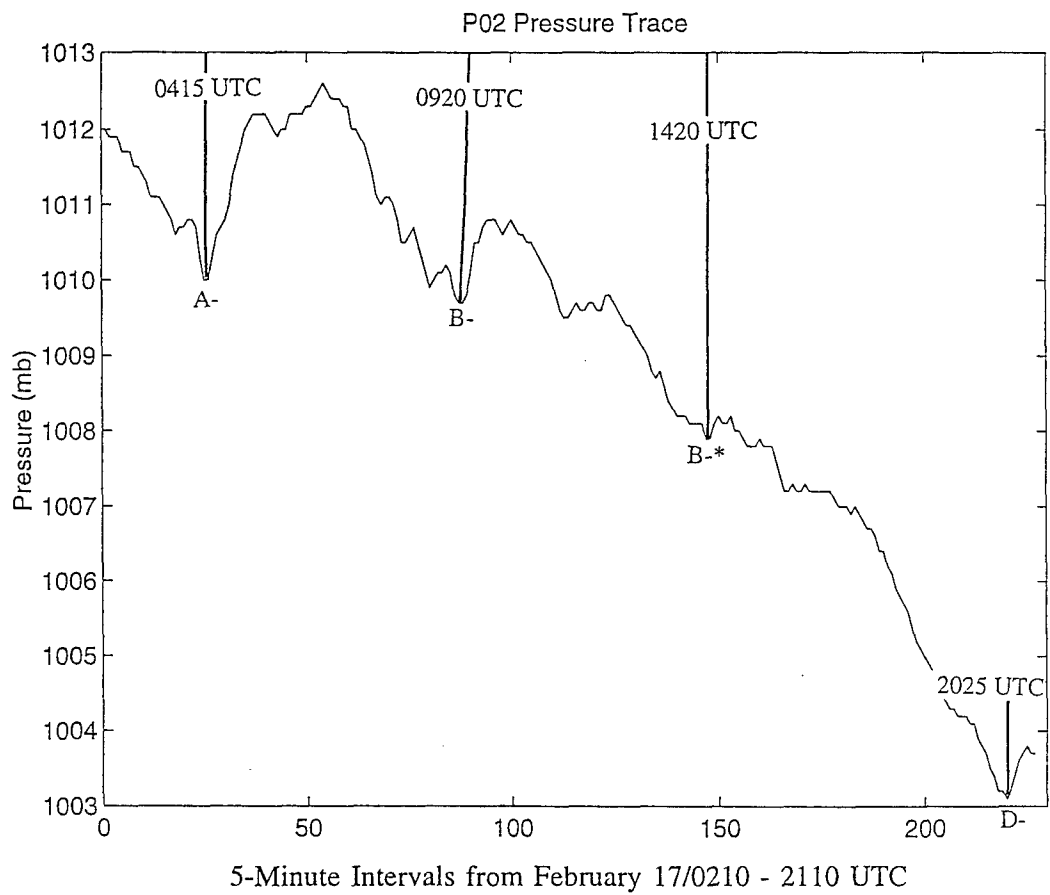


Figure 6.23. Raw pressure trace from station P02 from February 17/0200 - 2100 UTC. The wave signatures for A-, B-, B-\* and D- are indicated.

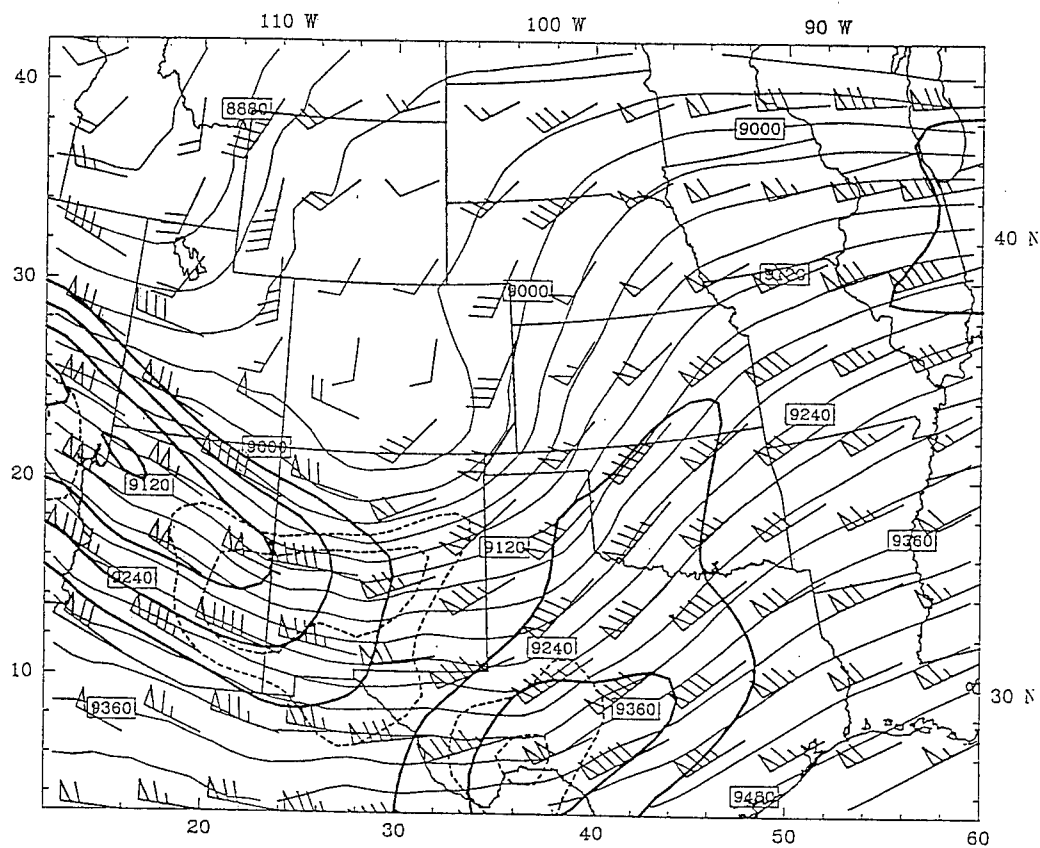


Figure 6.24. MM4 model 11-hr forecast of 300 mb heights (thin black lines), isotachs  $\geq 58$  ms $^{-1}$ , contour interval = 5 (heavy black lines) and geostrophic winds  $\geq 40$  ms $^{-1}$ , contour interval = 5 (dashed lines) valid 2300 UTC 16 February.

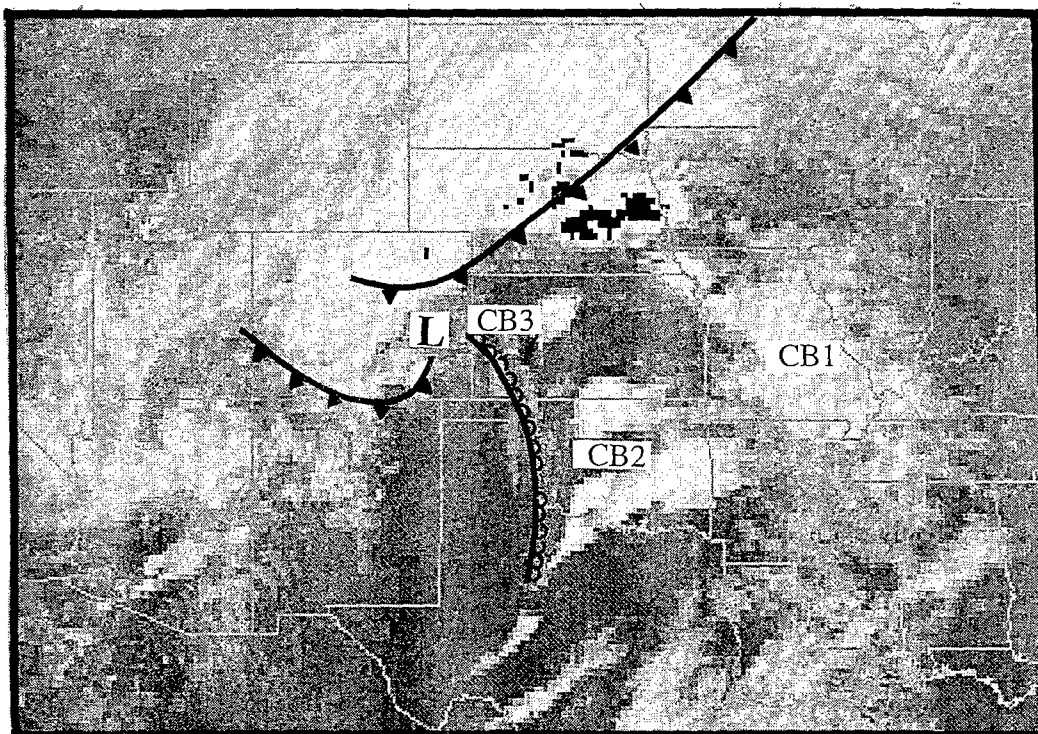


Figure 6.25. Satellite imagery valid 0102 UTC March 9. The locations of the surface low pressure center, dryline and fronts are indicated. Cloudbands 1, 2 and 3 are labeled.

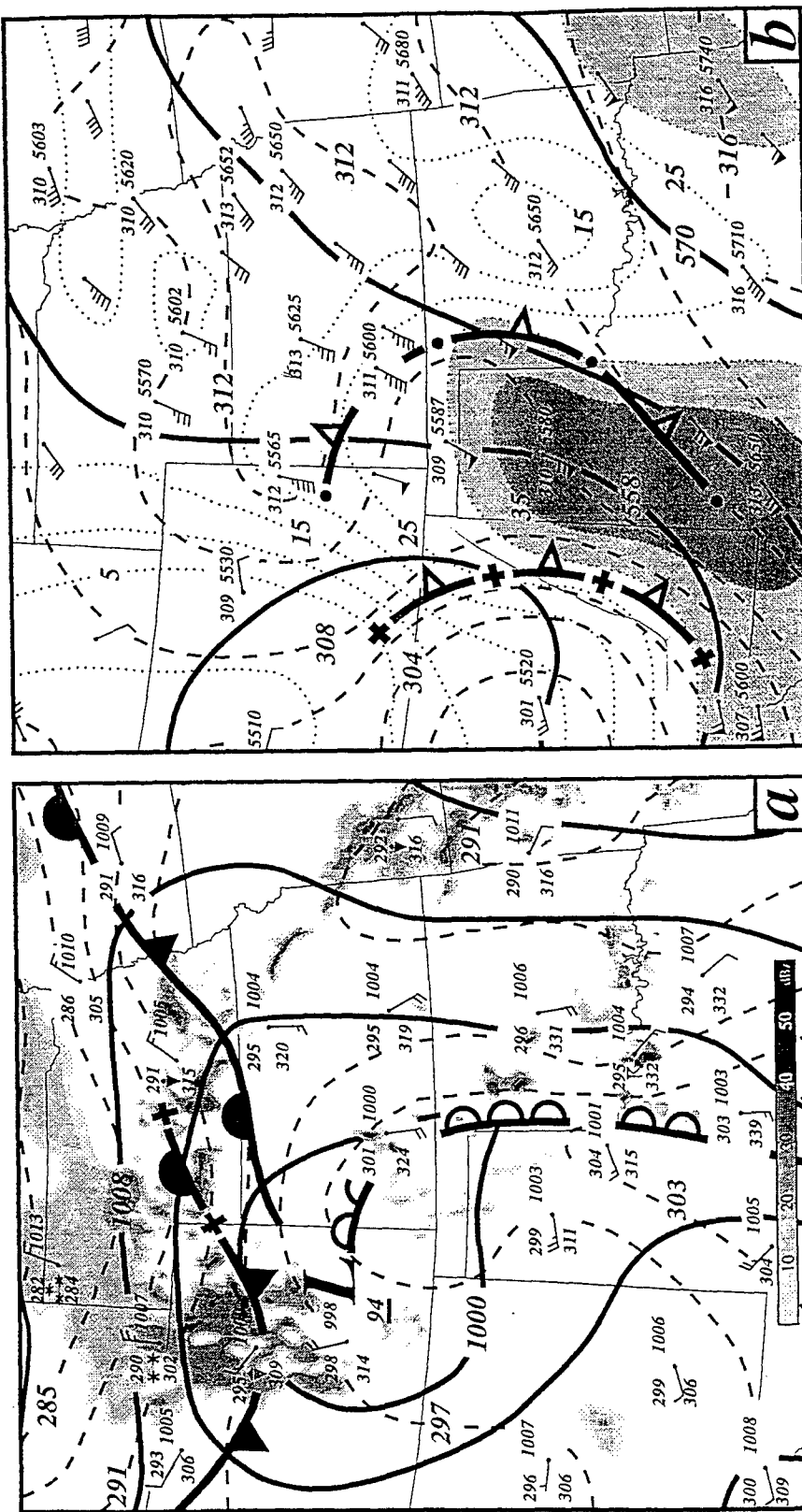


Figure 6.26. (a) 0000 UTC 9 March surface analysis: isobars (solid - mb), potential temperature (dashed - °K), radar echo's (shading - interval of 10 dBZ). Station plot: potential temperature, equivalent potential temperature, mean sea level pressure, observed weather, wind barb (full staff - 5  $\text{ms}^{-1}$ , half staff - 2.5  $\text{ms}^{-1}$ ). Surface dryline depicted by line of open semicircles. Frontolysis depicted by broken line separated by a cross. (b) 0000 UTC 9 March 500 mb analysis: heights (solid - dm), isotachs (dotted/shading -  $\text{ms}^{-1}$ ), potential temperature (dashed - °K). Station plot: potential temperature, equivalent potential temperature and wind barb (flag - 25  $\text{ms}^{-1}$ , full staff - 5  $\text{ms}^{-1}$ , half staff - 2.5  $\text{ms}^{-1}$ ). Cold front aloft depicted by line of open triangles. Frontogenesis depicted by broken line separated by a closed circle. Frontolysis depicted by broken line separated by a cross (Adams 1996).



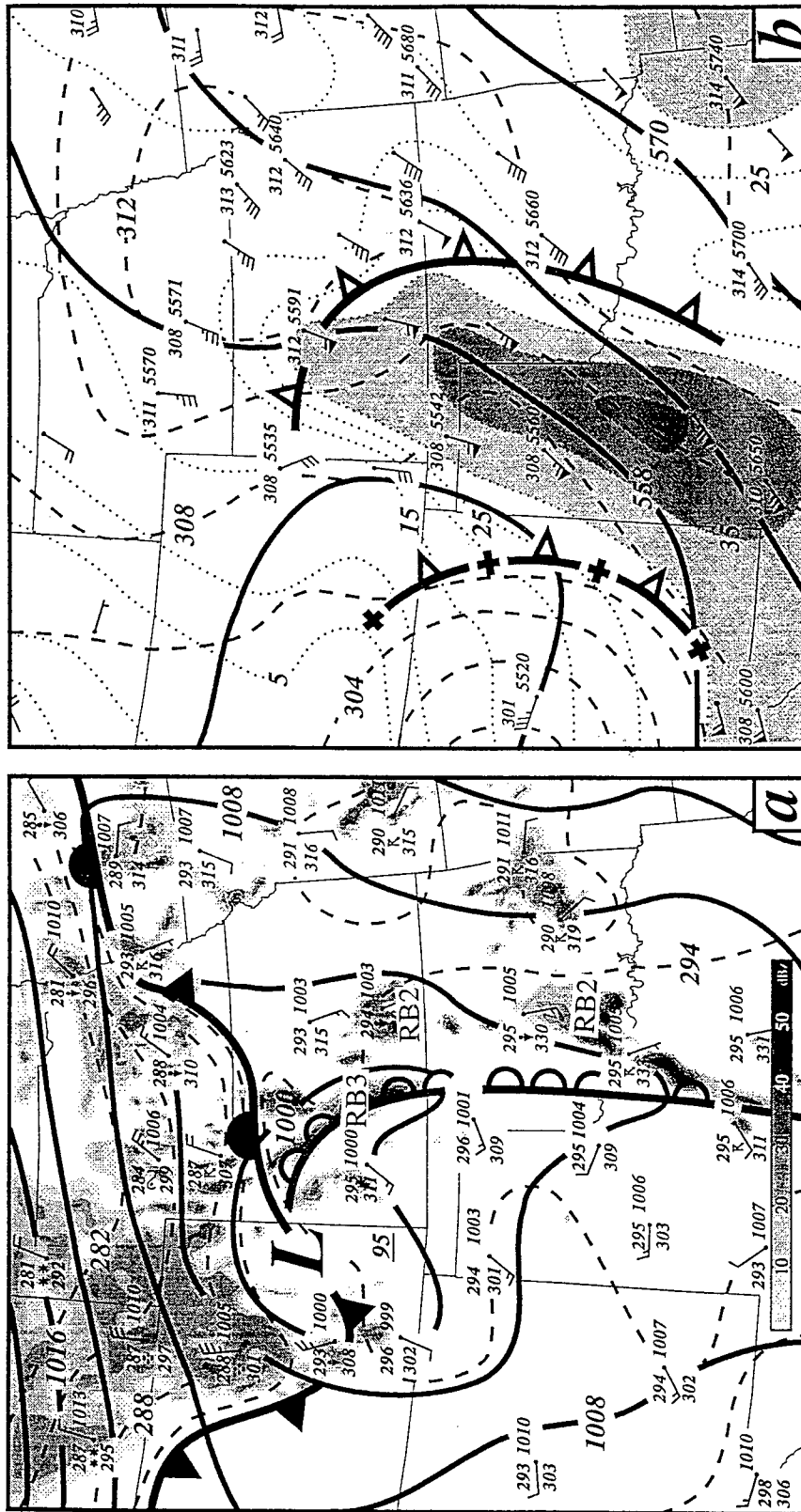


Figure 6.27. Same as Figure 6.26 except valid at 0300 UTC (Adams 1996) with rainbands 2 and 3 labelled RB2 and RB3 respectively.

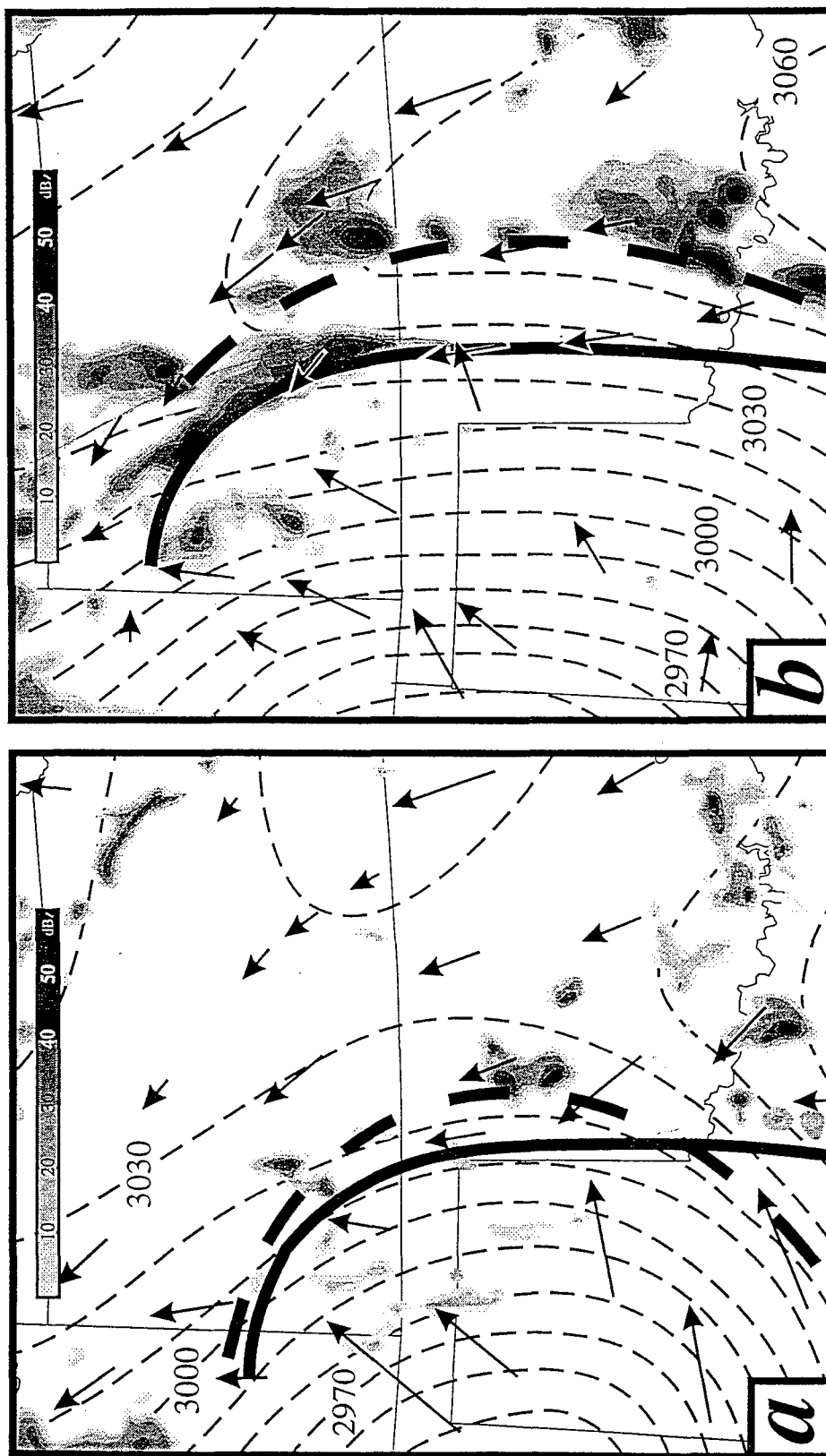


Figure 6.28. Depiction of the relationship between dryline (thick solid line), CFA (heavy dashed line) and developing convection (radar reflectivity at 10 dBz interval - shaded). Arrows depict surface wind vectors from PAM network. Retrieved 600 - 400 mb thickness are thin dashed line - (m). (a) 0000 UTC 9 March and (b) 0300 UTC 9 March (Adams 1996).

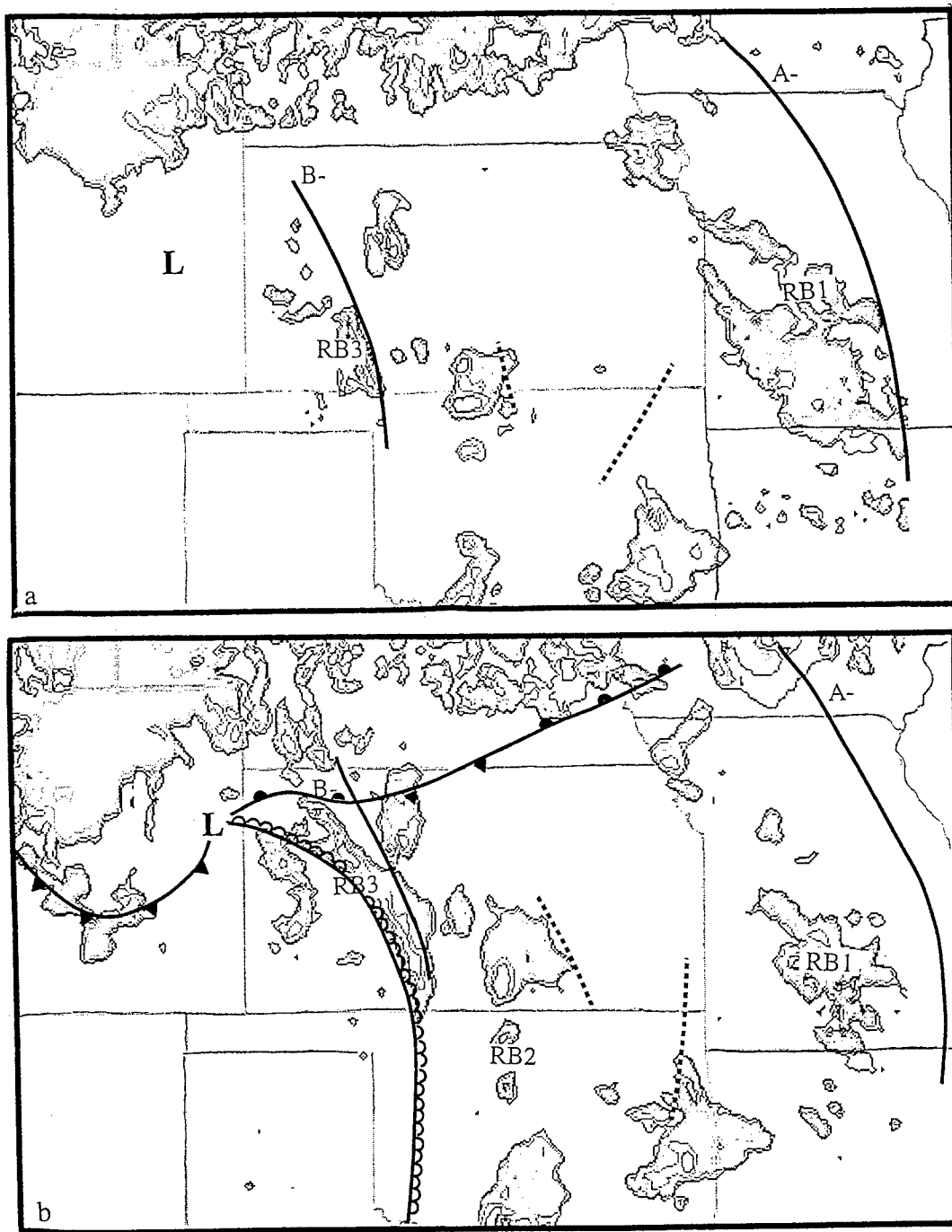
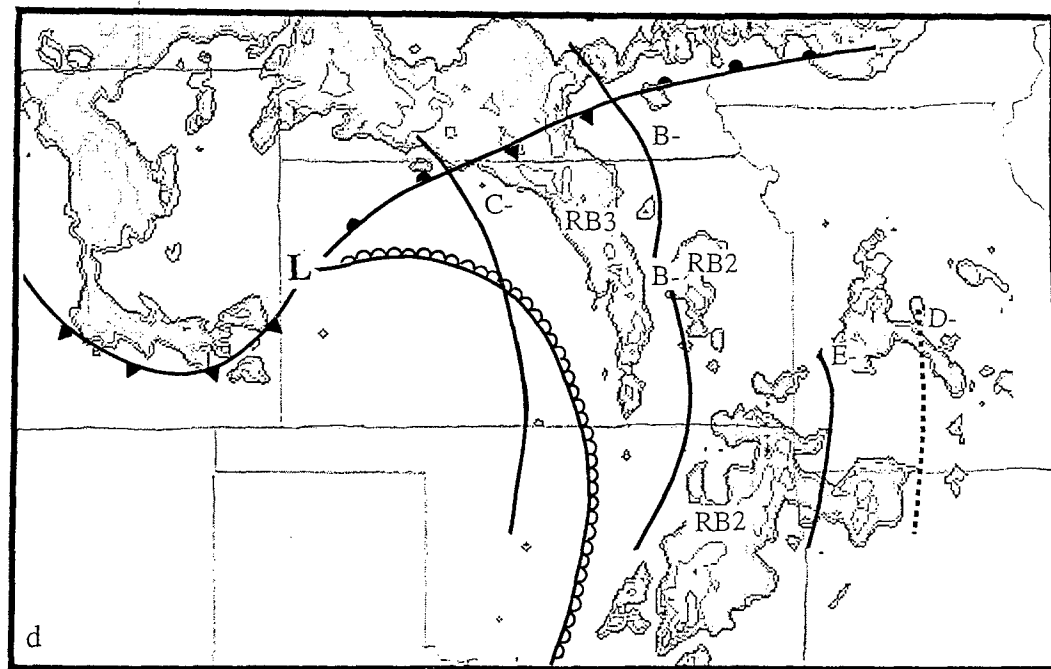
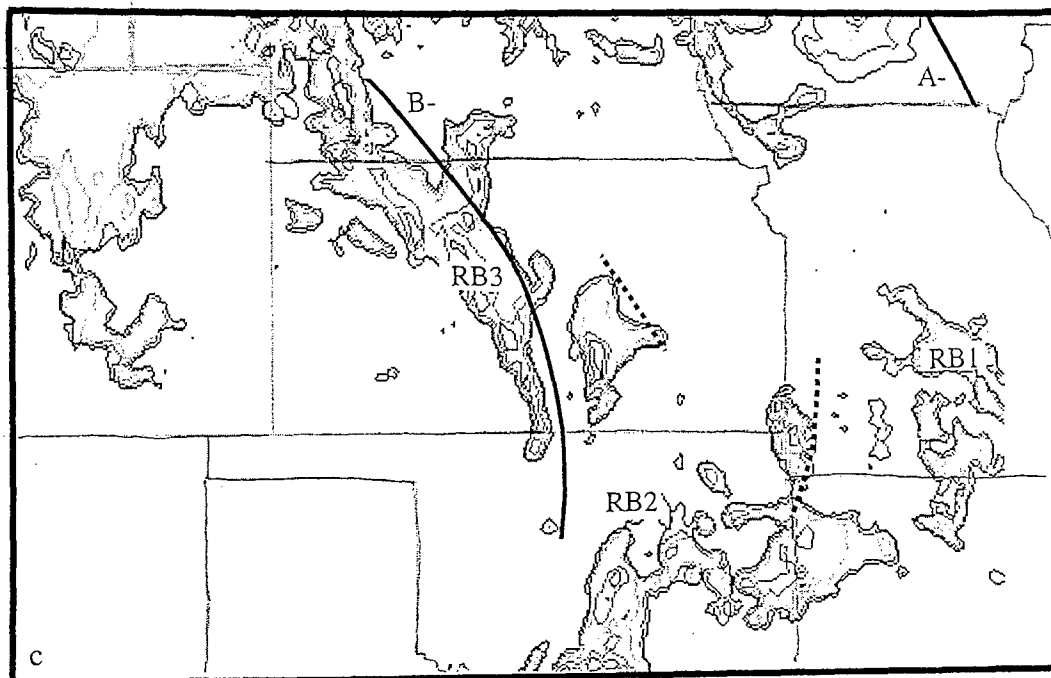
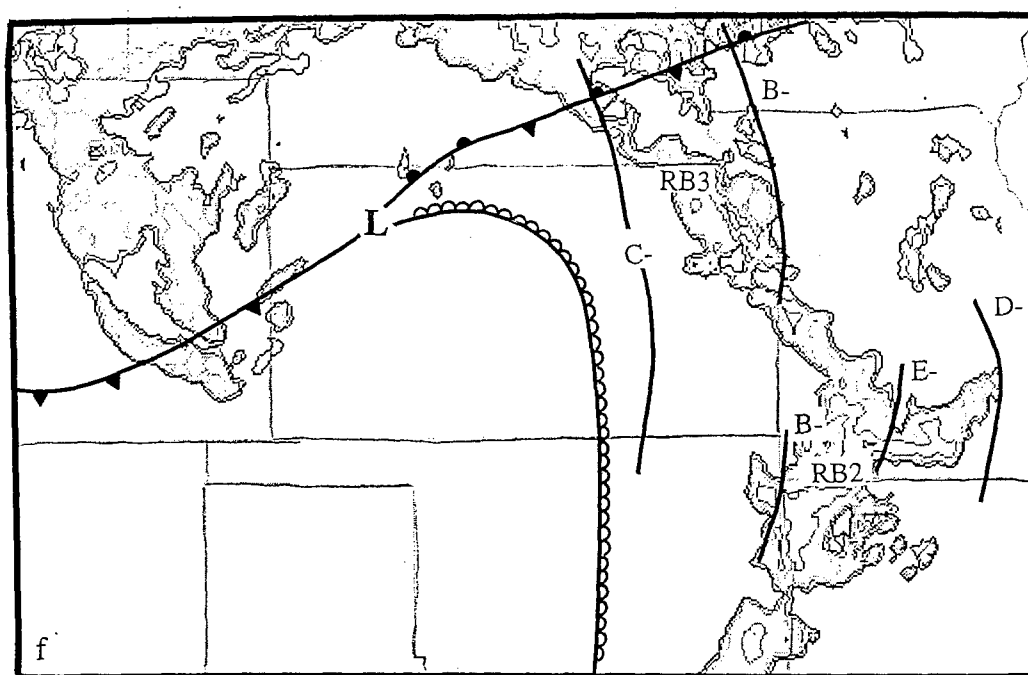
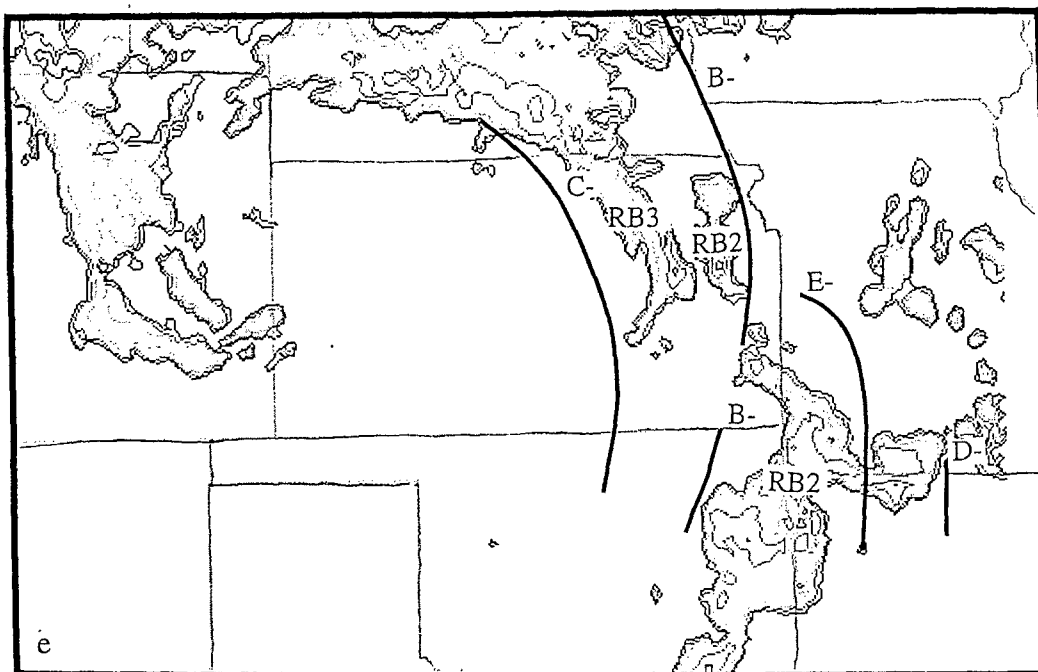
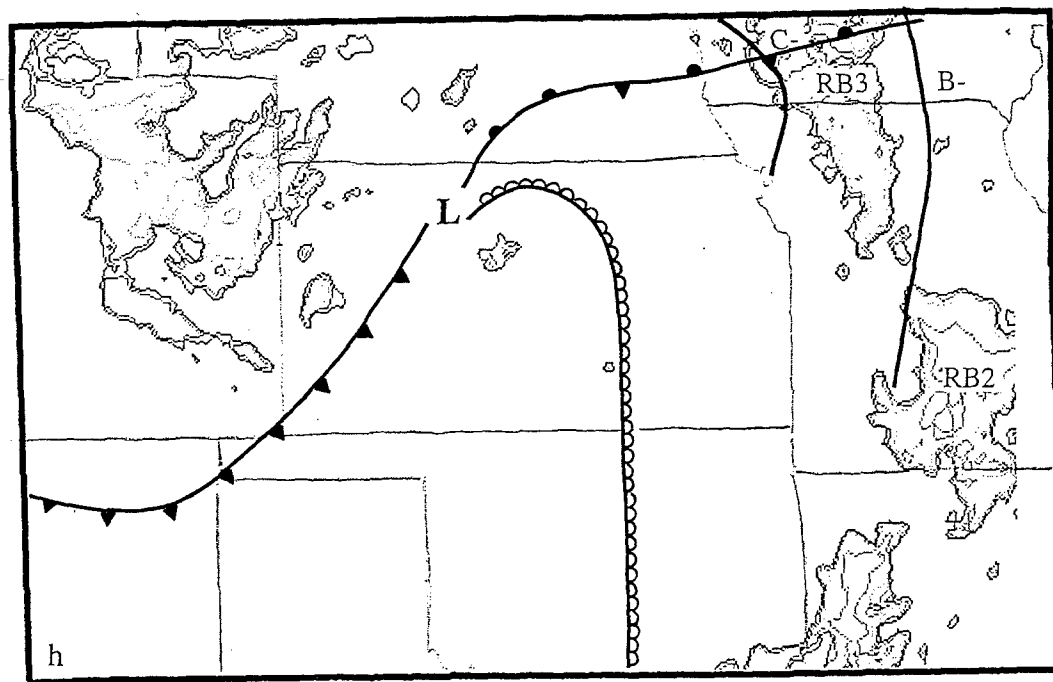
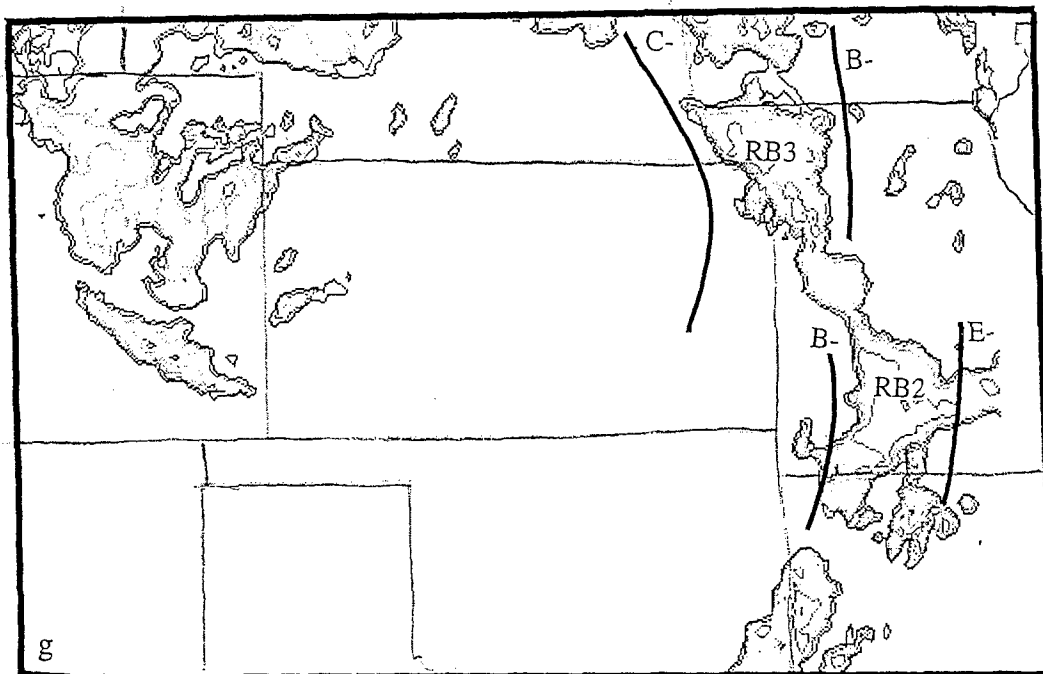


Figure 6.29. Radar imagery with isochrones (solid black lines) and rainbands for (a) 0202 UTC, (b) 0302 UTC, (c) 0402 UTC, (d) 0602 UTC, (e) 0702 UTC, (f) 0802 UTC, (g) 0902 UTC and (h) 1002 UTC. The dashed lines represent smaller, coherent signals identified in the objective analysis. The surface low pressure center and associated frontal features have been added to select images.







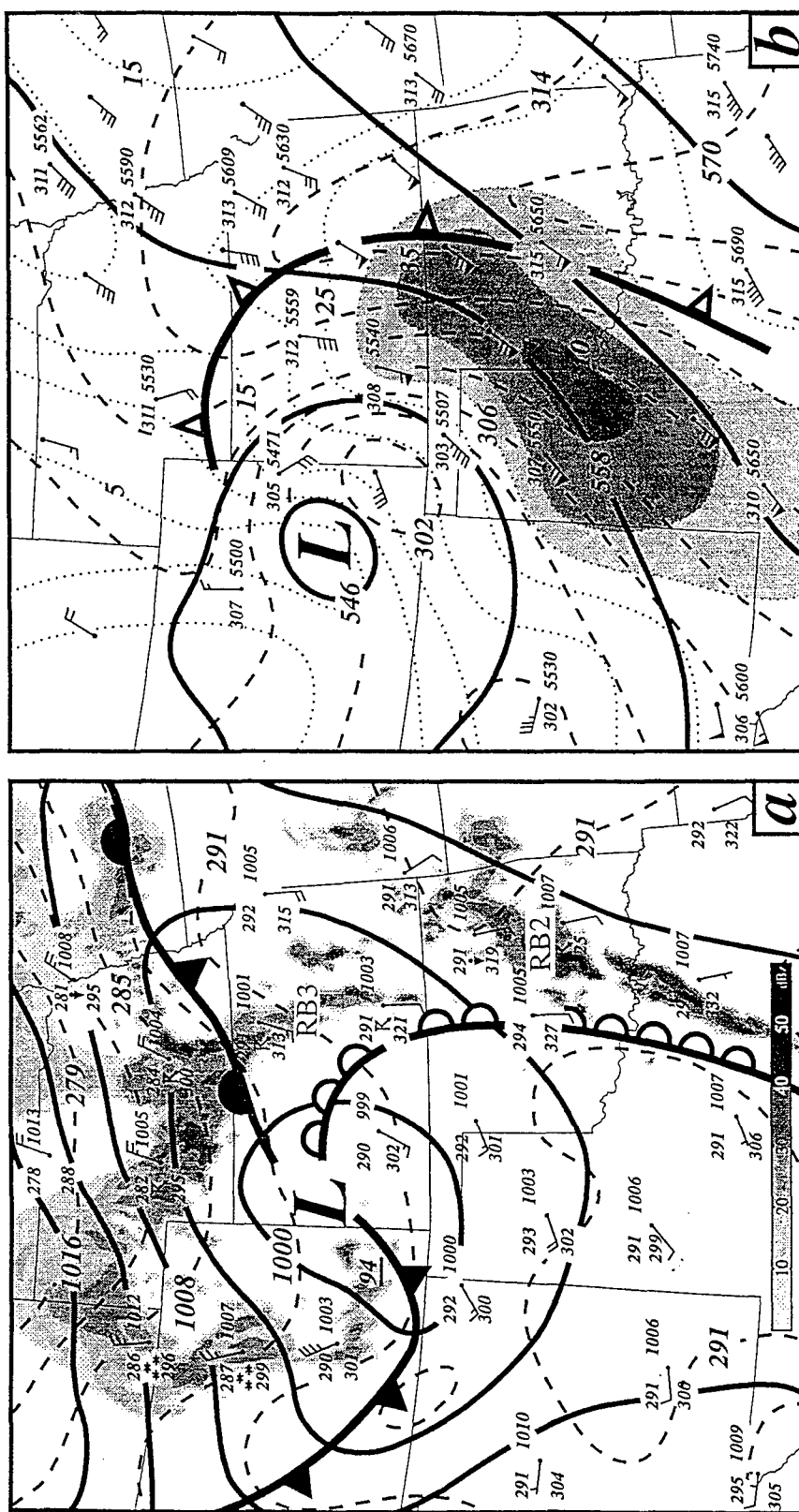


Figure 6.30. Same as Figure 6.26 except valid at 0600 UTC (Adams 1996) with rainbands 2 and 3 labelled RB2 and RB3 respectively.

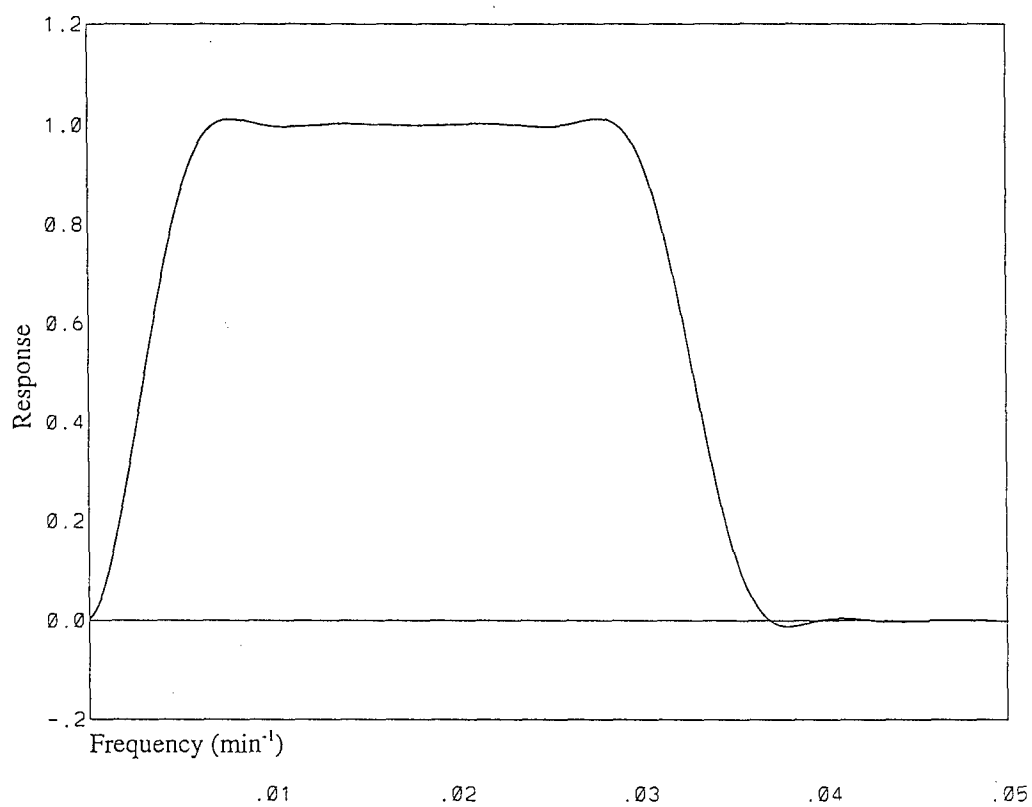
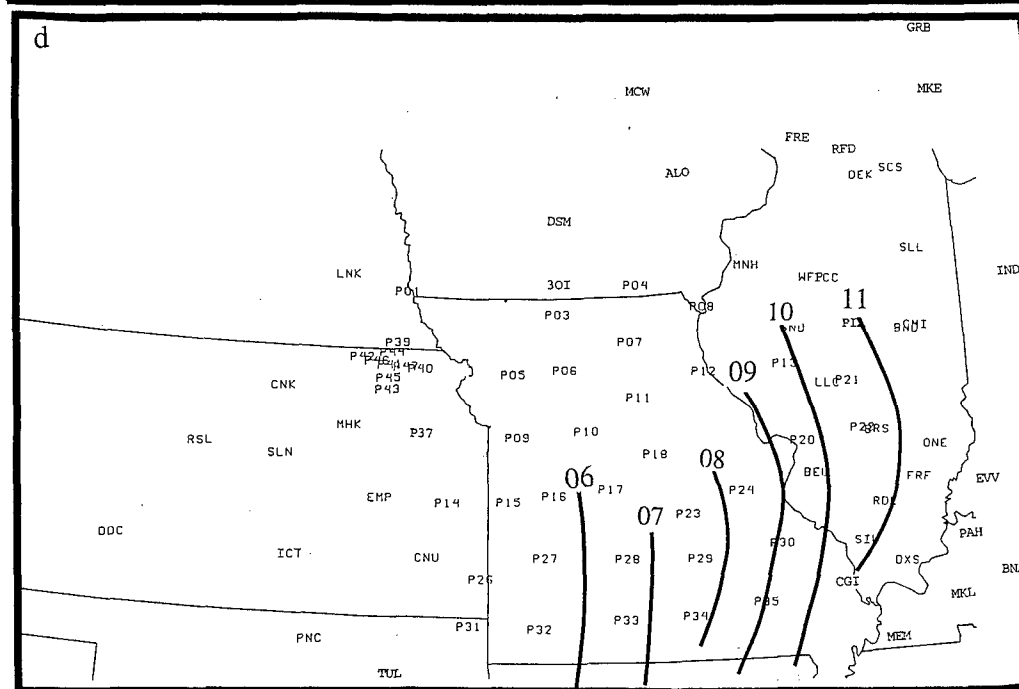
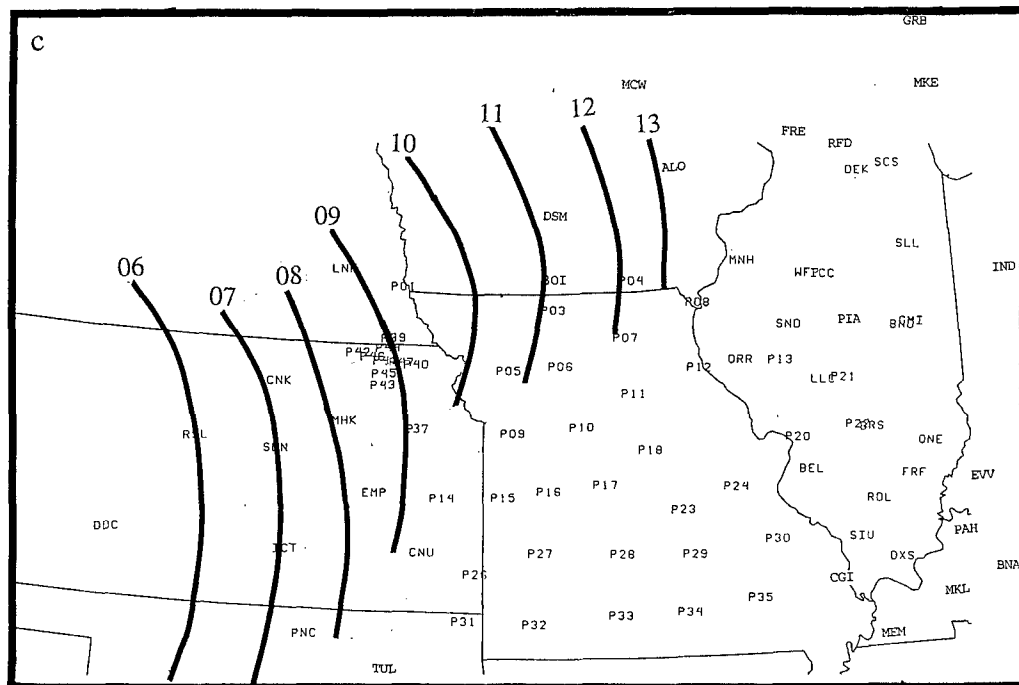
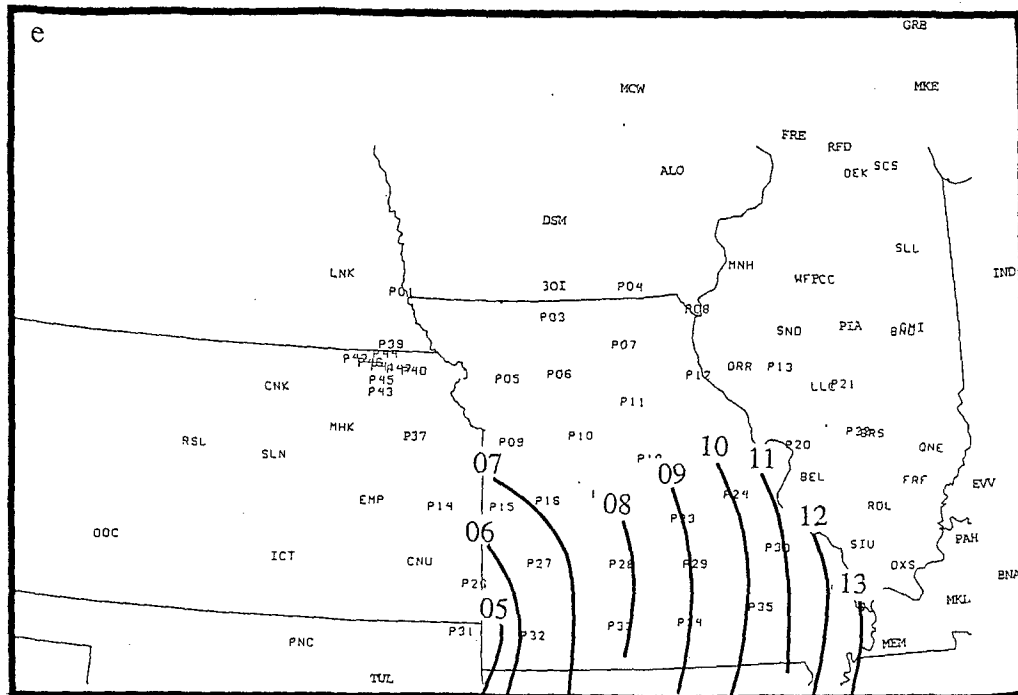


Figure 6.31. Response for the filter used in the March 9 gravity wave event with  $f_{c1} = 0.0028 \text{ min}^{-1}$  and  $f_{c2} = 0.0330 \text{ min}^{-1}$ .









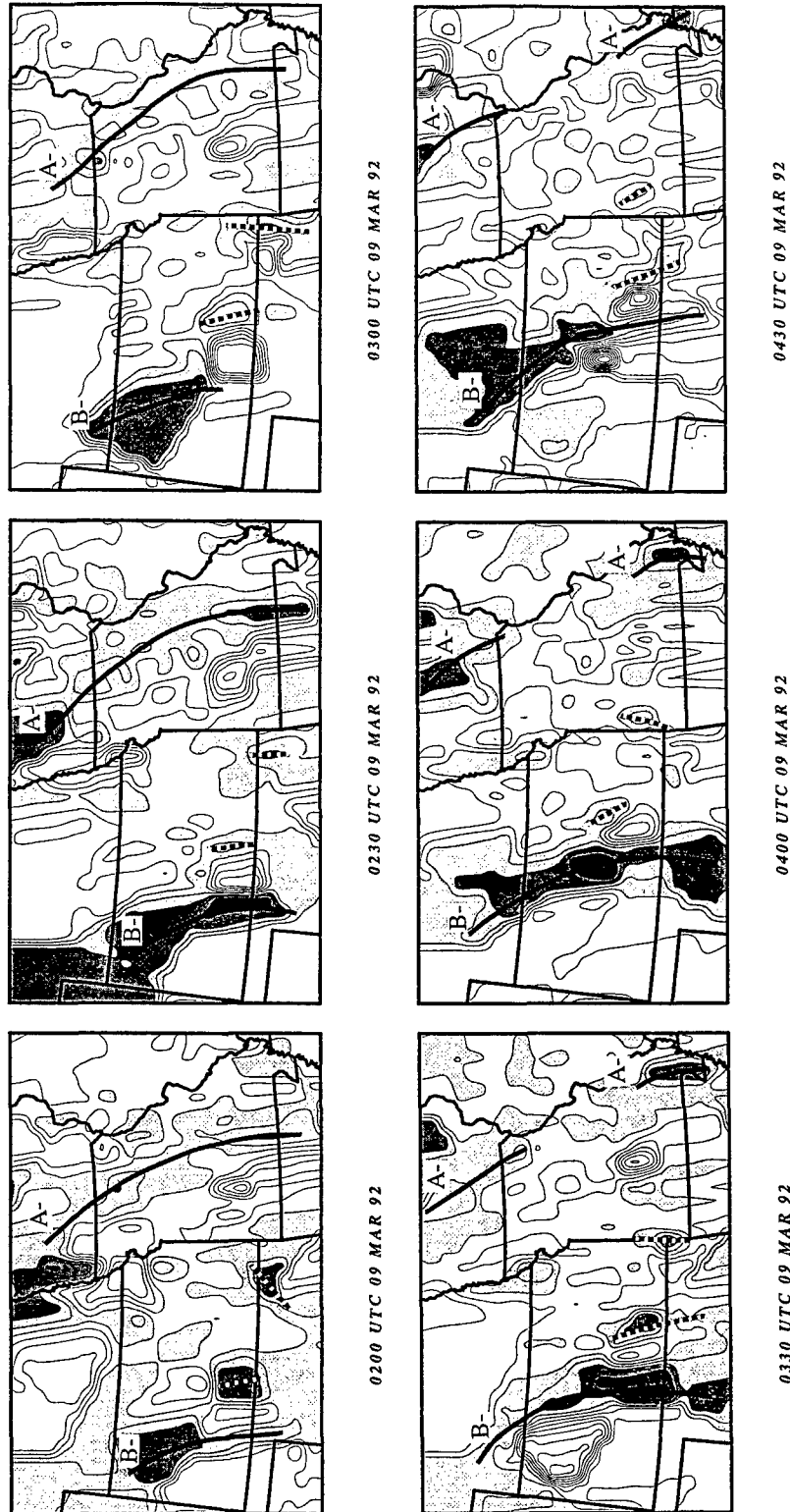


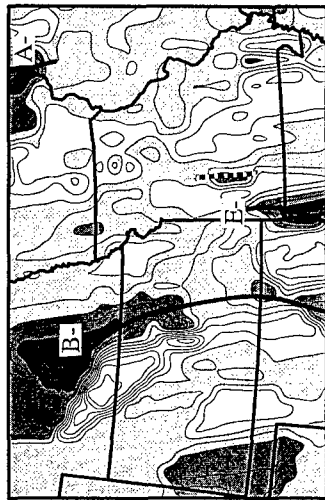
Figure 6.33. Time-to-Space Conversion output for the bandpassed ( $f_{c1} = 0.0028 \text{ min}^{-1}$  and  $f_{c2} = 0.0330 \text{ min}^{-1}$ ) pressure data with a grid-length of 32 km, and a tau value of 50 min. Plots begin at 0200 UTC on March 9 and continue every half-hour through 1330 UTC. Contouring is every 0.2 mb, with darker shading every 0.4 mb for negative values beginning at 0.0. The wave (A-, B-, C-, D- and E-) isochrones are indicated by black lines and dashed lines represent smaller, coherent signal.



0600 UTC 09 MAR 92



0730 UTC 09 MAR 92



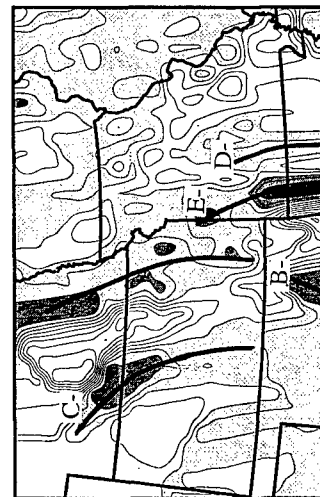
0530 UTC 09 MAR 92



0700 UTC 09 MAR 92



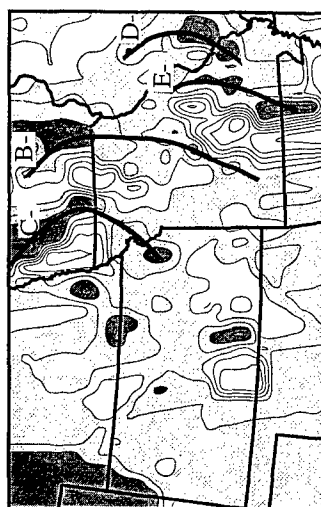
0500 UTC 09 MAR 92



0630 UTC 09 MAR 92



0900 UTC 09 MAR 92



1030 UTC 09 MAR 92



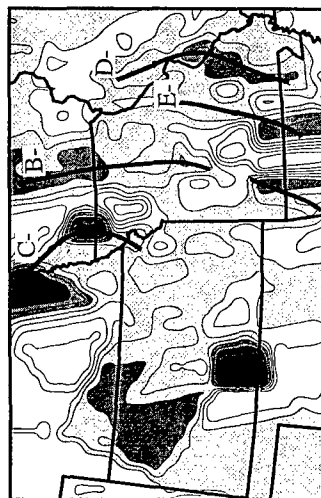
0830 UTC 09 MAR 92



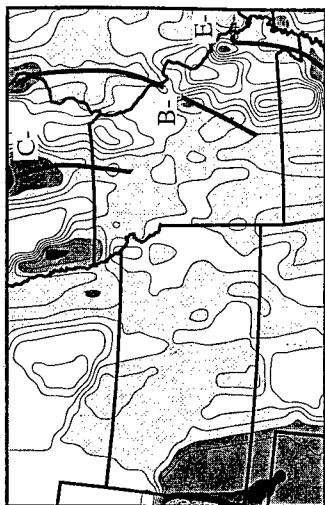
1000 UTC 09 MAR 92



0800 UTC 09 MAR 92



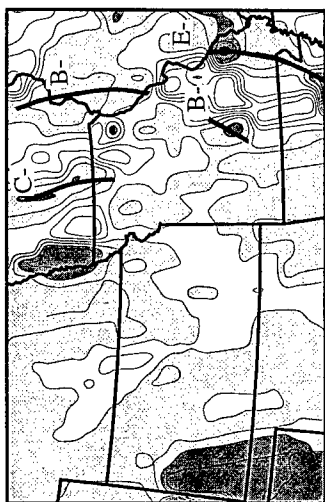
0930 UTC 09 MAR 92



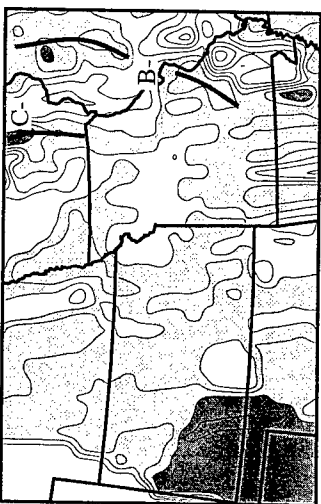
1200 UTC 09 MAR 92



1330 UTC 09 MAR 92



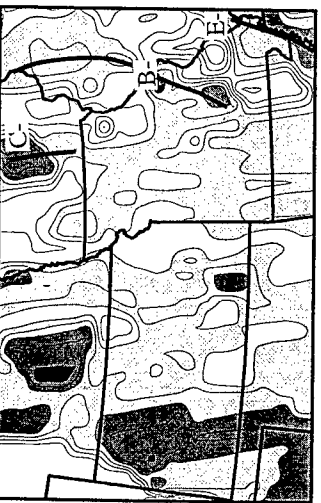
1130 UTC 09 MAR 92



1300 UTC 09 MAR 92



1100 UTC 09 MAR 92



1230 UTC 09 MAR 92

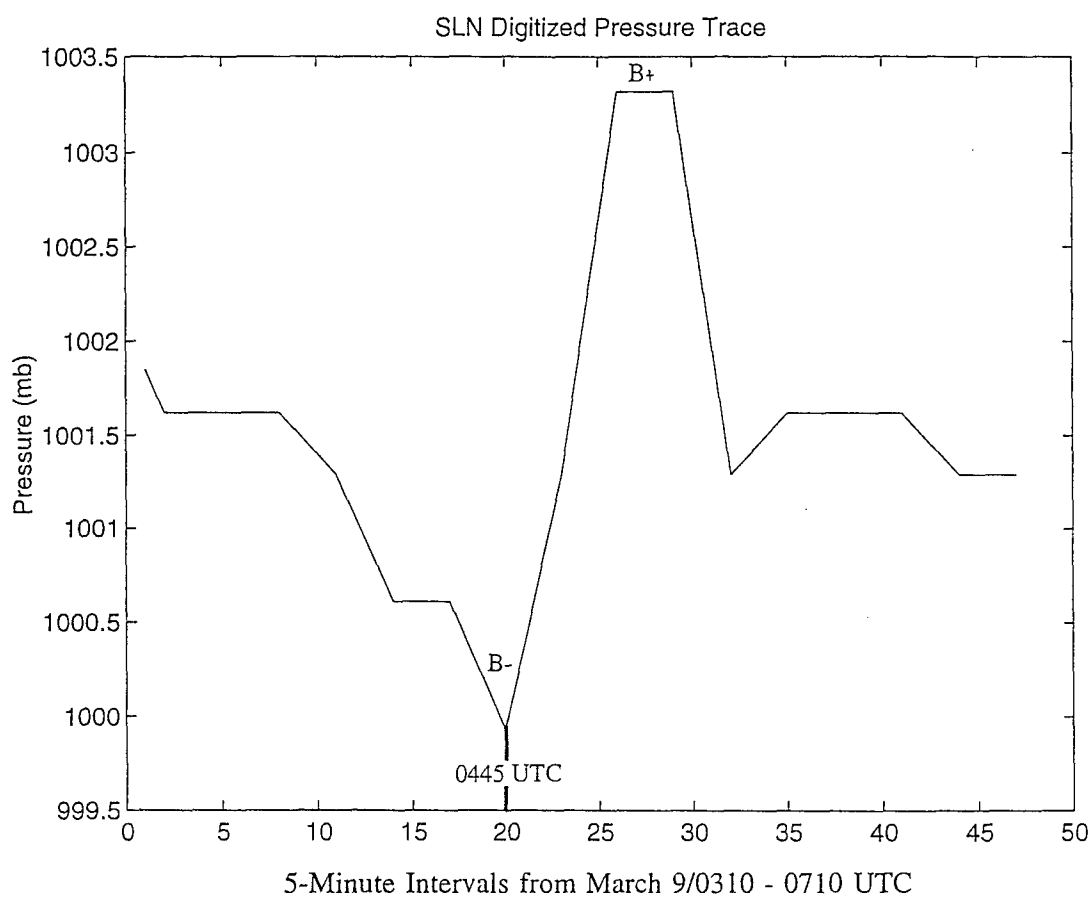


Figure 6.34. Digitized pressure trace from Salina, Kansas (SLN) valid 0300 - 0700 UTC March 9. The time the B- wave is identified has been labeled. The peak following B- (B+) can be classified as a wave of elevation.



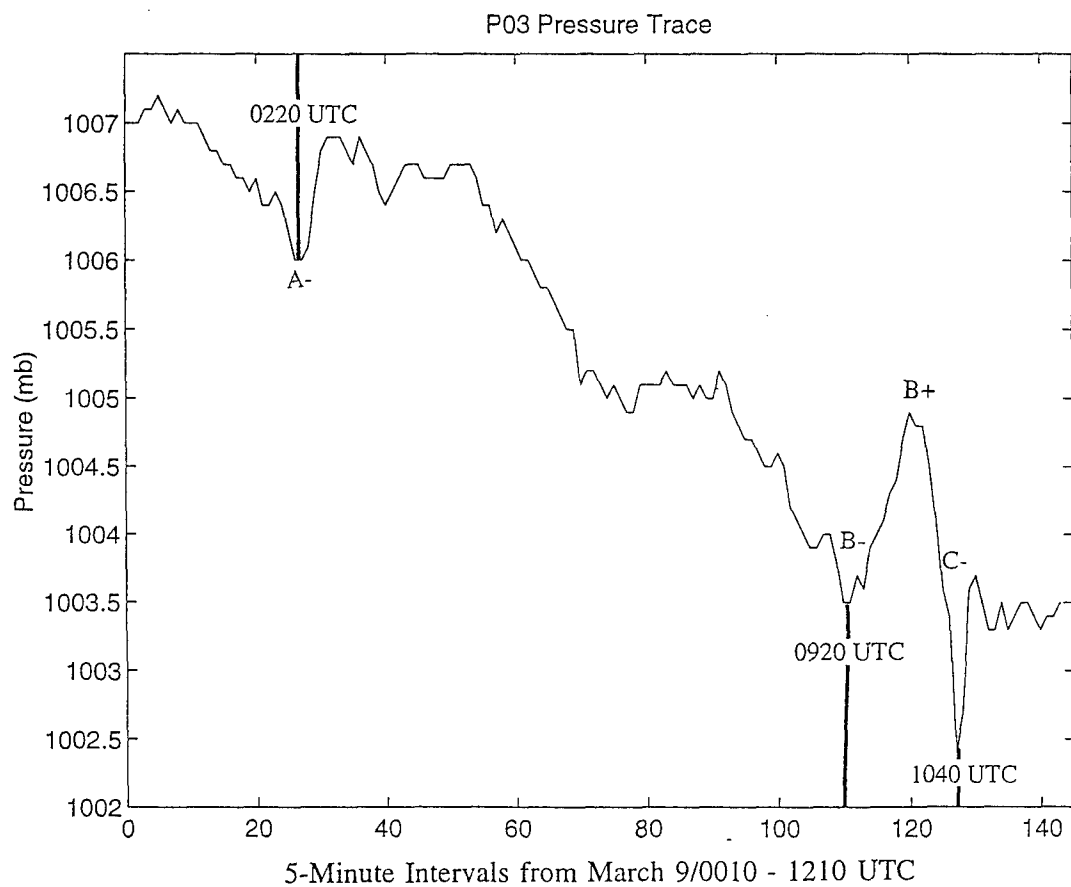


Figure 6.35. Raw pressure trace from Princeton, Missouri (P03) valid 0000 - 1200 UTC March 9. The times waves A-, B- and C- passed the station have been identified. (Note that the signature from B- to the crest following C- constitutes a wavelet.

